ZA8400150

PER-78

THE GEOLOGY AND GEOCHEMISTRY OF SOME EPIGENETIC URANIUM DEPOSITS NEAR THE SWAKOP RIVER, SOUTH WEST AFRICA

by

BRIAN BASIL HAMBLETON-JONES

NUCLEAR DEVELOPMENT CORPORATION OF SOUTH AFRICA (PTY) LTD
N U C O R
Private Bag X256 Pretoria 0001
October 1983

PER-78

THE GEOLOGY AND GEOCHEMISTRY OF SOME EPIGENETIC URANIUM DEPOSITS NEAR THE SWAKOP RIVER, SOUTH WEST AFRICA

by

BRIAN BASIL HAMBLETON-JONES

NOTE: This Report was originally published as a classified document (PIN-322 (CV)) but has been declassified.

NUCLEAR DEVELOPMENT CORPORATION OF SOUTH AFRICA (PTY) LTD
N U C O R
Private Bag X256 Pretoria 0001
October 1983

CONFIDENTIAL

THE GEOLOGY AND GEOCHEMISTRY OF SOME EPIGENETIC URANIUM DEPOSITS NEAR THE SWAKOP RIVER, SOUTH WEST AFRICA

by

BRIAN BASIL HAMBLETON-JONES

Promoter Dr C P Snyman
Department of Geology

Co-Promoter Prof C J Liebenberg
Department of Inorganic and
Analytical Chemistry

Submitted in partial fulfilment

of the requirements

for the degree of

DOCTOR OF SCIENCE

in the

Faculty of Science

University of Pretoria

May 1976

CONFIDENTIAL

ABSTRACT

This study comprises a geological and geochemical investigation of the uranium deposits in the region near the Swakop River which extends from the Langer Heinrich Mountain in the east to the end of the Tumas River in the west, and part of the region between the Khan and Swakop Rivers. The Langer Heinrich area, which includes the Bloed= koppie Flats, Gawib River Valley and surrounding regions totalling 180 km^2 in size, was mapped in detail.

Most of the area is covered by superficial deposits which unconformably overlie basement rocks of the Nosib and Swakop Groups. It is proposed that the informal term Namib group be used to include all these rocks, which were further subdivided into the chronostratigraphic Langer Heinrich calcrete and Tumas gypcrete formations. The Gemsbok calcrete formation unconformably overlies the Langer Heinrich calcrete formation.

The general geology of the basement rocks in the Langer Heinrich region only is discussed. The main litholo= gical units present are the Etusis, Chuos and Tinkas Formations; remaining rock types are the Salem, Bloedkoppie, Gawib and Horebis Granites and pegmatites. The Bloedkoppie Granite, which shows cross-cutting features to the Tinkas and Etusis Formations, is the main granite found in the area. Unusual weathering features are characteristic of the Bloedkoppie Granite, in which alveoles and tafoni are developed.

The general geology of the younger duricrust formations is discussed. These were deposited on a palaeotopographic base of Post-Gondwana and African erosion surface age. The duricrust deposits consist mainly of siliceous fluviatile clastic material that was cemented by calcite, carnotite and/or gypsum. Three genetic varieties of calcrete are represented at the Langer Heinrich, viz calcified breccia-conglomerate, hardpan calcrete and boulder calcrete. Gypcrete is classified in a similar manner into powder gypcrete, vuggy gypcrete and consolidated gypcrete. Towards the west of the area the proportion of gypsum with respect to calcite increases, which seems to be a function of aridity.

In the Gawib River Valley two phases for the precipitation of calcite were found, the first taking place on a much larger scale than the second and the precipitation of carnotite being concurrent with the latter phase. The precipitation of carnotite and the shape of the ore-body were governed primarily by the height and profile of the water-table above the basement rocks.

The epigenetic deposits in the Tumas River Valley were classified into two types, the Tumas and Langer Heinrich Types, with the former related to negative magnetic anomalies in the basement rocks. The geology of the anaerobic basins situated off the coast at Walvis Bay is discussed. These contain diatomaceous mud.

Analytical methods were developed for the separation of thorium, protactinium and uranium from geological materials using various chromatographic procedures. The basic techniques

were modified and adapted as required for the selective separation and purification of uranium from calcite. Alpha spectrometry, neutron activation analysis and delayed neutron counting were the main techniques used.

The occurrence of uranium in the region of study follows a unique geochemical cycle, and the geochemistry at each stage in the cycle was examined. The first stage in the uranium-geochemical cycle was the basement rocks. The rare-earth distribution between these rocks provided evidence concerning their paragenesis, and indicated that the Gawib and Bloedkoppie Granites were the result of partial melting of the Etusis Formation; also, that they are late-syntectonic in age.

The second stage in the geochemical cycle of uranium was the subsurface water. Predictions regarding mineral equilibria could be made from the chemical composition of the water. It was found that the uranium minerals soddyite and carnotite were the stable phases in this environment. From the prospecting aspect, 30 ppb uranium were considered anomalous, while values below this were regarded as background.

The third stage in the geochemical cycle of uranium concerns its occurrence in the duricrust deposits. The segregation of carnotite at the Langer Heinrich was brought about by upward diffusion of dissolved uranium caused by soil suction, and was precipitated by the nucleation of the uranyl cation on montmorillonite, and subsequent complexing with vanadate ions. Mechanisms for the formation of calcrete

and gypcrete are discussed. A new mechanism for the precipi= tation of gypsum is proposed which resulted mainly from the precipitation of calcium sulphate brought in by onshore fogs.

Isotopic disequilibrium measurements showed that uranium is still migrating, and that the age of the carno= tite precipitation is 30 000 years, based on the open-system model of uranium migration.

In the final stage of the geochemical cycle, the geochemistry of uranium in seawater and the diatomaceous muds is discussed. Organic matter was the main precipita= ting agent of uranium from seawater, and its heterogeneous distribution is due to selective uptake by particular organic compounds.

A classification system for the uranium deposits near the Swakop River, based on genetic relationships, is proposed and described in terms of the geochemical cycle of uranium, the mode of transport and mode of deposition. The relationships between the duricrust uranium deposits and the other uranium deposits of South Africa are compared.

SAMEVATTING

Die studie dek 'n geologiese en geochemiese ondersoek van die uraanafsettings in die omgewing van die Swakoprivier wat van die Langer Heinrich-gebergte in die ooste tot aan die einde van die Tumasrivier in die weste strek, asook 'n deel van die gebied tussen die Khan- en Swakoprivier. Die Langer Heinrich-gebied wat die Bloedkoppievlakte, die Gawibrivier=vallei en die omliggende gebiede behels, het 'n totale oppervlakte van 180 km^2 en is in besonderhede gekarteer.

Die grootste gedeelte van die gebied word deur oppervlakafsettings beslaan wat gesteentes van die Nosib- en Swakopgroep diskordant oordek. Daar word voorgestel dat die informele term Namibgroep gebruik word om al dié soorte gesteentes te omvat wat verder in die chronostratigrafiese Langer Heinrich-kalkreet- en Tumas-gipskreetformasie onder=verdeel is. Die Gemsbok-kalkreetformasie oordek die Langer Heinrich-kalkreetformasie diskordant.

Slegs die algemene geologie van die bodemgesteentes in die Langer Heinrich-gebied word bespreek. Die belang=rikste litologiese eenhede is die Etusis-, die Chuos- en die Tinkasformasies. Die oorblywende rotstipes is die Salem-, Bloedkoppie-, Gawib- en Horebisgraniete en -pegma=tiete. Die Bloedkoppiegraniet wat intrusiewe verhoudings ten opsigte van die Tinkas- en Etusisformasies vertoon, is die belangrikste graniet wat in die gebied gevind word. Buiten=gewone verweringseienskappe is kenmerkend van die Bloed=koppiegraniet waarin heuningkoekholtes en tafoni ontwikkel is.

Die algemene geologie van die jonger hardebank= formasie word bespreek. Hulle is op paleotopografiese vloer van pre-Gondwana- en Afrika-erosieoppervlakouderdom afgeset. Die hardebankafsettings bestaan hoofsaaklik uit silika= houdende fluviale klastiese materiaal wat deur kalsiet, karnotiet en/of gips aanmekaar gehou is. Drie genetiese variëteite van kalkreet kom in die Langer Heinrich voor, naamlik verkalkte breksiekonglomerate, hardebankkalkreet en rolblokkalkreet. Gipskreet word op dieselfde wyse in poeiergipskreet, kristalholtegipskreet en gekonsolideerde gipskreet ingedeel. Na die weste van die gebied styg die verhouding van gips tot kalsiet wat 'n funksie van dorheid skyn te wees.

In die Gawibriviervallei is twee fases vir die presipitering van kalsiet gevind. Die eerste het op 'n baie groter skaal as die tweede plaasgevind en karnotiet is gelyktydig met die laaste fase gepresipiteer. Die presipitering van karnotiet en die vorm van die ertsliggaam is hoofsaaklik deur die hoogte en profiel van die grond= watervlak bokant die bodemgesteentes bepaal.

Die epigenetiese afsettings in die Tumasriviervallei is in twee groepe ingedeel, naamlik die Tumas- en die Langer Heinrich-tipes. Eersgenoemde is aan die negatiewe magnetiese anomalieë in die vloergesteentes verwant. Die geologie van die anaërobiese bekkens van die kus van Walvisbaai word bespreek. Hulle bevat diatomeëslik.

Analitiese metodes vir die skeiding van torium, protaktinium en uraan uit geologiese materiaal is ontwikkel waarin verskeie chromatografiese prosedures gebruik word.

Die basiese tegnieke is na vereiste vir die selektiewe skeiding en suiwering van uraan uit kalsiet gewysig en aangepas. Alfaspektrometrie, neutronaktiveringsanalise en vertraagdeneutron-telling was die belangrikste tegnieke wat gebruik is.

Die voorkoms van uraan in die omgewing van di studie word deur 'n unieke geochemiese siklus bepaal en die geochemie is in elke stadium van die siklus ondersoek. Die eerste stadium in die geochemiese siklus van uraan is die bodem= gesteente. Die verspreiding van seldsame aarde tussen die gesteentes het bewyse aangaande hulle paragenese gelewer en het ook aangedui dat die Gawib- en Bloedkoppiegraniete die gevolg is van gedeeltelike smelting van die Etusisformasie, en ook dat hulle laat-sintektonies in ouderdom is.

Die tweede stadium in die geochemiese siklus van uraan is die ondergrondse water. Voorspellings oor mineraal= ewewig kon uit die chemiese samestelling van die water gemaak word. Daar is gevind dat die uraanminerale soddiet en karnotiet die stabiele fases in die omgewing was. Uit 'n prospekteeroogpunt beskou, is 30 dpb uraan as 'n anomalie beskou, terwyl waardes laer as hierdie syfer as agtergrond beskou is.

Die derde stadium in die geochemie van uraan hang saam met sy voorkoms in die hardebankafsettings. Die afskeiding van karnotiet in die Langer Heinrich is die gevolg van die opwaartse diffusie van opgeloste uraan deur grondsuiging. Die uraan is hierna deur kernvorming van die uranielkatioon op montmorilloniet en daaropvolgende

kompleksvorming met vanadaatione gepresipiteer. Meganismes vir die vorming van kalkreet en gipskreet word bespreek. 'n Nuwe meganisme vir die presipitering van gips word aan die hand gedoen. Dit het hoofsaaklik uit die presipitering van kalsiumsulfaat ontstaan wat deur mis van die kus af ingebring is.

Die onewewig in isotoopsamestelling van die uraan toon dat uraan nog steeds migreer, en dat die ouderdom van die karnotietpresipitering 30 000 jaar is, indien 'n oop sisteem vir die migrering van uraan aanvaar word.

In die finale stadium van die geochemiese siklus word die geochemie van uraan in seewater en in die diatomeëslik bespreek. Organiese materiaal was die belangrikste presipi= teermiddel van uraan uit seewater, en sy onreëlmatige ver= spreiding is aan selektiewe opname deur sekere organiese verbindings toe te skrywe.

'n Indeling op grond van genetiese verwantskappe word vir die uraanafsettings naby die Swakoprivier voorgestel en [illegible] in terme van die geochemiese siklus van uraan, en die transport- en afsettingsmetode beskryf. Die verwantskappe tussen die hardebank- en die ander uraanafsettings van Suid-Afrika word vergelyk.

CONTENTS

		Page
1.	INTRODUCTION	30
2.	ACKNOWLEDGEMENTS	3[illegible]
	PART I - GENERAL GEOLOGY	38
3.	REGIONAL GEOLOGY	3[illegible]
	3.1 Stratigraphy	3[illegible]
	3.2 Regional Structure	41
4.	THE GEOLOGY OF THE BASEMENT ROCKS	43
	4.1 Etusis Formation (NS_1G)	4[illegible]
	4.2 Chuos Formation (D_2G)	44
	4.3 Tinkas Formation (D_4S)	4[illegible]
	4.4 Salem Granite (GN_2)	4[illegible]
	4.5 Bloedkoppie Granite (G_1)	4[illegible]
	4.6 Gawib Granite (G_3)	54
	4.7 Horebis Granite (G_5)	5[illegible]
	4.8 Pegmatites	5[illegible]
5.	GENERAL GEOLOGY OF THE YOUNGER FORMATIONS	5[illegible]
	5.1 Geomorphology	5[illegible]
	5.1.1 Palaeogeomorphology	[illegible]
	5.1.2 Modern geomorphology	[illegible]
	5.2 Langer Heinrich Calcrete Formation	[illegible]
	5.3 Gemsbok Calcrete Formation	[illegible]
	5.4 Tumas Gypcrete Formation	[illegible]
6.	THE GEOLOGY OF THE URANIUM DEPOSITS	[illegible]
	6.1 Deposits in the Gawib River Valley	[illegible]
	6.2 Deposits in the Tumas River Valley	[illegible]

Page

6.3 Offshore Marine Deposits

6.4 Comparison Between the Langer Heinrich, Yeelerrie and Wyoming Uranium Deposits

PART II - ANALYTICAL METHODS

7. CHROMATOGRAPHIC SEPARATION, PURIFICATION AND SOURCE PREPARATION OF THORIUM, PROTACTINIUM AND URANIUM FROM GEOLOGICAL MATERIALS

7.1 Experimental Procedure for the Separation of Thorium, Protactinium and Uranium from Synthetic, and in Some Instances, Actual Samples

7.2 Experimental Procedure for the Purification of Thorium, Protactinium and Uranium from Synthetic, and in Some Instances, Actual Samples

7.3 Source Preparation of Thorium, Protactinium and Uranium from Synthetic Samples

7.4 Chromatographic Separation Scheme

8. NEUTRON ACTIVATION ANALYSIS OF THE BLOEDKOPPIE AND GAWIB GRANITES AND THE ROCKS OF THE TINKAS FORMATION

8.1 Experimental Procedure

9. DISSOLUTION AND ANALYSIS OF THE EPIGENETIC FRACTION OF CALCRETE BY NEUTRON ACTIVATION ANALYSIS

9.1 Neutron Activation Analysis

Page

10. CHROMATOGRAPHIC SEPARATION AND PURIFICATION OF URANIUM FOR MASS SPECTROMETRIC ANALYSIS 141

11. MISCELLANEOUS METHODS 145

11.1 Delayed Neutron Counting 145

11.2 X-Ray Diffraction Analysis 146

PART III - GEOCHEMISTRY 146

12. THE GEOCHEMISTRY OF THE BASEMENT ROCKS 146

12.1 Analytical Results 147

12.2 Geochemistry of Uranium in Granitic Rocks 149

12.3 Geochemistry of the Rare-Earth Elements and Their Bearing on the Origin of the Granitic Rocks 152

12.4 Summary 155

13. GEOCHEMISTRY OF THE SUBSURFACE WATERS OF THE NAMIB DESERT 157

13.1 Analytical Results 160

13.2 Characteristics and Classification of the Subsurface Waters 167

13.3 Factor Analysis 177

13.4 Geochemistry of Groups 1 and 2 Subsurface Waters 182

13.5 Solution Geochemistry of Uranium, Vanadium and Calcium 188

13.5.1 Uranium 189

13.5.2 Vanadium 198

13.5.3 Calcium 199

Page

13.6 Source of Ions in Solution 200

13.7 Geochemistry of Other Metallic Elements in the Subsurface Waters 201

13.8 Summary 204

14. GEOCHEMISTRY OF THE DURICRUST DEPOSITS 205

14.1 Analytical Results 206

14.2 General Chemistry of the Calcretes 213

14.3 Factor Analysis 214

14.4 Geochemistry of Individual Elements or Groups of Elements 223

14.4.1 Iron

14.4.2 Alumina and silica

14.4.3 Potassium, sodium and magnesium

14.4.4 The rare-earth elements

14.4.5 Vanadium and uranium

14.4.6 Geochemical mobility of the elements

14.5 Geochemistry and Origin of Calcrete

14.6 Geochemistry and Origin of Gypcrete 250

14.7 Isotopic Disequilibrium of Uranium 256

14.7.1 Isotopic equilibrium and dis= equilibrium

14.7.2 Geochronology

14.7.3 Mass spectrographic analysis

14.8 Summary

15. GEOCHEMISTRY OF THE DIATOMACEOUS MUDS

15.1 Geochemistry of the Muds

15.2 Summary

Page

16. CLASSIFICATION AND AGE RELATIONSHIPS OF THE URANIUM DEPOSITS

17. SUMMARY AND CONCLUSIONS

REFERENCES

APPENDIX 1

APPENDIX 2

LIST OF FIGURES

Page

Fig. 1 Gemini satellite photograph showing the areas included within this study. Approximate scale 1:800 000. (Courtesy, US Information Service).

Fig. 2 A schematic relationship between gypsum and calcium contents of the duricrusts in the Namib Desert with respect to the degree of aridity.

Fig. 3 Schematic profiles through the superficial duricrust deposits to the basement rocks at
(a) The Langer Heinrich area;
(b) Von Stryks pit in the bed of the Tumas River. The pit is only approximately 6 m deep and the geology below this point is only inferred. Information from seismic data tends to confirm this. (See Fig. 7).

Fig. 4 Geomorphological development of the sediments in the Gawib River Valley.

Fig. 5 A profile of gypsum accumulation in the Langer Heinrich calcrete formation which outcrops in the bed of the Gawib River.

Fig. 6 Lithological descriptions of profiles through the Gemsbok calcrete formation. For the site localities of the profiles refer to Map 1.
(a) Profile 1: Gemsbok calcrete formation in the west.
(b) Profile 2: Gemsbok and Langer Heinrich calcrete formations near the original prospecting campsite.
(c) Profile 3: Gemsbok calcrete formation in central part of the erosional fanglomerate.

Fig. 7 A seismic profile down the 15° line of longitude. (Courtesy, Anglo American Prospecting Co. Ltd).

Fig. 8 Profiles of the uranium ore-body in the Gawib River Valley as determined from the radiometric logs of the percussion borehole powders. The outline of the ore-body includes all those values above 0,1 kg eU_3O_8/t or 100 ppm eU_3O_8.

Page

Fig. 9 A cross section of the ore-body through profile C - C' to show the relationships between the mineralogy, host rock and basement rocks.

Fig. 10 A portion of the Langer Heinrich calcrete formation showing mineralization isopachs interpolated from percussion borehole data. Note position of profile C. (Compiled from maps of General Mining and Finance Co. Ltd).

Fig. 11 Seismic isopachs interpolated from seismic refraction data of the same locality as in Fig. 10. (Compiled from maps of General Mining and Finance Co. Ltd.).

Fig. 12 Sketch of a radioactive anomaly in the gypcrete in the bed of the Swakop River.

Fig. 13 Airborne magnetic axes and radiometric anomalies for the area between the Swakop River and the 23° 15' line of latitude.

Fig. 14 Diagrammatic representation of a Tumas type uranium deposit. Epigenetic uranium in gypcrete derived from a primary uranium source in alaskites.

Fig. 15 Four anaerobic basins on the continental shelf which are filled with diatomaceous mud.
(a) Basins in relation to depth of water.
(b) The distribution of uranium in the basins.

Fig. 16 Elution curves for thorium, protactinium and uranium from strong base anion exchange resin using Bio-Rad AG1-X8 in the chloride form.

Fig. 17 Absorption of elements by strong base anion exchange resin in hydrochloric acid. (Kraus and Nelson, 1956, p. 114).

Fig. 18 Elution curves for thorium, lanthanum and europium from strong base anion exchange resin using Bio-Rad AG1-X8 in the chloride form.

Fig. 19 Absorption of elements by strong base anion exchange resin in HCl-HF mixtures and HCl only. Thick lines give the distribution coefficients in the absence of HF. Thin lines give the distribution coefficients in the presence of HF. (Nelson, Kraus and Kraus, 1950, p. 344).

Page

Fig. 20 Absorption of elements by strong base anion exchange resin in nitric acid. (Buchanan and Faris, 1960, p. 365). 111

Fig. 21 Elution curves for the rare earths and thorium from strong base anion exchange resin using Bio-Rad AGI-X8 in the nitrate form. 113

Fig. 22 Elution curves for iron, manganese, arsenic and uranium using reversed phase liquid chromatography with tributylphosphate as the supporting substance and nitric acid and distilled water as the mobile phases. 11-

Fig. 23 Extraction coefficients of thorium, protactinium and uranium into amines at different concentrations of hydrochloric acid. P = primary amine, S = secondary amine, T = tertiary amine, Q = quarternary amine. (Ahrland et al, 1973, p. 578). 11-

Fig. 24 Elution curves for zirconium, niobium, hafnium and protactinium using reversed phase liquid chromatography with aliquat-33 as the stationary phase, teflon as the supporting substance and hydrochloric acid as the mobile phase. 11-

Fig. 25 A drawing of the electroplating cell used for the preparation of sources of thorium, protactinium and uranium. 11-

Fig. 26 Variation of alpha-particle activity of ^{238}U in relation to the thickness of the source, expressed as weight of U per unit surface area. 1-6

Fig. 27 Variation of alpha-particle activity of ^{238}U with electroplating time. 1-1

Fig. 28 Alpha spectra for thorium, protactinium and uranium isotopes. 1-

Fig. 29 Gamma-ray spectrum after a decay of nine days for the analysis of lanthanum, barium, lutetium and samarium in the Bloedkoppie Granite. 1-

Fig. 30 Gamma-ray spectrum after a decay of 37 days for the analysis of europium, cobalt, tantalum, rubidium, samarium, terbium, cesium, hafnium, protactinium (thorium) and cerium in the Bloedkoppie Granite. 1-

Fig. 31 Gamma-ray spectrum for the analysis of vanadium in the schists and granofelses of the Tinkas Formation. 1-1

Page

Fig. 32 Elution curves for zinc, europium, cobalt and scandium using reversed phase liquid chromatography with IBP as the stationary phase, supported on Kel-F and 5,5M HNO_3 as the mobile phase. The dashed line shows the activity distribution on the column and the unbroken lines the activity distribution in the eluate. 134

Fig. 33 Gamma-ray spectrum for the analysis of aluminium and vanadium in the epigenetic calcite fraction. 137

Fig. 34 Gamma-ray spectrum for the analysis of dysprosium in the epigenetic calcite fraction. 138

Fig. 35 Gamma-ray spectrum after four days' decay for the analysis of lanthanum, samarium, ytterbium and lutetium in the epigenetic calcite fraction. 139

Fig. 36 Gamma-ray spectrum after 13 days' decay for the analysis of cerium, iron, cobalt, scandium and europium in the epigenetic calcite fraction. 140

Fig. 37 Spectrum of ^{238}U and ^{235}U obtained from the mass spectrometer. 142

Fig. 38 Rare-earth abundances in the Etusis Formation and banded gneiss divided by the rare-earth abundances in chondrites, plotted against the atomic number. 157

Fig. 39 Rare-earth abundances in the Tinkas Formation and Salem Granite divided by the rare-earth abundances in chondrites, plotted against the atomic number. 158

Fig. 40 Rare-earth abundances in the Gawib and Bloedkoppie Granites divided by the rare-earth abundances in chondrites, plotted against the atomic number. 159

Fig. 41 The area and localities of the boreholes from which the subsurface water samples were taken. Each sample point is designated as follows: e.g. [12] (2)20 means that the sample was taken from borehole number 20, classified into Group 2, and contains 12 ppb U. 164

Fig. 42 Schoeller diagram, comparison of the ionic distributions in subsurface waters of the Namib Desert and seawater in terms of equivalents per million ionic species. 166

Fig. 43 Activity diagram for the system Na_2O-Al_2O_3-SiO_2-H_2O at 25 °C at unit activity of water and 100 kPa. Adapted from Helgeson *et al* (1969, p. 462). Subsurface water samples 30 and 31 from the Gawib River Valley fall into the montmorillonite field. 142

Fig. 44 Equilibrium plot for calcite or calcareous rocks as a function of temperature with respect to the subsurface brines. $pCa = -\log_{10}(Ca^{2+})$ and $pCO_3 = -\log_{10}(CO_3^{2-})$. The minimum, maximum and mean ($\bar{x}$) for all water samples are plotted. (Values taken from Table 19). Samples 30 and 31 from the Gawib River Valley are also plotted. The temperature for the subsurface water was assumed to be 20 °C. 143

Fig. 45 Equilibrium plot for quartz and amorphous silica as a function of temperature with respect to the subsurface brines. $pH_4SiO_4 = -\log_{10}(H_4SiO_4)$. The minimum, maximum and mean ($\bar{x}$) for all water samples are plotted. (Values taken from Table 19). Samples 30 and 31 from the Gawib River Valley are also plotted. The temperature for the subsurface water was assumed to be 20 °C. 144

Fig. 46 Variation diagram of uranium plotted against carbonate. Four groups in the water samples are indicated. The dashed lines give the approximate group boundaries. 147

Fig. 47 A plot of the X- and Y-canonical variables derived from a multivariate discriminant analysis of the data from 31 subsurface water samples. (+ = mean). 149

Fig. 48 Variation diagram of carbonate plotted against silica for Groups 1 and 2 subsurface waters. 166

Fig. 49 Multivariate regression analysis of uranium, carbonate and pH in the subsurface water samples from Group 1. 170

Fig. 50 Multivariate regression analysis of uranium, carbonate and pH in the subsurface water samples from Group 2. 171

Fig. 51 Aqueous equilibrium diagrams of the system U-O_2-H_2O-CO_2 at 25 °C and 100 kPa.
(a) $\Sigma CO_2 = 10^{-3}$
(b) $\Sigma CO_2 = 10^{-1}$
(Hostetler and Garrels, 1962, p. 146-147). 173

CONFIDENTIAL

Page

Fig. 52 The zone of weathering superimposed on an Eh-pH diagram. It occupies an area in the carnotite stability field. 1[illegible]

Fig. 53 Schematic diagram showing the thickness of sediment above an ephemeral water-table (——) and the leaching ability of water in relation to the time of rainfall (----). 19[illegible]

Fig. 54 Variation diagram of vanadium plotted against fluorine for the subsurface water samples from Groups 1 and 2. 19[illegible]

Fig. 55 Variation diagram of calcium plotted against sodium for the subsurface waters from Groups 1 and 2. 20[illegible]

Fig. 56 Change in composition of carbonated water during equilibration with calcite at various temperatures in the presence (A) and in the absence (B) of a vapour phase. (Gatle and Ball, 1973, p. 175). 2[illegible]

Fig. 57 Variation diagram of Al_2O_3 plotted against Fe_2O_3 (correlation coefficient r = 0,87) for the epigenetic fraction of the calcretes. (+ = mean). 2[illegible]

Fig. 58 The relationship between magnesium and calcium in epigenetic calcite as demonstrated by plotting the ratio MgO/FeO against MgO. 2[illegible]

Fig. 59 Relative percentage rare-earth concentrations in
(a) Epigenetic calcite, Langer Heinrich.
(• = H[illegible]-3, o = H[illegible]-5, × = H[illegible]-13, Δ = C5-15).
(b) Sediments from other parts of the world.
• = Belders Formation marble, USA;
× = average, 11 025 limestones from the Russian Platform;
o = composite of North American shales.
(Herrmann, 1970). 2[illegible]

Fig. 60 Distribution patterns of rare earths, normalized to the abundances in 20 chondritic meteorites.
× = epigenetic calcite, Langer Heinrich area.
o = average, 11 025 limestones from the Russian Platform.
(Herrmann, 1970). 2[illegible]

Fig. 61 Plots of the fractionation function La + Ce/Yb + Lu against
(a) sum of the rare earths;
(b) percentage iron oxide. 2[illegible]

Page

Fig. 62 Variation diagrams of rare-earth elements plotted against percentage iron oxide. 234

Fig. 63 Plots of the correlation coefficients of lutetium, dysprosium, samarium and lanthanum against the atomic number. 235

Fig. 64 (a) Variation diagram of uranium plotted against dysprosium for both mineralized and unmineralized calcretes. 237

(b) Variation diagram of vanadium plotted against dysprosium for both mineralized and unmineralized calcretes. 237

Fig. 65 Variation diagram of uranium plotted against vanadium for both mineralized and unmineralized calcretes.

Fig. 66 Geochemical mobility of the elements in the supergene environment. (After Dall' Aglio, 1971, p. [illegible].

Fig. 67 The geochemical mobility of the elements in the epigenetic calcite of sample HJ2-5, with respect to the Bloedkoppie Granite. Represented in terms of the removal index. 24

Fig. 68 The geochemical mobility of the elements in the epigenetic calcite of sample HJ2-15, with respect to the Bloedkoppie Granite. Represented in terms of the removal index. 247

Fig. 69 Pore water pressure distribution in a sediment. (After Schlichting, 1971, p. 9). 245

Fig. 70 Diffusion model for the formation of carnotite in layers and concretions at the Langer Heinrich. (After Berner, 1971, p. 103). 248

Fig. 71 A plot of the factor scores of factor 3 (Table 34) against carnotite mineralization in terms of the concentration of uranium. (Numbers as in Table 30). 249

Fig. 72 The sulphur cycle in the diatomaceous sediments of the continental shelf, the Atlantic Ocean and the Namib Desert. 254

Fig. 73 Schoeller diagram, comparisons of the ionic distributions in sea- and fogwaters in terms of equivalents per million ionic species. 255

Fig. 74 A flow diagram of uranium and the accumulation of daughter isotopes in an open-system model. 257

Page

Fig. 75 Profiles through the diatomaceous mud for phosphorus pentoxide, molybdenum, vanadium, uranium and loss on ignition at 500 °C. (Borehole SWA 38). 271

Fig. 76 Profiles through the diatomaceous mud for phosphorus pentoxide, molybdenum, vanadium, uranium and loss on ignition at 500 °C. (Borehole SWA 50). 271

Fig. 77 Variation diagram of vanadium plotted against uranium for the diatomaceous muds. Normalized with loss on ignition at 500 °C. 273

Fig. 78 Variation diagram of molybdenum plotted against uranium for the diatomaceous muds. Normalized with loss on ignition at 500 °C. 274

Fig. 79 A genetic classification for the Langer Heinrich and Tumas type uranium ore deposits in terms of the geochemical cycle and mode of transport and deposition. 2[illegible]

Fig. 80 The relationships of the duricrust deposits with respect to other types of uranium deposits in terms of ore-forming processes. 281

Fig. 81 Relationships between ages of host rock and the associated uranium mineralization.
(a) Age of host rock enclosing the uranium mineralization.
(b) Age of uranium mineralization. 2[illegible]

LIST OF TABLES

		Page
TABLE 1	Stratigraphic terminology for the rocks in the Damara orogen.	40
TABLE 2	Partial chemical analysis of the salt crust accumulating in a tafoni on the Bloedkoppie.	54
TABLE 3	Chronological development of the Namib Desert.	71
TABLE 4	General composition of the diatomaceous muds.	92
TABLE 5	Comparative criteria between the Langer Heinrich and Yeelerrie uranium deposits.	101
TABLE 6	Comparative criteria between the Langer Heinrich and Wyoming uranium deposits.	10
TABLE 7	Nuclear data for naturally occurring isotopes of thorium, protactinium and uranium.	10
TABLE 8	Nuclear data for radionuclides produced by thermal neutrons.	11
TABLE 9	Procedure for the chromatographic separation of thorium, protactinium and uranium from geological materials.	124
TABLE 10	Nuclear data for radionuclides produced by thermal neutrons.	12
TABLE 11	Procedure for the chromatographic separation of uranium from calcretes.	13
TABLE 12	Procedure for the chromatographic separation of uranium from calcrete, suitable for mass spectrometric analysis.	14
TABLE 13	Partial chemical analysis and trace element concentrations in the Bloedkoppie and Gawib Granites.	14
TABLE 14	Samples used in the geochemical interpretation of the rare-earth element distributions.	14
TABLE 15	Chemical analyses of Group 1 subsurface waters from the Namib Desert.	15
TABLE 16	Chemical analyses of Group 2 subsurface waters from the Namib Desert.	1

Page

TABLE 17 Chemical analyses of Group 3 subsurface waters from the Namib Desert. 163

TABLE 18 Chemical analyses of Group 4 subsurface waters from the Namib Desert. 164

TABLE 19 Means and range of concentrations of ions in subsurface waters from the Namib Desert for all 31 samples. 165

TABLE 20 Trace element analyses of subsurface waters from the Namib Desert. (Annual Prospecting Report, 1973, Prospecting Grant M46/3/209). 166

TABLE 21 Classification of the subsurface waters into groups, using multivariate discriminant analysis, and the calculated probability associated with each sample. 174

TABLE 22 Correlation matrices for log-transformed data of the subsurface waters from the Namib Desert for Groups 1 and 2. 181

TABLE 23 (a) Summary of the correlation matrix (Table 22) for the Group 1 subsurface water. 182

(b) Summary of the correlation matrix (Table 22) for the Group 2 subsurface water. 183

TABLE 24 Varimax matrices for Groups 1 and 2 subsurface waters. 185

TABLE 25 Correlation matrix of the log-transformed data of trace element concentrations in the subsurface waters of the Namib Desert. 203

TABLE 26 Partial whole-rock chemical analyses of calcrete powders from percussion boreholes at the Langer Heinrich. 208

TABLE 27 Uranium, carbonate and sulphate analyses of calcrete powders from percussion boreholes at the Langer Heinrich. 209

TABLE 28 Partial whole-rock chemical analyses of the hardpan calcrete of the Langer Heinrich calcrete formation. 210

TABLE 29 Semi-quantitative spectrographic analyses for trace elements in the calcrete powders from percussion boreholes at the Langer Heinrich. (Courtesy, Anglo American Research Laboratories). 211

Page

TABLE 30 Partial chemical analyses of the epigenetic fraction of calcrete powders from percussion boreholes at the Langer Heinrich. 213

TABLE 31 World average values for calcrete. (Goudie, 1972, p. 450). 214

TABLE 32 Correlation matrices of 13 samples of the epigenetic fraction of the calcretes from the Langer Heinrich.
(a) Untransformed data.
(b) Log-transformed data. 215

TABLE 33 Summaries of correlation matrices in Table 32.
(a) Untransformed data.
(b) Log-transformed data. 217

TABLE 34 Varimax matrix of 13 samples of the epigenetic fraction of the calcretes from the Langer Heinrich. 218

TABLE 35 Promax matrix of 13 samples of the epigenetic fraction of the calcretes from the Langer Heinrich.

TABLE 36 Correlation matrix of factors in the promax matrix of Table 35.

TABLE 37 Vanadium concentrations in the Tinkas Formation.

TABLE 38 Analyses of sea- and fogwaters (Courtesy, CSIR). 252

TABLE 39 Fog precipitation, equivalent rainfall in 1958 and actual mean rainfall at Swakopmund. (Nagel, 1962, p. 57). 253

TABLE 40 Precipitation of gypsum expressed as $CaSO_4$ in tons/km^2/month.

TABLE 41 $^{234}U/^{238}U$ activity ratios for the duricrusts of the Langer Heinrich and Von Stryks pit.

TABLE 42 $^{234}U/^{238}U$ activity ratio for the Bloedkoppie Granite.

TABLE 43 Disequilibrium ages of uranium mineralization by closed- and open-system models.

TABLE 44 $^{234}U/^{238}U$ atom ratios in calcrete from the Langer Heinrich and uranothorianite from Phalaborwa. 264

		Page
TABLE 45	The concentration of some elements in seawater (ppm). (Krauskopf, 1956, p. 3 and Allègre and Michard, 1974, p. 41).	266
TABLE 46	Element concentrations in two cores of diatomaceous muds.	268
TABLE 47	Concentration factors, relative to seawater, for the elements in diatomaceous muds.	269
TABLE 48	Maximum concentrations of elements in diatomaceous muds. (Calvert and Price, 1970, p. 594).	275

LIST OF PLATES

		Page
PLATE 1	Bloedkoppie Granite dome viewed across the Bloedkoppie Flats from the Gawib Ridge, with the Langer Heinrich Mountain in the background to the north. Granite outcrops in the middle foreground.	49
PLATE 2	Secretion pegmatite in the Bloedkoppie Granite with biotite crystallizing along and normal to the contacts.	49
PLATE 3	Photomicrograph showing weathering effects in the feldspars. Crossed nicols, magnification x 50.	51
PLATE 4	Alveoles in the Bloedkoppie Granite.	51
PLATE 5	Tafoni on the north-facing slope of the Bloedkoppie dome. Dimensions are approximately 10 m high, 10 m deep and 30 m wide.	
PLATE 6	Aerial photograph showing the fanglomerate of the Gemsbok calcrete formation in the Gawib River Valley.	
PLATE 7	Caverns and overhangs in the Gemsbok calcrete formation formed by deflationary processes.	
PLATE 8	Stone pavement on the Gawib Flats composed of angular to rounded quartz pebbles.	
PLATE 9	Flatter pebbles in schist in the Langer Heinrich calcrete formation orientated in the direction of waterflow as shown by the arrow.	
PLATE 10	Photomicrograph showing the pushing apart of detrital grains by calcite. D = detrital grain, C = calcite. Magnification x 50.	
PLATE 11	Photomicrograph showing how the panes of a biotite 'book' have been separated by the precipitation of calcite between them. Magnification x 50.	
PLATE 12	Photomicrograph illustrating a low degree of calcification. The black areas are pore spaces which frequently surround the detrital grains. Separation of grains by calcite precipitation is less extensive. Crossed nicols, magnification x 50.	

Page

PLATE 13 Photomicrograph showing rims of second generation calcite surrounding detrital grains. The black areas are carnotite crystals in a lighter calcite matrix. Magnification x 50. 72

PLATE 14(a) Electron photomicrograph of amorphous carnotite in calcrete. Magnification x 1 000. 74

PLATE 14(b) Electron scatter photomicrograph of uranium of the same area in Plate 14(a). 74

PLATE 14(c) Electron scatter photomicrograph of vanadium of the same area in Plate 14(a). 74

PLATE 15(a) Electron photomicrograph of platy carnotite in calcrete. Magnification x 1 000. 75

PLATE 15(b) Electron photomicrograph of platy carnotite in calcrete. Magnification x 3 000. 75

PLATE 15(c) Electron scatter photomicrograph of uranium of the same area in Plate 15(a). 75

PLATE 16 Photomicrograph showing the crystallization of carnotite (black areas) around detrital fragments. 76

PLATE 17 Hardpan calcrete overlying Bloedkoppie Granite. 165

PLATE 18 Photomicrograph of the hardpan calcrete. Detrital grains are set in a semi-opaque ferrugenous calcite matrix. Transparent second generation calcite has filled pore spaces and formed rims round the larger grains. Crossed nicols, magnification x 50. (Page 165 bound after page 74) 165

PLATE 19 A cross-sectional view through the Gemsbok calcrete formation in the western part of the area. 82

PLATE 20 Laminated zone of calcrete in the Gemsbok calcrete formation. 82

PLATE 21 Stratified zone in the Gemsbok calcrete formation. 83

PLATE 22 Large boulders (up to 300 mm in diameter) have been pushed apart by calcite crystallization. 83

LIST OF MAPS

MAP 1 In folder

1. INTRODUCTION

This study covers the areas of the Gawib River Valley, the Tumas River Valley, the Dorstrivier area and the diatomaceous muds in the anaerobic basins on the continental shelf. The localities are shown on the Gemini Satellite photograph (Fig. 1).

The main physical features are the Swakop, Khan and Kuiseb canyons, the Husab, Witpoort, Langer Heinrich, Schieferberge and Chuos Mountains, and the extensive flat regions which form the Namib Plain. Ephemeral drainage courses such as the Tumas River cross the plain from east to west.

Rainfall at Swakopmund over 35 years averages 18 mm per year (Nagel, 1962) which increases to 150 mm further inland (Smith, 1965, p. 6). Most of the precipitation in the Namib Desert is from fogs blown inland from the sea, and amounts to 130 mm per year (Nagel, 1962).

In the Namib Desert there are essentially two types of uranium deposits that are associated with the rocks of the Damara Orogen. The first of these is the primary "porphyry"-type mineralization (Armstrong, 1974) found in granitic rocks closely associated with the highest metamorphic grade. Deposits at Rössing and Goniakontes are typical examples. The second type of deposit comprises the epigenetic uranium occurrences which are found in the duricrusts which form a superficial calcareous cover over a large part of the Namib Desert. A number of mining companies

are currently engaged in prospecting programs embracing these two types of mineralization.

During 1970 and 1974 the Geological Survey of South Africa undertook airborne magnetic and aeroradiometric surveys of an area east of Walvis Bay. The most promising radiometric anomalies were subsequently taken out under concession by mining companies. To the north of the area, Anglo American Prospecting Co. Ltd took the farms Dorstrivier 15, Nordenburg 76, Vlakteplaas 110 and part of Bloemhof 109. In 1974 they were granted three concessions falling mostly within the Tumas River Valley. General Mining and Finance Corp. Ltd was granted the Gawib River Valley in the vicinity of the Langer Heinrich Mountain in 1973.

Uranium occurrences in calcrete have also been reported from Yeelerrie in Western Australia (Langford, 1974), Somalia (Dall'Aglio, 1974) and the Gobi Desert in China (personal communication, Dr A. Clark, AAEC). The chances are good that similar deposits will be discovered elsewhere, for deserts cover large areas of the earth's surface. Gypcrete uranium deposits may be unique to the Namib Desert, for as yet none have been reported from other parts of the world.

The main purpose of this investigation was to determine the geochemical behaviour of uranium and other elements, firstly in the primary environment of the basement rocks, secondly in the hydrological environment characterizing the subsurface waters, and finally in the epigenetic

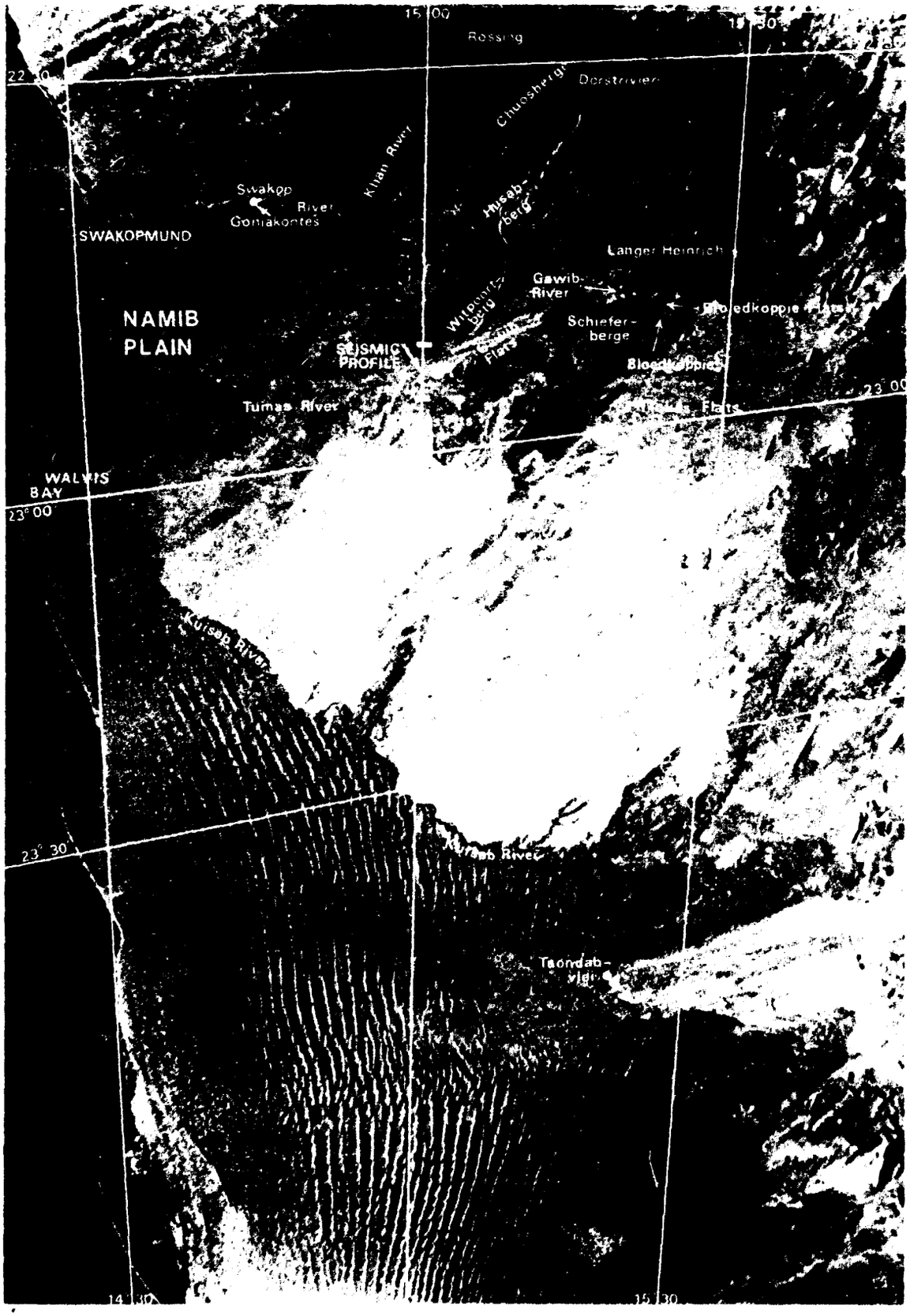


FIG 1 Gemini satellite photograph showing the areas included within this study. Approximate scale 1:800 000 *(Courtesy U S Information Service)*

environment of superficial rocks and diatomaceous muds.

The work was concentrated mainly around the Langer Heinrich uranium deposit, as this was the first major discovery of its kind in Southern Africa. It was the only area mapped in detail for this investigation. The geology of the remaining areas was obtained from maps supplied by Anglo American Prospecting Co. Ltd in their annual prospecting reports submitted to the Atomic Energy Board. (Annual Prospecting Reports, 1972, 1973, Prospecting Grant M46/3/209; Annual Prospecting Report, 1974, Prospecting Grant M46/3/430; Annual Prospecting Report, 1974, Prospecting Grant M46/3/433; Annual Prospecting Report, 1974, Prospecting Grant M46/3/487.)

The Langer Heinrich area was mapped directly onto aerial photographs at a scale of 1:36 000, from which the data was transferred to 1:25 000 topographical maps (Map 1). Some of the information regarding the basement rocks was compiled from Jacob (1974).

Whole-rock, powder, diatomaceous mud and water samples were collected. At the Langer Heinrich, only surface whole-rock samples of calcrete were taken, as no borehole cores were available at that time. Powder samples of calcrete from the percussion drilling program were readily available. Four boreholes were drilled specifi= cally for this investigation and were numbered HJ1, HJ2, J1 and AD1. Samples from borehole C5, not specifically drilled for this purpose, were also used. The localities of all five boreholes are shown in Map 1. The powder samples are representative of every half-metre in depth. With percussion drilling it was not possible to

obtain a sample from an exact depth, and any analytical value is therefore the mean for the half-metre it comprises.

Hand specimens of the basement rocks were obtained from the localities shown in Map 1. Each sample number was designated with the prefix LH.

Most of the water samples were obtained north of the Swakop River. The localities are given in Fig. 41. These samples were taken from existing farm boreholes by the Department of Water Affairs in Windhoek at the request of the Atomic Energy Board. Only two water samples, numbers 30 and 31, were obtained from boreholes HJ1 and J1 respectively at the Langer Heinrich, due to the lack of suitable equipment.

Diatomaceous muds were obtained from two cores, SWA 30 and SWA 50, supplied by Union Corp. Ltd. The localities are shown in Fig. 15. Representative samples were prepared from approximately 500 mm sections of core SWA 30, and 1 000 mm sections of core SWA 50.

Thin sections were prepared from most samples. Polished sections, impregnated with plastic, were made from selected calcrete samples. Certain whole-rock samples were analyzed by X-ray diffraction. Heavy minerals were separated from calcretes and basement rocks by heavy media using tetrabromoethane (SG = 2,98) and the Franz Isodynamic Separator. All concentrations were analyzed microscopically and by X-ray diffraction.

Approximately 50 calcrete samples from percussion boreholes were submitted for multi-element determinations

by emission spectrograph.

For the analytical techniques used refer to Part II.

2. ACKNOWLEDGEMENTS

Many people have been directly or indirectly involved in some or other aspect of this study. Some names might have been unintentionally omitted, and to these people I sincerely apologize.

Dr P.D. Toens initiated this study on epigenetic uranium deposits. His enthusiasm and unfailing support during field excursions were particularly invaluable. The co-operation of General Mining and Finance Corporation Ltd, Anglo American Corporation Ltd and their respective staff members is gratefully appreciated. In particular, I wish to thank Peter and Vicky Pickup, who were stationed at the Langer Heinrich, for their hospitality during my various visits to their camp. Union Corporation Ltd kindly supplied samples from cores of the diatomaceous muds.

Numerous people were involved with the analytical part of this work. Mr M.C.B. Smit offered valuable advice and always provided unfailing support in the setting up of instrumentation. Dr K.F. Fouché for his advice on separation procedures, Dr R.J.N. Brits for his help in the computer analysis of the gamma-ray spectra and other useful discussions, and Dr J. Turkstra for discussions of a general nature concerning neutron activation analysis are all acknowledged. Many hours of tedious labour were spent by Mrs E. Pretorius, Miss E. de Jager and Mr R. van Arken performing whole-rock analysis and other miscellaneous determinations by atomic absorption. Messrs F. Biddlecombe and F. Sunde are to be

thanked for all irradiations and endless hours of counting on the gamma spectrometer. The development of the procedures for the separation of thorium, protactinium and uranium was aided by Mr P. Beukes. Miss C. Jones assisted in the analytical work. Dr O. Strydom and his staff ran all the X-ray diffraction spectra.

Mrs N. Talacek is thanked for her patience in running statistical computer programs for the interpretation of geochemical data. Mrs E. Roy and Mrs H. Swart were responsible for the draughting of the diagrams and maps.

Dr C.P. Snyman, my promoter, and Dr W.J. de Wet are thanked for helpful suggestions and criticisms during the course of the work.

The final preparation of the manuscript involved many people. Mr D. Pretorius edited the draft, Miss D. Cawood typed the script and Mr W. van Heerden and his graphic arts department printed the final copies.

Lastly, I am most grateful to my family, who patiently tolerated many months of neglect.

PART I: GENERAL GEOLOGY

3. REGIONAL GEOLOGY

Interest in the geology of the Damara Orogenic Belt goes back to the end of the nineteenth century. Summaries of this work have been given by Smith (1965, p. 3) and later by Hugo (1974, p. 1-6). Gevers, in the mid-nineteen-thirties, was the first to complete a comprehensive study of the regional geology of this area (Jacob, 1974, p. 1). In 1969 and 1970 Jacob re-mapped the area in detail, thereby contributing to a better understanding of the complex geology.

Recent discoveries of uranium mineralization led to an upsurge in prospecting activities. Anglo American Prospecting Co. Ltd mapped the geology in its concession areas, and in the Dorstrivier area the mapping confirmed the work of Jacob (Annual Prospecting Report, 1973, Prospecting Grant M46/3/209). To the south and west of Jacob's area, and mainly in the Tumas River Valley, the continuation of the lithological features was proved. (Annual Prospecting Report, 1974, Prospecting Grant M46/3/430; Annual Prospecting Report, 1974, Prospecting Grant M46/3/433; Annual Prospecting Report, 1974, Prospecting Grant M46/3/487).

3.1 Stratigraphy

The South African Committee for Stratigraphy (SACS) draughted a South African Code of Stratigraphic Terminology and Nomenclature (1971). Based on the principles and guidelines set out in the Code, recommendations concerning

suitable informal nomenclature are presented for the super= ficial calcareous rocks which comprise large parts of the Namib Desert. With regard to the rocks of the Damara orogen, lithostratigraphic recommendations proposed by Kröner et al, 1974 (in Jacob, 1974, p. 4) are used.

The complete stratigraphic column is given in Table 1.

Jacob (1974, p. 3) discussed the terminology used for the rocks of the Damara orogen, and used the term Husab Formation (ibid, p. 5). According to SACS this is no longer acceptable, the term Karibib Formation being preferred as this is historically more appropriate (Hugo, 1974, p. 7). The name is derived from the marble of this unit which is mined in a quarry on the farm Karibib 54.

(Granite rocks are well developed throughout the sequence below the Namib group, and particular types are largely confined to certain lithological units. The meta= morphic equivalent of the Nosib Group is the Red Granite gneiss, and that of the Swakop Group is the Salem Granite. Other granites occurring within the area, for example alaskites, Bloedkoppie and Gawib Granites, are not confined to any lithological sequence).

The superficial calcareous rocks lie unconformably on the rocks of the Damara orogen which cover large areas of the Namib Desert. It is proposed that the term Namib group be used to include all these rocks. From east to west across the Namib Desert the calcareous rocks undergo compositional changes. In the east they are mainly

TABLE 1: STRATIGRAPHIC TERMINOLOGY FOR THE ROCKS IN THE DAMARA OROGEN

KHAN/SWAKOP AREA		
GROUP	SUBGROUP	FORMATION
NAMIB		GEMSBOK CALCRETE
	UNCONFORMITY	
		LANGER HEINRICH CALCRETE AND TUMAS GYPCRETE
MAJOR UNCONFORMITY		
SWAKOP	KHOMAS	WITPOORT AND TINKAS
		KARIBIB
		CHUOS
	UNCONFORMITY	
	HAKOS	RÖSSING
UNCONFORMITY		
NOSIB		KHAN
		ETUSIS
MAJOR UNCONFORMITY		

calcretes and in the west largely gypcrete. Terms such as the Langer Heinrich calcrete formation and the Tumas gypcrete formation are proposed to account for the compositional changes, although they are chronostratigraphically equivalent. Both names are derived from the Langer Heinrich Mountain and the Tumas River respectively, as the rocks are well represented in these areas.

The Gemsbok calcrete formation is lithologically similar to the Langer Heinrich calcrete formation, but the change in name is necessary due to the presence of an unconformity separating the two formations. The name Gemsbok is derived from the name of a tributary of the Gawib River which enters it from the south, close to a typical outcrop (Map 1).

3.2 Regional Structure

Structurally, the Damara orogen has been subjected to four episodes of deformation (Jacob, 1974, p. 34). The second phase was primarily responsible for the north-easterly structural direction, where anticlinoria and synclinoria were formed with a wavelength approximating 10 km (ibid., p. 38).

Nosib Group rocks and Red Granite gneiss outcrop mainly as large dome structures, with the anticlines being much broader than the intervening synclinal structures. In the Dorstrivier area, plastic deformation of the rock took place because folding was the main structural element. Very little faulting occurred (Annual Prospecting Report,

1973, Prospecting Grant M46/3/209).

Toens (1973) demonstrated that there are parallel relationships between the structural grain, metamorphic grade, magnetic susceptibility and radioactivity of the rocks of the Damara orogen. Magnetic and radiometric anomalies are intimately associated with high-grade metamorphism, particularly in rocks of the Nosib Group. On the other hand, the Nosib Group rocks comprising the Langer Heinrich Mountain have a low metamorphic grade with no corresponding magnetic or radiometric anomalies. Corner (1975) completed a traverse up the Swakop River, where he measured the radioactivity and magnetic susceptibility of all the rock types. He found that areas containing mineralized alaskites have associated negative magnetic anomalies which may be the result of remobilization of rocks and intrusion of alaskites in a new, but changed, magnetic field (Corner, 1975, p. 5).

4. THE GEOLOGY OF THE BASEMENT ROCKS

Only the Langer Heinrich region was mapped in detail (Map 1) and the description of the basement rocks is therefore confined to those found in that area.

Stratigraphically, with respect to the rocks in the Khan/Swakop area of the Damara orogen, the lithological sequence is incomplete, for the Khan, Rössing, Karibib and Witpoort Formations are absent. Consequently the Chuos and Tinkas Formations follow unconformably on the Etusis and Chuos Formations respectively. No limestone typical of the Karibib Formation is developed. Jacob (1974, p. 14, Fig. 1) schematically shows the relationship between the Karibib and Tinkas Formations within the area he mapped. Eastwards, the limestone disappears gradually to give way almost exclusively to the schists of the Tinkas Formation, except for localized development of thin limestone bands. Smith (1965, p. 22) reported similar findings in an area to the north.

4.1 Etusis Formation (Ns_1Q)

The Etusis Formation incorporates most of the Langer Heinrich Mountain and two small outcrops in the east.

The rocks are 'psephitic and psammitic' in character (Jacob, 1974, p. 10) and are composed of feldspathic quartzites and oligomictic conglomerate bands. The thicknesses of the latter are mostly between 100 mm and

200 mm, but do occur as thick as 15 m.

The pebbles are generally well rounded and are composed mainly of quartz with lesser amounts of granite, pegmatite and amphibolite. Metamorphism has not affected the rocks to any significant degree, but the pebbles in the conglomerate do show some elongation. Bedding planes are still easily recognizable, especially where the conglomerates are found.

The quartzites are composed of quartz, microcline and plagioclase with smaller amounts of biotite and muscovite. Magnetite and zircon are the main accessory minerals. The matrix of the conglomerate is similar to the quartzite, but has a greater proportion of magnetite and zircon (ibid., p. 93).

4.2 Chuos Formation (D_2G)

The Chuos Formation is developed only at the foot of the western slopes of the Langer Heinrich Mountain. It is a rock type of uncertain origin and has been variously described as a tillite, tilloid or diamictite. No evidence has been found to regard the Chuos Formation as being definitely of glacial origin (ibid., p. 17).

The rock is essentially schistose, having a cleavage direction parallel to the overlying schists of the Tinkas Formation. Metamorphism has elongated the pebbles parallel to the schistosity, giving the diamictite the appearance of an 'augen gneiss'. Quartz, quartzite and granite are the main constituents of the pebbles. Occasionally secretion

quartz veins are found.

Mineralogically, the matrix is composed of quartz, plagioclase, microcline, biotite and muscovite.

4.3 Tinkas Formation (D_4S)

The Tinkas Formation covers the largest area in the region mapped. It forms the prominent Schieferberge in the south and the Augawibberge in the south-east.

The most striking feature of these rocks is their banded appearance due to alternating fine-grained pelitic schists and calc-granofels bands. The thicknesses of the bands vary, with the latter not exceeding about 1 m. On outcrop, the calc-granofels is more resistant to weathering and stands out as a low narrow ridge.

Calc-granofels bands are 'massive and non-foliated' except where gneissic structures have developed in tight folds (ibid., p. 65). In hand-specimen, the rocks are melanocratic, sometimes greenish, fine-grained and extremely hard. Texturally they are either porphyroblastic or seriate (ibid., p. 67). Quartz, plagioclase and diopside are generally the major constituents. Other minerals such as microcline, hornblende, garnet, calcite and scapolite are also present to a greater or lesser extent.

The mineralogical assemblages of the pelitic schists belong to the amphibolite facies and correspond to the medium and high grades of metamorphism. Within the area mapped, the schists fall in the medium grade, as separation of the grades is found further to the north, at the 'beginning of anetexis

in gneisses' isograd (ibid., pp. 92 and 129).

The rocks are fine-grained with lepidoblastic texture and are composed of quartz, plagioclase, biotite, K-feldspar and cordierite. Minor minerals such as muscovite, sillimanite, andalusite and garnet are commonly found. (ibid., p. 93, Table 17). Biotite is responsible for the lepidoblastic texture.

4.4 Salem Granite (Gn_2)

The Salem granite is located to the north-east of the area. Good exposures, although very weathered, are found in the Tinkas River.

It is a porphyritic biotite granite, medium to coarse grained, and has a composition varying between granodiorite and granite (ibid., p. 144, Fig. 54). Mineralogically, the Salem Granite contains quartz, microcline, plagioclase and biotite. Phenocrysts consist of microcline perthite.

Stratigraphically the Salem Granite occurs above the Etusis Formation in the zone normally occupied by the Tinkas Formation.

4.5 Bloedkoppie Granite (G_1)

The Bloedkoppie Granite is the main granite found in the area, and is situated south-east of the Langer Heinrich Mountain. Its most striking physical feature is the prominent whale-back dome, called the Blutkuppe by the early German pioneers. Smaller granite outcrops are found

sporadically in the Bloedkoppie Flats which extend eastwards (Plate 1).

Intrusive features of the Bloedkoppie Granite are shown by cross-cutting relationships to the Tinkas Formation. Low intrusion temperatures are indicated, for there has been little alteration of the country rock, although in some localities migmatization and partial granitization over distances of a few tens of millimetres can be seen. Xenoliths are well represented and those of the Tinkas Formation are orientated towards the north-east. This indicates that the Bloedkoppie Granite was implaced during the period of regional deformation of the Damara Orogen and is therefore probably late-syntectonic in age. There is a notable difference between the xenoliths of the Tinkas and Etusis Formations, for the latter show a greater degree of alteration, whereas the former are hardly affected except for the smaller rafts.

The north-east orientation of xenoliths is parallel to younger aplitic intrusions and fracture patterns, along which deep weathering has produced gorges in the Bloedkoppie itself. In a north-westerly direction a second fracture pattern has developed containing coarse-grained secretion pegmatites. These pegmatites are pinkish in colour, with biotite and tourmaline crystals orientated at right angles to the contacts (Plate 2). Both fracture patterns cross each other at angles varying between 30° and 70°.

The Bloedkoppie Granite is very similar to the Salem Leucogranite, but is slightly more potassic (Jacob, 1974, p. 145). It is a medium-grained, but locally coarse-

grained, leucogranite with quartz, microcline, plagioclase and biotite as the main constituents. Accessory minerals such as zircon, apatite, allanite and ore are present. In places, the quartz grains are slightly smokey. Grain sizes of the feldspars vary locally up to 25 mm in longitudinal section. Texturally the rock is hypidiomorphic granular and has graphic intergrowths.

It was virtually impossible to obtain a fresh sample from the Bloedkoppie Granite pluton. Large sections of the granite were so weathered that individual grains had almost no coherence. Even the freshest pieces of granite had iron rims around biotite flakes, indicating that iron was gradually being released from the crystal structure as a result of weathering. Plate 3 illustrates typical weathering in the feldspars.

Unusual weathering features are developed on the Bloedkoppie Granite, and three basic types emerge. The first is exfoliation on both large and small scales, the former being more conspicuous on the Bloedkoppie dome, where large granite slabs cling to the steep slopes. Secondly, there is a type of weathering that results in a spongy texture and is referred to as alveoles (Plate 4). Thirdly, the development of large caverns (Plate 5) termed tafoni are to be found. Both alveoles and tafoni as found in other deserts of the world have been described by previous authors, but they occur most frequently in the foggy coastal type to which the Namib Desert belongs (Cooke and Warren, 1973, p. 58).

The shapes of the alveoles vary, but all have an essentially rounded entrance and the direction of penetration



PLATE 1 **Bloedkoppie Granite dome viewed across the Bloedkoppie Flats from the Augawibberge, with the Langer Heinrich Mountain in the background to the north. Granite outcrops in the middle foreground.**

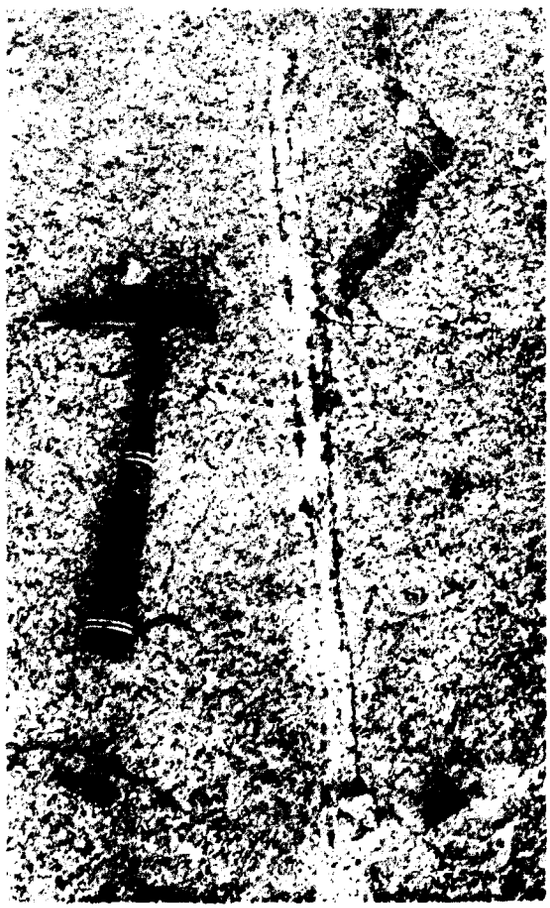


PLATE 2 **Secretion pegmatite in the Bloedkoppie Granite with biotite crystallizing along and normal to the contacts.**

of the hole is randomly orientated. No preferential siting of alveoles in the granite face is apparent, for they are not necessarily located towards the direction of the prevailing winds. Holes, in places, have completely eaten through the granite. The entrance sizes vary between 30 to 50 mm in diameter, and the holes penetrate up to 300 mm into the rock.

On a much larger scale, tafoni have developed on the north-facing slope of the Bloedkoppie. The size of these varies between 2 to 10 m in height and 4 to 20 m in length, with a depth penetration of as much as 10 m. All have arch-shaped entrances, with some flatter than others. Inner surfaces are concave and irregular (Plate 5). The origin of both alveoles and tafoni is puzzling, particularly with regard to the former. Granular disintegration, unevenly distributed on the rock surface, seems to be the most plausible explanation for the formation of the alveoles. Loci of disintegration bear no obvious relationship to a wind direction that could carry sand particles or nuclei of moisture.

Onshore fogs commonly penetrate inland as far as the Langer Heinrich (about 100 km from Swakopmund) and the dissolved salts they bear act as chemical etching agents. Penetration into the granite is by mechanical means and chemical reaction in microcracks along intergranular boundaries at the point of weakness. No evidence of salt crusts is found in the alveoles, but these may have been removed by rainfall.



PLATE 3 Photomicrograph showing weathering effects in the feldspars. Crossed nicols. Magnification x 50.



PLATE 4 Alveoles in the Bloedkoppie Granite.



PLATE 5 Tafoni on the north-facing slope of the Bloedkoppie dome. Dimensions are approximately 10 m high, 10 m deep and 30 m wide.

A directional aspect of the tafoni infers that a weakness at a point in the granite was brought about and aggravated by environmental factors such as differential temperatures and corrosive solutions. A north-facing slope in the southern hemisphere accumulates a greater amount of heat during the day than do southern slopes. This may have been sufficient to form a crack in the granite and thereby initiate a tafoni.

Examination of the inner faces of the tafoni shows that flaking and disintegration are taking place simultaneously, producing a constantly crumbling surface. Salt precipitation between the flakes is common. This indicates that the flaking is caused by initial chemical reaction, probably hydration of feldspars, followed by differential volumetric expansion of crystallizing salts.

X-ray diffraction analysis reveals that the chief constituents of the salt crust are sodium chloride and some other hydrated salt (probably a hygroscopic type) of which identification was not possible. A partial chemical analysis of the salt crust is given in Table 2.

Neither alveoles nor tafoni were found in the quartzites and schists of the Etusis and Tinkas Formations or the Gawib Granite, but they are locally developed in the Salem Granite. This observation therefore implies a textural and possibly a compositional control of the respective rock types, thereby inhibiting or promoting the formation of alveoles or tafoni.

TABLE 2: PARTIAL CHEMICAL ANALYSIS OF THE SALT CRUST ACCUMULATING IN A TAFONI ON THE BLOEDKOPPIE

Cation	%	Anion	%
Ca	1,8	Cl^-	52,6
Mg	1,0	SO_4^{2-}	2,9
Na	24,1	NO_3^-	0,13
K	0,04	CO_3^{2-}	0,58

4.6 Gawib Granite (G_3)

The Gawib Granite is situated in the south-western corner of the area. Structurally, it forms a pluton, with intrusive and cross-cutting relationships to the Tinkas Formations. It appears to be a composite intrusion of which the outer gneissic margin is older than the locally porphyritic interior. No large prominences are present as in the case of the Bloedkoppie Granite, but the Gawib Granite consists of rounded onion-foliated boulders of up to 2 m in diameter. The colour of weathered surfaces is an earthy brown.

The gneissic margins are granodioritic, but towards the centre the composition becomes more granitic (Jacob, 1974, p. 147).

Quartz, plagioclase, microcline, biotite and hornblende are the chief constituents, with epidote and sphene the main accessory minerals. Compared with the Bloedkoppie Granite the amount of microcline is much less, whereas the plagioclase and biotite contents are considerably greater.

4.7 Horebis Granite (G_g)

The Horebis Granite in outcrop is small and developed as a stock on the extreme west of the area. Contacts with other rock types are covered by sediments of the Gemsbok calcrete formation, but contact with the Gawib Granite is inferred, for in one locality they are separated by only one metre of soil.

It has an unusual spotted appearance due to the clusters, 10 to 30 mm in diameter, of black tourmaline. Both red and white varieties are found. Texturally, it is aplitic and composed of quartz and microcline with minor plagioclase.

4.8 Pegmatites

Pegmatites cover most of those types described by Jacob (1974, p. 154). The oldest type are the syntectonic homogeneous varieties developed in the regional foliation planes. The bulk of pegmatites, however, belong to the heterogeneous class, consisting of zoned and layered types, the latter being the more abundant of the two.

5. GENERAL GEOLOGY OF THE YOUNGER FORMATIONS

In the area of study surficial deposits cover large low-lying areas such as the Gawib River Valley, Gawib Flats, Tumas River Valley and certain areas of Dorstrivier. Basement rocks are exposed as mountains, inselbergs and canyons through this cover. The surficial deposits consist mainly of siliceous clastic material that has been cemented with calcite and/or gypsum. The nature of the clastics is variable. Particles are both rounded and angular, with sizes as small as 2 μm in clays to boulders of several metres in diameter.

The terminology adopted was an attempt to incorporate into the definitions some of the features mentioned above.

Duricrust

A general term for a rock formed in semi-arid and arid climates by the accumulation, in clastic materials, of minerals that have been precipitated from waters carrying dissolved ions in solutions. The nature of the precipitate can be calcium carbonate, calcium sulphate, silicon, aluminium, etc.

Calcrete

A duricrust containing calcium carbonate (calcite) cement.

Gypcrete

A duricrust containing calcium sulphate (gypsum) cement.

Six varieties of calcrete have been reported from Southern Africa (Netterberg, 1971, p. 2-6), viz. calcified soil, powder calcrete, nodular calcrete, honeycomb calcrete, hardpan calcrete and boulder calcrete. The classification is basically genetic, each type representing a stage in the development of calcrete (ibid., p. 8, Table 1). The sequence is essentially a time-based function according to which the calcium carbonate content increases with age.

Only three of the six calcrete varieties are represented at the Langer Heinrich, viz the calcified soil, the hardpan calcrete and boulder calcrete. For the purpose of this discussion, however, the term calcified soil is replaced by a synonymous term, calcified breccia-conglomerate. According to the Glossary of Geology (1972, p. 91), breccia-conglomerate is defined as 'a sedimentary rock consisting of both angular and rounded particles' and this describes more precisely the nature of the clastic host material being dealt with in this study.

According to Netterberg (1971, p. 2-6), calcified breccia-conglomerate represents the youngest variety of calcrete which in places is not well cemented, having calcium carbonate values between 10 and 50 per cent. Hardpan calcrete is an older and better developed calcified breccia-conglomerate, and has a higher calcium carbonate content. It forms a sheet-like layer over less consolidated and developed calcrete. Boulder calcrete is a disintegrated and weathered variety of hardpan calcrete.

Four stages have been recognized in the formation of calcrete horizons (Gile et al, 1966, p. 354) as follows:

Stage	Carbonate Morphology
1	Thin discontinuous pebble coatings.
2	Continuous pebble coatings.
3	Many interpebble fillings forming a plugged zone.
4	Laminated zone overlying plugged zone.

Discontinuous segregations form in the initial stages of calcium carbonate accumulations. As calcium carbonate precipitation proceeds, the zone becomes more continuous until the plugged stage, termed the k-horizon, is reached. Finally a laminated zone, having a high $CaCO_3$ content, forms upon the k-horizon.

Gypcrete can be classified in a similar manner as calcretes, and those represented are powder gypcrete, vuggy gypcrete and consolidated gypcrete. Powder gypcrete is a surface accumulation and is the youngest in the stages of development. Beneath the ground surface vuggy gypcrete forms, and consists of a zone of small interlocking desert roses. The oldest form is the consolidated gypcrete, which is similar to the hardpan calcrete in appearance.

The gypcretes of the Namib Desert are very extensive and form a veneer over most of the calcretes in the area being investigated. It appears that towards the coast the ratio between the gypsum and calcite contents of the duricrusts increases as shown in Fig. 2. The vertical scale gives the relative percentage of each component. At Swakopmund, and this may apply to the whole of the Namib Desert along the coast, the duricrusts consist mostly of gypcrete, but at the Langer Heinrich the gypsum veneer

is very thin and the calcite prodominates.

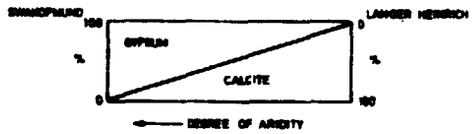
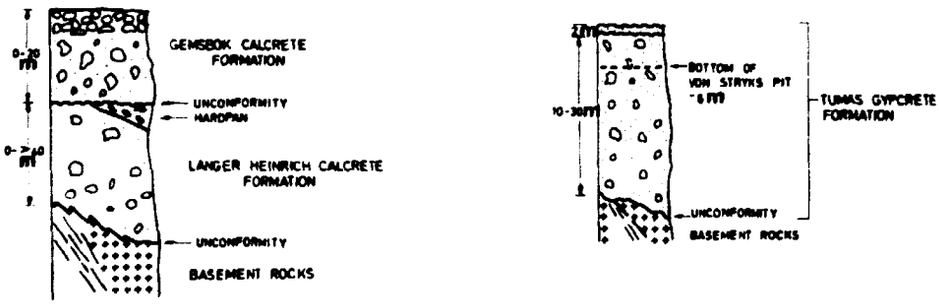


Fig. 2: A schematic relationship between gypsum and calcium contents of the duricrusts in the Namib Desert with respect to the degree of aridity.

Schematic profiles through the superficial duricrust deposits to the basement rocks are given in Fig. 3.



(a) (b)

Fig. 3: Schematic profiles through the superficial duricrust deposits to the basement rocks at
(a) The Langer Heinrich area;
(b) Von Stryks pit in the bed of the Tumas River. The pit is only approximately 6 m deep and the geology below this point is only inferred. Information from seismic data tends to confirm this. (See Fig. 7).

5.1 Geomorphology

Before describing the geology of the duricrust deposits, it is necessary to consider briefly the geomorpholo= gical sequence of events that culminated in the formation of

the present-day landscape of the Namib Desert. Greater emphasis is placed on the Gawib River and environs, as that area was mapped in greater detail.

5.1.1 Palaegeomorphology

The Namib Plain and the sediments comprising it are the consequence of successive erosion cycles (King, 1963; Dixey, 1955, p. 5-15; Gevers, 1942, p. 63; Truswell, 1971, p. 139-142) and the sequence of events is given in chronological order in Table 3. Following the separation of Africa from Gondwanaland, continental margins were warped downward by monoclinal flexing during early and mid-Cretaceous, thereby initiating a cycle of Post-Gondwana erosion. This was terminated by uplift in the late-Cretaceous, where the axis of greatest elevation was along the marginal zones of the continent. Lesser uplift took place on the outward and inward flanks of the axis. A new erosion cycle began, lasting between early Senonian and late-Oligocene and culminating in the African erosion surface. During this time humid conditions prevailed.

By the end of the Miocene, epeirogenic uplift brought about erosion of the African surface to produce the widely distributed Post-African landscape. Final uplift in the late Pliocene and early Quarternary tilted the margins outward. It is thought that this period of uplift was of a multicyclic nature. Erosion eventually produced the Quarternary surface. A feature of this last uplift was doming along a central axis, making the Namib Plain slightly convex.

TABLE 3: CHRONOLOGICAL DEVELOPMENT OF THE NAMIB DESERT

CAINOZOIC	QUARTERNARY		HOLOCENE or RECENT PLEISTOCENE
	TERTIARY		PLIOCENE MIOCENE OLIGOCENE EOCENE
MESOZOIC	CRETACEOUS	UPPER	DANIAN SENONIAN
		LOWER	TURONIAN CENONANIAN ALBIAN APTION NEOCOMIAN
	JURASSIC		

1. Gondwana erosion surface
2. Fragmentation of Gondwanaland - continental drift
3. Downwarping, marine transgression
4. Post-Gondwana erosion surface
5. Uplift
6. African erosion surface, humid climate, formation of initial Gawib and Tumas River Valleys.
7. Uplift
8. Post-African erosion surface - desert climate, Langer Heinrich calcrete and Tumas gypcrete formations developed.
9. Multi-cyclic uplifts
10. Quarternary erosion surface, Gemsbok calcrete formation developed, Swakop and Khan River canyons formed

The gouging out of the pre-alluvial Gawib River Valley between the Langer Heinrich Mountain and the Schieferberge is probably of Post-Gondwana and African erosion surface age. This was therefore the palaeotopo-

graphic base upon which the sediments, as found today, were deposited.

Fig. 4 illustrates diagrammatically the geomorphological development of the Gawib River Valley. Structural, erosional and sedimentary features can be traced up to the present time.

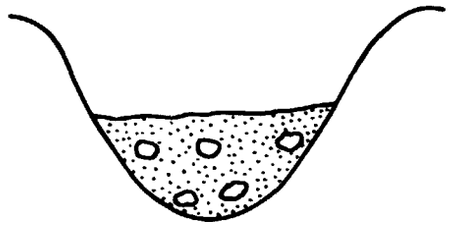
5.1.2 Modern geomorphology

The Gawib River drainage system is fed by tributaries originating between the Tinkas watershed in the east and the Gawib watershed in the west (Map 1). Most of the water that has flowed through the Gawib River Valley drained off the Tinkas watershed, deriving the bulk of its volume from the slopes of the Augawibberge and the Langer Heinrich Mountain. In the west, the Gawib watershed feeds water into streams running off the Schieferberge.

Mountainous terrain surrounds the Gawib River Valley. The Langer Heinrich Mountain to the north has an altitude of 1 052 m. The Schieferberge to the south are less impressive, attaining heights of 820 m. The mountains are in a youthful stage of erosion, characterized by steep - sided valleys and gullies.

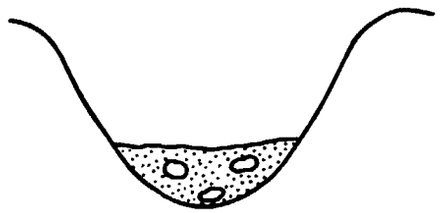
Fanglomerates are characteristic of desert environments (King, 1963). In the Gawib River Valley a remnant terrace of the Gemsbok calcrete formation has been preserved in an enclave of the more competent quartzites of the Etusis Formation (Plate 6). Normally fanglomerates in deserts advance outward from the mountain fronts, but in this

STAGE



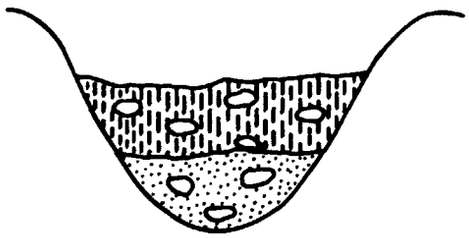
1

1. Deposition of continental breccia on African surface.
2. Initiation of the Langer Heinrich calcrete formation in desert conditions.
3. Precipitation of $CaCO_3$.



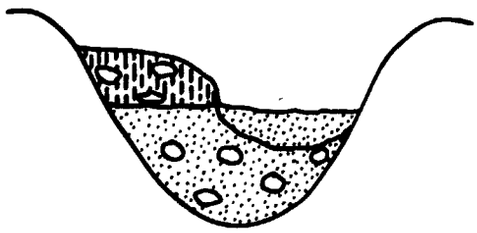
2

1. Uplift at end of Miocene.
2. Erosion of calcrete.
3. Continued precipitation of $CaCO_3$.
4. Langer Heinrich calcrete formation completed, but partially eroded.



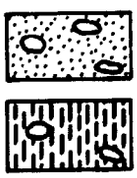
3

1. Multicyclic uplifts in the Pleistocene
2. Development of Gemsbok calcrete formation unconformably on the Langer Heinrich calcrete formation.



4

1. Continued Pleistocene uplift.
2. Present Gawib River channel formed, filled with Recent alluvium.
3. This was contemporaneous with erosion of Khan and Swakop River canyons.



LANGER HEINRICH CALCRETE FORMATION

GEMSBOK CALCRETE FORMATION

Fig. 4: Geomorphological development of the sediments in the Gawib River valley

case it is purely an erosional type. Mabbutt (1952, p. 345) describes similar terraces in the Ugab River Valley.

Formation of the fanglomerate in the Gawib River Valley is considered to have taken place by three processes:

(a) Erosion by the Gawib River when in flood.

(b) Erosion by cross-cutting tributaries originating from the Langer Heinrich Mountain.

(c) Mechanical rock-falls due to undercutting by wind and water erosion. Wind erosion has a tendency to cause differential deflation where the softer parts are preferentially eroded. The result is the formation of caverns and overhangs (Plate 7). Continuation of the deflationary processes causes the collapse of the overhangs and the development of scree slopes.

Stone pavements are found on the Gawib Flats in areas that are devoid of vegetation. They are surfaces which are covered by angular to round quartz pebbles of different sizes with diameters of up to 50 mm. The packing density of the pebbles is variable and it was observed that those areas with high packing densities contain pebbles that are rounder (Plate 8). This suggests that the denser the packing and the rounder the pebbles, the longer the stone pavement has been exposed to deflationary processes.

Stone pavements are formed after the removal of finer material by wind and/or water action, leaving a pebble residue on the surface. Loose boulders lying on top of the Gemsbok calcrete formation have been subjected to negligible cementing due to this phenomenon.

5.2 Langer Heinrich Calcrete Formation

The calcretes of the Langer Heinrich calcrete formation consist of the three types mentioned earlier. Calcified breccia-conglomerate forms the bulk of the formation and only in the north-east does a remnant hardpan calcrete unit remain (Map 1). Boulder calcrete is unimportant for it consists of loose boulders scattered in the alluvium.

The Langer Heinrich calcrete formation is a desert fluviatile sediment which was deposited and cemented in wadis of the Gawib River during the dry middle to late Tertiary. (The term 'Wadi' as applied in this context is the same as that used by Glennie (1970, p. 29), which implies 'a form of fluviatile transport which is sporadic and abrupt').

Evidence of deposition by water is shown in Plate 9. The larger and flatter pebbles of schist and quartzite are aligned in a westerly direction, suggesting a river flow parallel to the Gawib River today. Microscopic examination of orientated hand samples, taken from several localities along the Gawib River, showed no visual lineation of the smaller sand particles.

The calcified breccia-conglomerate is generally medium to coarse-grained with grain sizes between 0,5 and 45 mm. The distribution of grain size in the outcrops is not uniform, for in parts it is finer grained that in others. Grain sizes between 0,5 mm and 15 mm with an average of 2-3 mm constitute the finer-grained material.

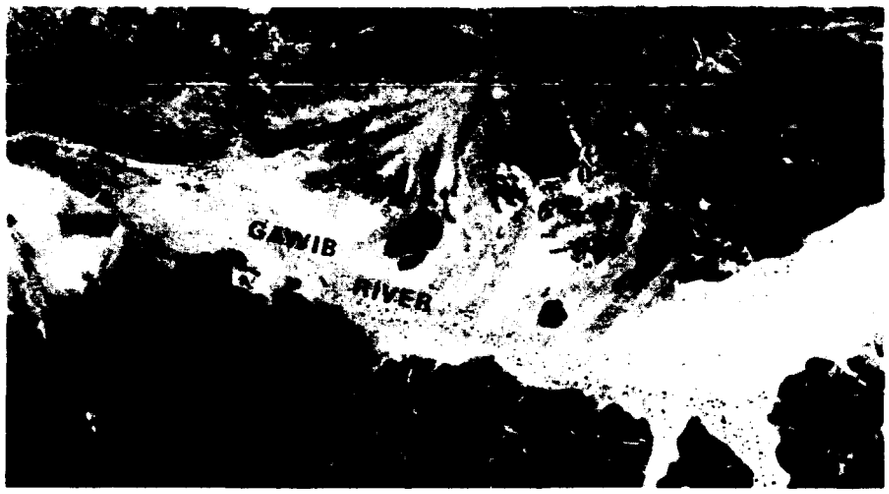


PLATE 6 Aerial photograph showing the fanglomerate of the Gemsbok calcrete formation in the Gawib River Valley.



PLATE 7 Caverns and overhangs in the Gemsbok calcrete formation formed by deflationary processes.



PLATE 8 Stone pavement on the Gawib Flats composed of angular to rounded quartz pebbles.

The pebbles are predominantly quartzite with lesser amounts of granite, quartz (sometimes smokey), feldspar and schist.

Rounding in the grains varies considerably and is dependent largely on their composition and fabric. Those pebbles which show bedding planes and schistosity are the least rounded, for example, the quartzites and schists of the Etusis and Tinkas Formations respectively. Quartz, granite and pegmatite pebbles have the highest degree of rounding. Most of the rounded pebbles have probably been derived from the conglomerate bands in the Etusis Formation, as water and river action is too sporadic to be of any significance. Glennie (1970, p. 33) points out that roundness is not a guaranteed criterion for indicating distance from source.

The mineralogical components of the calcified breccia-conglomerate are mainly calcite, quartz and feldspar, minor biotite and carnotite, with accessory clay such as montmorillonite and attapulgite. Dolomite is absent, which agrees with the statement of Mackenzie and Bricker (1971, p. 241) that dolomite cements do not form in younger sediments. Microscopical and X-ray diffraction analyses of heavy mineral concentrates in several samples show the presence of diopside, hornblende, biotite, ore, garnet, tourmaline, sphene, zircon, apatite as allogenic minerals as well as carnotite. This assemblage seems to be fairly general and indicates a provenance of pegmatites, Bloedkoppie Granite, schists and granofels of the Tinkas Formation, and the quartzites of the Etusis Formation. Carnotite is a mineral which was precipitated from solution and is therefore authigenic.



PLATE 9 Flatter pebbles of schist in the Langer Heinrich calcrete formation orientated in the direction of waterflow as shown by the arrow.

Montmorillonite and attapulgite represent weathering products. Attapulgite is found in those calcretes which have a slight greenish colouration, and predominates locally towards the west where the Gawib River turns northward. Montmorillonite is widely distributed and is found in the normal greyish calcrete.

Calcite and gypsum accumulation in the detrital material shows peculiar characteristics. The growth of crystals from solutions results in the detrital fragments being pushed apart. A stage is eventually reached where the grains are pushed apart to such an extent that they are no longer in contact with one another and 'float' in a sea of calcite or gypsum. The result is that there is an expansion of the sediment as a whole. If this expansion is large enough in a horizontal direction, pseudo-anticlines and synclines may develop (Goudie, 1973, p. 61). Plate 10 shows that there are no two detrital grains in contact. With an increase in age of the calcrete, the distance between the grains becomes larger. Plate 11 is particularly interes= ting, and demonstrates how the 'pages of a biotite book' have been separated by calcite precipitating between them. Goudie (1970, p. 42) reports that pressures resulting from crystal growth may reach approximately 5 000 kPa. Such pressures are sufficient to shatter rock fragments of which the tensile strength lies between 2 000 and 20 000 kPa.

Certain parts of the Langer Heinrich calcrete formation have a lower degree of calcification than others and Plate 12 illustrates such an example. The black areas are pore spaces, and the degree of separation of the grains

is not as large as that illustrated in Plate 10. Typically, the pores are located mainly along surfaces of the detrital grains and cut across calcite crystals to a lesser extent. Calcrete with this open structure may be considered to be the main acquifers which afford passageways to potentially mineralizing solutions.

A second generation of calcite precipitation has resulted in the filling of the pore spaces. Plate 13 shows rims of younger calcite surrounding the rock fragments. Within the calcite matrix, and also contributing to the cement, is carnotite (black crystals in Plate 13) which has a good platy morphology. In other cases carnotite exhibited no external crystal structure and it appeared as a generally amorphous mass.

In thin section, carnotite is almost opaque, having a dark green colour, whereas in polished section it is a translucent yellow.

Plates 14(a) to (c) and 15(a) to (c) are electron photomicrographs of carnotite mineralization in calcrete. Within the lower part of Plate 14(a) amorphous carnotite is concentrated, the presence of which is confirmed by the electron scatter photographs of uranium and vanadium in Plates 14(b) and (c) respectively. Carnotite with a platy structure is exhibited in Plates 15(a) and (b), the latter of which is an enlargement (x 3) of the former. Note the corresponding distribution of carnotite and uranium in Plates 15(a) and (c).

Carnotite is thought to have precipitated in the calcrete at about the same time as the second generation

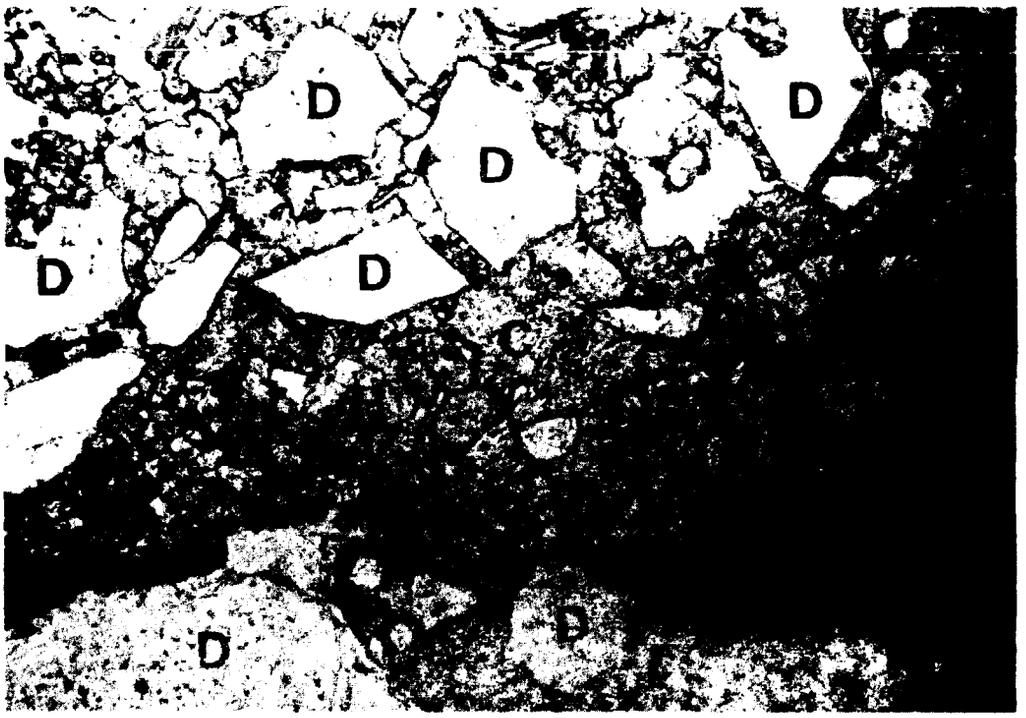


PLATE 10 Photomicrograph showing the pushing apart of detrital grains by calcite. D = detrital grains, C = calcite. Magnification x 50.

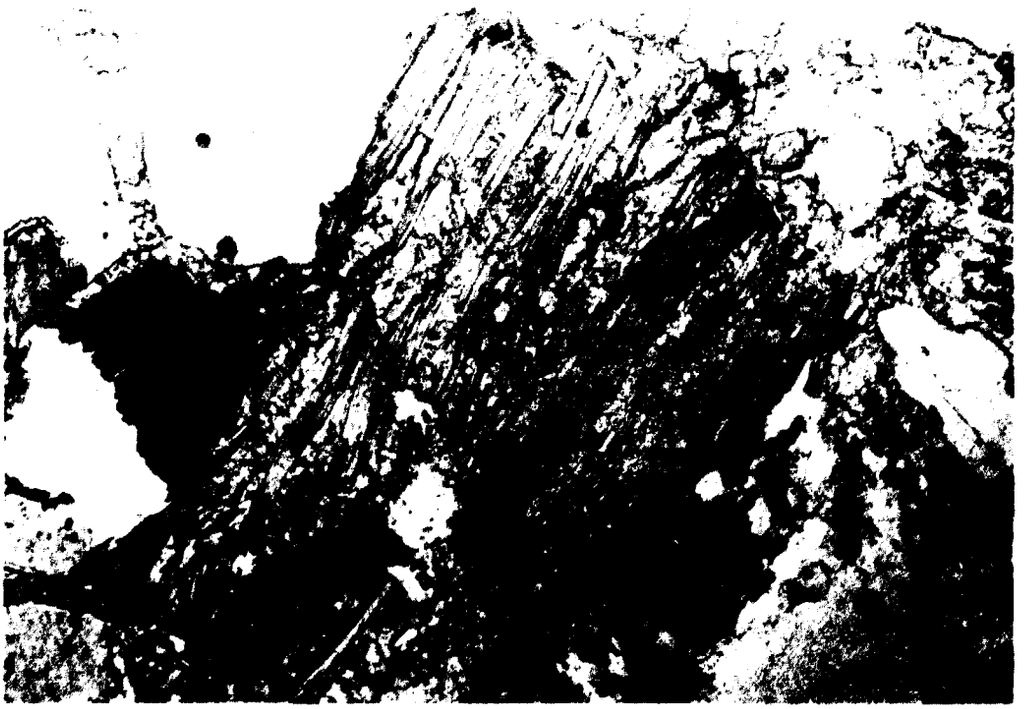


PLATE 11 Photomicrograph showing how the pages of a biotite 'book' have been separated by the precipitation of calcite between them. Magnification x 50.

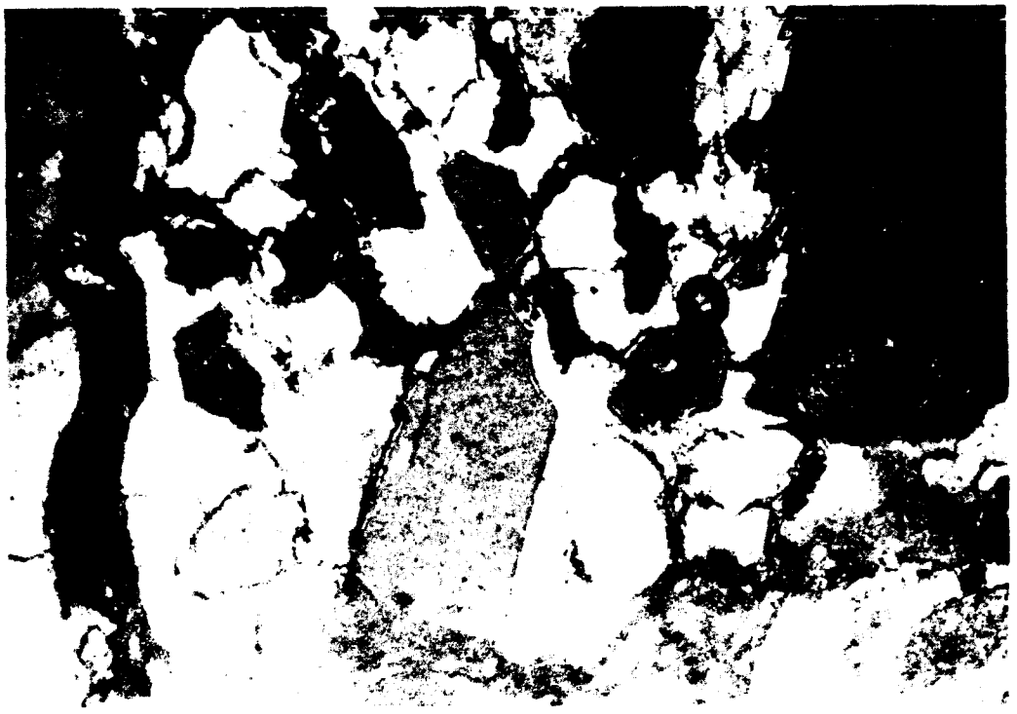


PLATE 12 Photomicrograph [illegible] pore spaces which [illegible] precipitation is less extensive. [illegible]



PLATE 13 *Photomicrograph showing rims of second generation calcite surrounding detrital grains.* The black areas are carnotite crystals in a lighter calcite matrix. Magnification x 50.

calcite. Characteristically, carnotite surrounds the detrital grains in the same way as the second generation calcite and is to a lesser extent crystallized as inclusions in single calcite crystals. Should it occur within the calcite matrix, some distance away from a detrital grain, it is often found on or close to boundaries of interlocking calcite crystals, which provided a more limited passageway to mineralizing solutions. The intimate association between rock fragments and carnotite, with the latter having crystal= lized in original pore spaces, is illustrated in Plate 16. Langford (1974, p. 519) noted similar features in the Yeelerrie uranium deposit of Western Australia.

Therefore it is concluded that there are at least two ages of calcite precipitation, with the first taking place on a much larger scale than the second. The latter had the tendency to seal up the pore spaces, and an examina= tion of Plates 13 and 16 show that there is almost no visible pore space remaining. A notable feature of the uranium mineralization is that it is monominerallic, having only carnotite present.

The hardpan capping of the Langer Heinrich calcrete formation lies stratigraphically above the calcified breccia-conglomerate, but is no longer found in contact with it. Plate 17 shows the hardpan calcrete overlying the Bloedkoppie Granite. Remnant boulders, i.e. boulder calcrete, are found scattered on the Bloedkoppie Flats. This suggests that the hardpan calcrete at one stage covered at least an area to the east of the region mapped.

PLATE 14(a) Electron photomicrograph of amorphous carnotite in calcrete. Magnification x 1 000.



PLATE 14(b) Electron scatter photomicrograph of uranium of the same area in Plate 14(a).



PLATE 14(c) Electron scatter photomicrograph of vanadium of the same area in Plate 14(a).



PLATE 15(a) Electron photomicrograph of platy carnotite in calcrete. Magnification x 1 000.

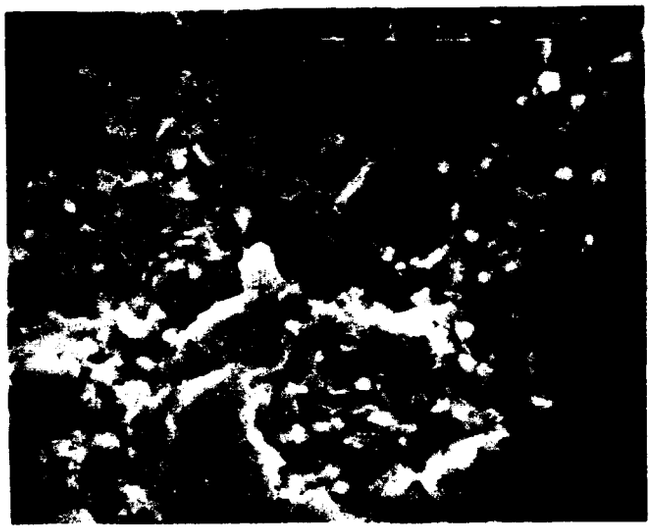


PLATE 15(b) Electron photomicrograph of platy carnotite in calcrete. Magnification x 3 000.

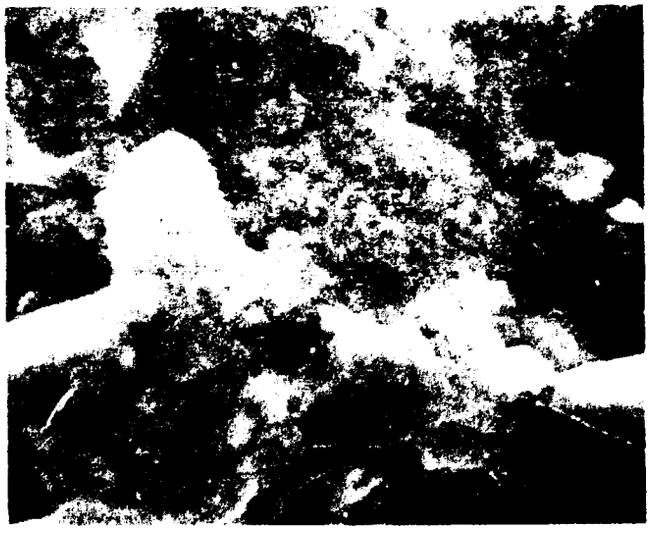


PLATE 15(c) Electron scatter photomicrograph of uranium of the same area in Plate 15(a).



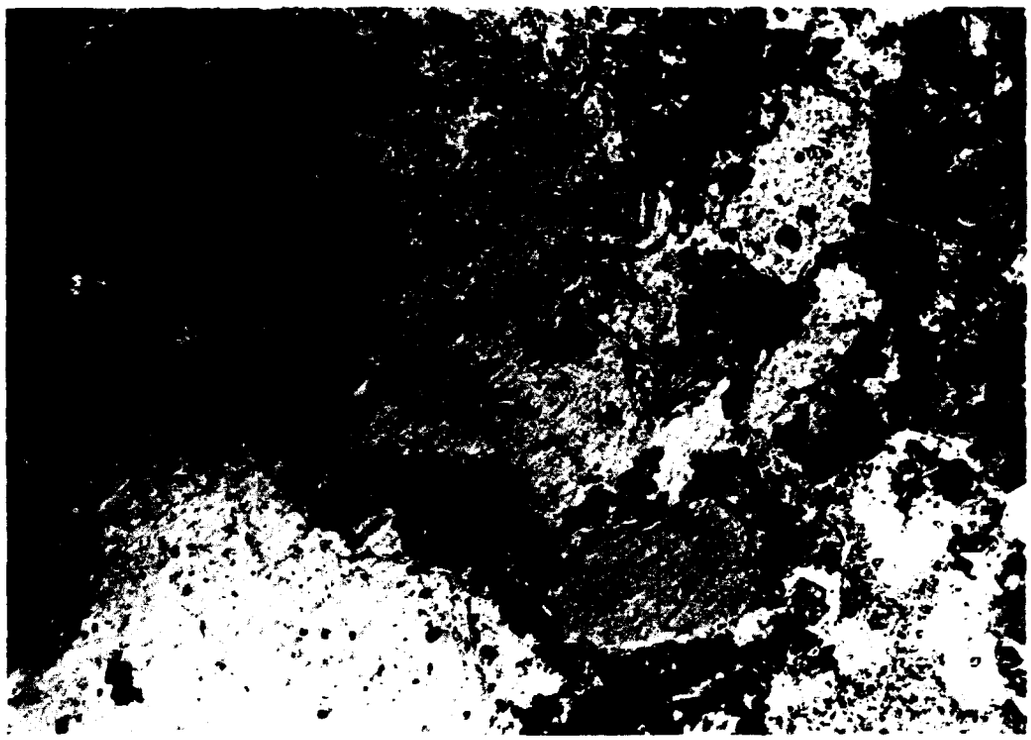


PLATE 16 Photomicrograph showing the crystallization of carnotite (black areas) around detrital fragments.



PLATE 17 Hardpan calcrete overlying Broadkopje Granite.

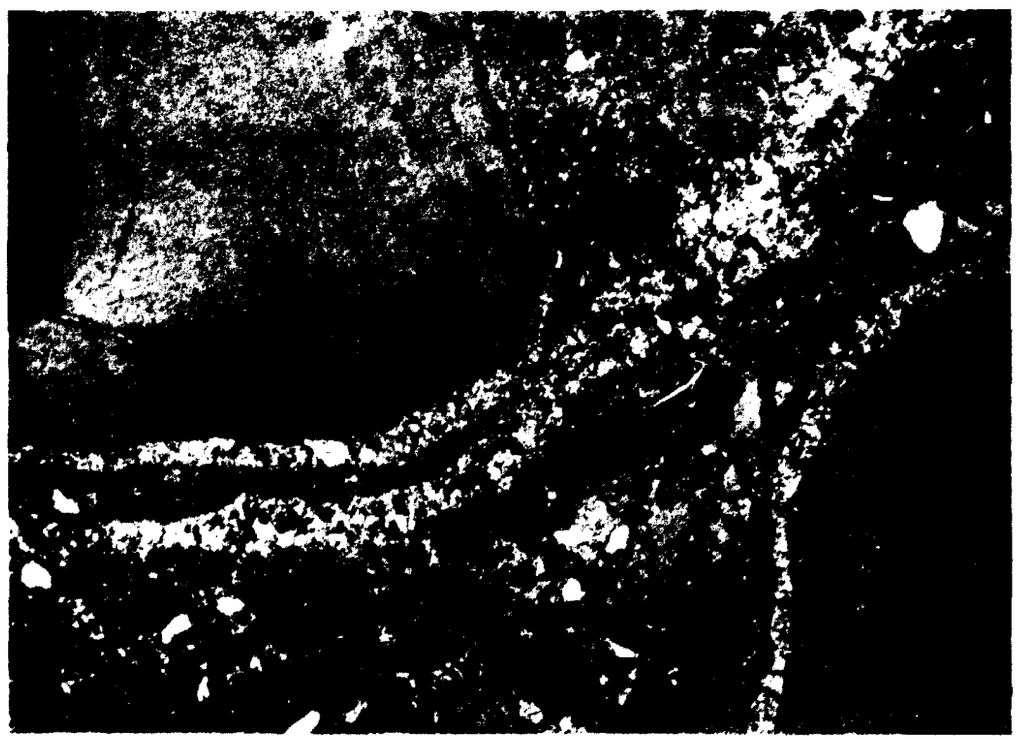


PLATE 18 Photomicrograph of the hardpan calcrete. Detrital grains are set in a semi-opaque ferrugenous calcite matrix. Transparent second generation calcite has filled pore spaces and formed rims round the larger grains. Crossed nicols. Magnification x 50.

Away from the Bloedkoppie Flats and westward into the Gawib River Valley the hardpan calcretes is not found at the contact between the Langer Heinrich calcrete and Gemsbok calcrete formations. This may be an erosional feature, since it was removed prior to the deposition of the latter.

In outcrop, the hardpan calcrete is also a breccia-conglomerate, having pebbles as large as 200 mm but generally averaging 20-30 mm in diameter. The matrix is a semi-opaque, fine-grained, brown-coloured ferrugenous calcite. (The presence of iron in the calcite was confirmed by qualitative electron probe analysis). Compared with the calcified breccia-conglomerate, the detrital grains in the hardpan calcrete have a higher degree of separation, which suggests a greater $CaCO_3$ content. This is substantiated by a higher CaO content in the analysis (Table 28). Larger grains have a higher degree of roundness than the smaller sand particles (Plate 18).

Fractures and original pore spaces have been filled with a second generation calcite which is not opaque. This implies that the conditions for the precipitation of the two types of calcite were dissimilar, for the latter phase contained no iron. It will be remembered that in the calcareous breccia-conglomerate two similar phases of calcite precipitation took place, the last one concurrent with the carnotite mineralization. Therefore this may provide evidence that the conditions under which the cogenetic carnotite and second generation calcite formed were at variance with those of the primary epigenetic calcite.

No uranium mineralization was found in the hardpan, but boulder calcrete lying in the alluvium of the Bloedkoppie Flats contained uranium in places (Table 28, sample LH-24). Gypcrete accumulations at the Langer Heinrich are included in this section because they are found to be mainly associated with the sediments of the Langer Heinrich calcrete formation. Information about the gypcrete was obtained from one cutting in the Gawib River bed. Fig. 5 is a diagrammatic sketch of the profile which was only about 1 m deep. Gypsum does, however, extend to greater depths. Sample HJ1-1, from borehole HJ-1 which is in the same vicinity as the profile in Fig. 5, has a sulphate content of 12 per cent at a depth of 0,5 m (Table 27). The sulphate tends to decrease with depth and reaches an average background value of between 0,01 and 0,02 per cent.

5.3 Gemsbok Calcrete Formation

In the Gawib River Valley the Gemsbok calcrete formation is preserved in enclaves of the harder basement of the Etusis and Tinkas Formations. Further west it forms the surface of the Gawib Flats.

The Gemsbok calcrete formation rests unconformably on the Langer Heinrich calcrete formation (Fig. 4(a)). Exposures of the contact are not very clear due to overlying scree and alluvium. Northwest of the area mapped, very distinct contacts were found in a stream channel.

Profiles through the Gemsbok calcrete formation are seen in terraces in the erosional fanglomerates. A typical view through the formation, but not to the base, is illustrated

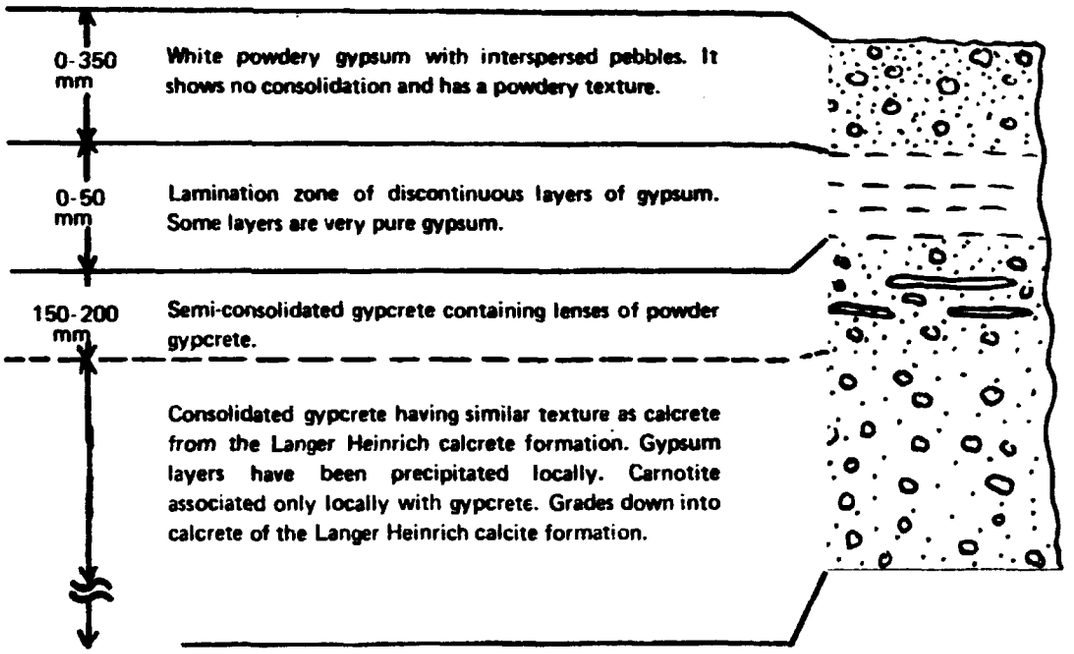


Fig. 5 A profile of gypsum accumulation in the Langer Heinrich calcrete formation which outcrops in the bed of the Gawib River.

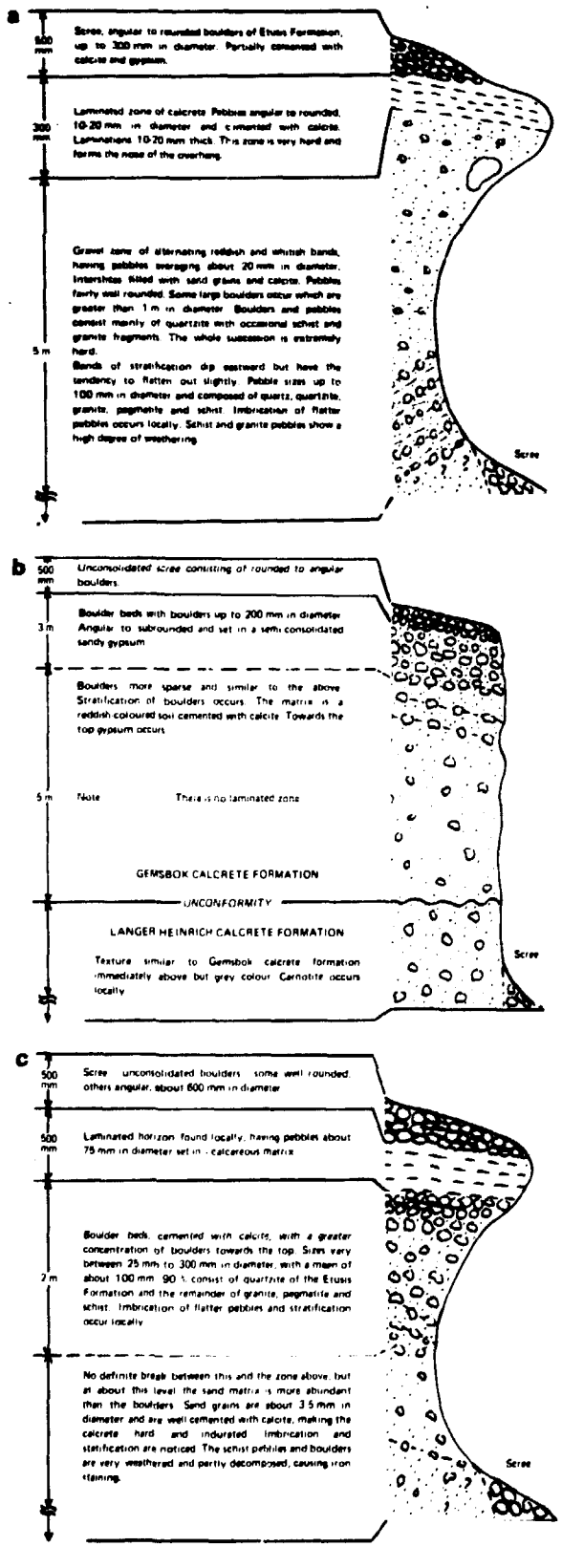


Fig. 6 **Lithological descriptions of profiles through the Gemsbok calcrete formation. For the site localities refer to Map 1.**

(a) Profile 1 : Gemsbok calcrete formation in the west, west.

(b) Profile 2 : Gemsbok and Langer Heinrich calcrete formations near the original prospecting campsite.

(c) Profile 3 : Gemsbok calcrete formation in central part of the erosional fanglomerate.

in Plate 19. Minor differences between profiles in other localities were noted, but they were in general fairly uniform. Lithological descriptions of three profiles are given in Fig. 6. The laminated (Plate 20) and stratified (Plate 21) zones do not occur throughout the length of the Gemsbok calcrete formation.

Broadly, the Gemsbok calcrete formation is a breccia-conglomerate with similar lithological characteristics as the Langer Heinrich calcrete formation. It is well cemented with calcite and most pebbles are well pushed apart. Even larger boulders (Plate 22) up to 300 mm in diameter have been separated, which again testifies to the high pressures involved during crystal growth of calcite. The upper layers of the boulder beds (Fig. 6(b)) have been partially cemented with gypsum, which may account for the absence of a laminated layer.

Flatter pebbles of quartzite and schist are imbricated, indicating a general water direction away from the Langer Heinrich Mountain.

Schist fragments are sometimes totally decomposed and only remnant outlines of the original pebbles still remain. The degree of weathering is so high that they have almost been transformed into soil.

Stratification is found where pebbles commonly as large as 70 mm in diameter are aligned along bedding planes. In the case for the stratification presented in Plate 21, the beds dip towards the east. This is roughly perpendicular to the direction of the stream channel. Glennie (1970,



PLATE 19 A cross-sectional view through the Gemsbok calcrete formation in the western part of the area.



PLATE 20 Laminated zone of calcrete in the Gemsbok calcrete formation.



PLATE 21 Stratified zone in the Gemsbok calcrete formation



PLATE 22 Large boulders (up to 300 mm in diameter) have been pushed apart by calcite crystallization.

p. 30) mentions that the tyoe of sedimentation is related to the velocity of the stream, and that at lower stream velocities ripples may form at right angles to the direction of flow. At higher velocities the ripples become larger and are arranged in the same direction as above. For the example shown in Plate 21 the velocity must have been fairly high to have formed the large ripples, several metres in wavelength, and to have carried the heavy load of pebbles. Furthermore, a slurry with a low water-to-sediment ratio is capable of supporting pebbles of greater size. (ibid., p. 29).

Mabbutt (1952) describes a terrace in the Ugab River Valley, which may be correlated with the Gemsbok calcrete formation, and dates it as lower to middle Pleistocene on the basis of artifacts. Archaeologically this corresponds to the Chelles-Acheul age, between 45 000 and 500 000 years. (Netterberg, 1969(a), p. 89).

5.4 Tumas Gypcrete Formation

The Tumas gypcrete formation consists of the gypcretes in the Tumas River Valley.

Lithologically the rocks are similar in appearance to the calcretes of the Langer Heinrich and Gemsbok calcrete formations, but in this case the cement is composed mostly of gypsum in the upper layers.

The three basic types of gypsum are the powder, vuggy and consolidated varieties. The powder gypcrete appears to be mainly a surface accumulation commonly associated with vuggy gypcrete which occurs just below the surface and

attains a maximum depth of about 2 m. Vuggy gypcrete derives its name from the cavernous structure it develops, which has the appearance of microcaves due to the crystallization of interlocking desert roses. Both powder and vuggy gypcrete are fairly pure as they contain very little detrital material. Carnotite has crystallized in patches and is not uniformly distributed; it therefore appears to be epigenetic with respect to the gypsum.

The consolidated gypcrete lies below the vuggy gypsum, and the best exposures are seen in Von Stryks pit. It is an indurated, well cemented and hard breccia-conglomerate. There is no evidence of desert roses, the disappearance of which is a consolidation effect. Sporadic carnotite mineralization is found towards the top of the consolidated gypcrete, but lower down in Von Stryks pit it vanishes.

Pebbles are both angular and rounded. The latter type were probably derived from thick conglomerate bands of the Etusis Formation nearby. The largest pebbles found were 200 mm but usually they were only about 10 mm in diameter. The 'pushing apart' effect of the gypsum was noticeable.

Fig. 7 is a preliminary interpretation of a seismic profile down the 15° 00' line of longitude. The interpretation is tentative and subject to revision, but has nevertheless yielded a considerable amount of useful data.

Four basic seismic velocities were detected and interpreted as follows:

570- Unconsolidated sand and gravel, probably including alluvium and powder, and vuggy gypcrete.

CONFIDENTIAL

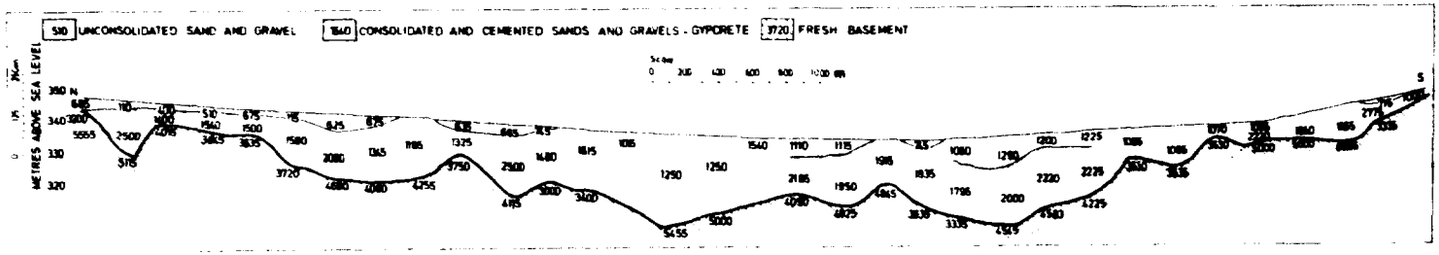


Fig. 7: A seismic profile down the 15° line of longitude. (Courtesy, Anglo American Prospecting Co. Ltd.)

CONFIDENTIAL

1540 - Cemented sands and gravels - consolidated gypcrete.

2500 - This velocity has not been interpreted successively as yet. Mr B. Corner, of the Geology Division of the Atomic Energy Board (personal communication), pointed out that some calcretes have a high degree of consolidation and can maintain seismic velocities similar to the basement rocks. By analogy this may apply to the consolidated gypcrete.

3720 - Basement rocks.

The seismic pattern derived seems to correspond with the facts as observed in Von Stryks pit, with the exception that no basement rocks were intersected in the latter due to its shallowness. The length of the profile is 8 km, with a gypcrete overburden of between 5 and 30 m thick. This indicates a broad and shallow pre-alluvium topography which is typical of early Tertiary erosion surfaces (Mabbutt, 1952, p. 359). It is suggested that this profile may be fairly representative of the palaeotopography from the Gawib Flats to the present-day coastline.

6. THE GEOLOGY OF THE URANIUM DEPOSITS

In this section the geological characteristics of the actual mineralized areas of the uranium ore deposits are discussed.

6.1 Deposits in the Gawib River Valley

Percussion drilling has been the main technique used in evaluating the ore-body. The resultant powders were radiometrically logged in the field using a calibrated scintillometer. Based on this information, the shape and nature of the ore-body was deduced. Unfortunately adequate sampling during percussion drilling is impossibe below the water-table. Thus, a complete assessment of the characteris= tics of the ore-body was limited and all information obtained concerned the upper portions only. It is known, however, that carnotite extends below the water-table.

Initially a few conventional boreholes were drilled but proved unsatisfactory due to a very poor core recovery. A comparison of the $CaCO_3$ values of the powders from the boreholes (Table 27) reveals the presence of as little as 2 to 9 per cent $CaCO_3$. This would account for the bad core recovery. In places the calcrete is therefore only partially consolidated and has a structure similar to that shown in Plate 12.

Radiometric logs of the percussion borehole powders provided data for the construction of profiles depicting the shape, size and general morphology of the ore-body. Fig. 8

gives a selection of profiles drawn by General Mining and Finance Corp. Ltd showing the configuration of the ore-body at cut-off values of 100 ppm eU_3O_8.

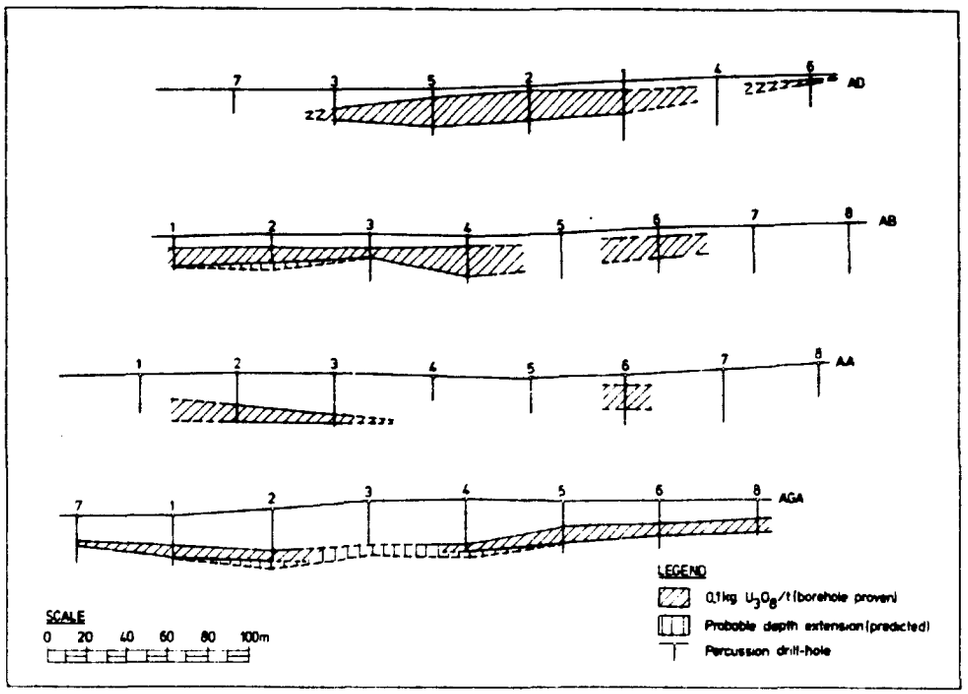


Fig. 8: Profiles of the uranium ore-body in the Gawib River Valley as determined from the radiometric logs of the percussion borehole powders. The outline of the ore-body includes all those values above 0,1 kg eU_3O_8/t or 100 ppm eU_3O_8.

Structurally, the ore-body has a tabular shape but does lack continuity. Boreholes 4 and 5, for example, in profiles AD and AB respectively, did not intersect mineralization, whereas adjacent boreholes did. In profile AA, ore was still being found at the water-table in boreholes 2 and 3. It is reasonable to assume that the uranium ore extends below the water-table. As a whole, the ore-body is undulatory as observed in profile AGA.

The ore-body is not homogeneous for there is segrega= tion of the uranium ore into layers or pockets. This discon= tinuity of mineralization suggests a concretionary type of uranium accumulation.

Although the vertical scale of the ore-body as depicted by profile C in Fig. 9 is exaggerated, it serves a useful

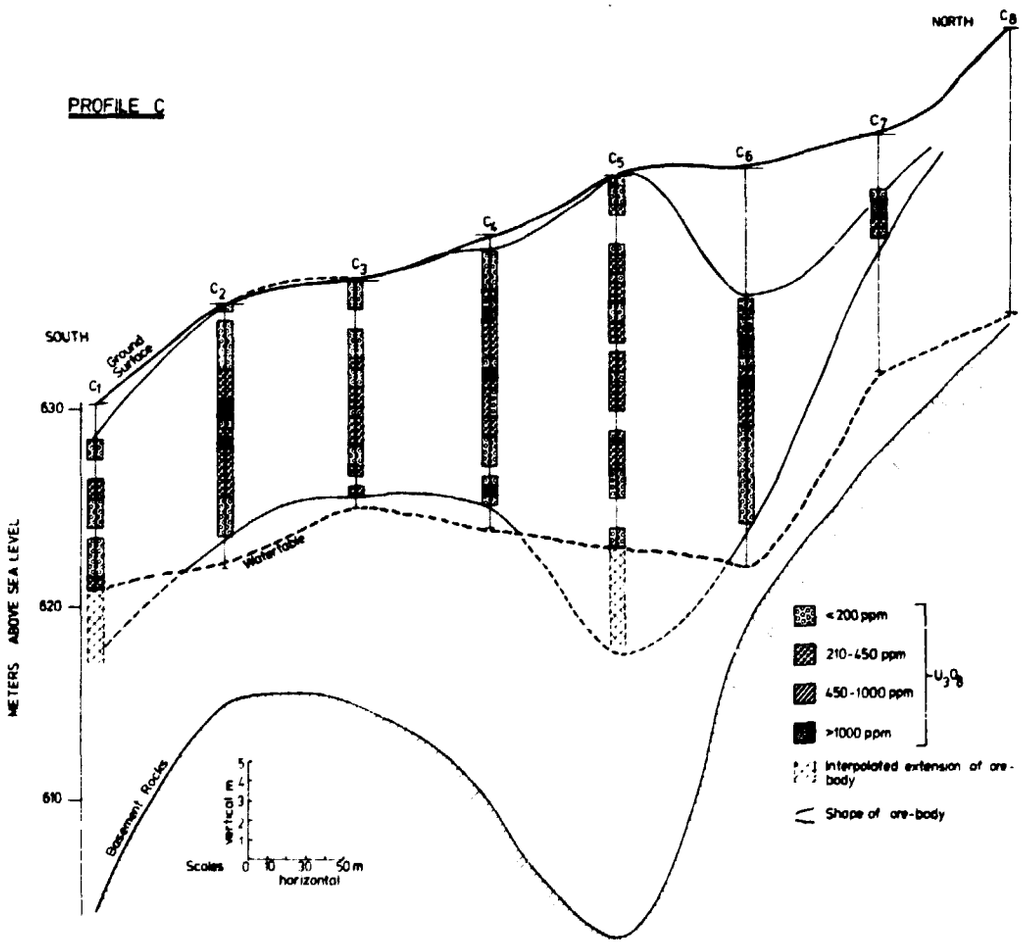


Fig. 9: A cross section of the ore-body through profile C which shows the relationships between the ore-body, water-table and basement rocks.

purpose to illustrate certain aspects. Boreholes C1 and C8 were drilled to the water-table. The definition of the water-table is rather arbitrary, as the site geologist regarded it as the point where the emerging powder became damp. A fair= ly high degree of inaccuracy must therefore be involved.

The profile of the basement rocks, as revealed from seismic data, is undulating, having a 10 m high hump to the south which rises to 25 m above the lowest point to the north. On this uneven floor lies the Langer Heinrich calcrete forma= tion in which the water-table is almost parallel to the contours of the underlying basement rocks. Towards the north, the depth of the water-table decreases significantly and ground= water is almost absent at borehole C8. Similarly, there is a corresponding reduction in the thickness of the ore-body. Therefore the shape and thickness of the ore-body seems to be governed in part by the height and profile of the water- table above the basement rocks. Mineralization in boreholes C1 and C5 was intersected at the water-table, and the extension below it has been inferred. This assumption is substantiated by comparing isopachs of the mineralization in Fig. 10 with the seismic contours of the basement in Fig. 11. (Fig. 10 indicates the locality of profile C while the locality of the area is given in Map 1.) Depressions in the basement rocks as shown by the seismic work correspond with thicker mineralized areas, particularly in the area of profile C.

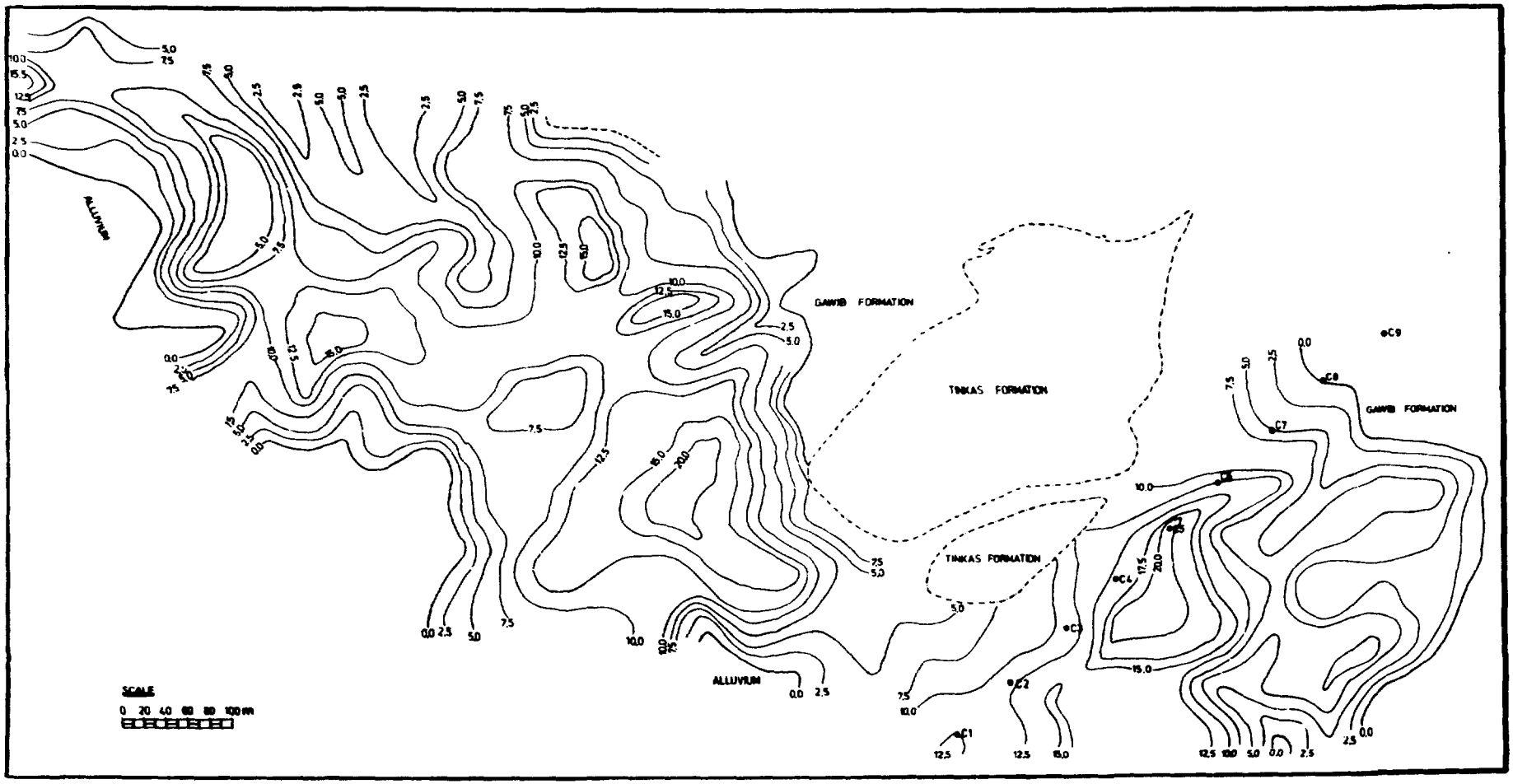


Fig. 10 A portion of the Langer Heinrich calcrete formation showing mineralization isopachs interpolated from percussion borehole data. Note position of profile C. (Compiled from maps of General Mining and Finance Co. Ltd.)

CONFIDENTIAL

CONFIDENTIAL

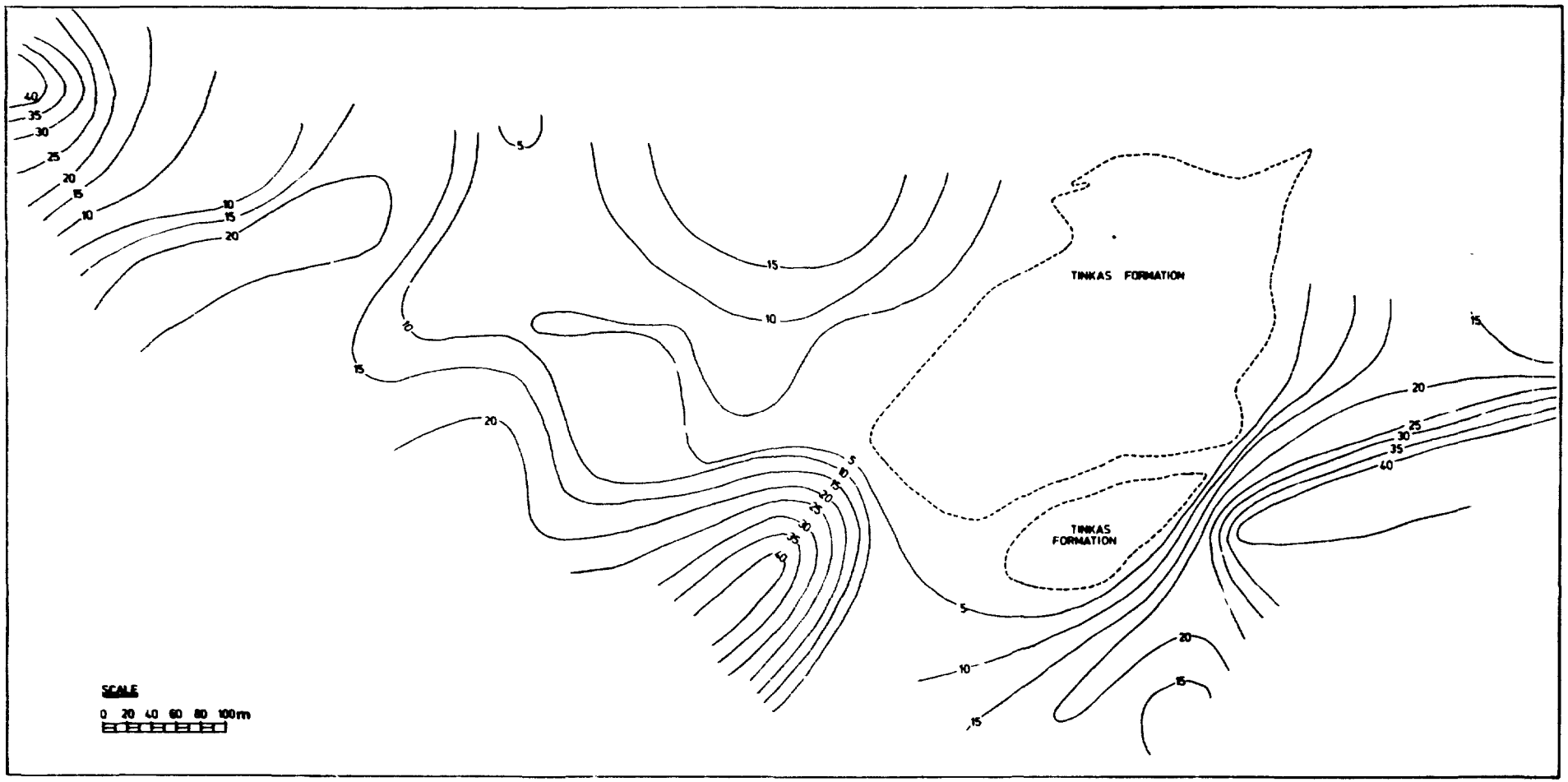


Fig. 11 Seismic isopachs interpolated from seismic refraction data of the same locality as in Fig. 10. (Compiled from maps of General Mining and Finance Co. Ltd.)

CONFIDENTIAL

6.2 Deposits in the Tumas River Valley

Very little information was available concerning the subsurface characteristics of the epigenetic uranium ore deposits in the Tumas River Valley, as no drilling work had been done. Surface outcrops, as well as airborne magnetic and aeroradiometric techniques have so far provided the only data.

Fig. 12 is a schematic representation of a surface radiometric anomaly situated in the banks of the Tumas River. The radioactivity is confined to a reddish gypsum layer near the top. Values of 150 to 300 ppm eU_3O_8 were measured by calibrated scintillometer. On top of the bank all radio= activity disappeared. The surface gypsum is powdery and contains poorly developed desert roses. About 100 mm below the surface the gypsum becomes the consolidated variety, and it seems that the occurrence is very similar to that in Von Stryk's pit, except that no mineralization could be visually detected as it was too finely disseminated in the host rock.

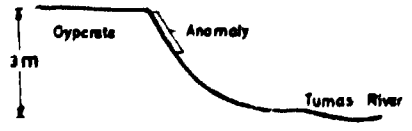


Fig. 12: Sketch of a radioactive anomaly in the gypcrete in the banks of the Tumas River.

Axes of airborne magnetic anomalies and aeroradiometric anomalies south of the Swakop River, and including the Tumas River Valley, are superimposed as in Fig. 13. Only the

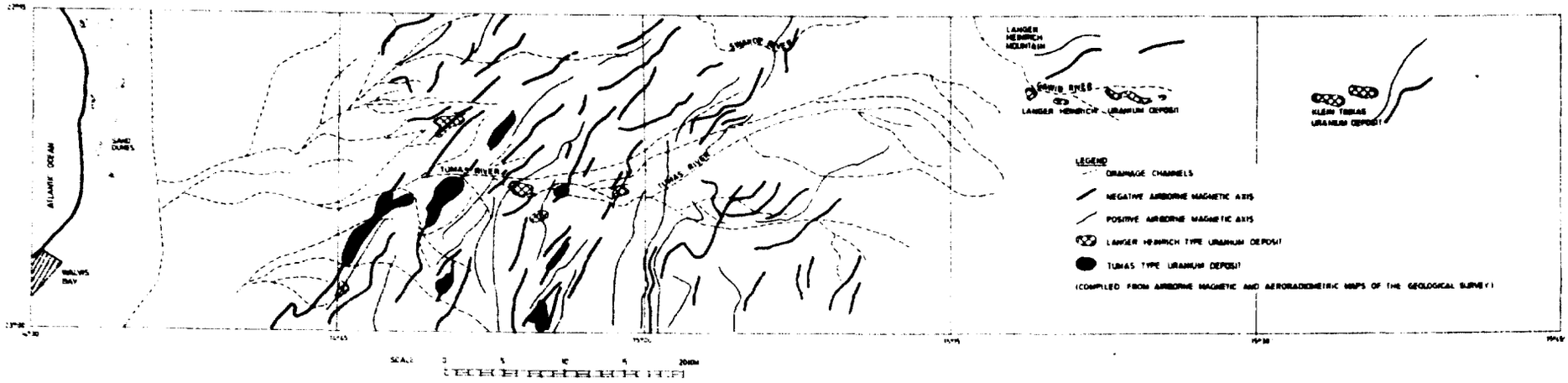


Fig. 13: Airborne magnetic axes and aeroradiometric anomalies for the area between the Swakop River and the 23° 00' line of latitude.

aeroradiometric anomalies of epigenetic origin situated in calcrete and gypcrete are shown. Most of the anomalies lie above negative magnetic axes. The remainder, those that are cross-hatched, seem to be associated with drainage channels.

Two types of uranium deposits are therefore indicated for this area.

(a) The Tumas Type - epigenetic deposits in calcrete and gypcrete having a direct relationship between negative airborne magnetics and aeroradiometrics (Fig. 13). This type of deposit is given the name Tumas because of its wide occurrence in the Tumas River drainage system. Such a relationship implies that the source of the epigenetic uranium in the gypcrete was the basement rocks, probably of alaskitic type, occurring beneath the superficial cover of the Namib group rocks. This hypothesis is based on the findings of Corner (1975) that the alaskites are associated with negative magnetic anomalies. Superficial radioactivity is a secondary uranium dispersion halo which was precipitated by upward migration of mineralizing solutions. Fig. 14 is a diagrammatic sketch of the principles outlined above.

(b) The Langer Heinrich Type - epigenetic deposits in calcrete and gypcrete which are not related to negative airborne magnetic anomalies. These deposits are called the Langer Heinrich Type because the largest known and best developed deposit is situated in that vicinity.

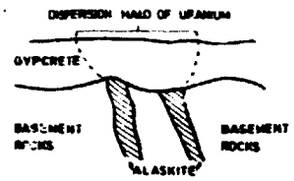


Fig. 14: Diagrammatic representation of a Tumas type uranium deposit. Epigenetic uranium in gypcrete derived from a primary uranium source in alaskites.

6.3 Offshore Marine Deposits

The continental shelf off the coast at Swakopmund is approximately 100 km wide, upon which a series of basins, filled with diatomaceous muds, are situated.

Geological prospecting for uranium in the basins was undertaken by Preussag AG of Germany, and Union Corporation Ltd. The purpose behind their investigation was to determine whether the muds of the basins contained economically viable uranium deposits. Mapping of the muds was done in both a horizontal and vertical direction using bathometric and echographic techniques. Investigations covered an area of the continental shelf between 19° 00' S to 25° 30' S and ranged up to 100 km from the coast (Meyer, 1973).

Bathometric profiles showed that the continental shelf has a smooth gradual slope and lies between 50 and 150 m below the surface at distances of 10 and 70 km from the coast respectively. Meyer (ibid., p. 315) points out that there seems to be no relationship between the morphology of the shelf and the distribution of the diatomaceous mud. The muds in the basins cover a total surface area of 19 000 km^2 and

have a maximum depth of about 15 m.

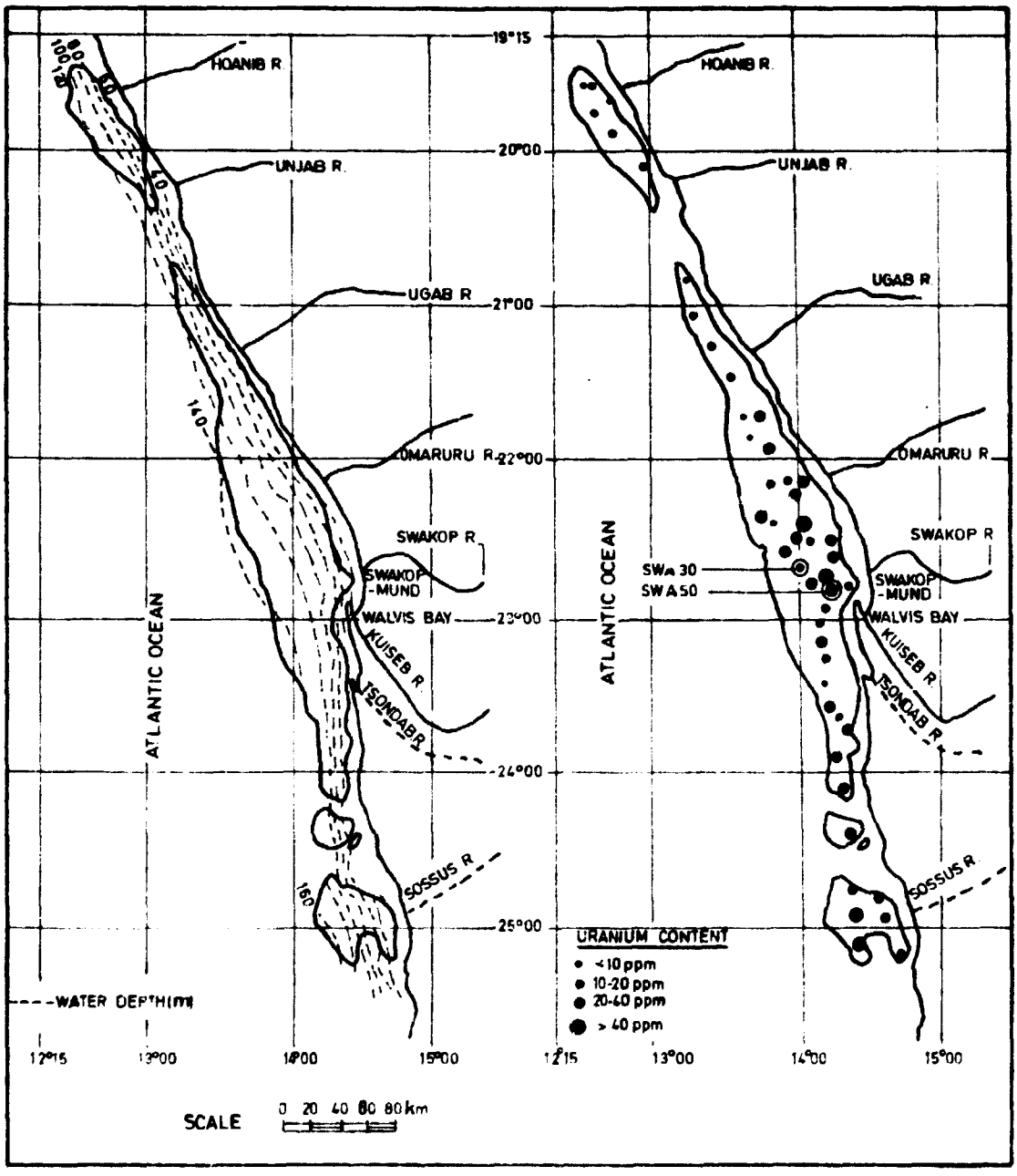


Fig. 15 Four anaerobic basins on the continental shelf which are filled with diatomaceous mud.
(a) Basins in relation to depth of water.
(b) The distribution of uranium in the basins.

Four basins have been recognized (Fig. 15), the largest of which lies between 21° 00' S and 24° 00' S, with

its centre just off Swakopmund. A protrusion situated off Swakopmund, normal to the strike of the basins, may be an infilled channel scoured out by the Swakop River. Because it is filled with diatomaceous mud, the relative age relationships indicate that it may have formed in the Tertiary, while the subcontinent was at a higher elevation or at a lower sea-level. South of Walvis Bay a fault scarp structure occurs parallel to the coast. (Confidential files, Union Corporation Ltd).

The mud is olive green in colour, with laminations due to slight colour variations. Essentially it is composed of skeletal diatoms (genus Chaeloceras)(Calvert and Price, 1970, p. 594), organic matter, terrigeneous constituents and water (Table 4).

TABLE 4: GENERAL COMPOSITION OF THE DIATOMACEOUS MUDS

Constituent	%	Reference
Organic Matter	19-40	Calvert and Price (1970, p. 594, Table 2)
Terrigeneous material	6-34	
Water	77-93	Meyer (1973, p. 316)

Below the diatomaceous mud a silty to sandy layer was found in places but at other localities there is a fossil shell layer containing remains of gastropods, lamellibranchs and sharks' teeth (Meyer, 1973, p. 316).

Palaeontological investigations date the muds to be of Holocene age, but the lower fossil shell layer is late

Pleistocene. Relationships within the latter reveal glacial changes in the level of the ocean, especially during the last interglacial of Eemian age.

Hart and Currie (1960, p. 204) describe the mud as azoic, due to the absence of marine life near the bottom. Characteristically, the muds have a high hydrogen sulphide content which has been responsible for the suffocating gaseous eruptions from time to time. The origin of the azoic zone has been ascribed by them (ibid.) to a deficiency in the soluble oxygen content of the upwelled water of the Benguela Current. Conditions of this nature stimulate the activity of sulphate-reducing bacteria which have been found in the sediment (Baturin, 1949, in Hard and Currie, 1960, p. 204).

6.4 Comparison Between the Langer Heinrich, Yeelerrie and Wyoming Uranium Deposits

Information concerning the Yeelerrie deposit was derived from Von Backström (1974), Dall'Aglio et al (1974) and Langford (1974), and that of Wyoming deposits from Rackley (1971) and Grutt (1972). There are some fundamental similarities between the ore deposits mentioned which are worthwhile enumerating. These are listed in Tables 5 and 6.

Certain similarities between the Langer Heinrich and Wyoming uranium deposits are compared in Table 6. The major dissimilarity is, however, the nature of the diagenesis, for the former is a calcrete occurrence whereas the latter is

mainly a sandstone with little calcite. Grutt (1972, p. 74) mentions that the location of calcareous concretions and calcareous cemented sandstones in relation to uranium deposits may be a possible exploration guide. As yet no such deposits have been reported in the USA.

TABLE 5: COMPARATIVE CRITERIA BETWEEN THE LANGER HEINRICH AND YEELERRIE URANIUM DEPOSITS

Comparative Criteria	Langer Heinrich Uranium Deposit	Yeelerrie Uranium Deposit
Age	(a) Calcrete - of the Langer Heinrich calcrete formation - Miocene to Pliocene	(a) Calcrete - Pliocene to nearly Pleistocene
	(b) Carnotite - Recent, 30 000 years.	(b) Carnotite - Pleistocene
Climate	Desert	Semi-desert
Host rock	Desert fluviatile breccia-conglomerate deposited in Gawib River, cemented with calcite. Grey to brown in colour	Detrital quartz and feldspar, clay and calcite forming low-level calcrete deposits along major drainage. Fine-grained and porcellaneous. Grey to brown colour
Provenance	Crystalline basement, quartzites, schists, granofels, granites and pegmatites	Basement rocks composed of granites and greenstones. Laterites
Stratigraphic features	(a) Sediments deposited on unconformity - African erosion surface - Cretaceous to Tertiary	(a) Sediments deposited on unconformity - Cretaceous to Tertiary

Comparative Criteria	Langer Heinrich Uranium Deposit	Yeelerrie Uranium Deposit
	(b) Epeirogenic uplift initiated new erosion cycle	(b) Epeirogenic uplift initiated new erosion cycle
Deposit type	(a) Tabular and concretionary, layers separated in places by barren zones	(a) Tabular, horizontal layers
	(b) Uranium occurs as fillings in pore spaces surrounding detrital grains	(b) Uranium occurs as irregular fillings in small fractures and cavities
Mineralization	Yellow to greenish carnotite	Yellow carnotite
Paragenesis	(a) Precipitated from subsurface water by soil suction and nucleation	(a) Precipitated from surface water by reduction in partial pressure of CO_2
	(b) Source of uranium and vanadium in basement rocks. Vanadium mainly from Tinkas Formation	(b) Source of uranium - granites. Source of vanadium - laterites
Associated elements	Uranium and vanadium	Uranium and vanadium
Environment	Oxidizing	Oxidizing

TABLE 6: COMPARATIVE CRITERIA BETWEEN THE LANGER HEINRICH AND WYOMING URANIUM DEPOSITS

Comparative Criteria	Langer Heinrich Uranium Deposit	Wyoming Uranium Deposits
Host rock	Fluviatile breccia-conglomerate derived from granite, quartzite and schist. Cemented by calcite. If calcite cement is removed a similar rock type as in Wyoming remains.	Fluviatile sandstones. derived from granitic rock, arkosic to subarkosic, medium-grained to conglomeritic, angular and poorly sorted. Limited calcite cement.
Depositional environment	The Langer Heinrich calcrete formation is a channel-type deposit and it is not unlikely that alluvial fans radiated from the Langer Heinrich Mountain during the upper Tertiary.	Sediments in the Gas Hills, Wind River Basin and West Shirley Basin were deposited in alluvial fans. In the East Shirley Basin sediments were deposited in channels and flood basins.
Structural and stratigraphic features	The uparched areas about the Gawib River are the Langer Heinrich Mountain and the Schieferberge, which are both structural orogenic features. Geomorphologically, the region has been subjected to successive uplifts.	Material was derived from uparched regions and deposited in adjoining intermountain areas.
Hydrodynamic environment	Carnotite precipitated along with the second generation calcite, possibly brought about by changing hydrodynamic conditions.	Following deposition of arkose, uplift changed the hydrodynamic conditions resulting in the onset of oxidizing conditions and carnotite precipitation.
Transportation	Migration of mineralization solutions is controlled by permeability of the host rock. Those sections with low calcite content were the best passageways.	Migration of mineralizing solutions is controlled by permeability within the host rock.

From the comparisons in Table 6 it is very clear that there are noticable similarities between the type of host rocks. The most outstanding and common feature is the necessity to have a continental breccia-conglomerate or poorly sorted sandstone-type rock formed in drainage channels which provide suitable passageways to mineralizing solutions. Also, it was the change in hydrodynamic conditions that brought about the precipitation of carnotite in both instances.

PART II: ANALYTICAL METHODS

7. CHROMATOGRAPHIC SEPARATION, PURIFICATION AND SOURCE PREPARATION OF THORIUM, PROTACTINIUM AND URANIUM FROM GEOLOGICAL MATERIALS

The relative abundances of some of the naturally occurring isotopes of the elements thorium, protactinium and uranium are used for dating purposes and in particular in Pleistocene geochronology (Rosholt, 1970, p. 173). Table 7 gives the necessary nuclear data of the respective isotopes used in this study which are all long-lived and alpha emitters. In alpha spectrometry the separation of the elements from geological materials and from each other are a prerequisite in applying this technique to age determinations because ^{230}Th and ^{234}U peaks overlap and thin sources are required.

Analytical methods and procedures for the separation of metal ions have received considerable attention over the past three decades. Numerous techniques were developed which predominantly involved anion exchange and reversed phase liquid chromatography. The most satisfactory system for the separation of thorium, protactinium and uranium was found to be anion exchange in the chloride form. Each separated fraction obtained from geological materials was found unsuitable for analysis due to the presence of contaminants, which therefore necessitated the use of subsequent purification processes to be applied to each element. Thorium was selectively absorbed onto anion exchange resin in the nitrate form. Reversed phase liquid

chromatography was applied in different forms to both protactinium and uranium.

TABLE 7: NUCLEAR DATA FOR NATURALLY OCCURRING ISOTOPES OF THORIUM, PROTACTINIUM AND URANIUM

Element	Isotope	Half-life (years)*	α-Energy (MeV)*
Th	^{230}Th	8×10^4	4,68
Pa	^{231}Pa	$3,25 \times 10^4$	5,06
U	^{238}U	$4,51 \times 10^9$	4,20
	^{235}U	$7,1 \times 10^8$	4,40
	^{234}U	$2,47 \times 10^5$	4,77

*Lederer et al (1968)

No attempt was made to recover the elements quantitatively through the various stages of separation. Known amounts of isotopic spikes for the respective elements were added in order to determine the chemical yields. Analysis of the separated fractions was done by alpha spectrometry which required a source for each element to be prepared by electrodeposition.

7.1 Experimental Procedure for the Separation of Thorium Protactinium and Uranium from Synthetic, and in Some Instances, Actual Samples

Anion exchange chromatography, using strong base resins in the chloride form, is efficient in separating these elements due to the remarkably different adsorption charac-

teristics of their anionic chloride complexes.

Elution curves for the separation of thorium, protactinium and uranium are given in Fig. 16 and were derived from the experimental procedures.

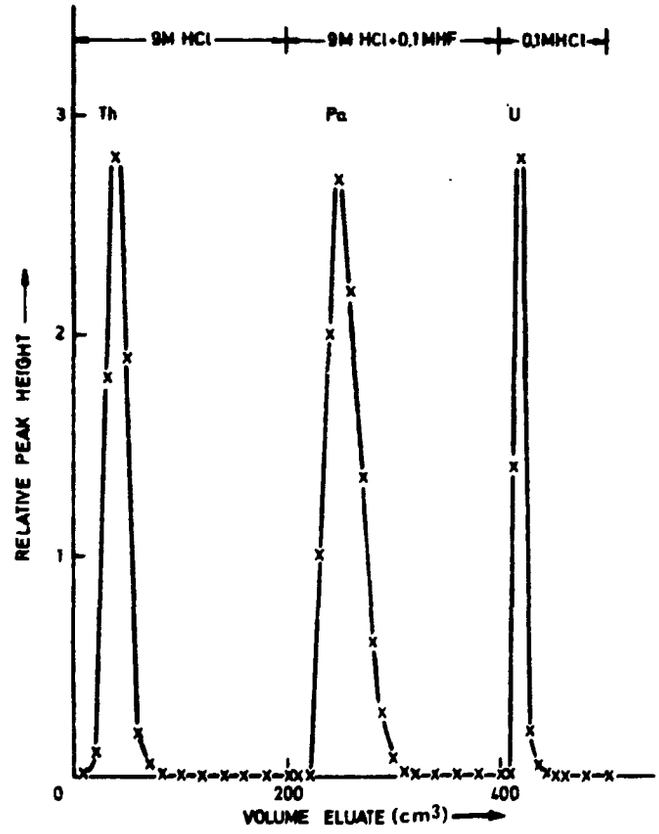


Fig. 16: Elution curves for thorium, protactinium and uranium from strong base anion exchange resin using Bio Rad AG1-X8 in the chloride form.

Fig. 17 summarizes the adsorption of the elements at different hydrochloric acid molarities, which are given as a function of the log of the distribution coefficient (Kraus and Nelson, 1956, p. 118).

CONFIDENTIAL

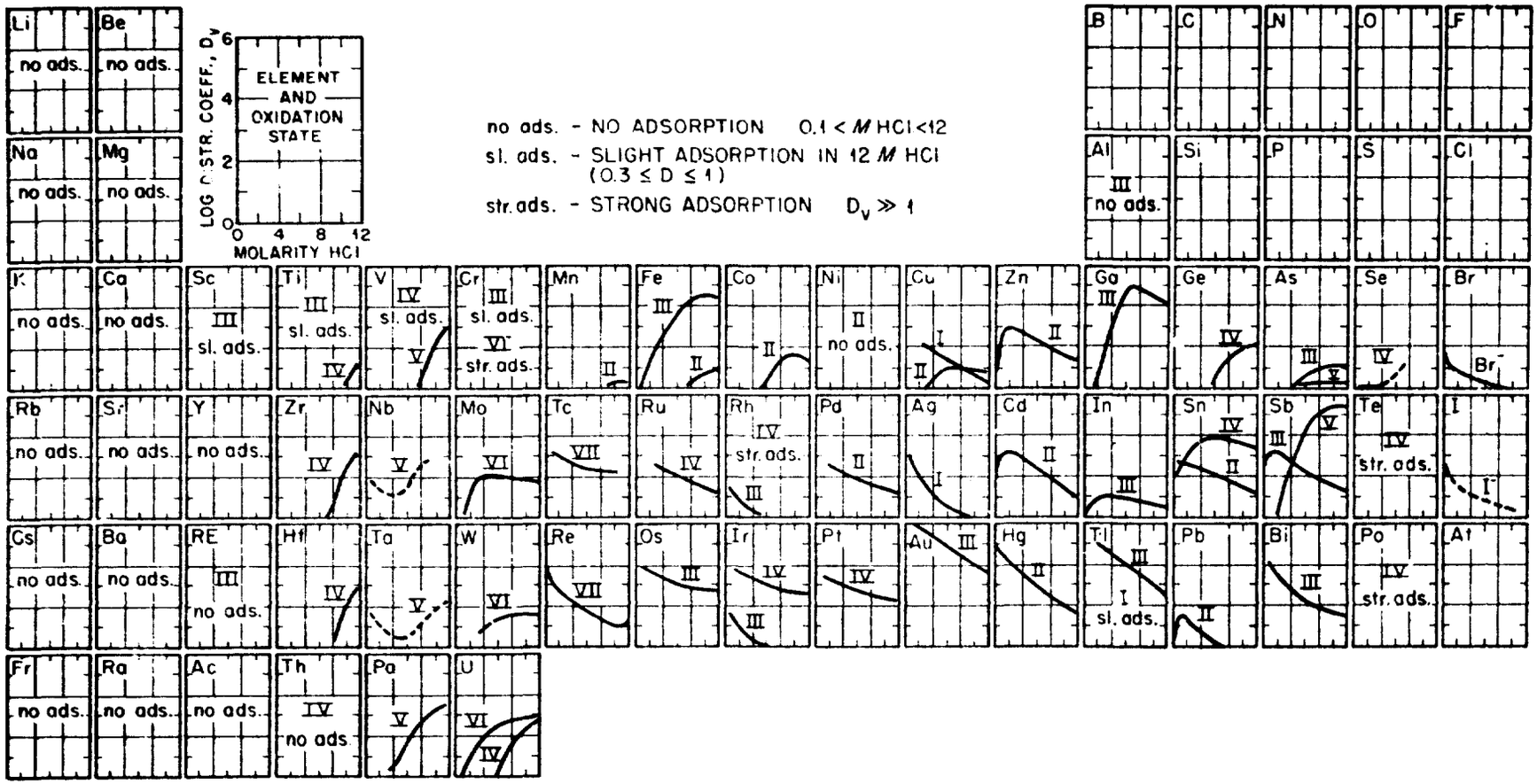


Fig. 17: Absorption of elements by strong base anion exchange resin in hydrochloric acid. (Kraus and Nelson, 1956, p. 118).

CONFIDENTIAL

The elution curve for thorium was produced in the following manner. Thorium is not adsorbed throughout the total hydrochloric acid concentration range. This also applies to the alkali metals, alkaline earths, rare earths etc. Other elements such as uranium, protactinium, titanium, zirconium, hafnium and iron (III) are strongly adsorbed at high molarities. A 9M hydrochloric acid solution containing thorium, lanthanum and europium was passed through the anion exchange resin column. Ten cm^3 portions of the eluate were collected. Five cm^3 of each were titrated with 0,01M EDTA and xylenol orange indicator at pH 3,0 to 3,5 to determine the thorium concentration (Strelow, 1959, p. 1201). A further 2 cm^3 of each portion was evaporated to dryness in quartz tubes and the residue irradiated for three hours in the hydraulic facility of SAFARI-1.

After four days of decay the gamma spectrum of each fraction was analyzed for thorium and the rare earths. Nuclear data for the isotopes used are given in Table 8. The elution data are presented in Fig. 18, from which it was noted that thorium and the rare earths were co-eluted.

Rapid elution of protactinium was accomplished with a 9M hydrochloric acid - 0,1M hydrofluoric acid mixture. In addition, uranium IV and VI can also be separated in this manner. Oxidation of all the uranium to the VI state was essential prior to loading the sample solution onto the column. (Kraus et al, 1956, p. 2694). The adsorption characteristics of elements from hydrochloric acid-hydrofluoric acid mixtures are given in Fig. 19.

TABLE 8: NUCLEAR DATA FOR RADIONUCLIDES PRODUCED BY THERMAL NEUTRONS

Element	Target Isotope	Isotopic Abundance[1] (%)	Thermal Neutron Activation Cross Section (Barn)[1]	Product Isotope	Half-life[2]	γ-Ray Photopeak measured[3] (keV)
Th	^{232}Th	100	7,4	^{233}Pa	27 d	312
La	^{139}La	99,9	9,6	^{140}La	40,22 h	1 595
Eu	^{151}Eu	47,8	3 100	^{152}Eu	12 y	1 408
U	^{238}U	99,3	2,73	^{239}Np	2,35 d	277
Fe	^{58}Fe	0,33	1,2	^{59}Fe	45 d	1 099
	^{54}Fe	5,82	2,8	^{54}Mn	303 d	835
As	^{75}As	100	4,5	^{76}As	26,5 h	559
Zr	^{94}Zr	17,4	0,075	^{95}Zr	65 d	724
				^{95}Nb	33 d	766
Hf	^{180}Hf	35,2	12,6	^{181}Hf	42,5 d	482
Ce	^{140}Ce	88,5	0,54	^{142}Ce	33 d	145

[1] Chart of the Nuclides

[2] Lederer et al (1968)

[3] Adams and Dams (1969)

Titanium, zirconium, hafnium, germanium and protactinium have large distribution coefficients for hydrochloric acid molarities below four in hydrochloric acid-hydrofluoric acid mixtures. In this work 9M hydrochloric acid - 0,1M hydrofluoric acid mixture was used to elute protactinium because the distribution coefficient of protactinium in this

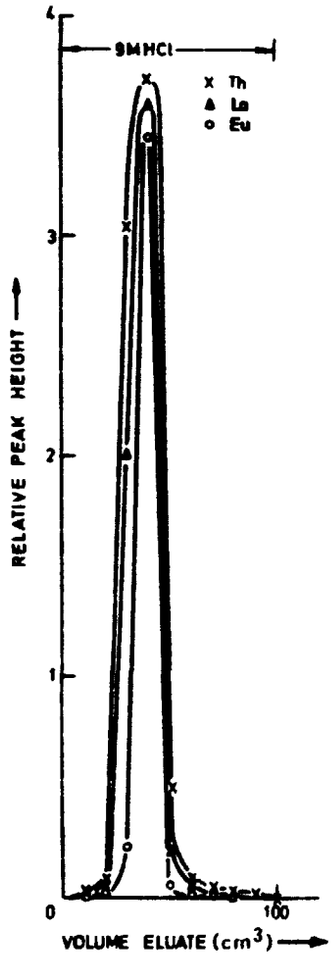


Fig. 18: Elution curves for thorium, lanthanum and europium from strong base anion exchange resin using Bio-Rad AG1-X8 in the chloride form.

system is nearly zero. The elution curve for protactinium (Fig. 16) was determined using the gamma-emitting ^{233}Pa isotope (Table 8). A sharp separation from both thorium and uranium is shown.

During the course of this investigation it was found that ^{231}Pa was completely lost during the separation process whereas the spike ^{233}Pa was recovered with good yield. The

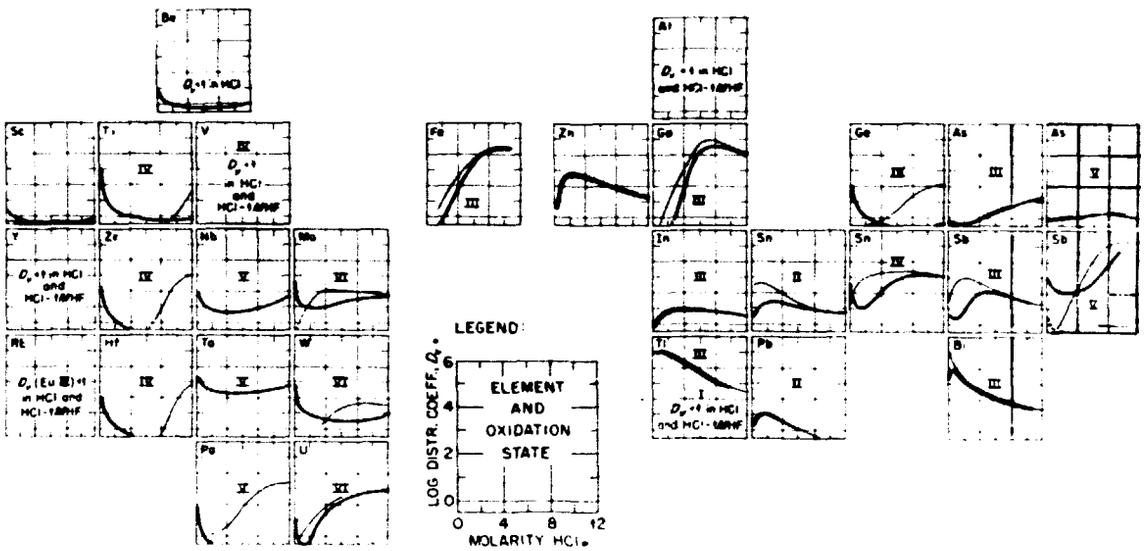


Fig. 19: Absorption of elements by strong base anion exchange resin in HCl-HF mixtures and HCl only. Thick lines give the distribution coefficients in the absence of HF. Thin lines give the distribution coefficients in the presence of HF. (Nelson, Rush and Kraus, 1960, p. 346).

reason for the anomalous behaviour of ^{231}Pa and ^{233}Pa is probably due to both species being in different chemical forms. Since ^{233}Pa is synthetically produced, it would be in the form of an anionic chloride complex, whereas naturally occurring ^{231}Pa may be in the form of a complex oxide species in a highly oxidizing environment (Ahrland et al, 1973, p. 470). To ensure that both isotopes were in identical chemical states, the following procedure was adopted. Carnotite was separated by heavy media using TBE (1, 1, 2, 2, tetrabromoethane, SG = 2,96) and the Franz Isodynamic Magnetic Separator to remove magnetic impurities. The carnotite was initially digested and fumed with concentrated hydrofluoric acid. Successive fumings with concentrated

perchloric and hydrochloric acids respectively were subsequently required.

Elution of uranium was accomplished using 0,1M hydrochloric acid. Iron (III) was co-eluted and was a major contaminant in the separation of uranium from geological materials. Two cm^3 portions of each five cm^3 eluate fraction were evaporated to dryness in polythene capsules and irradiated in the pneumatic facility of SAFARI-1 for 15 minutes. After a decay of one day the ^{239}Np peak was measured (Table 8), from which the uranium elution curve was plotted (Fig. 16).

7.2 Experimental Procedure for the Purification of Thorium, Protactinium and Uranium from Synthetic, and in Some Instances, Actual Samples

In aqueous solutions of nitric acid, thorium forms a stable hexanitrate anionic complex and is adsorbed on strong base anion exchange resin in the nitrate form. Adsorption is best in 8M nitric acid with very few other elements being co-adsorbed (Fig. 20)(Buchanan and Faris, 1960, p. 365). Selectivity of this method is good as thorium can be separated from most elements, including anions.

To test the suitability of the method the following procedure was followed. A granite sample was dissolved and loaded onto an anion exchange resin column in the nitrate form. Two cm^3 portions of the eluted ten cm^3 fractions were evaporated in quartz ampoules and irradiated in the hydraulic facility for two hours. After a decay of

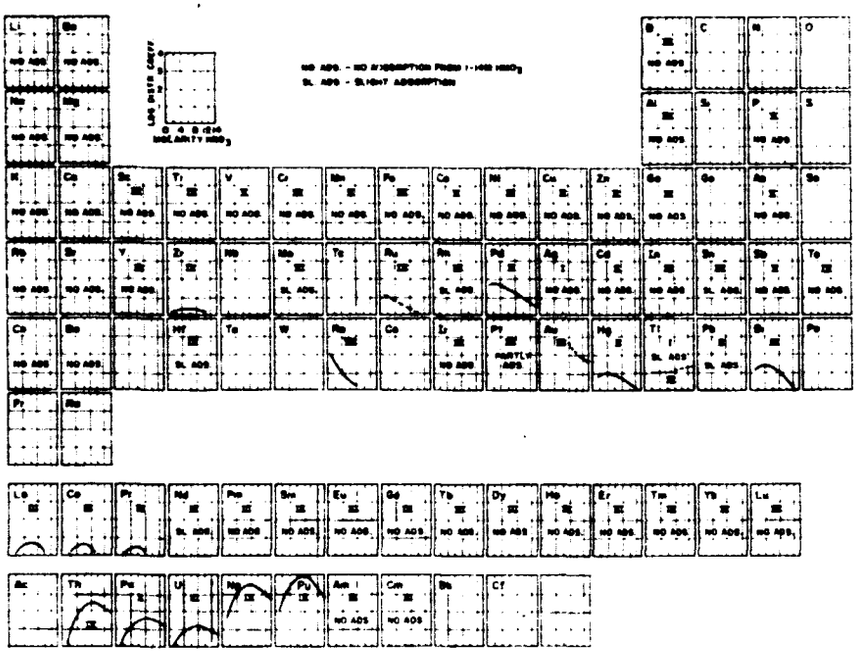


Fig. 20: Absorption of elements by strong base anion exchange resin in nitric acid. (Buchanan and Faris, 1960, p. 365).

two days the samples were counted. From the data, elution curves for lanthanum, cerium and thorium were drawn (Fig. 21) which show a sharp separation between the rare earths and thorium.

The purification of uranium involved the technique of reversed phase liquid chromatography having a stationary phase of tributyl phosphate (TBP) supported by Kel-F powder (Kel-F is polychlorotrifluoroethylene) (Hamlin et al, 1961). Uranium was selectively extracted into the TBP phase from a 5,5M nitric acid solution. Impurities such as iron (III) were quantitatively eluted with the nitric acid. Uranium was eluted with distilled water. To test the efficiency of the separation, the isotopes ^{59}Fe, ^{54}Mn and ^{76}As were used as

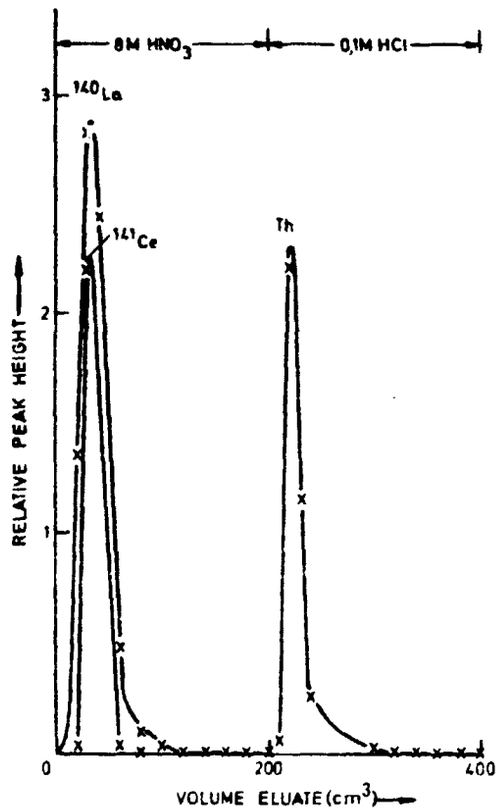


Fig. 21: Elution curves for the rare earths and thorium from strong base anion exchange resin using Bio-Rad AGI-X8 in the nitrate form.

tracers. These were produced by the irradiation of an iron foil (Table 8). ^{75}As was a contaminant and was therefore studied simultaneously. Ten cm^3 portions of the eluate were counted on a gamma spectrometer and in 5,5M nitric acid ^{59}Fe, ^{54}Mn and ^{76}As were quantitatively eluted. As uranium (^{238}U) is not a gamma emitter it would not be counted directly. Two cm^3 fractions of the eluted portions were evaporated in polythene capsules and irradiated for 15 minutes. After a decay of one day the samples were counted. Elution curves for the system are shown in Fig. 22. A sharp separation

between iron and uranium was achieved.

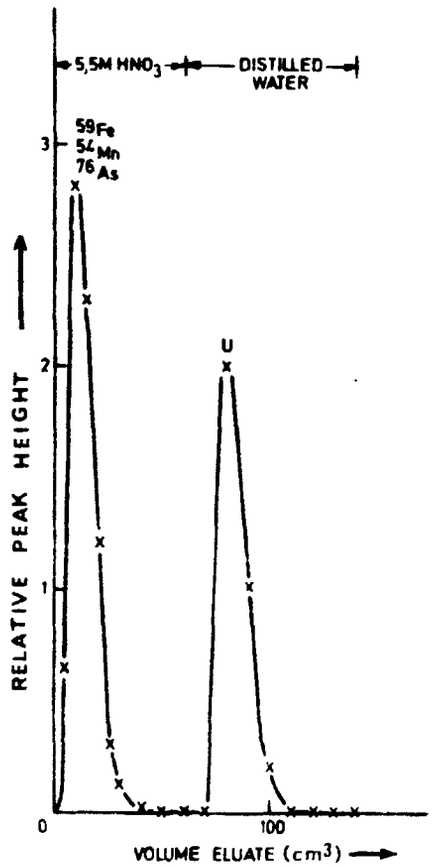


Fig. 22: Elution curves for iron, manganese, arsenic and uranium using reversed phase liquid chromatography with tributylphosphate as the supporting substance and nitric acid and distilled water as the mobile phases.

Protactinium was purified using a modified version of the reversed phase liquid chromatographic method proposed by Stronski (1969) to separate thorium, protactinium and uranium. A quarternary amine, aliquat-336, was used as the stationary phase supported on teflon powder, and the mobile phase was concentrated hydrochloric acid. Fig. 23 shows the variations in extraction coefficient of thorium, protactinium and uranium with increasing concentrations of hydrochloric acid (Ahrland et al, 1973, p. 578).

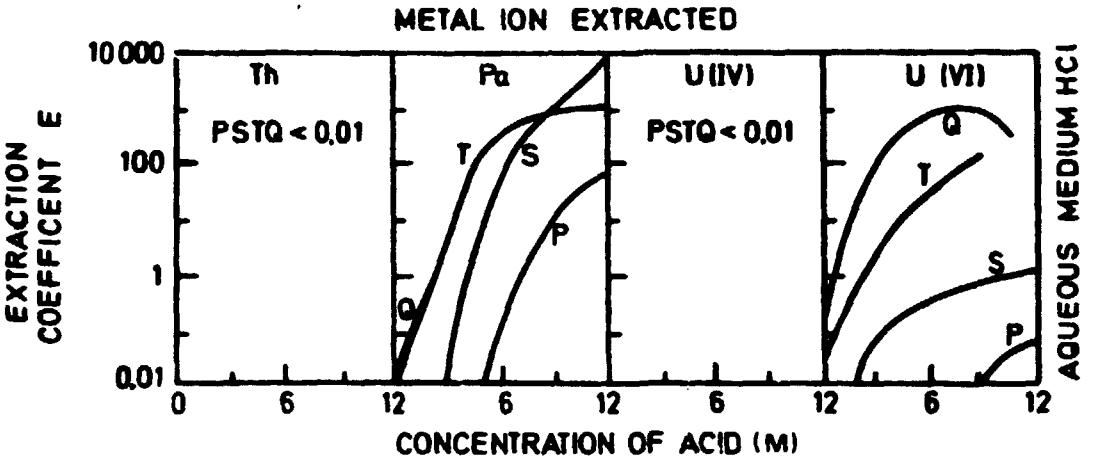


Fig. 23: Extraction coefficients of thorium, protactinium and uranium into amines at different concentrations of hydrochloric acid. P = primary amine, S = secondary amine, T = tertiary amine, Q = quarternary amine. (Ahrland et al, 1973, p. 578).

Both protactinium and uranium behave in a similar manner throughout the whole concentration range. Experimentally this fact was substantiated here and showed that the method of Stronski must be viewed with caution. Therefore for the purification of protactinium by this technique no uranium may be present in the initial solution.

Contaminants of protactinium were titanium, zirconium and hafnium, and in order to test whether these elements could be separated, the following procedure was adopted. The isotopes ^{95}Zr, ^{95}Nb (a decay product of ^{95}Zr), ^{181}Hf and ^{233}Pa were used as tracers (Table 8). Five cm^3 portions of eluate were counted on a gamma spectrometer. In concentrated hydrochloric acid protactinium was extracted into the aliquat-336 and sharp separation between protactinium and the contaminants was achieved. A recovery of 96 per cent

for ^{233}Pa was obtained and the remaining four per cent could not be eluted (Fig. 24).

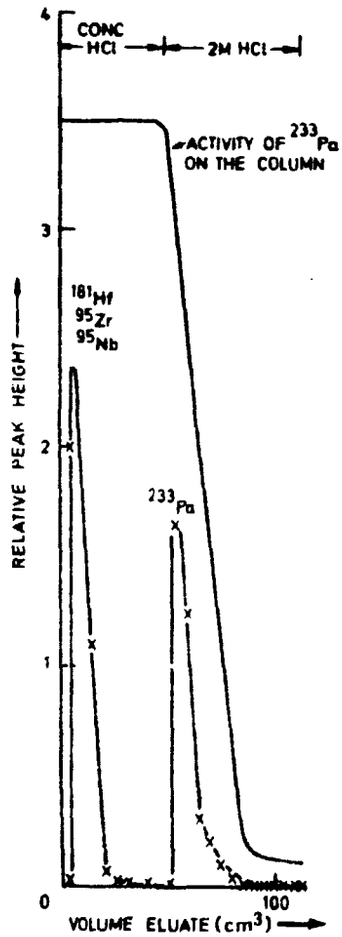


Fig. 24: Elution curves for zirconium, niobium, hafnium and protactinium using reversed phase liquid chromatography with aliquat-336 as the stationary phase, teflon as the supporting substance and hydrochloric acid as the mobile phase.

7.3 Source Preparation of Thorium, Protactinium and Uranium from Synthetic Samples.

Four basic requirements are necessary in preparing sources suitable for α-spectrometry. The source material must be

(a) as pure as possible,

(b) deposited in a small area on a disc,

(c) as thin as possible,

(d) evenly distributed.

The method adopted for the preparation of sources was based on an ammonium chloride system (Mitchell, 1960). The element was dissolved in hydrochloric acid, taken up in ammonium chloride and electroplated for about two hours at a current of 0,5 amps and about 8 volts dc. Due to excessive heating problems of the electrolyte at a high current, the low amperage and longer electroplating time were chosen. Water circulating around the cell helped to dissipate the heat. A drawing of the cell is shown in Fig. 25.

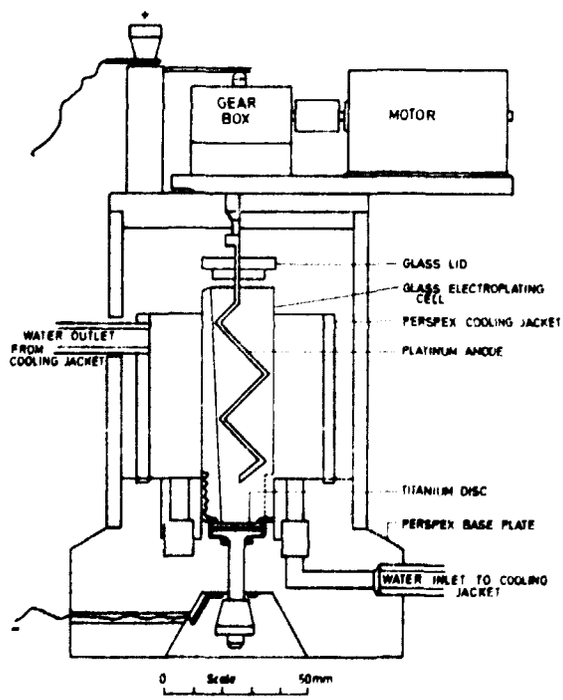


Fig. 25: A drawing of the electroplating cell used for the preparation of sources of thorium, protactinium and uranium.

When α-particles pass through the source material they may suffer an energy loss, giving rise to a tailing effect on the low energy side of a peak. This is caused by the deposit being too thick. Variation of α-particle activity in relation to the thickness of the deposit is given in Fig. 26. For the case of uranium, sources with no more than 60 μg U/cm² can be used. Values greater than this cause the relationship to diverge from linearity, which is a function of energy loss. The ideal situation, where there is no energy loss, is given by the dashed line in Fig. 26.

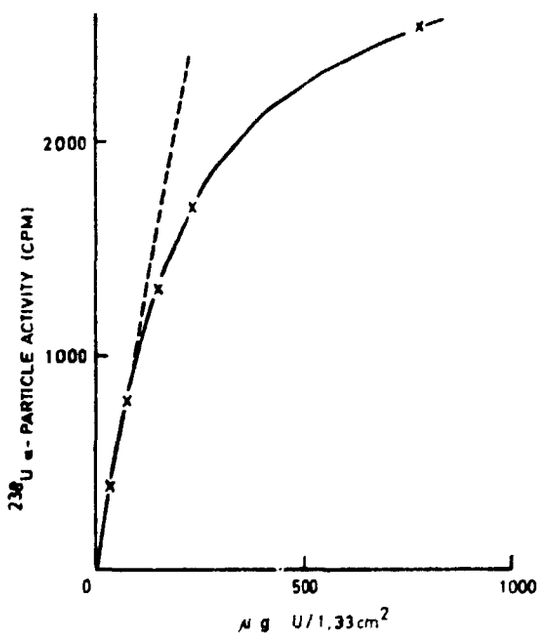


Fig. 26: Variation of alpha-particle activity of ^{238}U in relation to the thickness of the source, expressed as weight of U per unit surface area.

As electroplating time was important to ensure a good yield, a plot of α-particle activity versus electroplating time showed the minimum time required for maximum deposition

of target material (Fig. 27).

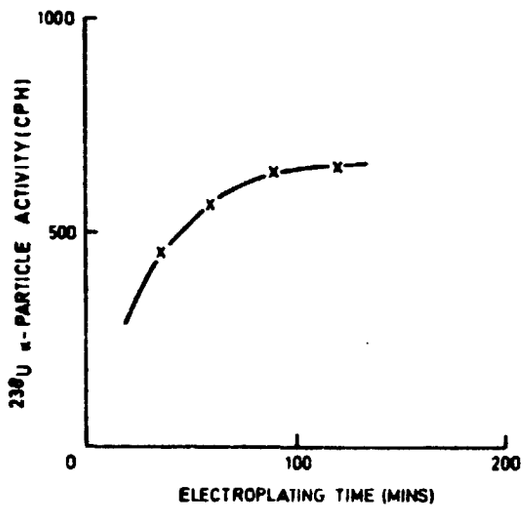


Fig. 27: Variation of alpha-particle activity of ^{238}U with electroplating time.

After electroplating uranium for 90 minutes the curve flattens out and no further uranium is plated. To ensure maximum deposition, a time of two hours was adopted.

A titanium disc was used as a backing for the source material. After plating, Dooley et al (1966, p. 1369) heated the disc for a few seconds in a gas flame before use. This technique was found to be unsatisfactory as titanium reacts easily with oxygen and nitrogen, resulting in the formation of a coating over the deposit. Loss of α-particle energy and poorer resolution of the α-spectrum resulted. Good results were obtained when the disc was heated on a hot plate for two minutes (about 400 °C). Counting was done on a detector system consisting of a surface barrier silicon detector (Princeton Model PD-15-20-300) located in a vacuum chamber. A Tennelec power supply, preamplifier, amplifier and a biased amplifier were coupled to a Intertechnique 400

multichannel analyzer (Model SA 40B) for the spectral analysis. Data were recorded using an interlinked IBM typewriter, and the processing was done manually by adding together the pulses in each channel over the required MeV range.

Typical α-spectra for thorium, protactinium and uranium isotopes are shown in Fig. 28.

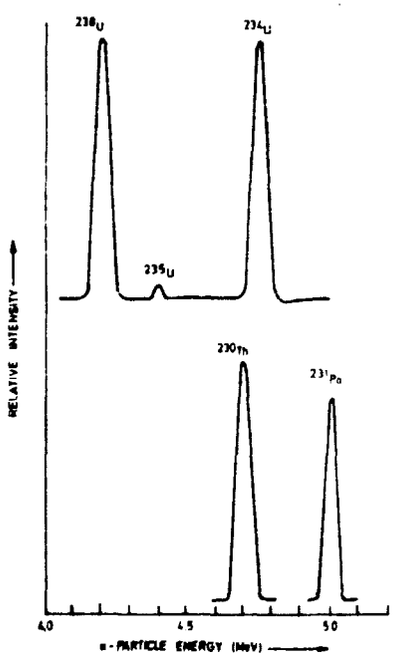


Fig. 28: Alpha spectra for thorium, protactinium and uranium isotopes.

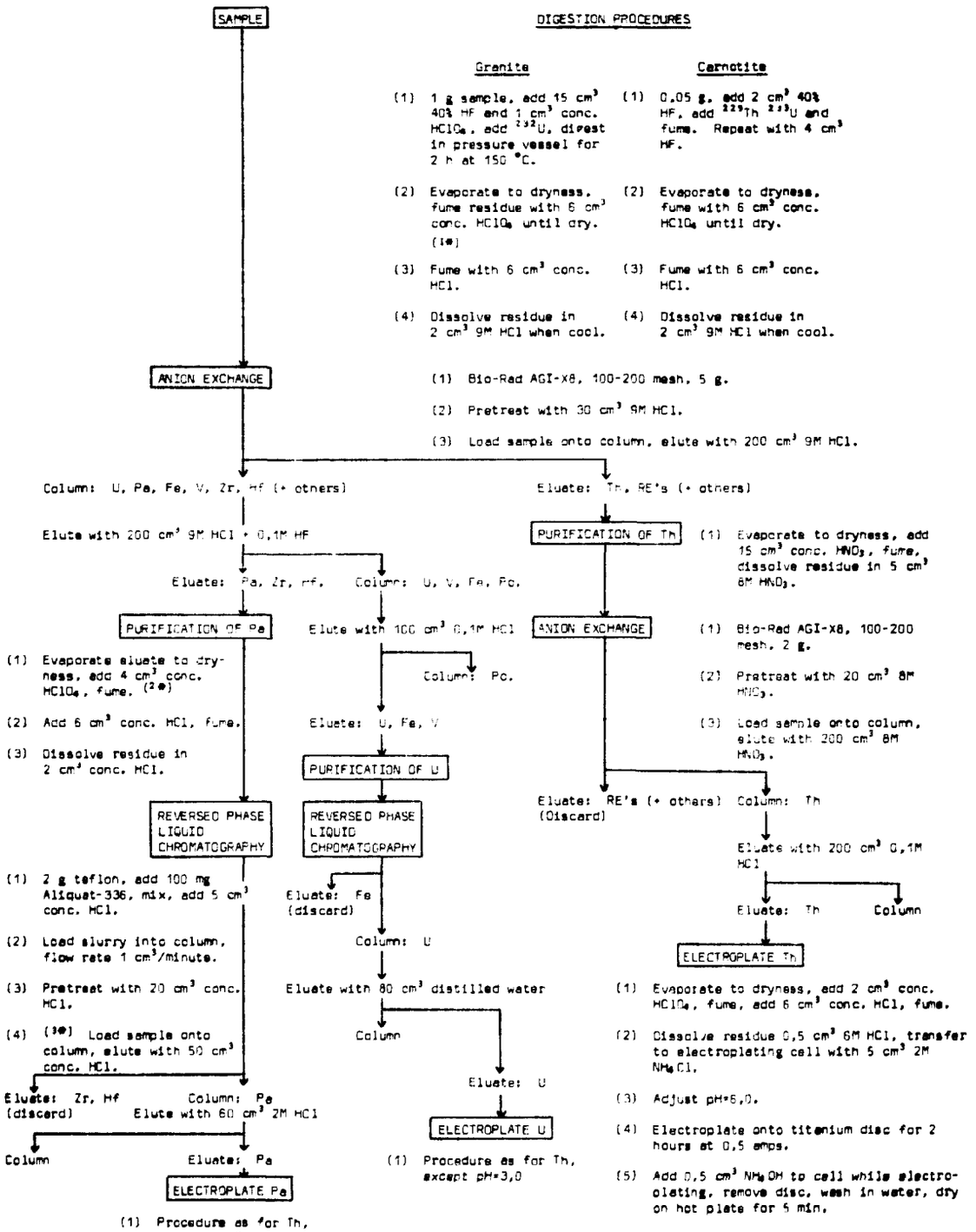
7.4 Chromatographic Separation Scheme

Two rock types, granite and calcrete, were analyzed in this scheme. In the former only uranium was separated on a whole-rock basis, whereas in the latter, carnotite was selectively separated by heavy media as described in Section 7.1. Table 9 gives the detailed procedure for the

chromatographic separation of thorium, protactinium and uranium from geological materials.

The preparation of purification of the spikes ^{229}Th, ^{233}Pa and ^{232}U are given in Appendix 1. Calculations for the determination of the chemical yield for thorium, protactinium and uranium are given in Appendix 2.

TABLE 9: PROCEDURE FOR THE CHROMATOGRAPHIC SEPARATION OF THORIUM PROTACTINIUM AND URANIUM FROM GEOLOGICAL MATERIALS



NOTES: 1* - When the term 'dry' appears in the text it means that the residue must not be baked but allowed to remain slightly moist. This statement applies generally.

2* - Removes all traces of HF, which does not allow extraction into Aliquat-336.

3* - Monitor sample at each stage for radioactivity as a quality control.

8. NEUTRON ACTIVATION ANALYSIS OF THE BLOEDKOPPIE AND GAWIB GRANITES AND THE ROCKS OF THE TINKAS FORMATION

Non-destructive neutron activation analysis (NAA) has been applied to the analysis of a diverse range of rock types with great success. Turkstra et al (1971) and Rasmussen (1973) discuss the methods and techniques applicable to this type of analysis. Certain elements are not easily measured using NAA either due to their nuclear properties or the overwhelming presence of a specific interfering activity. For elements of lower concentration and those with interfering isotopes, a greater sensitivity may be achieved from post-irradiation radiochemical separations (Morrison et al, 1969). In this work only the non-destructive method was used for the analysis of the long-lived isotopes of trace elements in the granites and for the short-lived isotope of vanadium in the Tinkas Formation. The nuclear properties of the radionuclides and the energies of the photopeaks used in the determination are given in Tables 8 and 10.

Of the elements analyzed, there were no interfering nuclear reactions - neither (n,p) nor (n,α) from fast neutrons. The type of reactions that could occur were summarized by Turkstra et al (1971, p. 116).

8.1 Experimental Procedure

A standard solution containing the elements listed in Table 10, and including lanthanum, thorium, cerium, hafnium and

europium from Table 8 (with the exception of aluminium, vanadium and dysprosium) was prepared. Approximately 0,25 g were accurately weighed into quartz ampoules, dried under infra-red lamps and sealed. About 0,2 g of each sample was weighed out, sealed in the same manner and irradiated for six hours in the C-position of the poolside rack irradiation facility of SAFARI-1. The neutron flux for this region of the reactor is about 3×10^{18} n $m^{-2}s^{-1}$ at 20 MW with a cadmium ratio of 60 for ^{60}Co (1 333 keV) which is a measure of the epithermal flux contribution to the total neutron flux. The higher the cadmium ratio, the lower the epithermal flux. Therefore, due to the presence of uranium the C-position was used in order to minimize the possibility of the formation of interfering activities from fission products.

Counting was done on the system available, a 50 cm^3 Ge(Li) coaxial detector coupled to a Canberra preamplifier. Output pulses were amplified by a Canberra amplifier, after which the spectral analysis was done using an Intertechnique 4 000 multichannel analyzer. Data were accumulated on magnetic tape using an Ampex TMZ, start-stop tape recorder. Thereafter the data were processed using Yule's (1968) smoothed first derivitive method, as modified by Brits (1975) to calculate the integrated peak areas for the spectrum. The resolution for the system is 3 keV for the 1 333 keV ^{60}Co peak and has a calibration of 0,55 keV/channel. The samples were counted for 30 minutes after a decay of nine days for the elements lanthanum, barium, lutetium and samarium, and 37 days for the elements europium, cobalt, tantalum, rubidium, scandium, terbium, cesium, hafnium, protactinium and cerium.

TABLE 10: NUCLEAR DATA FOR RADIONUCLIDES PRODUCED BY THERMAL NEUTRONS

Element	Target Isotope	Isotopic Abundance[1] (%)	Thermal Neutrons Activation Cross-Section[1] (Barn)	Product Isotope	Half-life[2]	γ-Ray Photopeak measured[3] (keV)
Al	^{27}Al	100	0,24	^{28}Al	2,31 m	1 779
V	^{51}V	99,8	4,9	^{52}V	3,76 m	1 434
Dy	^{164}Dy	28,2	2 200	^{165}Dy	2,32 h	95
Sm	^{152}Sm	26,7	210	^{153}Sm	47 h	103
Lu	^{176}Lu	2,6	2 100	^{177}Lu	6,7 d	208
Ba	^{130}Ba	0,1	11	^{131}Ba	12 d	496
Rb	^{85}Rb	72,2	0,7	^{86}Rb	18,7 d	1 077
Tb	^{159}Tb	100	22	^{160}Tb	72,1 d	879
Sc	^{45}Sc	100	13	^{46}Sc	83,9 d	889
Ta	^{181}Ta	100	21	^{182}Ta	115 d	1 222
Cs	^{133}Cs	100	29	^{134}Cs	2,05 y	796
Co	^{59}Co	100	17	^{60}Co	526 y	1 173
Zn	^{64}Zn	48,9	0,47	^{65}Zn	245 d	1 115

[1] Chart of the Nuclides

[2] Lederer et al (1968)

[3] Adams and Dams (1969)

Spectra derived from Bloedkoppie Granite are shown in Figs. 29 and 30 for the two counting periods, respectively.

All the photopeaks used for the analysis of the elements in Tables 8 and 10 are essentially free from interfering peaks of other isotopes, with the exception of ^{141}Ce and ^{153}Sm. ^{141}Ce has a small interference peak from ^{59}Fe at 145 keV, and ^{153}Sm has an interference from the 100 per cent relative intensity ^{239}Np peak at 103 keV. Removal of these interferences was done by obtaining a pure spectrum of both ^{59}Fe and ^{239}Np, from which the relative peak intensities of the various lines could be calculated. ^{46}Sc (889 keV) has an interference from ^{110m}Ag (885 keV), but as silver was not detected, it was discounted.

Approximately 0,2 g of sample from the schists and granofelses of the Tinkas Formation were accurately weighed into polythene capsules. Irradiations were carried out in the pneumatic facility of SAFARI-1, which has a thermal neutron flux of about $2,9 \times 10^{18}$ n m^{-2} s^{-1} at 20 MW, and a cadmium ratio of 33. Samples were irradiated for 20 seconds, allowed to cool for three minutes, and counted for five minutes.

The greatest problem concerning the analysis of vanadium is the high concentration of aluminium. Both ^{28}Al and ^{52}V have very short half-lives, and therefore vanadium has to be counted in its presence. In Fig. 31 the ^{52}V peak lies almost on top of the ^{28}Al Compton edge, thereby reducing its sensitivity and consequently the detection limit.

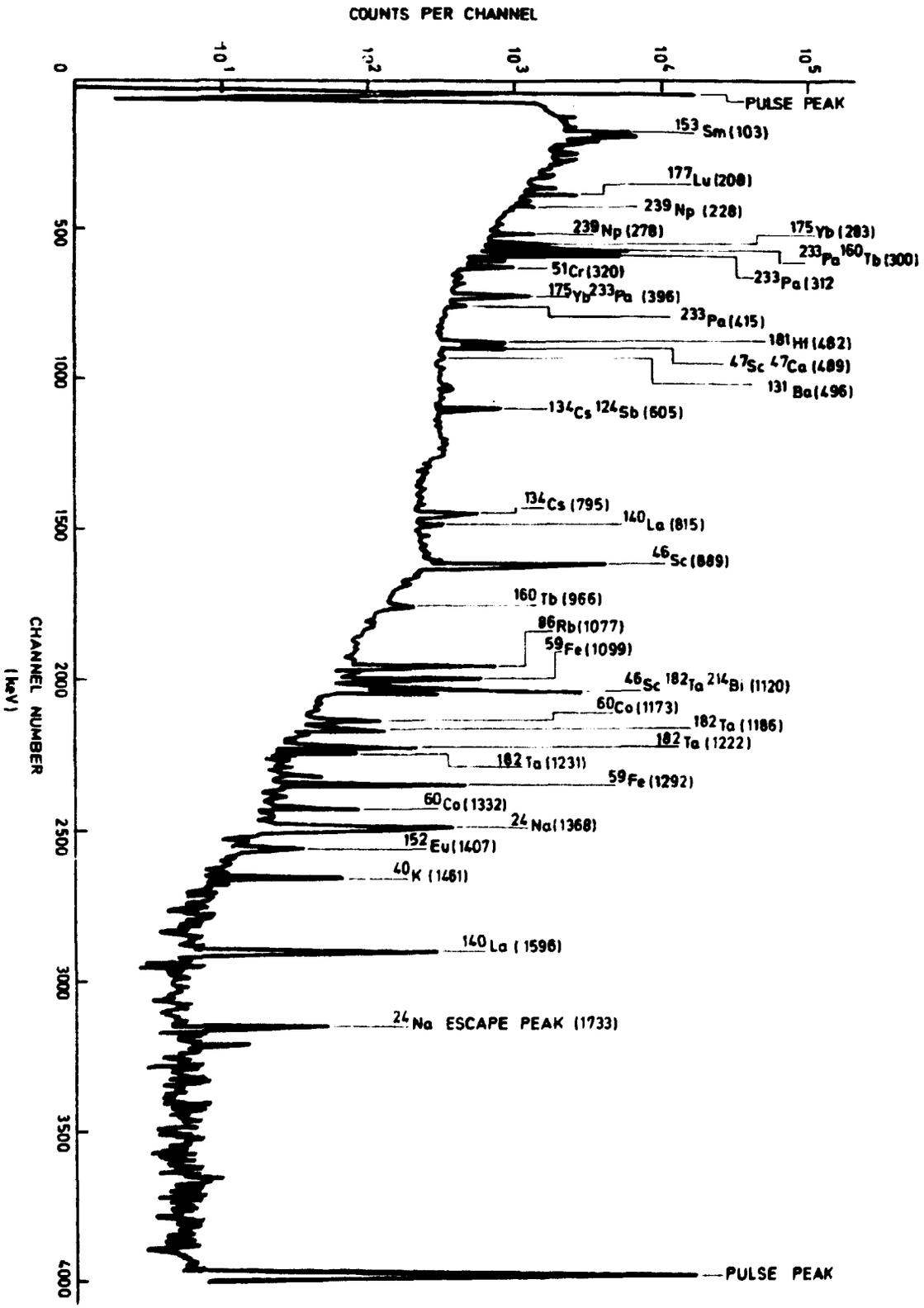


Fig. 29: Gamma-ray spectrum after a decay of nine days for the analysis of lanthanum, barium, lutetium and samarium in the Bloedkoppie Granite.

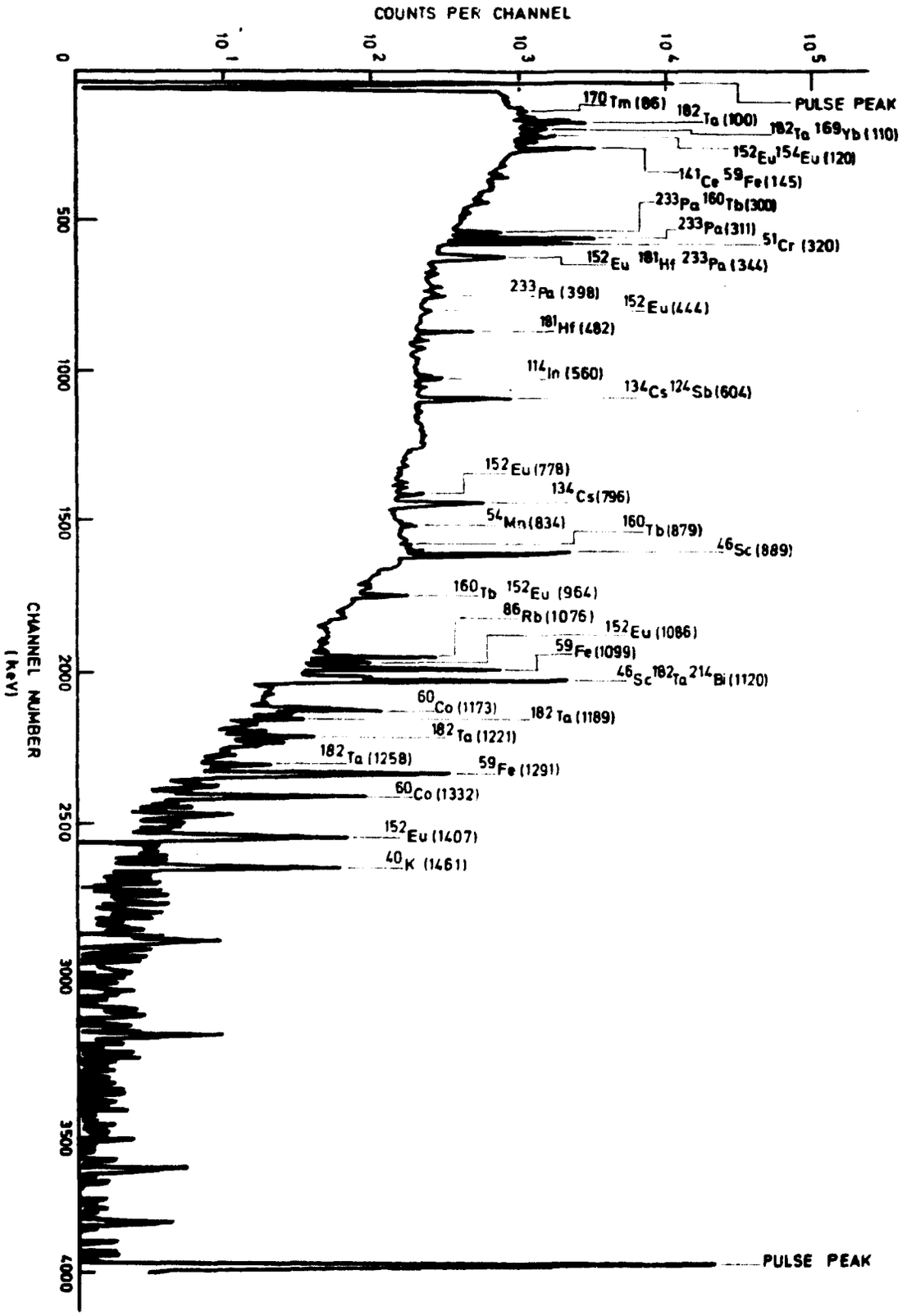


Fig. 30: Gamma-ray spectrum after a decay of 37 days for the analysis of europium, cobalt, tantalum, rubidium, samarium, terbium, cesium, hafnium, protactinium (thorium) and cerium in the Bloedkoppie Granite.

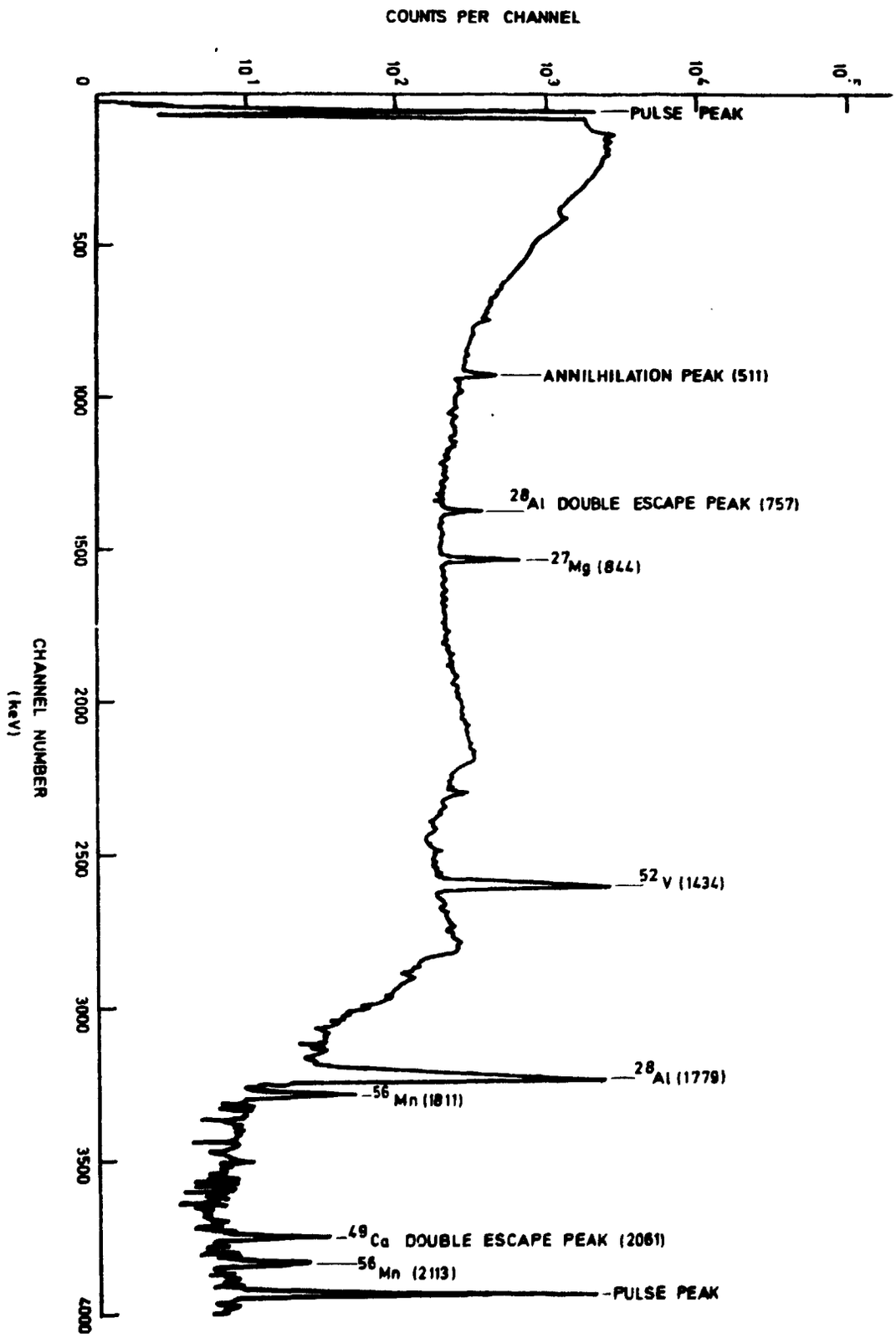


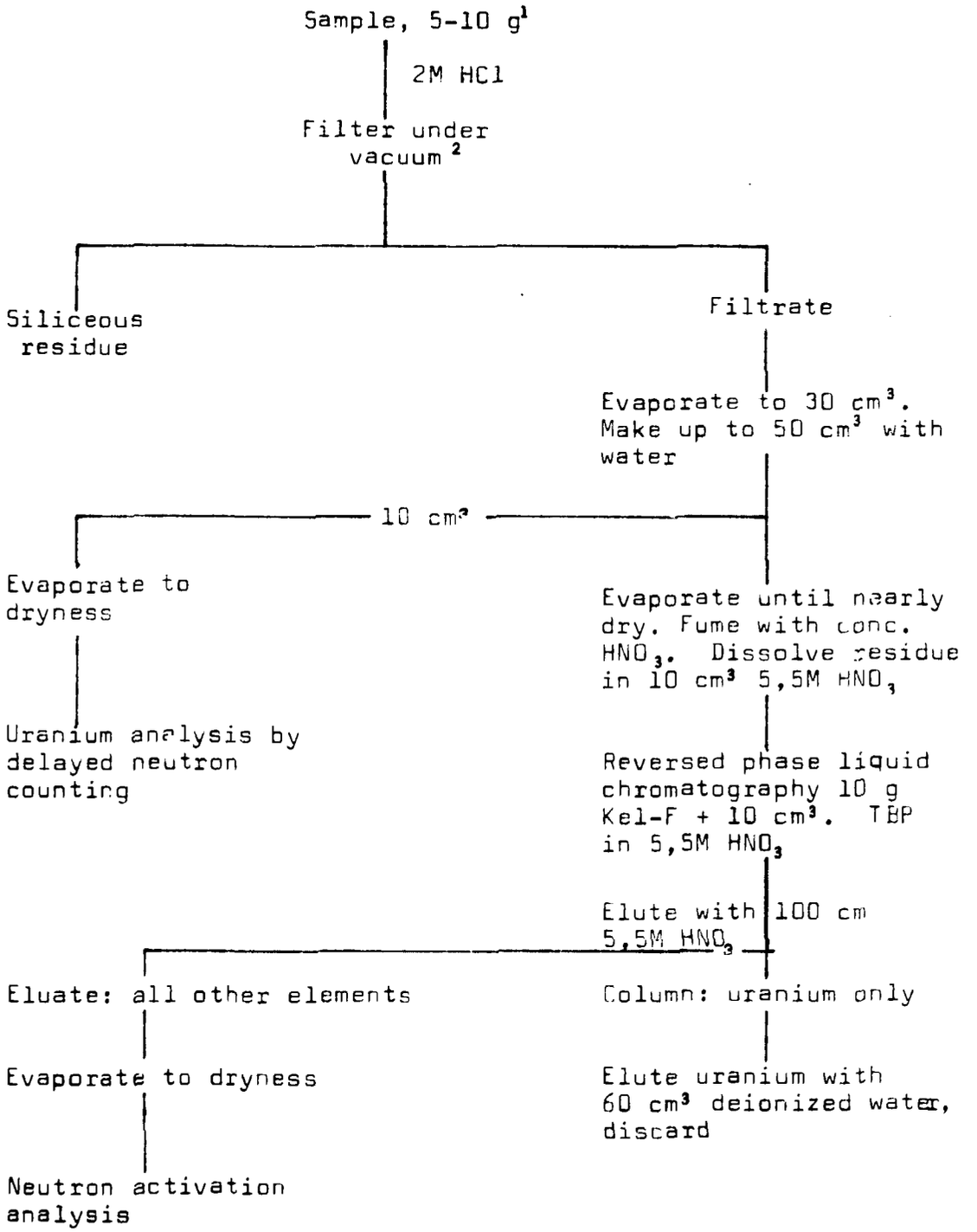
Fig. 31: Gamma-ray spectrum for the analysis of vanadium in the schists and granofelses of the Tinkas Formation.

9. DISSOLUTION AND ANALYSIS OF THE EPIGENETIC FRACTION OF CALCRETE BY NEUTRON ACTIVATION ANALYSIS

The object of this analysis was to determine the distribution of trace elements within the epigenetic calcite-carnotite fraction of the calcretes, which contain about 10 to 50 per cent $CaCO_3$ (Table 27). Both calcite and carnotite are epigenetic minerals which were precipitated from aqueous solution. Along with these minerals, elements in trace quantities were simultaneously precipitated. Calcretes of the Langer Heinrich formation have, in places, high uranium contents, in some instances over 15×10^3 ppm and as little as 20 ppm in others. Neutron activation analysis of samples with such high uranium concentration is further complicated due to the errors introduced from fission products and crowding of the spectrum with ^{239}Np peaks. Therefore it was found necessary to selectively remove uranium. The method adopted for this was reversed phase liquid chromatography using TBP absorbed onto Kel-F, as outlined in Table 11 and based on the method given in Table 9.

In order to ascertain whether there were significant losses of some trace elements during the separation procedure, radioactive tracers of europium, cobalt, scandium and zinc were made for test purposes (Table 10).

TABLE 11: PROCEDURE FOR THE CHROMATOGRAPHIC SEPARATION OF URANIUM FROM CALCRETES



NOTES:

1 The weight of sample used was dependent on the $CaCO_3$ content.

2 PVC, 0,45 mm Sartorius membrane filter, type SM128, was used.

The radioactive sample was dissolved in 5,5M HNO_3, loaded onto the test column and counted to measure the initial gamma activity present. Ten cm^3 fractions were successively removed. After each fraction both the column and the eluate were counted separately.

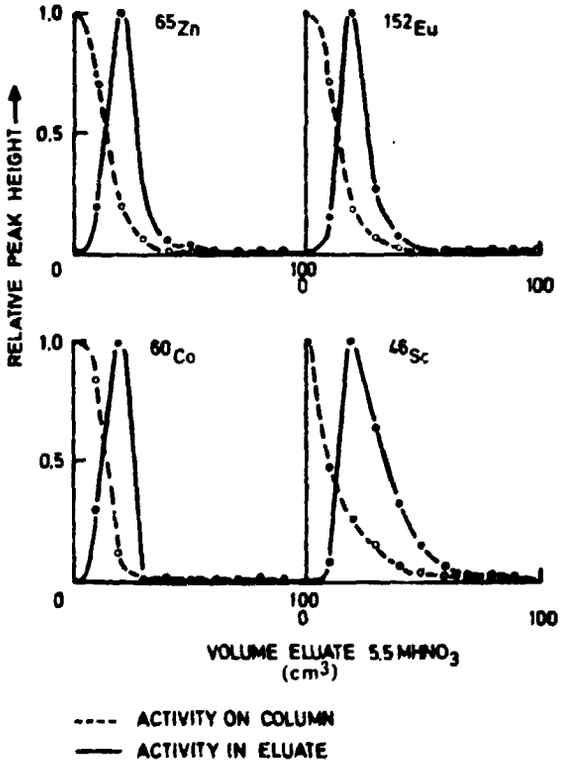


Fig. 32: Elution curves for zinc, europium, cobalt and scandium using reversed phase liquid chromatography with TBP as the stationary phase, supported on Kel-F and 5,5M HNO_3 as the mobile phase. The dashed line shows the activity distribution on the column and the unbroken lines the activity distribution in the eluate.

The results are plotted in Fig. 32 and show the relative activity distribution of the nuclides on the column and in the eluate in terms of eluate volume. After 100 cm^3 of 5,5M HNO_3, no nuclides were detected on the column or in the eluate. The conclusions were, firstly, that there was no retention of those elements on the column,

and secondly, that a very good separation from the uranium was achieved, thereby confirming data published by Hamlin et al (1961, p. 1 549).

9.1 Neutron Activation Analysis

The nuclear data concerning the elements determined in the calcite fraction are given in Tables 8 and 10. The elements are aluminium, vanadium, dysprosium, lanthanum, samarium, ytterbium, lutetium, cerium, scandium, cobalt and europium. Interferences were similar to those described in Chapter 8.

The following experimental procedures were adopted. A stock solution of calcium nitrate was prepared as a standard. To this, known amounts of the above elements were added. Calcium nitrate was used because the samples, when eventually evaporated down, were in a similar form. Calcium nitrate is hygroscopic, which caused problems, especially when weighing the samples for the aluminium, vanadium and dysprosium determinations. Water was taken up rapidly, and it was found necessary to redry the samples before finally weighing. For the short-lived isotopes, the samples were weighed into polythene capsules. Complete dryness could not be achieved due to the relatively low melting point of polythene. A small analytical weighing error was therefore present for aluminium, vanadium and dysprosium. As far as the remaining elements were concerned, the samples were weighed into quartz ampoules which could be heated to higher temperatures, thereby driving off the moisture.

Approximately 100 mg samples were used for all determinations.

Initially the polythene capsules were irradiated in the pneumatic facility of the reactor for two minutes, allowed to decay for one minute, and counted for five minutes. Aluminium and vanadium were determined by this method. Fig. 33 is a gamma spectrum of aluminium and vanadium from which both elements have good relative intensities. A period of approximately two weeks was allowed to elapse, after which the same samples were reirradiated for ten minutes. After a decay period of 70 to 120 minutes the samples were counted for the analysis of dysprosium. (Fig. 34).

The second batch of samples weighed into quartz ampoules were irradiated in the C-position of the poolside rack for eight hours in order to obtain a flux with the lowest possible epithermal neutron flux contribution. This was done to minimize the production of fission products from uranium that might not have been completely removed in the extraction process. The samples were counted after four days for lanthanum, samarium, ytterbium and lutetium (Fig. 35) and finally after 13 days for cerium, iron, scandium, cobalt and europium (Fig. 36).

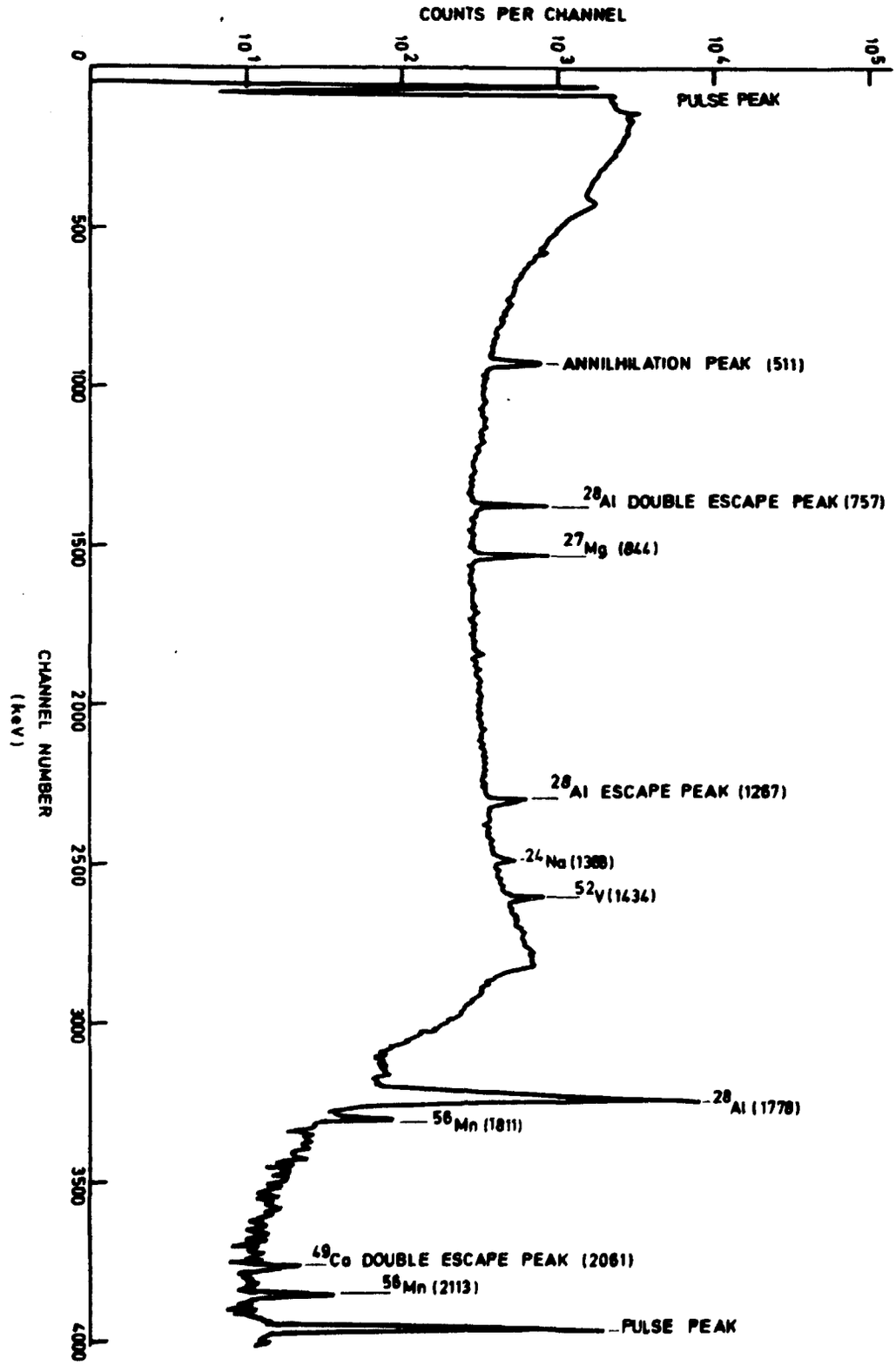


Fig. 33: Gamma-ray spectrum for the analysis of aluminium and vanadium in the epigenetic calcite fraction.

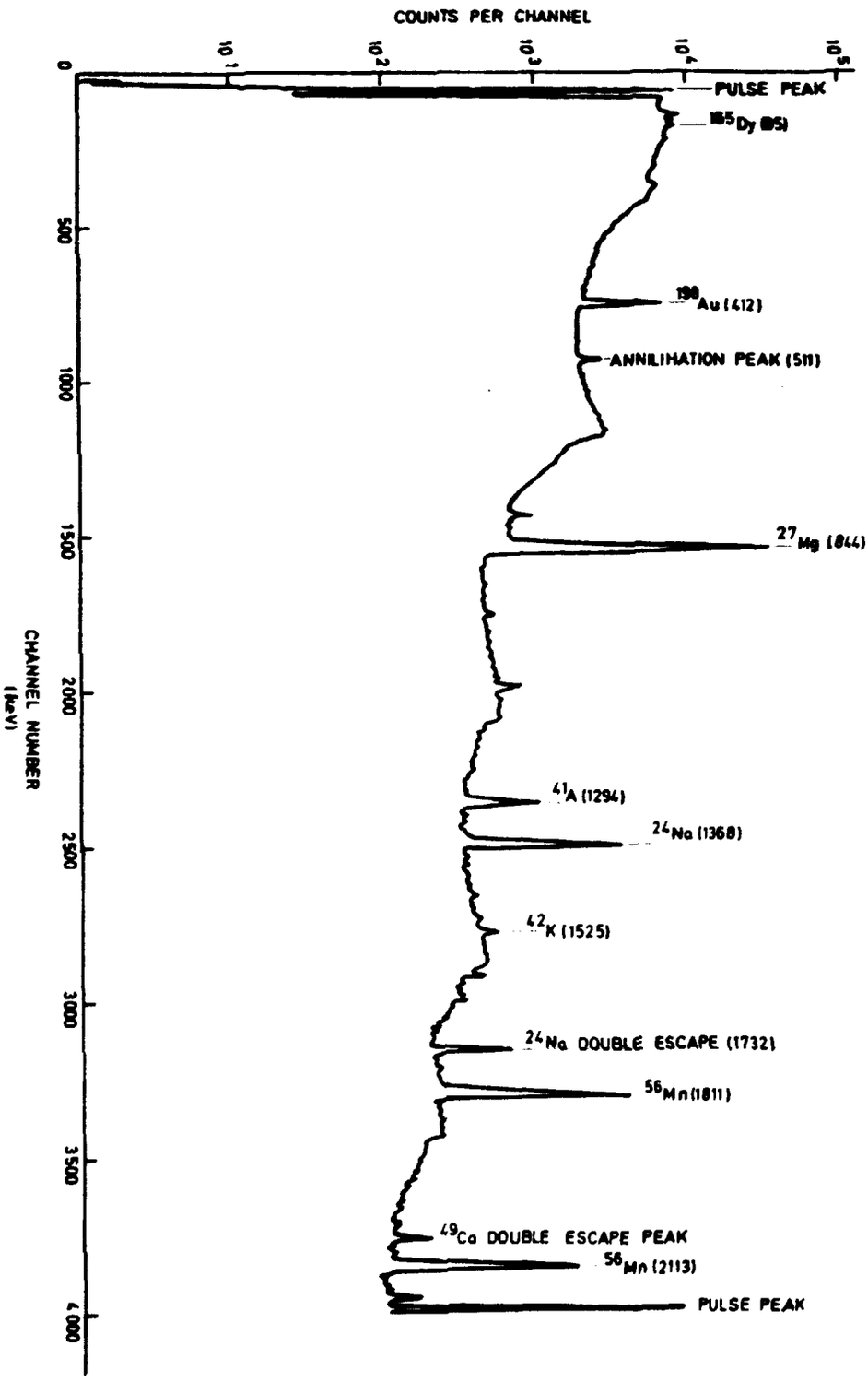


Fig. 34: Gamma-ray spectrum for the analysis of dysprosium in the epigenetic calcite fraction.

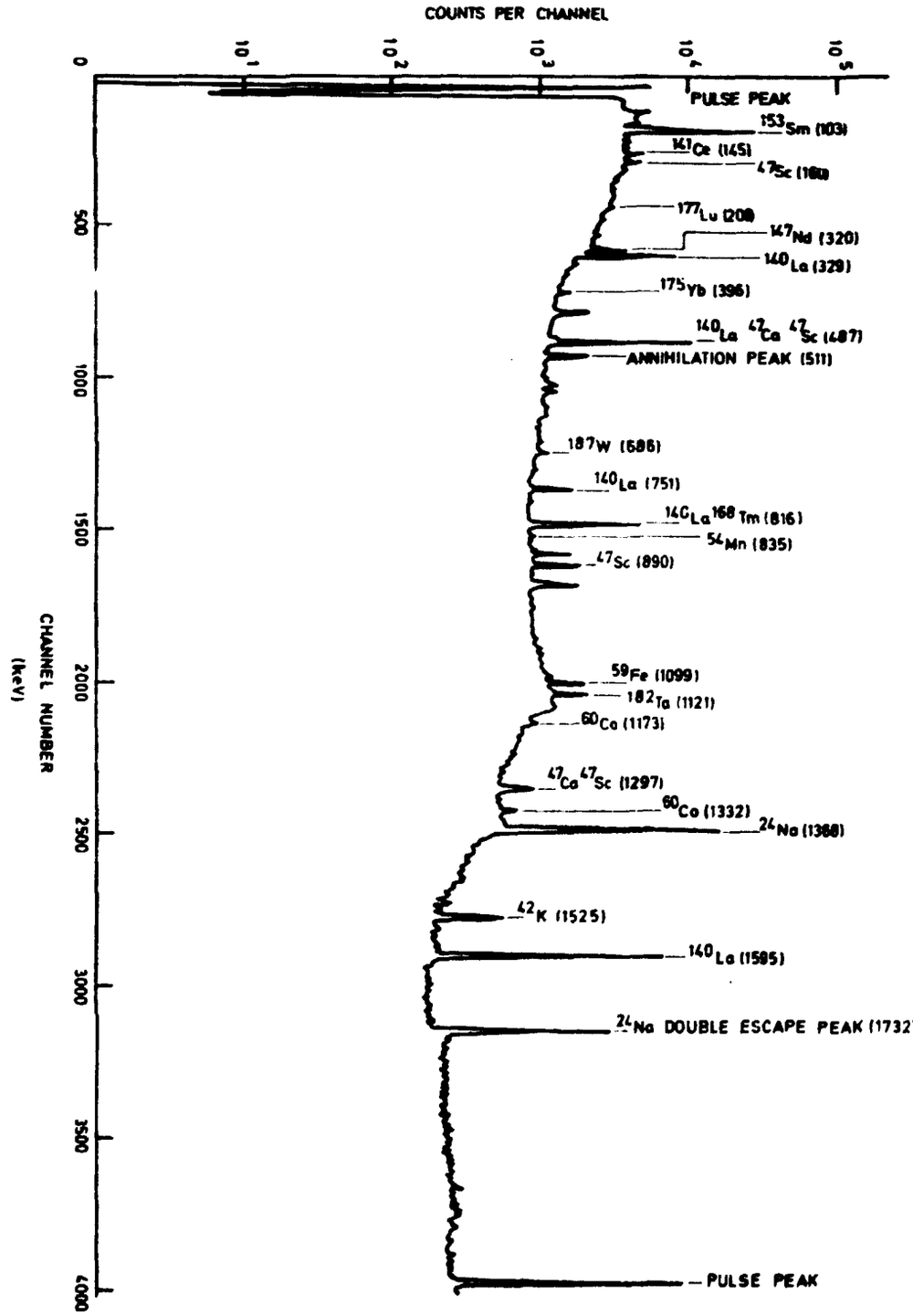


Fig. 35: Gamma-ray spectrum after four days' decay for the analysis of lanthanum, samarium, ytterbium and lutetium in the epigenetic calcite fraction.

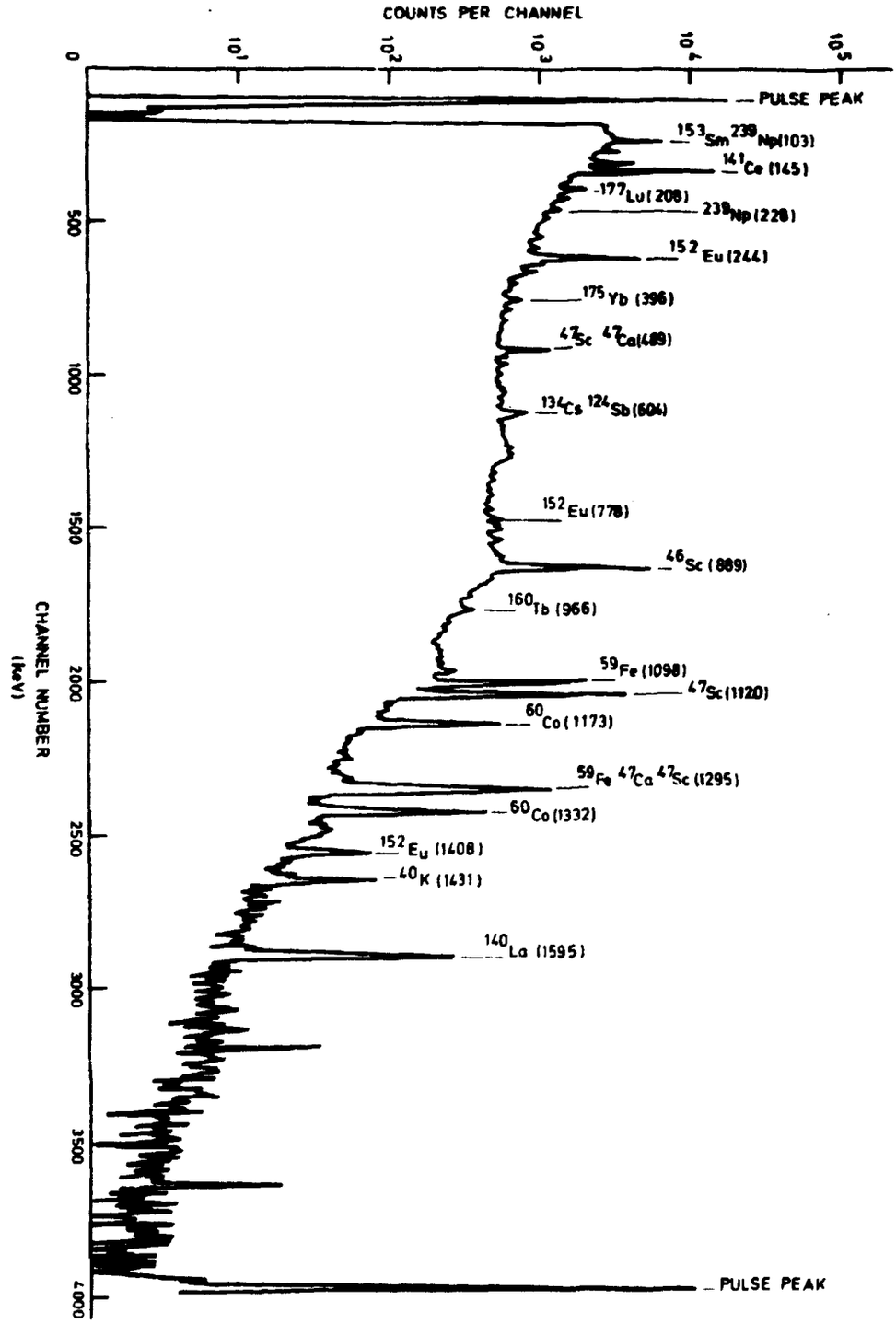


Fig. 36: Gamma-ray spectrum after 13 days' decay for the analysis of cerium, iron, cobalt, scandium and europium in the epigenetic calcite fraction.

10. CHROMATOGRAPHIC SEPARATION AND PURIFICATION OF URANIUM FOR MASS SPECTROMETRIC ANALYSIS

The technique employed for this purpose was a modification of the existing methods used in this study to separate and purify uranium (Table 9). Of prime importance was the high purity of the uranium, for it must be free of all organic compounds, cations and anions (with the exception of nitrate). The reason for this was the ultra sensitivity of the mass spectrometer to the presence of interfering species, which results in unstable performance. The end result was a considerable reduction of the quality of the analytical data obtained.

Three stages were required for the purification procedure (Table 12). These are similar to those described earlier.

(a) Separation of uranium from thorium, alkalis, alkaline earths and rare earths by anion exchange in the chloride form.

(b) Purification of uranium using tributyl phosphate in reversed phase liquid chromatography.

(c) Removal of traces of tributyl phosphate by ashing and separation of phosphate using anion exchange in the chloride form.

Three samples were processed in this manner, two of calcrete from the Langer Heinrich and one of uranothorianite from Phalaborwa.

The quality of the spectrum is dependent on two major parameters, the first being the correct functioning of the

mass spectrometer, and the second the quality of the separation. On the assumption that the first was of high quality, any instrumental instability was therefore due to poor analytical separation. A good spectrum capable of giving high precision is shown in Fig. 37.

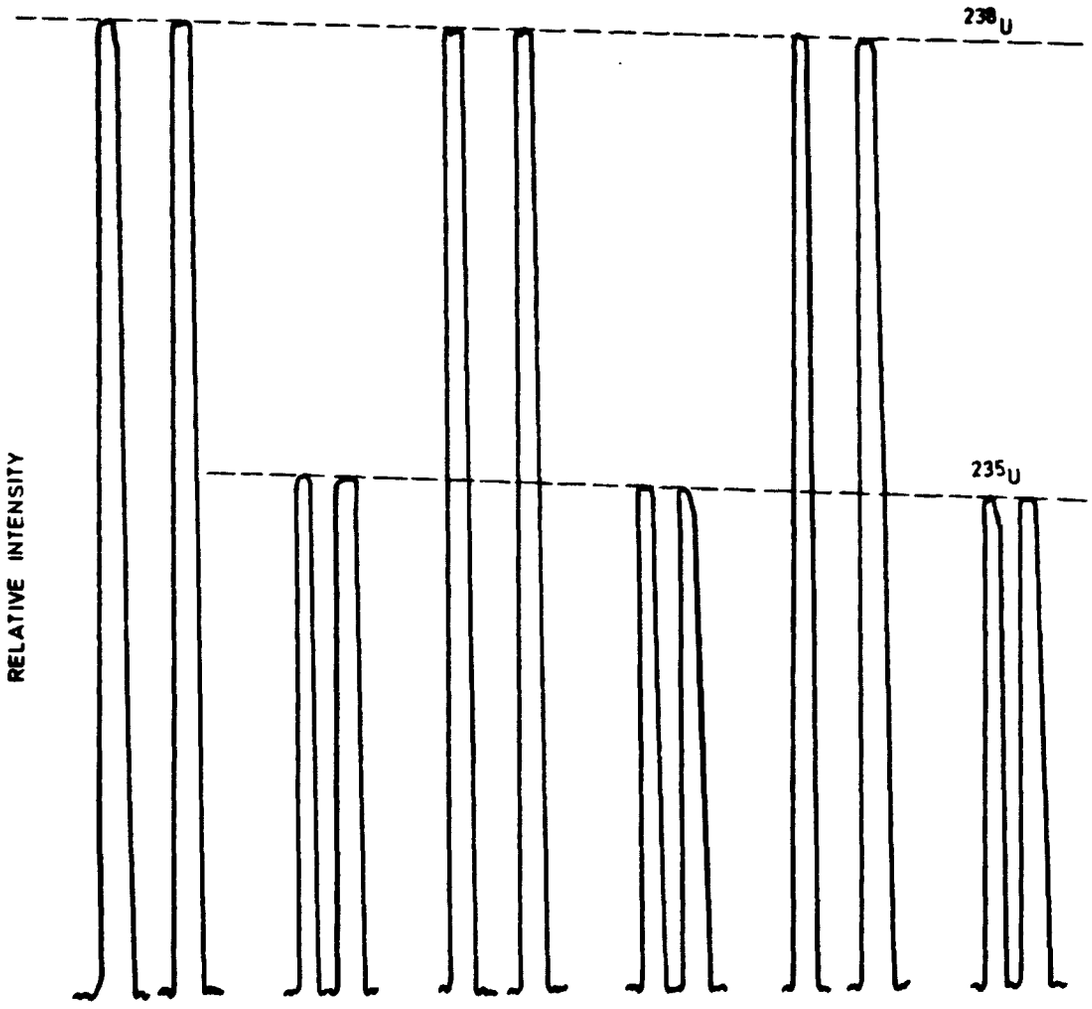
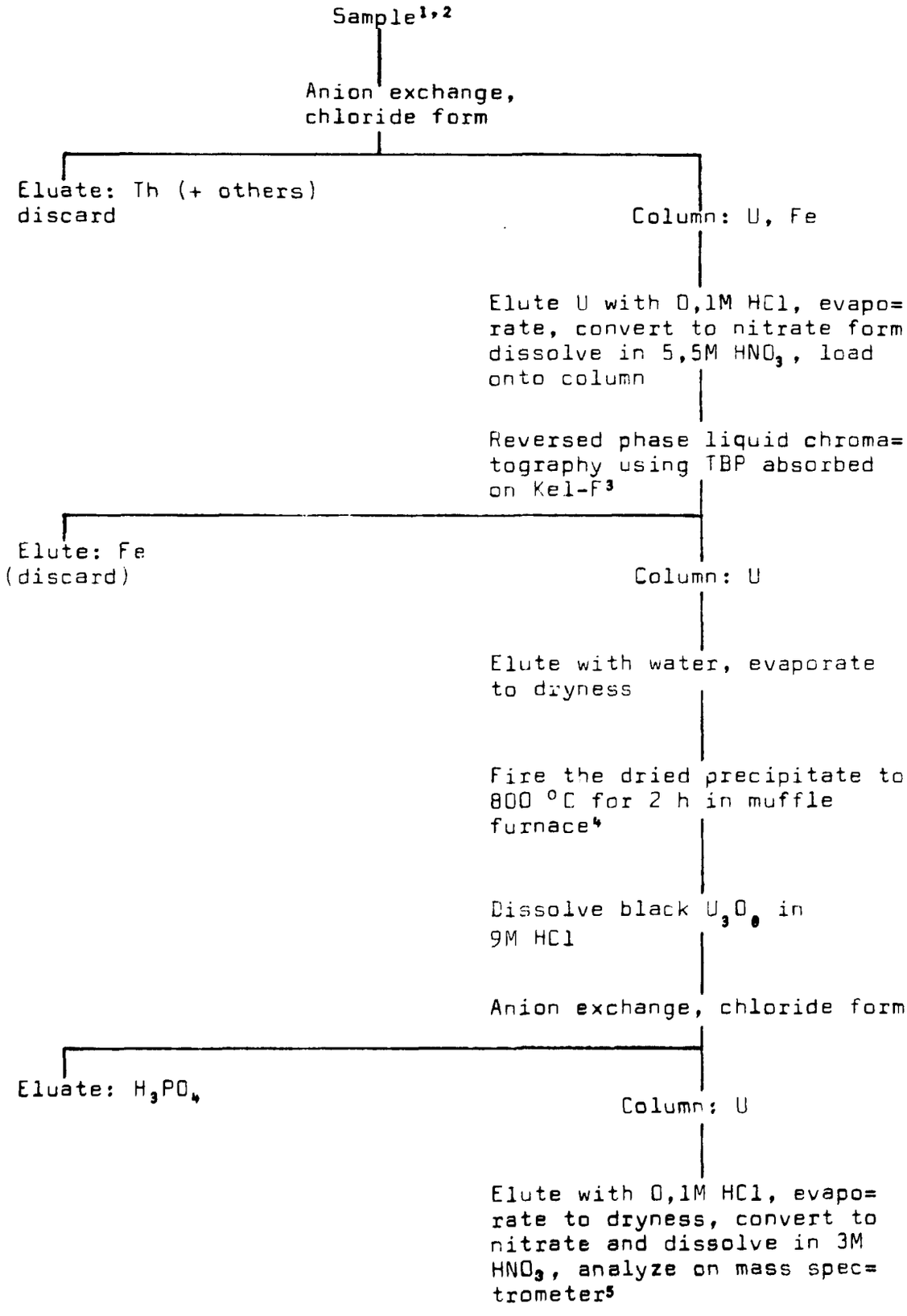


Fig. 37: Spectrum of ^{238}U and ^{235}U obtained from the mass spectrometer.

TABLE 12: PROCEDURE FOR THE CHROMATOGRAPHIC SEPARATION OF URANIUM FROM CALCRETE, SUITABLE FOR MASS SPECTROMETRIC ANALYSIS



[1] Uranothorianite was dissolved in a mixture of concentrated HF and $HClO_4$. Fumed with an excess of $HClO_4$ to ensure the complete oxidation of U^{4+} to U^{6+}. Finally converted to the chloride form by fuming with concentrated HCl.

[2] The weight of sample required was such that the concentration of uranium in the final solution was greater than 3 mg/cm^3 but less than 20 mg/cm^3.

[3] At this stage all reagents used were of the highest purity. The purity of water was equivalent to that produced by triple distillation.

[4] Uranium was fired to destroy the organic TBP. The phosphate remaining was converted to phosphoric acid and removed by anion exchange.

[5] The nitric acid used for the final dissolution of the uranium was fresh, such that no decomposition products as nitrites and dissolved NO_2 were present.

11. MISCELLANEOUS METHODS

11.1 Delayed Neutron Counting

Delayed Neutron Counting is based on the emission of neutrons from a few fission products after the irradiation of ^{235}U with neutrons in a reactor. Approximately 0,03 g of sample was accurately weighed into polythene capsules and sealed. The samples were irradiated in the pneumatic facility for 40 seconds. After a decay of 20 seconds the samples were counted for one minute.

The counting system used was designed and built by the National Institute for Metallurgy. It consists of a ring of eight boron triflouride tubes mounted in a tank of water. Pulses from the tubes pass through an amplifier and a discriminator, and are finally counted.

The standards consisted of standard uranium ores supplied by the Australian Atomic Energy Commission and The International Atomic Energy Agency. A standard calibration graph was drawn and the counts versus U_3O_8 concentration plotted.

11.2 X-Ray Diffraction Analysis

X-ray diffraction was used for qualitative mineralogical identification. All samples were ground down to pass -325 mesh. Clay mineral identification was done on approximately the 2 micron size fraction. A very dilute HCl solution was added to a slurry of this fraction in order to remove any calcite present.

PART III: GEOCHEMISTRY

12. THE GEOCHEMISTRY OF THE BASEMENT ROCKS

The basement rocks constituted the source of all the epigenetic uranium mineralization in the duricrusts from the Gawib River to the Tumas River and also the accumulations in the diatomaceous muds off the coast in the Atlantic Ocean. This, therefore, was the starting point of the geochemical cycle of uranium for the region in this study. A geochemical analysis of certain aspects of some of the basement rocks was very pertinent to this investigation, especially from the point of view of their paragenesis. The rare-earth abundances and trends were found to be useful as indicators of the geochemical and evolutionary sequences.

12.1 Analytical Results

Partial chemical analyses and trace element concentrations in the Bloedkoppie and Gawib Granites are given in Table 13. Analyses of other basement rock types form part of a geochemical investigation (DAMJU Project) concerning the uranium mineralization of the Damara Orogen, the report of which is still in preparation. A list of the samples used here is given in Table 14.

12.2 Geochemistry of Uranium in Granitic Rocks

The mean uranium concentrations in the Bloedkoppie and Gawib Granite are 18 ppm and 9 ppm respectively. The Gawib Granite has a Th/U ratio of 3,5 which is very close

CONFIDENTIAL

TABLE 13: RADIAL CHEMICAL ANALYSIS AND TRACE ELEMENT CONCENTRATIONS IN THE KLOEDKOPPIE AND GAMIB GRANITES

	KLOEDKOPPIE GRANITE												GAMIB GRANITE		
%	LH 4	LH 5	LH 6	LH 8	LH 10	LH 16	LH 43	HJ2-20	HJ2-26	HJ2-30	HJ2-36	HJ2-39	LH 29	LH 30	LH 45
SiO_2	74,9	74,1	72,0	74,1	74,5	73,4	73,3	69,5	70,3	70,1	70,5	69,7	60,5	59,7	58,4
TiO_2	0,123	0,232	0,219	0,177	0,064	0,051	0,117	0,107	0,091	0,225	0,229	0,229	0,14	0,59	0,79
Al_2O_3	13,17	13,13	13,70	13,14	13,64	13,56	13,04	14,21	13,80	13,16	13,88	13,52	15,53	15,45	16,30
Fe_2O_3	1,36	2,16	2,13	1,79	1,23	1,10	1,48	1,27	1,13	2,06	1,96	1,89	5,70	5,69	6,26
MnO	0,03	0,06	0,063	0,038	0,056	0,06	0,057	0,024	0,036	0,068	0,048	0,056	0,12	0,10	0,12
MgO	0,14	0,28	0,29	0,21	0,12	0,05	0,16	0,36	0,18	0,34	0,35	0,35	1,96	2,01	1,09
CaO	0,87	1,25	1,37	0,86	0,68	0,79	1,19	1,69	1,43	1,55	1,49	1,36	5,79	5,17	4,94
Na_2O	2,78	3,05	3,53	3,04	4,02	4,11	3,54	3,36	3,95	3,42	3,19	3,16	3,35	3,53	2,75
K_2O	5,04	4,91	4,30	5,21	4,30	4,01	4,89	4,42	4,26	4,74	4,48	4,65	3,05	2,83	2,91
P_2O_5	0,05	0,08	0,08	0,113	0,04	0,03	0,04	0,17	0,18	0,12	0,13	0,09	0,27	0,25	0,24
ppm															
Ba	499				184	212	240				658	567	887	1 083	1 083
Ce	112				45	30	95				102	80	137	120	125
Co	2,1				2,4	1,6	2,3				3,1	3,1	13	13	13
Cs	7,4				11,3	24,5	8,1				10,8	13,1	3,2	1,8	2,0
Eu	1,3				0,5	0,3	1				1	1	2,4	2,3	2,3
Hf	3,7				5,3	1,8	4,1				4,5	4,7	5,9	5,8	5,7
La	37				19	7	32				40	32	62	58	58
Li	37	63	97	36	60	113	56	38	40	55	78	79	108	21	29
Lu	0,3				1,0	0,5	0,9				0,8	0,8	0,5	0,5	0,6
Rb	309				375	521	240				317	329	144	130	139
Sc	3,3				4,1	5,3	3,8				5,5	5,6	12	12	14
Sm	5				6	3	13				9	8	11	11	11
Ta	1,1				5,9	4,5	3,9				4,1	5,1	1,5	1,4	1,1
Tb	0,7				2,0	0,7	2,4				1,4	1,3	1,1	1,4	1,4
Th	27,2				35,8	18,8	50,1				23,1	16,9	20,1	14,1	15,4
U	24	19	18	3	14	21	11	16	17	24	10	10	4	3	4
Yb	1,1				3,4	3,9	3,4				3,1	3,1	3	2	2

CONFIDENTIAL

TABLE 14: SAMPLES USED IN THE GEOCHEMICAL INTERPRETATION OF THE RARE-EARTH ELEMENT DISTRIBUTIONS

Rock Type	DJP Sample No.
Salem Granite	44, 49, 50, 114
Tinkas Formation	98, 100
Banded gneiss	22, 24, 29, 80
Etusis Formation	25, 26, 29, 31, 33, 34, 43

Analyst, Dr R.J.N. Brits - Chemistry Division, Atomic Energy Board.

to the world average of 3,0. In the Bloedkoppie Granite, on the other hand, the Th/U ratio varies between 0,9 and 2,6, indicating an over-abundance of uranium. This is responsible for the weak aeroradiometric anomaly associated with the Bloedkoppie Granite. Uranium does not correlate with any other element in Table 13. This is not entirely surprising when one considers the high degree of weathering of the Bloedkoppie Granite.

The common rock-forming minerals do not easily accommodate uranium for it cannot substitute for any element of its own size, e.g. calcium and sodium, as the balancing of excess electrical charges is virtually insurmountable, and more so if uranium occurs in the form of the uranyl cation, UO_2^{2+}. Consequently it is either concentrated in late magmatic fluids or expelled from the magma chamber (Armstrong, 1974, p. 628). In the first instance the tendency will be to form its own minerals such as uraninite, or to substitute in the crystal lattices of accessory minerals. In granite rocks which

contain low concentrations of uranium, e.g. the Bloedkoppie Granite, the uranium is dispersed as ionic or molecular disseminations. These molecules are usually found in crystal structures, adsorbed on crystal surfaces, in lattice defects or in fluid inclusions. The tendency will therefore be for uranium to be progressively concentrated within a differentiated suite of igneous rocks.

The mode of transportation of uranium in a magma has been the subject of several investigations. Poty et al (1974, p. 569) studied fluid inclusions in granites and demonstrated a correlation between the uranium and carbon dioxide contents of the fluid. This suggested to them that the uranium was transported as a uranyl carbonate complex. Bhose et al (1974, p. 50) drew attention to the affinity of uranium for the halogens and the subsequent removal of volatile uranium hexafluoride in the escaping gases. Furthermore the role of the uranium-halogen complex formation, rather than increasing oxygen fugacity, prevents the precipi= tation of uranium. Thermodynamically Kaspar and Hejl (1970, p. 301) calculated that uraninite crystallizes at low oxygen fugacities, that is, a reducing atmosphere favours its precipitation whereas an oxidizing atmosphere suppresses it.

Precipitation of uranium from a magma is nevertheless still a partly unsolved problem. Poty et al (1974, p. 569) suggest that precipitation is promoted by unmixing of the uranyl carbonate complex from the solution. They further state that the reduction of uranium by the oxidation of iron (II) to iron (III) is largely an inadequate mechanism to precipitate uranium as the occurrence of hematite is not always

associated with uranium mineralization. In the Damara orogen the correlation between the aeroradiometrics and airborne magnetics suggests an association of uranium with iron. Many alaskites have a red hematitic halo which indicates a relationship between uranium and iron. The following reaction might have been responsible for the precipitation of uranium in this instance:

$$4Fe_3O_4 + UO_2(CO_3)_2 \cdot 2H_2O^{2-} \rightleftharpoons 6Fe_2O_3 + UO_2 + CO_2 + 2H_2O$$

magnetite — uranyl dicarbonate complex — hermatite — uraninite

Dissociation of magnetite and oxidation of the iron (II) component took place within the framework of the redox reaction. Complete dissociation of the uranyl dicarbonate complex took place by the acceptance of four electrons from the decomposing magnetite.

Preliminary results of the DAMJU project indicate that uranium was precipitated when the magmatic fluids were very alkaline and in particular at the stage when potash feldspar predominated over the sodium-rich feldspars at low oxygen fugacity.

12.3 Geochemistry of the Rare-Earth Elements and Their Bearing on the Origin of the Granitic Rocks

Before discussing the rare-earth element distributions in the basement rocks, it is pertinent to briefly review the geochemistry of the rare earths in granitic rocks (Taylor, 1965, p. 160; Haskin et al, 1966, p. 231; Philpotts and

Schnetzler, 1968; Koljonen and Rosenberg, 1974).

In general, through the whole sequence of magmatic differentiation, the rare earths concentrate in the more acid phases and the lighter elements tend to become enriched relative to the heavier ones. This is due to the lanthanide contraction according to which the ionic radius decreases with increasing atomic number and results in preferential depletion of the smaller elements (gadolinium to lutetium) in the residual melt.

Normally the rare earths are trivalent, but depending on the environmental conditions, Eu^{2+} and Ce^{4+} may exist. The well-known europium anomaly is due to the preferential inclusion of Eu^{2+} in the Ca^{2+} sites of plagioclase feldspars. It was found that during differentiation processes the crystallization of approximately 15 per cent plagioclase feldspar results in a 5 per cent depletion of europium in the remaining melt. Continuing crystallization of plagioclase will bring about larger europium anomalies in the residue.

Relationships between the rock types of the Damara orogen were established by Jacob (1974) through field and petrological evidence. An attempt was made here to see whether the geochemical relationships of the rare earths in the respective rock types fitted his postulates concerning the origin of the Banded Gneiss, Salem, Gawib and Bloedkoppie Granites. The problems to consider are, firstly, the relationships between the sedimentary rocks and their ultrametamorphic equivalents, and secondly, the relationships between the granites. The procedure adopted was to normalize the rare-earth concentrations in the rocks with the correspon=

ding concentrations of the rare-earth elements in chondritic meteorites. This eliminated the odd-even effect as shown in Figs. 38, 39 and 40.

Jacob (1974, p. 86) considered that the banded gneisses were derived from sediments characterizing the Khan and Etusis Formations. The rare-earth trends in the Etusis Formation and the banded gneiss are similar (Fig. 38).

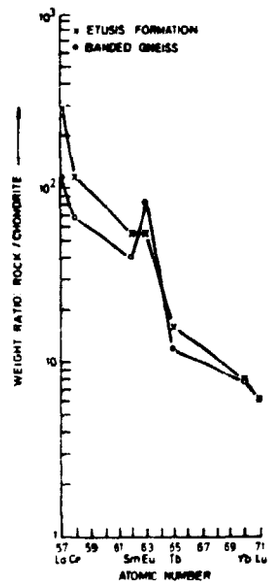


Fig. 38: Rare-earth abundances in the Etusis Formation and banded gneiss divided by the rare-earth abundances in chondrites, plotted against atomic number.

Both rock types have positive europium anomalies, but the banded gneiss has the greater relative europium enrichment of the two suites. The trends agree with the postulate, suggested by Jacob, that the origin of the banded gneiss was due to metamorphic differentiation. The large positive europium anomaly of the banded gneiss resulted from a depletion of the more volatile constituents of the Etusis Formation, leaving a more basic residue rich in plagioclase. Depletion

of the lighter rare earths in this basic residue is typical of a partial fractional melting process.

According to Jacob (1974, p. 167) the Salem Granite was derived from the Khomas Subgroup rocks 'on the high temperature side of the anatexis-in-gneiss boundery'. Crystallization of the Salem Granite anatectic melt by 'filter-press' action resulted in the Bloedkoppie Granite forming from the displaced acid residues. The Gawib Granite was late to post-tectonic in age (Jacob, 1974, pp. 30 and 167). Smith (in Jacob, 1974, p. 30) considered the Gawib Granite to be older than the Salem Granite due to the intrusive relationships of the latter.

The rare-earth patterns of both the Tinkas Formation and the Salem Granite are very similar (Fig. 39) which suggests that the Salem Granite was derived from the former. Both rock types are enriched in samarium, and Koljonen and Rosenberg (1974, p. 254) report a similar anomaly in a granite derived from a sediment. It appears that the rare earths are essentially resistant to metamorphic and metasomatic processes (ibid., p. 249) and consequently their distributions in the original rock and the derivitives remain very similar. The close similarities (Fig. 39) indicate that the Salem Granite was a product of complete melting of the Khomas Subgroup. These trends confirm the findings of Jacob.

The rare-earth patterns for both the Bloedkoppie and Gawib Granites (Fig. 40) show that both granites are depleted in europium, the degree of depletion in the former being the most significant.

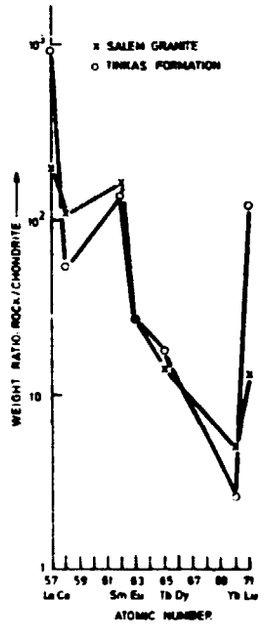


Fig. 39: Rare-earth abundances in the Tinkas Formation and Salem Granite divided by the rare-earth abundances in chondrites, plotted against the atomic number.

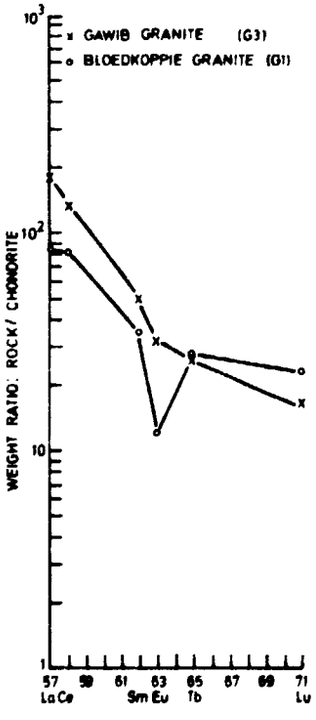


Fig. 40: Rare-earth abundances in the Gawib and Bloed= koppie Granites divided by the rare-earth abundances in chondrites, plotted against the atomic number.

The patterns of the Bloedkoppie and Gawib Granites are generally similar, implying that both are genetically related and that the Bloedkoppie Granite is the most fractionated of the two. It is evident that the rare-earth distributions for these granites are similar to the trends of the Etusis Formation and the banded gneiss. There is no resemblance to the distributions in the Salem Granite (Fig. 39).

It is considered, therefore, that as a result of partial melting of the Etusis Formation at depth, the resultant melt fractionated into the acid Bloedkoppie Granite phase and the more basic Gawib Granite phase. Both granites are more differentiated than the parent rocks from the evidence of the negative europium anomaly. This evidence and that of the north-east orientation of the xenoliths in the Bloedkoppie Granite tends to fall more in line with Smith's work and that the Bloedkoppie and Gawib granites might well be of late syntectonic age. The close proximity of the Etusis Formation comprising the Langer Heinrich Mountain provided the source material for these granites.

12.4 Summary

The banded gneiss was derived from the Etusis Formation by metamorphic differentiation. The Salem Granite was the product of complete melting of the Tinkas Formation, or more broadly, the Khomas Subgroup. Finally, a magma derived from partial melting of the Etusis Formation crystallized into an acid Bloedkoppie Granite phase and a residual, but

more basic, Gawib Granite phase. Both granites are therefore late syntectonic in age. The significance behind the paragenesis of the Bloedkoppie Granite is that it was derived from the Nosib Group rocks. Therefore the Nosib Group was the initial source of the uranium in this later-forming granite which ultimately contributed to the supply of the epigenetic uranium in the Gawib River Valley.

13. GEOCHEMISTRY OF THE SUBSURFACE WATERS OF THE NAMIB DESERT

The geochemistry of the subsurface waters of the Namib Desert was studied with two main objectives in mind. Firstly, the concentration and distribution of uranium in subsurface waters was investigated to determine whether it reflected the likelihood of uranium mineralization in the enclosing rocks. Secondly, an attempt was made to establish the underlying principles that govern the leaching and migration of uranium in the arid environment of the Namib Desert. Furthermore the subsurface waters form the second phase in the geochemical cycle of uranium.

Gableman (1970, p. 326) defined certain characteristics necessary for a fluid to form uranium ores. These are:

'1. Corrosiveness: It must be capable of altering rock by leaching and replacement.

2. Penetrability: It must be capable of permeating dense rocks impenetrable by fresh ground-waters.

3. Concentration: It must have a high concentration of a large variety of mineral ions and mineralizers in addition to the dominant uranium, vanadium, etc.

4. Selectivity: Its chemical character must enable it to react only to certain host rock chemical environments.'

Butler (1969, p. 85) and Gableman (1970, p. 325) are of the opinion that the ore fluids are meteoritic waters having a high concentration of dissolved salts. Isotopic

studies in natural brines (Clayton et al, 1966, in Gableman, 1970) have confirmed both this and the fact that the total salinity content was derived from the rocks through which the water moved. Hellewig (1969) described the movement of subsurface waters from the Namib Desert in general and concluded that the concentration of the dissolved solids increased towards the coast. This, he pointed out, is due to the dissolution of subsurface marine salt deposits.

The mean annual rainfall in the Namib Desert is very low and over a period of 35 years it is only 17,9 mm at Swakopmund (Table 39). On the assumption that inland figures are of the same order of magnitude, recharging of the acquifers is a very slow process. In fact most of the rain is more than likely to be removed from the surface by evapora= tion before it has a chance to replenish the acquifers. So the system being dealt with is one of partial stagnation.

The area from which samples 1 to 29 were taken lie- between the Swakop River in the south and the Khan River in the north (Fig. 41). Samples 30 and 31 were taken from boreholes HJ-1 and J-1 respectively in the Gawib River Valley (Map 1).

Geological mapping of the area was done by Jacob (1974) and the Anglo American Prospecting Co. Ltd. The latter was concerned with the evaluation of uranium ore reserves over the farms Dorstrivier 15, Nordenburg 76, Vlakteplaas 110 and Bloemhof 109. (Annual Prospecting Reports (1972, 1973) Prospecting Grant M46/3/209). Most of the concession held by Anglo American Prospecting Co. Ltd. is covered by calcrete

CONFIDENTIAL

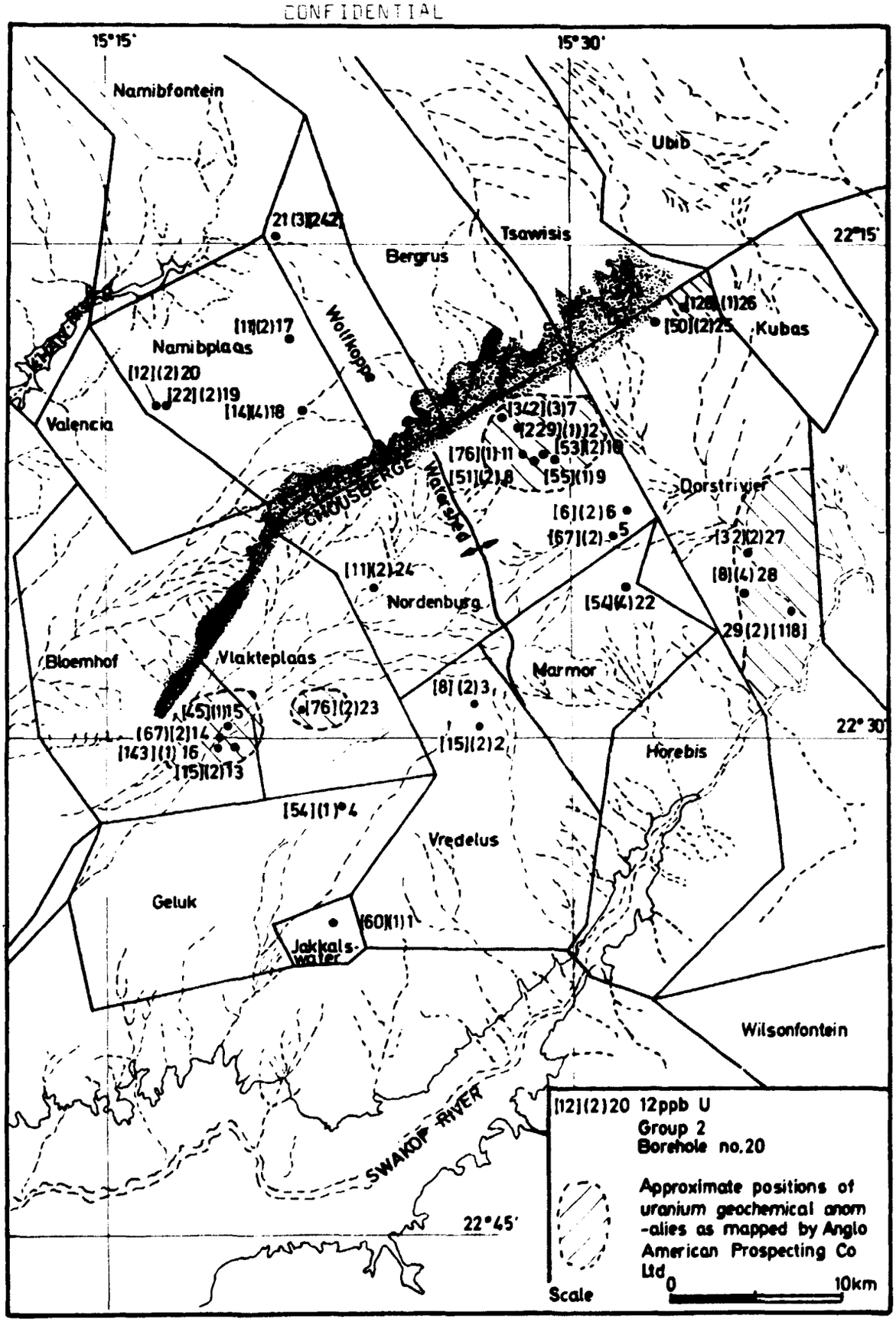


Fig. 41: The area and localities of the boreholes from which the subsurface water samples were taken. Each sample point is designated as follows: e.g. [12] (2)20 means that the sample was taken from borehole number 20, classified into Group 2, and contains 12 ppb U.

CONFIDENTIAL

deposits, with the exception of the mountainous areas (Chuosberge) and the eroded southern portion of Dorstrivier. Surface geochemical prospecting delineated several radioactive anomalies with uranium contents above 15 ppm in calcrete on the farms Bloemhof, Vlakteplaas and the northern part of Dorstrivier. In the southern part of Dorstrivier the anomaly is mainly on granite (Gn_1).

Uranium crystallized into the minerals carnotite and soddyite, which are found together. Mineralization in the calcretes on Bloemhof and Vlakteplaas is of low grade, the highest value being 388 ppm U_3O_8. Generally the range of values for U_3O_8 lies between 5 ppm and 90 ppm, with most of it concentrated within the upper 10 m of the calcrete. Bedrock was intersected at depths between 6 m and 47 m.

The watershed of the Chuosberge dominates the main drainage system of this area (Fig. 41). It runs approximately north-east, separating rivers flowing southwards to the Swakop River from those flowing northwards to the Khan River. One minor watershed runs north-south through the farm Nordenburg and influences only the southward flowing rivers.

13.1 Analytical Results

Water samples numbers 1 to 31 were classified into four groups and are listed in Tables 15 to 18. Table 19 gives the means and range of values for all the samples.

TABLE 15: CHEMICAL ANALYSES OF SHORT TERM GROUNDWATERS FROM THE NAIB DEPOSIT

	1	4	9	11	12	15	16	26	31	MEAN	MINIMUM	MAXIMUM
pH	8,0	7,2	9,2	7,8	8,3	7,5	7,9	8,3	7,8	8,0	7,2	9,2
*CONDUCTIVITY	9 800	18 500	4 700	8 000	5 400	8 300	8 400	4 000	12 800	8 878	4 700	18 500
*TDS (ppm)	7 695	15 285	3 419	5 085	3 630	5 735	5 590	2 870	10 840	5 883	2 870	15 285
Na (ppm)	1 360	3 480	544	870	560	1 100	1 [illegible]	488	1 760	1 [illegible]	488	3 480
K (ppm)	50	340	24	50	44	[illegible]	110	16	93	89	16	340
Ca (ppm)	1 008	1 [illegible]38	4[illegible]	672	367	[illegible]	357	240	1 304	783	240	1 [illegible]38
Mg (ppm)	202	[illegible]89	104	[illegible]36	[illegible]04	1[illegible]	196	139	74	173	74	289
U (ppb)	60	54	53	72	[illegible]04	49	143	128	107	99	45	229
V (ppb)	58	74	[illegible]4	13	4	[illegible]7	54	10	[illegible]5	41	4	79
Sr (ppb)	5 705	11 219	[illegible] 782	3 534	2 667	[illegible] 152	5 819	3 100	1 [illegible]95	4 958	395	[illegible]1 219
Ba (ppb)	346	[illegible]73	137	198	1[illegible]7	[illegible]14	589	460	488	365	137	[illegible]73
SO_4 (ppm)	678	1 [illegible]96	484	820	486	1 39[illegible]	856	307	[illegible]08	[illegible]66	327	1 596
NO_3 (ppm)	165	127	5	2	60	14	[illegible]3	96	9	58	2	165
SiO_2 (ppm)	15	20	10	15	21	[illegible]8	40	40	25	[illegible]4	10	40
F (ppm)	1,8	[illegible],4	0,5	1,1	[illegible],[illegible]	[illegible],9	1,4	[illegible],2	3,5	1,6	0,5	3,5
Cl (ppm)	3 47[illegible]	[illegible] [illegible]00	1 [illegible]05	[illegible] 550	1 330	[illegible] [illegible]70	[illegible] 400	910	1 600	[illegible] [illegible]11	910	[illegible] [illegible]00
CO_3 (ppm)	84	[illegible]0	[illegible]7	[illegible]2	204	[illegible]8	132	13[illegible]	90	91	[illegible]7	204

* Conductivity, units, mho.

* TDS = Total dissolved solids.

CONFIDENTIAL

CONFIDENTIAL

TABLE 1: CHEMICAL ANALYSES OF GROUP 1 SURFACE WATERS FROM THE NAMIB DESERT

	2	3	5	11	6	10	12	14	17	19	20	23	24	25	27	29	MEAN	MIN.	MAX.
pH	7,0	7,4	7,3	6,8	7,2	6,4	7,3	7,5	7,7	6,1	7,9	7,8	8,0	7,5	7,2	7,4	7,4	7,0	8,4
*Conductivity	4 680	3 100	5 300	1 [illegible]	4 [illegible]	1 400	6 300	1 [illegible]80	3 [illegible]	[illegible]	[illegible]	2 [illegible]70	1 190	3 600	7 650	10 000	5 [illegible]	2 210	10 000
*TDS (ppm)	3 [illegible]4	2 [illegible]5	3 [illegible]1	4 [illegible]75	3 [illegible]75	2 [illegible]50	[illegible]	4 [illegible]45	[illegible]	[illegible]	[illegible]	5 [illegible]5	1 980	[illegible]70	4 910	7 [illegible]4	3 [illegible]8	1 [illegible]0	7 [illegible]4
Na (ppm)	353	204	508	[illegible]	[illegible]	148	1 [illegible]7	870	[illegible]	[illegible]	[illegible]	807	348	330	730	1 220	652	208	1 220
K (ppm)	12	[illegible]	45	3[illegible]	18	47	10[illegible]	84	[illegible]	[illegible]	11	42	28	24	10	80	36	[illegible]	133
Ca (ppm)	604	397	489	[illegible]76	[illegible]1	258	55[illegible]	441	[illegible]48	[illegible]16	[illegible]13	[illegible]51	200	290	735	[illegible]41	432	118	735
Mg (ppm)	107	[illegible]4	109	157	47	[illegible]4	164	169	77	58	71	1[illegible]	83	126	157	431	142	51	431
[illegible] (ppm)	15	8	[illegible]7	5	[illegible]1	[illegible]3	88	[illegible]7	13	[illegible]	12	[illegible]7	11	50	30	118	43	4	118
[illegible] (ppb)	[illegible]7	[illegible]7	38	[illegible]	21	11	28	38	31	[illegible]4	34	[illegible]0	5	50	30	20	26	5	50
Sr (ppb)	2 [illegible]34	2 [illegible]74	3 803	4 [illegible]67	3 [illegible]47	820	6 [illegible]61	5 [illegible]56	1 [illegible]40	1 [illegible]40	[illegible]50[illegible]	6 [illegible]170	4 500	3 000	7 [illegible]00	[illegible]9 [illegible]60	4 856	820	[illegible]3 [illegible]60
Ba (ppb)	248	102	169	[illegible]16	181	54	168	171	144	37	[illegible]5	232	[illegible]91	365	766	[illegible]68	244	[illegible]7	766
NO_3 (ppm)	[illegible]94	180	[illegible]38	[illegible]56	425	4[illegible]4	[illegible]70	617	[illegible]17	1[illegible]	[illegible]41	[illegible]17	[illegible]74	[illegible]44	617	1 192	484	180	1 192
NO_2 (ppm)	150	[illegible]6	80	[illegible]91	[illegible]1	8	32	33	54	9	14	9[illegible]	2	43	90	103	62	2	150
SiO_2 (ppm)	30	30	[illegible]0	1[illegible]	30	40	[illegible]5	25	41	41	40	[illegible]5	15	[illegible]5	40	30	30	15	40
F (ppm)	1,2	0,7	1,3	0,8	0,7	0,4	1,0	1,1	1,[illegible]	1,5	1,5	1,[illegible]	0,8	1,2	1,0	1,5	1,0	0,4	1,5
Cl (ppm)	1 260	805	1 300	1 780	1 [illegible]05	763	2 [illegible]75	2 [illegible]45	760	516	[illegible]7[illegible]	2 [illegible]075	820	810	2 200	2 925	1 376	516	2 925
[illegible] (ppm)	105	111	183	76	155	156	171	168	147	147	159	132	78	168	168	189	145	76	189

* Conductivity units, mho.

* TDS = Total dissolved solids

CONFIDENTIAL

CONFIDENTIAL

TABLE 17: CHEMICAL ANALYSES OF GROUP 3 SUBSURFACE WATERS FROM THE NAMIB DESERT

	7	21	30	MEAN	MIN.	MAX.
pH	7,1	7,5	7,5	7,4	7,1	7,5
*CONDUCTIVITY	2 700	6 780	5 400	4 960	2 700	6 780
+TDS (ppm)	1 870	5 170	4 045	3 695	1 870	4 045
Na (ppm)	264	740	555	520	264	740
K (ppm)	20	54	42	39	20	54
Ca (ppm)	229	735	450	471	229	735
Mg (ppm)	94	161	77	81	77	161
U (ppb)	342	242	298	294	242	342
V (ppb)	16	5	18	13	5	18
Sr (ppb)	1 550	838	47 772	16 203	838	47 772
Ba (ppb)	129	207	210	182	129	210
SO_4 (ppm)	223	1 440	360	674	223	1 440
NO_3 (ppm)	52	48	2	34	2	52
SiO_2 (ppm)	40	25	10	25	10	40
F (ppm)	0,4	1,5	2,5	1,5	0,4	2,5
Cl (ppm)	515	1 600	1 600	1 238	5,5	1 600
CO_3 (ppm)	95	105	68	89	68	105

* Conductivity units, mho.

+ TDS = Total dissolved solids.

TABLE 18: CHEMICAL ANALYSES OF GROUP 4 SUBSURFACE WATERS FROM THE NAMIB DESERT

	18	22	28	MEAN	MIN.	MAX.
pH	7,3	7,4	7,5	7,4	7,3	7,5
* CONDUCTIVITY	1 800	3 830	2 130	2 587	1 800	3 830
+ TDS (ppm)	1 130	2 375	1 355	1 620	1 130	2 375
Na (ppm)	136	200	186	174	136	200
K (ppm)	7	15	16	13	7	16
Ca (ppm)	187	397	182	255	182	395
Mg (ppm)	47	145	49	80	47	145
U (ppb)	14	15	8	12	8	15
V (ppb)	3	6	10	6	3	10
Sr (ppb)	1 472	2 392	3 430	2 431	1 472	3 430
Ba (ppb)	31	166	469	222	31	469
SO_4 (ppm)	89	339	144	191	89	339
NO_3 (ppm)	4	21	23	16	4	23
SiO_2 (ppm)	40	25	40	35	25	40
F (ppm)	0,7	0,4	0,4	0,5	0,4	0,7
Cl (ppm)	340	903	345	529	340	903
CO_3 (ppm)	210	219	204	211	204	219

* Conductivity units, mho.

+ TDS = Total dissolved solids.

TABLE 19: MEANS AND RANGE OF CONCENTRATIONS OF IONS IN SUBSURFACE WATERS FROM THE NAMIB DESERT FOR ALL 31 SAMPLES

	MEAN	MINIMUM	MAXIMUM
pH	7,7	7,0	9,2
*CONDUCTIVITY	5 933	1 800	18 500
+TDS (ppm)	4 306	1 130	15 285
Na (ppm)	721	136	3 480
K (ppm)	49	6	340
Ca (ppm)	512	118	1 638
Mg (ppm)	142	49	431
U (ppb)	81	6	342
V (ppb)	27	3	79
Sr (ppb)	5 754	826	47 772
Ba (ppb)	271	31	766
SO_4 (ppm)	585	89	1 596
NO_3 (ppm)	54	2	165
SiO_2 (ppm)	28	10	40
F (ppm)	1,2	0,4	3,5
Cl (ppm)	1 639	340	7 700
CO_3 (ppm)	130	54	219

* Conductivity units, mho.

+ TDS = Total dissolved solids.

Analysis of samples 1 to 29 was done by the Department of Water Affairs in Windhoek according to their routine methods for water analysis. The analysis of the two samples from the Gawib River and the analyses for strontium, barium, vanadium and uranium for all samples were done at the Atomic Energy Board. Conventional atomic absorption flame procedures were used for strontium and barium, whereas the carbon rod method was used for vanadium. Uranium was analyzed using the technique of delayed neutron counting.

In Table 20 the concentrations of some trace elements in subsurface waters are given which were analyzed by Anglo American Corp. Ltd (Annual Prospecting Report (1973) Prospecting Grant M46/3/209). There is no relationship between the samples in Table 20 and those of Tables 15 to 18.

TABLE 20: TRACE ELEMENT ANALYSES OF SUBSURFACE WATERS FROM THE NAMIB DESERT. (ANNUAL PROSPECTING REPORT (1973) PROSPECTING GRANT M46/3/209

ppb	W1	W2	W3	W4	W5	W6	W7	W8	$\bar{X}$	MIN.	MAX.
U	110	110	25	55	102	51	136	55	81	25	136
Pb	34	45	19	50	78	38	31	43	42	19	78
Cu	10	11	10	16	17	19	15	17	14	10	19
Ni	22	29	11	23	32	19	15	22	22	11	32
Ag	17	10	4	18	19	24	9	9	14	4	24
Zn	24	22	11	1 000	34	35	12	12	21*	11	1 000
Cu	2	3	2	4	4	3	2	3	3	2	4

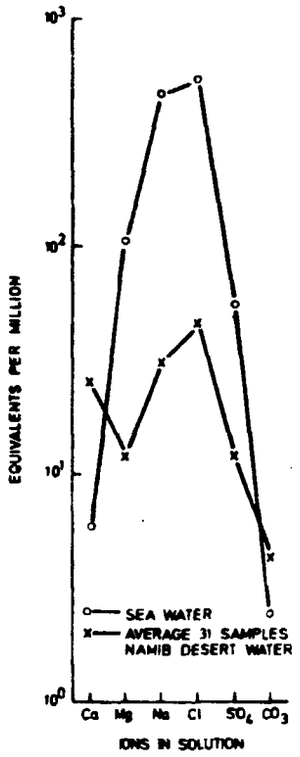
* The mean value for Zn does not include the 1 000 ppb value in sample W4.

13.2 Characteristics and Classification of the Subsurface Waters

Very wide variations in the values were found for some elements, for example potassium and uranium, where the concentrations differ by factors of about 60. Variation in the contents of carbonate and silica is less extreme and the maximum values are only a factor four greater than the minimum values. Sodium and potassium are the most abundant cations, followed by magnesium and potassium. The major anions in order of abundance are chloride, sulphate and carbonate. All the remaining ionic species are present only in trace amounts.

A convenient way to describe the composition of brines is their relationship to the composition of seawater. Fig. 42 is a Schoeller diagram representing the ions in solution in terms of their equivalents per million (Parker, 1969, p. 120). The comparisons between the concentrations of calcium, magnesium, sodium, chloride, sulphate and carbonate in seawater (Table 38) and the average values for 31 Namib Desert waters (Table 19) are shown.

The total concentrations of the elements in the Namib Desert waters are in general lower with respect to seawater. Calcium and carbonate are, however, relatively enriched, the former being greater by a factor of approximately four. Magnesium is depleted relative to its neighbours, calcium and sodium, but this anomaly is not observed in seawater. Reasons for this were expressed by Bentor (1969, p. 84) who found that two mechanisms may apply



– Fig. 42: Schoeller diagram, comparison of the ionic distributions in subsurface waters of the Namib Desert and seawater in terms of equivalents per million ionic species.

in this situation. Firstly, magnesium is incorporated into the calcite lattice, and secondly, magnesium may be exchanged for a cation in montmorrilonite clay. The similarities between the Namib Desert brine patterns and those of certain brines in the USA (Parker, 1969, p. 119) are very striking, especially in their depletion of magnesium.

In natural brines some elements in solution do not normally exist in the purely ionic form, but as ion associations or coordination complexes. The major ions, for example magnesium, form ion pairs, whereas the trace elements, for example vanadium, form coordination complexes. Truesdell and Jones (1969, p. 58) point out that magnesium is particularly susceptible to the formation of ion pairs, with

silica being a principal contributer, followed by carbonate and sulphate. This feature may also account for the fractionation of magnesium as shown in Fig. 42. Garrels and Thompson (1962, p. 57) determined that for seawater 87 per cent of the magnesium occurs as the free ion, 11 per cent as the $Mg-SO_4$ pair, and 1 per cent as the $Mg-HCO_3$ pair. No value for the $Mg-SiO_2$ pair was listed. In solutions supersaturated with silica, magnesium remains in solution, but in the saturation field for amorphous silica, minerals such as montmorillonite and attapulgite may develop. Fig. 43 shows the positions of samples 30 and 31 from the Langer Heinrich plotted on an activity diagram. Both

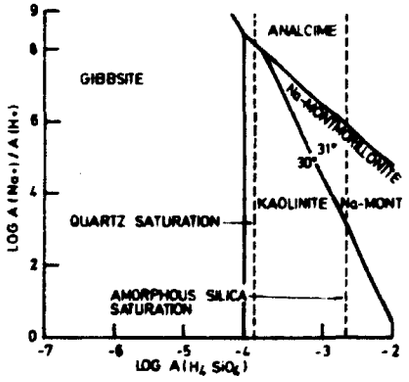


Fig. 43: Activity diagram for the system $Na_2O-Al_2O_3-SiO_2-H_2O$ at 25 °C at unit activity of water and 100 kPa. Adapted from Helgeson et al (1969, p. 462). Subsurface water samples 30 and 31 from the Gawib River Valley fall into the montmorillonite field.

samples fall in the montmorillonite field and below the level of amorphous silica saturation. Although this is a sodium montmorillonite, it nevertheless demonstrates the stability of montmorillonite in the calcretes of the Gawib River Valley. Hess (1966, p. 306) points out that an

activity diagram (Fig. 43) strictly only applies under ideal conditions where all phases are stoichiometric and activities are equivalent to concentrations. The subsurface waters in the Namib Desert are certainly not ideal solutions and caution must be exercised in the interpretation of activity diagrams.

Mineral equilibria relationships for calcite and silica, predicted from thermodynamic considerations (Kramer, 1969), are shown in Figs. 44 and 45. On the assumption that the temperature of the subsurface waters in the Namib Desert is 20 °C (the temperature was not measured and it is therefore likely that fluctuations will occur to either side of this value) the values for samples 30 and 31, as well as the minimum and maximum values given in Table 19, have been plotted on the diagrams. All values in Fig. 44 plot well

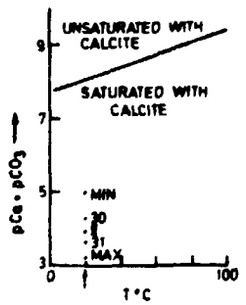


Fig. 44: Equilibrium plot for calcite or calcareous rocks as a function of temperature with respect to the subsurface brines. $pCa = -\log_{10}(Ca^{2+})$ and $pCO_3 = -\log_{10}(CO_3^{2-})$. The minimum, maximum and mean (x) for all water samples are plotted. (Values taken from Table 19). Samples 30 and 31 from the Gawib River Valley are also plotted. The temperature for the subsurface water was assumed to be 20 °C.

into the field saturated with calcite, indicating that the waters are saturated with respect to calcite. This is to be

expected in calcretes. The waters are therefore capable of precipitating calcite so that the development of calcrete is still in progress. In Fig. 45 the points tend to cluster nearer to the equilibrium line for amorphous

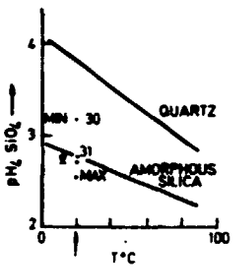


Fig. 45: Equilibrium plot for quartz and amorphous silica as a function of temperature with respect to the subsurface brines. $pH_4SiO_4 = -\log_{10}(H_4SiO_4)$. The minimum, maximum and mean ($\bar{x}$) for all water samples are plotted. (Values taken from Table 19). Samples 30 and 31 from the Gawib River Valley are also plotted. The temperature for the subsurface water was assumed to be 20 °C.

silica. Kaolinite was not found at the Langer Heinrich. Kramer (1969, p. 48) points out that the quartz equilibrium line actually represents the kaolinite-potassium feldspar-potassium mica equilibrium. All samples fall well below this equilibrium line, indicating that these minerals are unstable under the conditions prevailing in the Namib Desert. The more stable montmorillonite is therefore the coexisting phase present, which was confirmed by X-ray diffraction.

The water samples were taken over a very large area on both sides of the watershed of the Chuosberge and associated with several different rock types. For this reason they have very wide ranges in the abundances of their

soluble species. Under these circumstances the probability that the samples can be grouped is very likely. Grouping was suggested from the correlation matrix of all 31 samples. Generally it can be accepted that there is a fairly good degree of correlation between uranium and carbonate, but in this matrix almost zero correlation was found. A plot of these two values (Fig. 46) showed that four groups possibly exist.

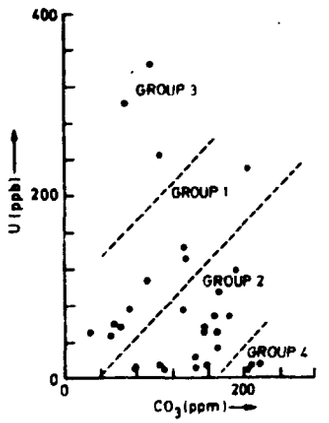


Fig. 46: Variation diagram of uranium plotted against carbonate. Four groups in the water samples are indicated. The dashed lines give the approximate group boundaries.

To test whether this classification had any merit, a multivariate discriminant analysis in a stepwise manner was performed using the computer program BMD07M (Dixon, 1967), called DISC. At each step one variable was entered into a set of discriminating variables, based on the statistical F test. For each sample a mahalanobis distance and a probability function were determined giving the likelihood of the sample fitting within the specified group. Finally a set of canonical variables was calculated in order to represent the distribution of the groups in a two-dimensional way. Furthermore, in accordance with the

F-tolerance limits set, elements were selected that could best discriminate between the groups.

The variables used for the discrimination were pH, total dissolved solids, sodium, potassium, calcium, magnesium, uranium, vanadium, sulphate, fluorine, chlorine and carbonate. F-values for inclusion and deletion were 2,1 and 2,0 respec= tively, from which uranium, carbonate, sodium and sulphate were the most discriminating functions for separating the groups. Canonical variables calculated for each group and their respective means are plotted in Fig. 47. A very good

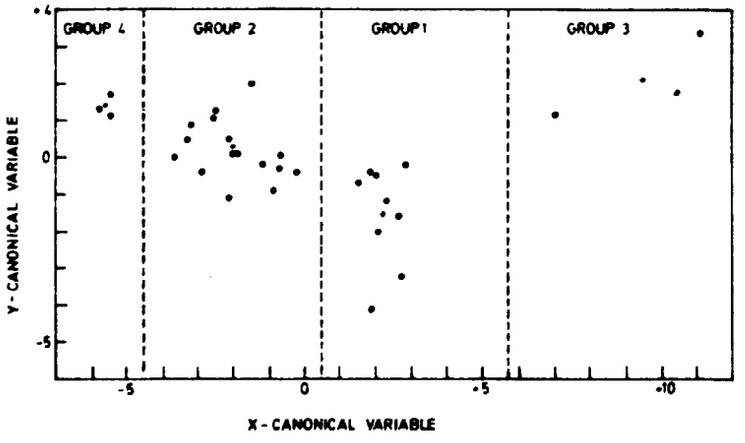


Fig. 47: A plot of the X- and Y-canonical variables derived from a multivariate discriminant analysis of the data from 31 subsurface water samples.(+ = mean).

separation of the four groups is shown. Group 3 has the greatest variance. The probability that most samples will fall within their specified groups is generally greater than 98 per cent (Table 21).

TABLE 21: CLASSIFICATION OF THE SUBSURFACE WATERS INTO GROUPS, USING MULTIVARIATE DISCRIMINANT ANALYSIS, AND THE CALCULATED PROBABILITIES ASSOCIATED WITH EACH SAMPLE

INITIAL GROUPING OF THE SUBSURFACE WATERS	GROUPING BASED ON DISCRIMINANT ANALYSIS OF CHEMICAL DATA			
	GROUP 1	GROUP 2	GROUP 3	GROUP 4
GROUP 1	(1) (2) 1 1,0 4 1,0 9 1,0 11 1,0 12 1,0 15 1,0 16 1,0 26 1,0	31 1,0		
GROUP 2	23 0,14	2 1,0 3 1,0 5 0,98 6 0,98 8 1,0 10 1,0 13 1,0 14 1,0 17 0,93 19 0,99 20 0,80 23 0,86 24 0,99 25 0,99 27 0,88 29 0,98		17 0,07 20 0,20 27 0,12
GROUP 3			7 1,0 21 1,0 30 1,0	
GROUP 4				16 1,0 22 1,0 28 1,0

(1) Sample number
(2) Probabilities

CONFIDENTIAL

CONFIDENTIAL

Group 2 has four samples with probabilities below 98 per cent. Sample 23 has a 14 per cent chance of falling into Group 1, whereas samples 17, 20 and 27 have 7 per cent, 20 per cent and 12 per cent chance respectively of falling into Group 4. These low probabilities were disregarded due to their high loadings associated with Group 2.

The question now arises: how are these four groups distributed within the drainage patterns? Each borehole (Fig. 41) is marked with the sample number, group number (round brackets) and uranium concentration in ppb (square brackets). There seems to be no uniformity in the distribution of the samples in their groups. Four boreholes situated close to each other on the farm Bloemhof are presented by Groups 1 and 2. In the north-eastern corner of Nordenburg six boreholes, also clustered together, fall within Groups 1 and 3. Northwards, across the Chuosberge, Groups 2, 3 and 4 are found. Waters within the same drainage channels also fall within different groups.

Unfortunately no information was available concerning the depth of the borehole, the quality of the casing or the frequency of the pumping, for these factors are important in evaluating the mineralizing characteristics of the water. The depth of the borehole and the quality and length of casing will determine the depth from where the sample was obtained. Ultimately these parameters may account for the discrepancies in the contents of the dissolved solids. A second possibility, although unlikely, to account for group differences within nearby boreholes is that they may be fed from different acquifers.

A very close coherence was observed between the uranium concentrations of the subsurface waters and the surface uranium geochemical anomalies (Fig. 41). Certain exceptions are the high values on Jakkalswater, Marmor and in the south-eastern corner of Nordenburg. Lack of informa= tion concerning the uranium mineralization within these areas may account for this. North of the Chuosberge only one sample has a significant uranium concentration; here again no information on mineralization was available from this area. It may therefore be inferred that there is a reasonable probability that uranium mineralization may be present in the Wolfkoppe area. Samples 13 and 28 occur within mineralized areas but have low uranium concentrations. No reason can be given for this feature which may be due to a large number of causes, some of which were enumerated above.

A second classification, although very rough, has therefore been established. Those waters with uranium concentrations above 30 ppb are generally located within zones of potentially high uranium concentration. Values below this level may be regarded as background. In the USA 5 ppb uranium is background, whereas 10 ppb uranium is anomalous (Butler, 1969, p. 85). Care must be exercised with the interpretation of the uranium concentration in water because, assuming that the values of samples 13 and 28 reflect the actual situation, deviations from ideality can nevertheless occur. Two conditions may prevail that could account for anomalously high uranium values:

(a) An uneconomical uranium source undergoing weathering. For example, sample 29 with 118 ppb uranium is situated in Red Granite gneiss terrain. Figures quoted by Anglo American Prospecting Co. Ltd gave a mean of 14,5 ppm U_3O_8 for the Red Granite gneiss in the southern sector of Dorstrivier (Annual Prospecting Report (1973) Prospecting Grant M46/3/209).

(b) Water was in contact with a potential uranium deposit at or below the water-table, for example, the calcrete uranium deposits on the farm Bloemhof.

Therefore for waters in the Namib Desert the following applies: Uranium concentrations of 30 ppb or more reflect a potentially mineralized zone nearby. Uranium concentrations less than 30 ppb generally do not indicate mineralization. However, background uranium values do not necessarily mean that potential mineralization is absent, and anomalous values (greater than 30 ppb) do not necessarily imply a uranium deposit below or nearby.

13.3 Factor Analysis

Important parameters determining the distribution of the elements in the hydrological environment have been outlined by Spencer et al (1968, p. 981), viz:

(a) Composition of the source rocks and the weathering processes that act upon them.

(b) Nature of transporting processes and mechanisms of deposition.

They further pointed out that mechanisms involved in the evolution of sediments usually occur under non-equilibrium conditions, making interpretation of the analyses all that more complicated. Furthermore it becomes increasingly more difficult when a large number of variables are considered. Twenty-five samples (Groups 1 and 2) were analyzed for 17 variables, giving a total of 425 independent parameters (Tables 15 and 16). The technique adopted was factor analysis using the computer program GEO, a modified version of that written by Cameron (1967).

The distribution of elements within a system is controlled by a set of parameters. The classical method for the interpretation of the results rested solely on the application of variation diagrams and the more elementary statistics such as regression and means. Although these methods still form the basis of interpretation, more sophisticated approaches such as factor analysis were developed to be used in conjunction with them.

Factor analysis is capable of simultaneously deriving relationships, both correlated and uncorrelated, between many variables in a large number of samples. Herbosch (1974, p. 367) states that 'in an unknown field the factor analysis operates like a creative method of exploration of hypotheses'.

The steps involved in the factor analysis were the following:

(a) Calculation of a correlation matrix between the variables using both normal and transformed data and including the means and standard deviations.

(b) Calculation of eigenvalues from which the unrotated factors were determined along with their corresponding percentage variability to explain each factor.

(c) Orthogonal rotation of the vectors yielding a varimax matrix containing the number of factors as specified by a minimum eigenvalue of 0,5.

(d) Listing of the factors' scores which determine the contribution of each sample to a factor in the varimax matrix.

(e) Rotation of vectors forming oblique factors in the promax matrix. Herbosch (1974) notes that natural phenomena essentially follow the oblique rotation as opposed to the orthogonal.

(f) From the promax method, correlations between factors are obtained. The number of rotations is determined by the parameter of obliquity (KMIN).

(g) The factor scores for the promax are finally calculated.

Interpretations of the factor analysis data for the water samples were based upon the varimax matrix only because no further useful information could be derived from the promax rotations in this instance.

13.4 Geochemistry of Groups 1 and 2 Subsurface Waters

The waters were classified into four groups, the last two containing only three samples each. Consequently Groups 3 and 4 were not included in the geochemical interpretations by factor analysis.

Although the samples were classified into two main groups, the geochemistry of each is very similar. Discussion will initially be concerned with comparisons, and will terminate with the geochemistry of some of the elements.

The means of the variables in Group 1 (Table 15) are marginally and in some cases very much higher than those for Group 2, e.g. sodium is 1 272 ppm and 552 ppm respectively. For nitrate, silica and carbonate the reverse applies, e.g. carbonate is 91 ppm and 145 ppm respectively. Based upon log-transformed data, correlation matrices for Groups 1 and 2 are given in Table 22. Table 23 contains summaries compiled from the matrices. Only those correlations for the 99 per cent and 95 per cent confidence limits were included in Table 23.

Most variables correlate directly with the conductivity and total dissolved solids, and inversely with the pH. One of the most noteworthy features is the correlation at 99 per cent confidence limit between uranium and carbonate in both groups, which emphasizes their close coherence. In Group 2, uranium correlates with other variables, but at the 95 per cent level. Table 22 shows that uranium correlates marginally with other variables below the 95 per cent level.

Varimax matrices for Groups 1 and 2 are given in Table 24.

TABLE 3.3: CORRELATION MATRICES FOR LOG-TRANSFORMED DATA OF THE SUBBREAK WATERS FROM THE NAMIB DESERT FOR GROUPS 1 AND 2.

GROUP 1

CORRELATION MATRIX OF 9 SAMPLES

	MEAN	STD DEV	pH	Cond	TDS	Na	K	Ca	Mg	Cl	SO_4	Sr	Ba	SO_4	NO_3	SiO_2	F	Cl	CO_3
pH	0.9010 00	0.5108-01	1.000	-0.829	-0.786	-0.818	-0.779	-0.686	-0.813	...189	-0.515	-0.457	-0.305	-0.471	-0.164	-0.330	-0.616	-0.712	-0.130
Cond	0.3900 01	0.2110 00	-0.829	1.000	0.989	0.964	0.918	0.903	0.825	-0.356	0.736	0.411	0.578	0.660	0.114	-0.061	0.585	0.854	-0.171
TDS	0.3740 01	0.2395 00	-0.786	0.989	1.000	0.981	0.883	0.922	0.836	-0.368	0.759	0.360	0.603	0.618	0.168	-0.077	0.635	0.812	-0.200
Na	0.3020 01	0.2770 00	-0.818	0.964	0.981	1.000	0.928	0.855	0.829	-0.373	0.797	0.495	0.677	0.670	0.201	0.010	0.619	0.865	-0.183
K	0.1780 01	0.3832 00	-0.779	0.918	0.888	0.928	1.000	0.714	0.854	-0.203	0.638	0.507	0.563	0.719	0.141	0.076	0.398	0.841	-0.037
Ca	0.2800 01	0.2800 00	-0.686	0.903	0.922	0.855	0.714	1.000	0.844	-0.565	0.688	0.565	0.799	0.652	0.087	-0.393	0.463	0.742	-0.440
Mg	0.2210 01	0.1810 00	-0.813	0.825	0.836	0.829	0.854	0.843	1.000	-0.617	0.739	0.717	0.695	0.780	0.180	0.359	-0.020	-0.114	0.629	0.191
Cl	0.1940 01	0.2400 00	0.189	-0.356	-0.368	-0.373	-0.203	-0.565	0.017	1.000	-0.624	-0.468	0.070	-0.716	0.211	0.603	0.008	-0.486	0.929
SO_4	0.1450 01	0.4530 00	-0.515	0.738	0.759	0.797	0.638	0.688	-0.739	-0.624	1.000	0.471	0.959	0.698	0.007	-0.078	0.487	0.614	-0.523
Sr	0.3620 01	0.2760 00	-0.457	0.411	0.360	0.495	0.507	0.565	0.717	-0.468	0.471	1.000	0.701	0.965	0.442	0.004	0.011	0.777	-0.237
Ba	0.2500 01	0.3560 00	-0.609	0.578	0.603	0.677	0.563	0.799	0.695	0.070	0.959	0.701	1.000	0.879	0.447	0.580	0.873	0.438	0.270
SO_4	0.2890 01	0.3110 00	-0.471	0.660	0.618	0.670	0.719	0.652	0.780	-0.716	0.698	0.965	0.879	1.000	-0.255	-0.370	-0.065	0.718	-0.634
NO_3	0.1410 01	0.4830 00	-0.164	0.114	0.168	0.201	0.141	0.007	0.359	0.211	0.007	0.442	0.447	-0.255	1.000	0.357	0.310	0.246	0.353
SiO_2	0.1340 01	0.1990 00	-0.330	-0.061	-0.077	0.010	0.076	-0.388	-0.020	0.603	-0.078	0.004	0.580	-0.370	0.357	1.000	0.407	-0.192	0.768
F	0.1870 00	0.2840 00	-0.616	0.585	0.635	0.619	0.398	0.463	-0.111	1.000	0.487	0.013	0.873	-0.065	0.310	0.407	1.000	0.320	0.201
Cl	0.3330 01	0.2190 00	-0.712	0.854	0.812	0.865	0.841	0.742	0.624	-0.486	0.614	0.777	0.438	0.718	0.248	-0.192	0.320	1.000	-0.272
CO_3	0.1890 01	0.2730 00	-0.130	-0.171	-0.200	-0.183	-0.037	-0.440	0.191	0.929	-0.523	-0.237	0.270	-0.634	0.353	0.768	0.201	-0.272	1.000

GROUP 2

CORRELATION MATRIX OF 14 SAMPLES

	MEAN	STD DEV	pH	Cond	TDS	Na	K	Ca	Mg	Cl	SO_4	Sr	Ba	SO_4	NO_3	SiO_2	F	Cl	CO_3
pH	0.8840 00	0.3140-01	1.000	-0.584	-0.557	-0.426	-0.067	-0.684	-0.744	-0.339	-0.475	-0.531	-0.534	-0.369	-0.640	-0.051	-0.503	-0.558	-0.327
Cond	0.3670 01	0.1940 00	-0.584	1.000	0.993	0.934	0.505	0.858	0.861	0.584	0.159	0.814	0.675	0.899	0.614	0.274	0.124	0.991	0.232
TDS	0.3610 01	0.2100 00	-0.557	0.993	1.000	0.905	0.558	0.889	0.886	0.523	0.109	0.809	0.664	0.887	0.676	-0.284	0.107	0.986	0.183
Na	0.2680 01	0.2310 00	-0.426	0.934	0.905	1.000	0.740	0.657	0.859	0.631	0.233	0.870	0.526	0.904	0.352	0.262	0.219	0.933	0.297
K	0.1410 01	0.3670 00	-0.067	0.505	0.558	0.740	1.000	0.185	0.703	0.656	0.203	0.426	0.122	0.718	-0.037	-0.307	0.030	0.558	0.314
Ca	0.2580 01	0.2530 00	-0.684	0.858	0.889	0.657	0.185	1.000	0.834	0.729	0.682	0.898	0.716	0.941	0.880	-0.283	0.101	0.862	0.029
Mg	0.2097 01	0.2420 00	-0.744	0.861	0.886	0.859	0.703	0.834	1.000	0.718	0.567	0.712	0.615	0.837	0.453	-0.275	-0.128	0.862	0.233
Cl	0.1470 01	0.4170 00	-0.339	0.584	0.523	0.631	0.656	0.729	0.718	1.000	0.580	0.431	0.239	0.698	0.069	0.163	0.265	0.516	0.749
SO_4	0.1310 01	0.3480 00	-0.475	0.159	0.109	0.233	0.203	0.682	0.567	0.580	1.000	0.642	0.355	0.139	0.109	0.479	0.695	0.104	0.695
Sr	0.3660 01	0.3380 00	-0.531	0.814	0.809	0.870	0.426	0.898	0.712	0.431	0.642	1.000	0.778	0.917	0.472	-0.388	0.384	0.836	0.119
Ba	0.2260 01	0.3470 00	-0.534	0.675	0.664	0.526	0.122	0.716	0.615	0.239	0.355	0.778	1.000	0.669	0.596	-0.338	0.185	0.685	0.011
SO_4	0.2630 01	0.1430 00	-0.369	0.899	0.887	0.904	0.718	0.941	0.837	0.698	0.139	0.917	0.669	1.000	0.191	-0.270	0.070	0.863	0.335
NO_3	0.1690 01	0.4460 00	-0.640	0.614	0.676	0.352	-0.037	0.880	0.453	0.069	0.109	0.472	0.596	0.191	1.000	-0.112	0.128	0.601	-0.001
SiO_2	0.1421 01	0.1360 00	-0.051	0.274	-0.284	0.262	-0.307	-0.283	-0.275	0.163	0.479	-0.388	-0.338	-0.270	-0.112	1.000	0.184	-0.311	0.559
F	-0.1420-01	0.1600 00	-0.503	0.124	0.107	0.219	0.030	0.101	-0.128	0.265	0.695	0.384	0.185	0.070	0.128	0.184	1.000	0.109	0.361
Cl	0.3780 01	0.2380 00	-0.558	0.991	0.986	0.933	0.558	0.862	0.862	0.516	0.104	0.836	0.685	0.863	0.601	-0.311	0.109	1.000	0.154
CO_3	0.1570 01	0.2110 00	-0.327	0.232	0.183	0.297	0.314	0.029	0.233	0.749	0.695	0.119	0.011	0.335	-0.001	0.559	0.361	0.154	1.000

TABLE 23(a): SUMMARY OF THE CORRELATION MATRIX (TABLE 22) FOR THE GROUP 1 SUBSURFACE WATER

LOG TRANSFORMATION

	99%	95 %	99%	95 %
	+		-	
pH			Cond, Na	TDS,K,Cl
Conductivity	TDS, Na, K, Ca, Cl	V		
TDS	Na, K, Ca, Cl	V		
Na	K, Ca, V, Cl	Ba, SO_4		
K	Cl	Ca, SO_4		
Ca		V, Cl		
Mg		Sr		
U	CO			
V		SO_4		
Sr		Cl		
Ba	F			
SO_4		Cl		
NO_3				
SiO_2		CO_3		
F				
Cl				
CO_3				

TABLE 23(b): SUMMARY OF THE CORRELATION MATRIX (TABLE 22) FOR THE GROUP 2 SUBSURFACE WATER

LOG TRANSFORMATION

	99 %	95 %	99 %	95 %
	+		-	
pH			Ca	Cond, TDS, Sr, Ba, NO_3, F, Cl
Conductivity	TDS, Na, Ca, Mg, Sr, Ba, SO_4, Cl	K, U, NO_3		
TDS	Na, Ca, Mg, Sr, Ba, SO_4 NO_3, Cl	K, U		
Na	K, Ca, Mg, Sr, SO_4, Cl	U, Ba		
K	Mg, U, SO_4	Cl		
Ca	Sr, Ba, SO_4, NO_3, Cl	Mg		
Mg	Sr, SO_4, Cl	U, Ba		
U	SO_4, CO_3	V, Cl		
V	F, CO_3			
Sr	Ba, SO_4, Cl			
Ba	Cl	NO_3, SO_4		
SO_4	Cl			
NO_3		Cl		
SiO_2	CO_3			
F				
Cl				
CO_3				

TABLE 24: VARIMAX MATRICES FOR GROUPS 1 AND 2 SUBSURFACE WATERS

SUBSURFACE WATER FROM NAMIB DESERT GROUP 1

LOG TRANSFORMATION

VARIMAX MATRIX ACCOUNTING FOR 90,7 PER CENT OF TOTAL PROBLEM VARIANCE

	FACTOR	1	2	3	4
SUM OF SQUARES		7,036	3.474	2.464	2.442
0.822	pH	0.842	0.120	0.197	-0.245
0.988	COND	-0.966	0.150	-0.109	0.142
0.965	TDS	-0.938	0.192	-0.045	0.217
0.992	Na	-0.925	0.194	-0.161	0.269
0.923	K	-0.917	0.009	-0.278	0.061
0.877	Ca	-0.847	0.395	0.045	-0.002
0.916	Mg	-0.176	-0.186	-0.910	-0.145
0.935	U	0.234	-0.932	0.100	0.051
0.890	V	-0.632	0.582	0.065	0.384
0.960	Sr	-0.264	0.333	-0.859	0.201
0.922	Ba	-0.513	-0.155	-0.059	0.795
0.855	SO_4	-0.638	0.575	-0.230	-0.255
0.731	NO_3	0.054	-0.176	-0.533	0.643
0.777	SiO_2	0.005	-0.657	-0.016	0.588
0.885	F	-0.537	-0.122	0.235	0.725
0.981	Cl	-0.760	0.276	-0.569	0.058
0.996	CO_3	0.066	-0.972	-0.069	0.204

SUBSURFACE WATER FROM NAMIB DESERT GROUP 2

LOG TRANSFORMATION

VARIMAX MATRIX ACCOUNTING FOR 89,7 PER CENT OF TOTAL PROBLEM VARIANCE

	FACTOR	1	2	3	4
SUM OF SQUARES		6.034	2.404	4.959	1.856
0.819	pH	0.111	0.215	-0.731	0.476
0.985	COND	-0.750	-0.002	0.649	-0.042
0.981	TDS	-0.705	0.024	0.695	-0.002
0.930	Na	-0.869	0.012	0.386	-0.162
0.873	K	-0.921	-0.003	-0.144	-0.062
0.956	Ca	-0.338	0.065	0.915	0.008
0.912	Mg	-0.847	0.007	0.430	0.101
0.857	U	-0.749	-0.502	0.046	-0.209
0.848	V	-0.123	-0.647	0.041	-0.642
0.866	Sr	-0.598	0.265	0.556	-0.359
0.734	Ba	-0.299	0.227	0.738	-0.221
0.932	SO_4	-0.882	-0.043	0.389	0.012
0.865	NO_3	-0.027	-0.039	0.928	0.031
0.887	SiO_2	0.301	-0.888	-0.093	-0.009
0.929	F	-0.007	-0.173	0.118	-0.941
0.960	Cl	-0.720	0.069	0.660	-0.038
0.917	CO_3	-0.338	-0.857	-0.020	-0.260

PAGE 185
BETWEEN
PAGES 76 - 77

Group 1

Factor 1: 41 per cent of the variance. High negative loadings on conductivity, total dissolved solids, sodium, potassium, calcium and chloride and moderate loadings on barium, vanadium and fluoride. High positive loading on pH.

Factor 2: 20 per cent of the variance. High negative loadings on uranium, carbonate and silica. Moderate positive loadings on vanadium and strontium.

Factor 3: 15 per cent of the variance. High negative loadings on magnesium and strontium and moderate loadings on nitrate and chloride.

Factor 4: 15 per cent of the variance. High positive loadings on barium and fluoride and moderate loadings on nitrate and silica.

Group 2

Factor 1: 36 per cent of the variance. High negative loadings on conductivity, total dissolved solids, sodium, potassium, magnesium, uranium, sulphate and chloride, with a moderate loading on strontium.

Factor 2: 14 per cent of the variance. High negative loadings on silica and carbonate with moderate loadings on uranium and vanadium.

Factor 3: 29 per cent of the variance. High positive loadings on conductivity, total dissolved solids, calcium, barium, nitrate and chloride, with a moderate loading on strontium. High negative loading on pH.

Factor 4: 11 per cent of the variance. High negative loadings on vanadium and fluoride.

The main difference between the two groups is that in Group 1 the main constituents occur in factor 1, which includes pH, whereas in Group 2 they are divided between factors 1 and 3. Only the pH is totally located in factor 3. This all suggests that both groups have different sources for their water. In factor 2 of Group 1, uranium and silica have moderate negative loadings and vanadium has a positive loading. This suggests that due to high loadings of the same sign of uranium and silica, a uranyl silicate in place of a uranyl vanadate is likely to form in this system. In factor 2 of Group 2 moderately high negative loadings are associated with uranium, vanadium and silica. Both uranyl vanadate and uranyl silicate are the most probable stable phases. Therefore it was possible to predict from the chemistry of the subsurface waters which uranium minerals were most likely to be found. X-ray diffraction analysis of the uranium ore revealed that both carnotite (uranyl vanadate) and soddyite (uranyl silicate) are found in close association. No soddyite has so far been identified at the Langer Heinrich but is is predicted that soddyite can occur as a stable phase because sample 31 was classified into Group 1 (Table 15). pH is one of the controlling factors for the liberation of the dissolved salts from the source rocks (Feth et al, 1964) and this would account for the different signs. The activity of the H^+ ion is more vigorous for Group 1 as compared to Group 2, implied by the percentage variances of the respective

factors. Carbonic acid was virtually the only source of H^+ ions formed by the reaction of carbon dioxide and water as shown in the following equations at 25 °C and 100 kPa pressure (Feth et al, 1964; Hostetler and Garrels, 1962).

$$CO_2 + H_2O \rightleftharpoons H_2CO_3 \qquad (13.1)$$

$$H_2CO_3 \rightleftharpoons H^+ + HCO_3^- \quad K = 10^{-6,38} \qquad (13.2)$$

$$HCO_3^- \rightleftharpoons H^+ + CO_3^{2-} \quad K = 10^{-10,31} \qquad (13.3)$$

Therefore carbon dioxide enhances the reaction of water on rocks by the liberation of H^+. A direct manifestation of this is the relationship between carbonate and silica in Fig. 48 where there is a systematic relationship between the two

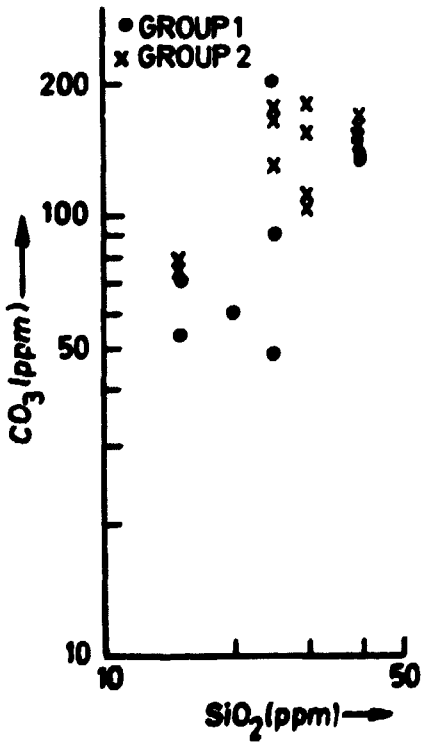


Fig. 48: Variation diagram of carbonate plotted against silica for Groups 1 and 2 sub= surface waters.

variables. Silica was obviously derived from the leaching and dissolution of the rock forming minerals. The high factor loadings with the same sign on silica and uranium do suggest a common source. When compared with Group 2, the higher reactivity of H^+ in Group 1 suggested that it behaved to a greater extent more like an open system where there is a constant replenishment of carbon dioxide from the atmosphere. A further point which added more weight to this hypothesis was that the mean total dissolved solids for Group 1 was greater than Group 2. By implication the bore= holes representing Group 1 derive their water from shallower depths than do those of Group 2. This would resolve the situation found on Bloemhof, where boreholes of both groups are within very close proximity of each other.

Szalay and Samsoni (1969) conducted a series of experiments concerning the leachability of uranium from powdered igneous rocks using 0,2 per cent sodium bicarbonate solutions. Since these aspects are important in the under= standing of uranium migration, a summary of their findings is given here.

1. The solubility of uranium in granites is much greater than in other types of igneous rocks.
2. The concentration of uranium in the water is a function of the amount of leachable uranium present in the source rocks rather than the occurrence of a hidden ore-body below.
3. Water circulating through granite detritus attains an equilibrium concentration of uranium after a period

of three to five hours. If the water is removed and replaced by a fresh solution, a new but lower equilibrium concentration is attained and indicates that the amount of leachable uranium decreases. If uranium is added to the initial solution it will asymptotically approach the original equilibrium concentration after a period of time. A decrease of uranium in solution can only be accounted for by adsorption onto grain surfaces.

The reactivity of the H^+ ion in the leaching ability of the subsurface water on rock detritus can be described in terms of the carbonate content as shown by equations (13.1), (13.2) and (13.3). Therefore the uranium concentration must be considered in terms of the pH and carbonate content.

A stepwise multivariate regression analysis was performed on both groups individually by the computer program BMD02R (Dixon, 1967), called STEP. This program computes a sequence of multiple linear regression equations in a step=wise manner, with one variable being added at each step. The variables, carbonate and pH were regressed in terms of uranium, being the dependent variable. Log transformations of carbonate and uranium only were done, as pH was already a log function. The following function was derived from the data of Group 1 samples (Table 15).

$$\log U = -0,71 + 0,9 \log CO_3^{2-} + 0,11\ pH \qquad (13,4)$$

The uranium values calculated in terms of this equation are plotted against the original uranium values in Fig. 49. All points cluster very closely around the line of equal ratio, which demonstrates that the solubility of uranium is primarily controlled by carbonate concentration and pH.

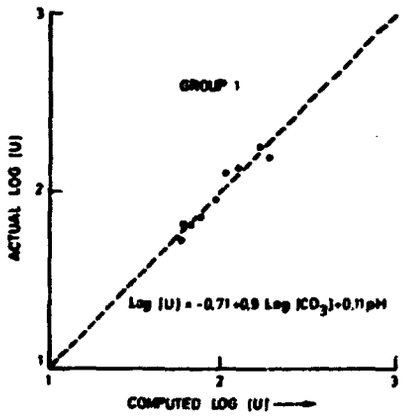


Fig. 49: Multivariate regression analysis of uranium, carbonate and pH in the subsurface water samples from Group 1.

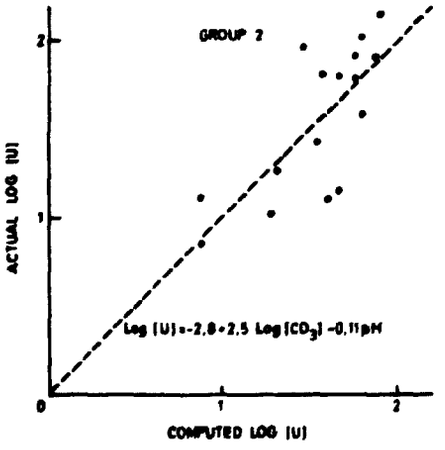


Fig. 50: Multivariate regression analysis of uranium, carbonate and pH in the subsurface water samples from Group 2.

A similar equation was derived from the data of Group 2 samples (Table 16).

$$\log U = -2,8 + 2,5 \log CO_3^{2-} - 0,11\ pH \qquad (13.5)$$

The plot of the computed values against the actual values (Fig. 50) shows a marked scattering of points about the equal ratio line. This implies that the uranium concentrations in Group 2 were not purely a function of pH and carbonate content, but that other influencing parameters acted upon this group and that the group was in a partially closed system with respect to carbon dioxide replenishment. Different sources of the waters for both groups are inferred, for if they were of the same source, equations (13.4) and (13.5) would have had the same coefficients. Dall'Aglio et al (1974, p. 41) derived a similar type of equation for conditions found in a part of the Italian Alps. Therefore for each system an equation may be derived that is best suited to it. The general application of one equation to describe all systems with different concentrations of uranium, carbonate and pH is therefore not possible.

13.5 Solution Geochemistry of Uranium, Vanadium and Calcium

13.5.1 Uranium

At this stage some of the theoretical aspects of the solubility of uranium in water will be studied.

Uranium in the basement rocks of the Langer Heinrich will oxidize from the (+IV) to the (+VI) state to form the uranyl cation as follows,

$$UO_2 \rightleftharpoons UO_2^{++} + 2e \qquad (13.6)$$

In the presence of carbonate ions two stable uranyl carbonate complexes will form at 25 °C and 100 kPa.

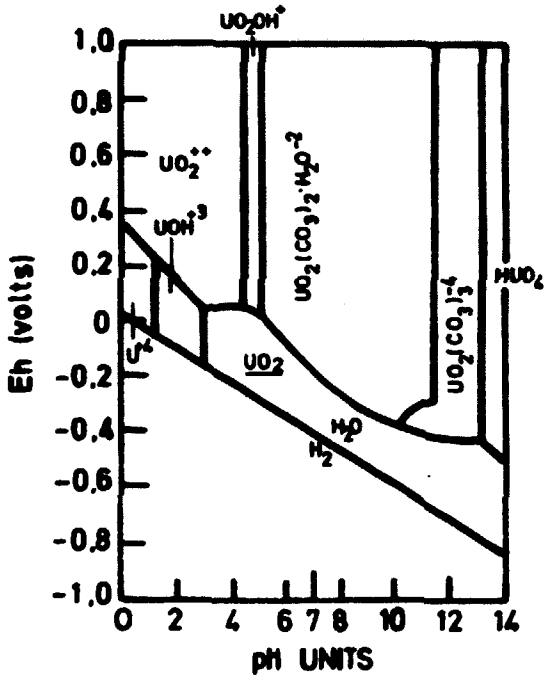
$$UO_2^{2+} + 2CO_3^{2-} + 2H_2O \rightleftharpoons UO_2(CO_3)_2 \cdot 2H_2O^{2-} \quad K = 10^{-20,4} \qquad (13.7)$$

$$UO_2^{2+} + 3CO_3^{2-} \rightleftharpoons UO_2(CO_3)_3^{4-} \quad K = 10^{-24,2} \qquad (13.8)$$

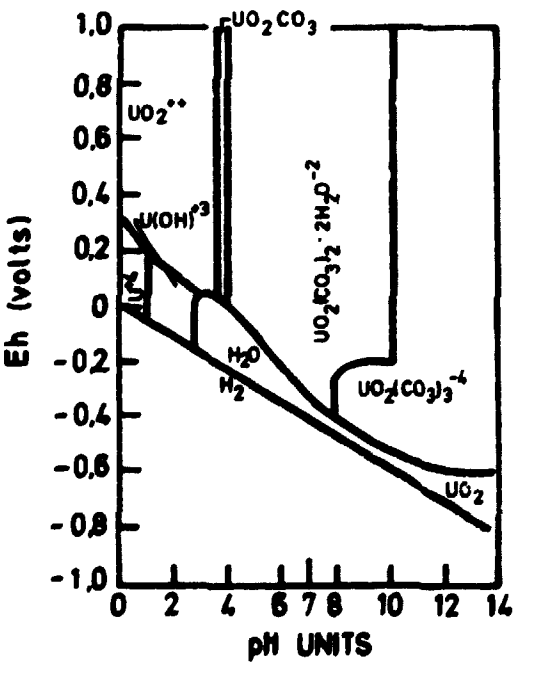
The uranyl dicarbonate complex (UDC)(equation 13.7) and the uranyl tricarbonate complex (UTC)(equation 13.8) are the soluble and stable ions in alkaline solution. The equilibrium constants, K, demonstrate that the stability of the uranyl carbonate complexes is greater at higher carbonate concentrations (Hostetler and Garrels, 1962). The partial pressure of carbon dioxide (P_{CO_2}) has a marked effect on the stabilities of both UDC and UTC. At a higher P_{CO_2}, UDC is converted to UTC.

$$UO_2(CO_3)_2 \cdot 2H_2O_2^{2-} + CO_2 \rightleftharpoons UO_2(CO_3)_3^{4-} + 2H_2O \qquad (13.9)$$

The stabilities of UDC and UTC are shown in Figs. 51(a) and (b) in terms of Eh, pH and P_{CO_2}. (Hostetler and Garrels, 1962, p. 146-147). Comparing these figures, it is noted that the fields of UDC and UTC are increased when $P_{CO_2} = 10^{-1}$, which happens at the expense of the other phases. If the P_{CO_2} decreases to $10^{-3,8}$ then all the UTC disproportionates in the reverse direction of equation (13,9) and its field in Fig. 51(a) will disappear completely.



(a)



(b)

Fig. 51: Aqueous equilibrium diagrams of the system $U-O_2-H_2O-CO_2$ at 25 °C and 100 kPa.
(a) $\Sigma CO_2 = 10^{-3}$
(b) $\Sigma CO_2 = 10^{-1}$
(Hostetler and Garrels, 1962, p. 146-147).

To make meaningful use of Eh-pH diagrams, the range of values that should be considered must be within the limits as determined by nature. The stability of aqueous solutions is limited by the dissociation of water. According to Hansuld (1966), these conditions seldom occur in nature when determined from actual field measurements. Sato (1960) took a considerable number of Eh-pH readings from natural waters of different sources and found that they occupied a restricted area to which he referred as the zone of weathering. This zone falls in the carnotite field in Fig. 52.

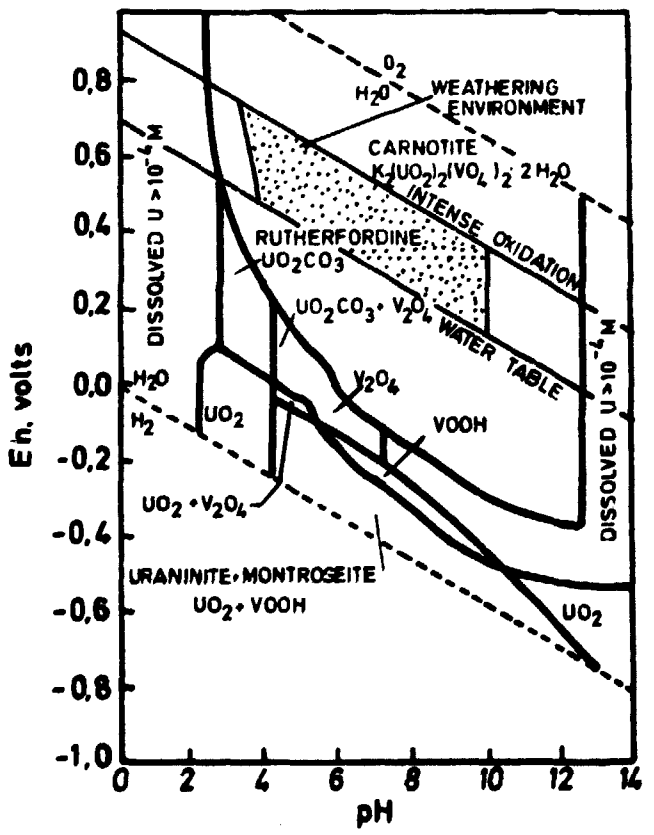


Fig. 52: The zone of weathering superimposed on an Eh-pH diagram. It occupies an area in the carnotite stability field.

Uranyl ions are precipitated from solution after disproportionation of the UDC complex (the reverse of equation 13.7), by vanadate ions with the vanadium in the (+V) state according to the following equation:

$$2K^{+} + 2UO_2^{2+} + 2H_2VO_4^{-} + 3H_2O \rightleftharpoons K_2(UO_2)_2(VO_4)_2 \cdot 3H_2O + 4H^{+} \quad (13.10)$$

Consideration should now be given to the state of the water-table under the Bloedkoppie Flats and the Gawib River sediments, i.e. whether it is perennial or ephemeral. Boreholes sunk into the sediments of the Gawib River Valley revealed that there is a definite water-table that exists all year round. Borehole HJ-2, located on the Bloedkoppie Flats and drilled to a depth of 30 m, did not intersect water at all. The upper 9 m were uranium-rich calcrete, which indicates that water was once present but has now gone, and the remainder was barren granite (Table 27). This would suggest that the water in the Gawib River Valley is perennial, whereas under the Bloedkoppie Flats it is ephemeral, forming only after heavy rainfall.

Distinction must be made between the reactivities of both ephemeral and perennial ground-water. The former, within its lifespan, will be constantly replenished with air and carbon dioxide from the atmosphere and overlying sediments and would vigorously react with the minerals during the period of contact. Perennial water, due to lack of recharge, would not be as aggressive because of the exhaustion of its supplies of carbon dioxide.

It is therefore considered that the uranium in the basement rocks was mobilized largely by ephemeral subsurface water which had an increased supply of carbon dioxide.

The implication is, for the successful dissolution of uranium in large enough quantities to form an ore-deposit of the Langer Heinrich type, a partial dynamic system must be postulated which is dependent on ephemeral water re= plenishment. Under stagnant conditions no deposit of any magnitude would form. An ephemeral water-table is one that is constantly moving until it no longer exists or until the residual water becomes stagnant. After heavy rainfall the water percolates down to the deepest levels possible, where a water-table will form and the level will rise if the supply is of sufficient magnitude. Upon cessation of the supply the water-level will start to drop, largely by down-gradient migration. The model is schematically drawn in Fig. 53.

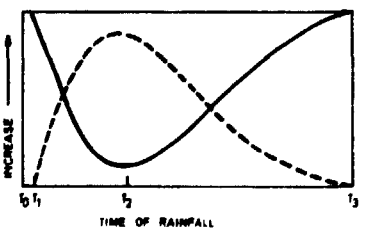


Fig. 53: Schematic diagram showing the thickness of sediment above an ephemeral water-table (——) and the leaching ability of water in relation to the time of rainfall (----).

T_0 = Time at which no water-table exists or the existing water is stagnant, i.e. a period of no rainfall. Sediment thickness above water-table at maximum and

leaching ability of the water at zero.

T_1 = Time at which rain falls.

T_2 = Time at which maximum depth of water-table occurs, i.e. sediment thickness above water-table is at a minimum and leaching ability of water at a maximum. This is followed by a cessation in water supply and a reduction of leaching ability.

T_3 = Time at which the water-table ceases to exist or becomes stagnant, i.e. sediment thickness above water-table at maximum and leaching ability reduced to zero. This is equivalent to T_0 for the next ephemeral cycle.

If this cyclic model is compounded, sufficient uranium will be leached and transported to its final place of deposition, which may be a considerable distance from the source.

13.5.2 Vanadium

The association of vanadium with fluorine in factor 4 of Groups 1 and 2 (Fig. 54) hints that there is a relation= ship between them. A fluoro-vanadate coordination complex may possibly form under these conditions. Griffith and Wickins (1968) have reported the existence of a vanadium-fluorine complex of the type $(VO_2F_4)^{3-}$.

13.5.3 Calcium

The solubility of calcium in aqueous solutions is enhanced by the concentration of the alkali metals.

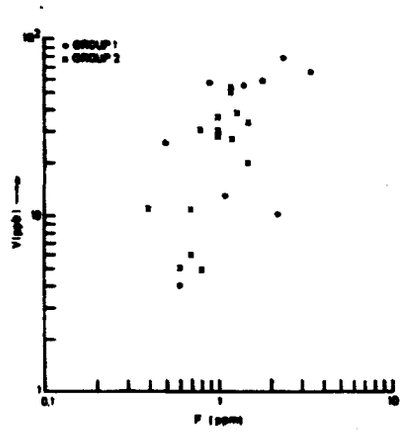


Fig. 54: Variation diagram of vanadium plotted against fluorine for the subsurface water samples from Groups 1 and 2.

(Netterberg, 1969(b), p. 230). Fig. 55 is a plot of calcium against sodium which shows a positive relationship between the two elements and confirms Netterberg's findings. This relationship is important with regard to the precipitation of calcite from the subsurface waters, for the higher the concentration of the alkali metals the greater the solubility of calcium and therefore the inhibition to some degree of the precipitation of calcite. Furthermore Netterberg (1971, p. 9) has the following to say with regard to the sclubility of calcium carbonate in natural waters.

> '... an increase in water content, CO_2 content, and pressure and a decrease in temperature favour the solution of carbonate, while an increase in temperature and a decrease in water content, CO_2 content, and pressure favour the precipitation of carbonate.'

Fig. 56 reveals that water with a vapour phase has a higher calcium concentration than water with no vapour phase.

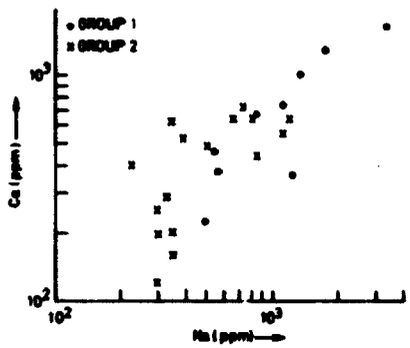


Fig. 55: Variation diagram of calcium plotted against sodium for the subsurface waters from Groups 1 and 2.

This suggests that the greater the distance of a point above the water-table in a sediment (i.e. closer to the surface), the lower the partial pressure of carbon dioxide and water vapour content. The result is a lowering of the calcium concentration in the water by the precipitation of calcite.

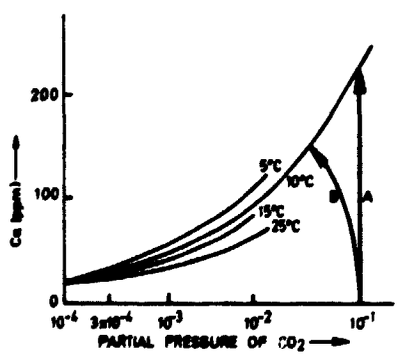


Fig. 56: Change in composition of carbonated water during equilibration with calcite at various temperatures in the presence (A) and in the absence (B) of a vapour phase. (Ostle and Ball, 1973, p. 175).

13.6 Source of Ions in Solution

Soluble contents of the subsurface waters of the Namib Desert were derived from several sources.

Feth et al (1964, p. 41) outlined the reaction of carbon dioxide and water on andesine feldspar:

$$6Na_{0,66}\ Ca_{0,33}\ Al_{1,33}\ Si_{2,66}\ O_8 + 6CO_2 + 18H_2O \rightarrow$$
$$3Na_{0,66}\ Al_{2,66}\ Si_{1,33}\ O_{10}(OH)_2 + 2Ca^{2+} + 2Na^{+} + 6H_4SiO_4 + 6HCO_3^{-} \quad (13,11)$$

From this reaction a multitude of ions (and montmorillonite) are formed. Disintegration of feldspar therefore probably constitutes the main source of these ions. Carbon dioxide, needed to initiate the reaction, is mainly of atmospheric origin. A small amount of chloride, sulphate, nitrate and fluoride have been derived from the weathering of biotite and amphiboles.

The second most important source of ions are the fogs. Analyses of the fogs are given in Table 38 and the salt crust from the Langer Heinrich in Table 2.

13.7 Geochemistry of Other Metallic Elements in the Subsurface Waters

Table 20 lists the results of analyses on eight samples of subsurface water taken from boreholes on the Dorstrivier concession of Anglo American Prospecting Co. Ltd. Unfortunately these boreholes do not coincide with those listed in Tables 15 to 18. Therefore a comprehensive geochemical analysis cannot be done because no values for the major constituents are available. Nevertheless it may be useful to see how the elements behave in saline water and especially their relationship, if any, to uranium.

Krauskopf (1956) considered the type of ionic species in solution for some of the elements in seawater. As we are dealing in this case with a brine, although somewhat different from seawater, it is accepted that the metal species in solution will be similar. Below is a list of the most likely species that may occur in solution.

Element	Ionic Species
U	$UO_2(CO_3)_2 \cdot 2H_2O^{2-}$
Pb	$PbCl^+$, Pb^{2+}
Cu	Cu^{2+}, $CuCl^+$
Ni	Ni^{2+}
Ag	$AgCl_2^-$
Zn	Zn^{2+}
Co	$CoCl^+$

Table 25 gives the correlation coefficients of the samples. Significant correlations at the 95 per cent confidence limits are found between lead, nickel and cobalt. Correlations slightly below the 95 per cent level occur between lead and silver, nickel and silver, and zinc and cobalt. No significant correlation between uranium and any element is found.

The varimax matrix of the factor analysis after log transformation yields two factors which account for 78 per cent of the total variability. Factor 1 with 44 per cent of the variability has high positive loadings on lead, copper, silver, zinc and cobalt. Factor 2, with the remaining 34 per cent variability, has high negative loadings on uranium, lead and nickel and to a lesser extent silver.

TABLE 25: CORRELATION MATRIX OF THE LOG TRANSFORMED DATA OF TRACE ELEMENT CONCENTRATIONS IN THE SUBSURFACE WATERS OF THE NAMIB DESERT

TRACE ELEMENTS IN SWA WATER LOG TRANSFORMATION

CORRELATION MATRIX OF 8 SAMPLES

	MEAN	STD DEV	U	Pb	Cu	Ni	Ag	Zn	CO
U	0.185D 01	0.247D 00	1.000	0.478	0.028	0.560	0.404	-0.077	0.011
Pb	0.159D 01	0.177D 00	0.478	1.000	0.561	0.921	0.694	0.424	0.854
Cu	0.115D 01	0.113D 00	0.028	0.561	1.000	0.275	0.541	0.293	0.628
Ni	0.131D 01	0.150D 00	0.560	0.921	0.275	1.000	0.648	0.329	0.724
Ag	0.108D 01	0.253D 00	0.404	0.694	0.541	0.648	1.000	0.531	0.560
Zn	0.150D 01	0.639D 00	-0.077	0.424	0.293	0.329	0.531	1.000	0.642
CO	0.442D 00	0.128D 00	0.011	0.854	0.628	0.724	0.560	0.642	1.000

CONFIDENTIAL

CONFIDENTIAL

Satisfactory interpretations of the results at this stage are not possible until further research is done in this direction.

13.8 Summary

The study of the distribution of ionic species in the subsurface waters of the Namib Desert provided an insight into the physico-chemical processes involved during epigenesis of the calcretes. The waters have a high degree of calcite saturation, implying that the formation of calcrete is still taking place. Montmorillonite and not kaolinite is the stable clay. Only Groups 1 and 2 were used in the geochemical interpretations, as too few samples were available from Groups 3 and 4. It was possible to predict from the chemistries of Groups 1 and 2 which uranium minerals were most likely to be found. Group 1 had soddyite (uranyl silicate) as the stable phase and Group 2 had both soddyite and carnotite (uranyl vanadate) as the stable phases. X-ray diffraction analysis confirmed the presence of these coexisting minerals.

The uranium distribution was described in terms of pH and carbonate content by multivariate regression analysis, and equations were derived from Groups 1 and 2. The straight line plots of the equations demonstrated the dependency of the uranium concentration of the pH and the concentration of carbonate in the water. The solution geochemistry of uranium, vanadium and calcium is discussed which included the mechanisms of dissolution and transport of the ions in solution.

From the prospecting aspect, uranium concentrations of 30 ppb or more reflect potential mineralization nearby. Uranium concentrations less than 30 ppb generally do not indicate mineralization. However, background uranium values do not necessarily mean that mineralization is absent and values greater than 30 ppb do not necessarily imply a uranium deposit in the vicinity.

Soluble contents of the waters were derived from, firstly, the reaction between carbon dioxide and feldspars, and secondly, the dissolved contents of the onshore fogs.

14. GEOCHEMISTRY OF THE DURICRUST DEPOSITS

It was observed that carnotite and calcite are intimately associated in the calcrete. The question now arises: what were the controlling factors, from the geochemical standpoint, that resulted in the precipitation of these minerals and all the associated epigenetic major and trace elements? This chapter therefore deals with the factors which influenced the dissolution, transportation and precipitation of elements in duricrust deposits.

14.1 Analytical Results

Most of the analytical work for this section was done on samples of calcrete powder obtained from boreholes of percussion drilling at the Langer Heinrich. Tables 26 and 27 are the results of partial whole-rock analyses of the powdered calcrete. Atomic absorption was used for the analyses in Table 26. In Table 27 the following analytical methods were used: uranium - delayed neutron counting; carbon dioxide (for $CaCO_3$) - Leco gas absorption; and sulphate-photometry. Partial whole-rock chemical analysis for the hardpan of the Langer Heinrich formation is given in Table 28. Analysis was by atomic absorption and delayed neutron counting.

Semi-quantitative spectrographic analysis for trace elements in the calcrete powder is given in Table 29.

Partial chemical analyses of the epigenetic fractions of calcrete powders are given in Table 30. The calcrete was

leached with dilute hydrochloric acid from which the detrital residue was filtered off. The filtrate was evaporated to dryness and it was upon this dried portion that the analyses were performed. All calculations were therefore based on the weight of sample taken from the dried acid soluble fraction and not on the weight of the whole rock. The value for the detritus was nearly the difference in weight between the whole-rock sample initially used and the residue after leaching and filtration.

The major elements including barium and strontium were analyzed by conventional flame atomic absorption, lead and vanadium by atomic absorption using the carbon rod technique, and uranium by delayed neutron counting. The remaining trace elements were determined by non-destructive neutron activation analysis.

TABLE 26: PARTIAL WHOLE-ROCK CHEMICAL ANALYSES OF CALCRETE POWDERS FROM PERCUSSION BOREHOLES AT THE LANGER HEINRICH

	Borehole HJ2						Borehole J1						Borehole HJ1				Borehole C5										Borehole AD1											
%	HJ2-6 (3)*	HJ2-8 (4)	HJ2-10 (5)	HJ2-13 (6,5)	HJ2-15 (7,5)	HJ2-18 (9)	J1-4 (2)	J1-6 (3)	J1-10 (5)	J1-11 (5,5)	J1-12 (6)	J1-14 (7)	HJ1-1 (0,5)	HJ1-2 (1)	HJ1-3 (1,5)	HJ1-4 (2)	C5-5 (2,5)	C5-10 (5)	C5-12 (6)	C5-13 (6,5)	C5-14 (7)	C5-15 (7,5)	C5-18 (9)	C5-24 (12)	C5-27 (13)	C5-28 (14)	C5-36 (18)	AD1-6 (3)	AD1-12 (6)	AD1-16 (8)	AD1-17 (8,5)	AD1-19 (9,5)	AD1-20 (10)	AD1-25 (12,5)	AD1-28 (14)	AD1-29 (14,5)	AD1-30 (15)	AD1-31 (15,5)	AD1-32 (16)	AD1-48 (24)
[illegible]	40,0	55,0	58,3	64,3	44,4	65,7	64,8	63,0	58,6	60,4	50,5	60,0	43,7	53,8	60,4	51,2	42,5	50,8	56,0	54,3	56,4	53,4	49,8	58,2	59,[illegible]	59,3	56,4	59,1	70,1	55,7	57,1	46,9	51,2	60,6	68,1	60,4	45,3	47,1	74,3	68,4
[illegible]	0,14	0,14	0,18	0,18	0,12	0,21	0,24	0,22	0,26	0,19	0,21	0,30	0,13	0,14	0,12	0,19	0,21	0,17	[illegible]	0,31	0,39	0,48	0,70	0,12	0,45	[illegible]	0,17	1,14	0,20	0,14	0,12	0,13	0,10	1,22	0,13	0,11	0,11	0,11	0,50	0,47
[illegible]	7,60	9,63	9,89	10,60	8,17	10,9[illegible]	8,20	9,52	9,88	9,08	9,07	11,07	5,54	8,01	8,99	10,60	7,56	8,11	9,04	7,03	[illegible]	10,77	7,85	9,12	9,45	9,09	8,96	8,87	10,46	8,52	7,70	7,35	7,77	10,10	10,84	9,12	7,65	7,73	8,95	11,50
[illegible]	1,33	1,38	1,77	1,87	1,35	2,17	2,07	1,78	2,36	2,01	1,99	2,96	0,92	0,95	0,86	4,28	1,40	1,26	1,53	2,01	2,52	3,76	1,29	0,97	3,28	2,71	1,45	1,76	1,98	1,37	1,31	1,32	1,04	2,13	1,14	1,24	1,17	1,21	2,36	2,87
[illegible]	0,02	0,02	0,04	0,04	0,02	0,05	0,04	0,05	0,06	0,07	0,04	0,11	0,02	0,03	0,03	0,05	0,02	0,03	0,04	0,03	[illegible]	0,04	0,01	0,02	0,08	0,07	[illegible]	0,03	0,07	0,03	0,02	0,03	0,03	0,09	0,03	0,03	0,03	0,03	0,19	0,25
[illegible]	0,81	0,79	0,90	0,89	0,73	0,91	0,99	1,05	2,82	1,06	1,04	1,46	0,56	1,20	0,85	2,65	0,90	0,80	0,73	1,01	1,53	[illegible]	1,01	0,83	1,77	[illegible]	1,01	3,45	3,42	2,24	2,11	1,95	1,76	1,46	1,16	1,09	1,20	0,88	1,76	1,32
[illegible]	24,7	13,82	12,48	7,40	23,06	5,55	8,12	9,33	12,07	9,85	15,19	[illegible]	18,86	14,89	12,03	12,[illegible]	21,58	15,83	12,55	13,1[illegible]	9,62	11,93	[illegible]	[illegible]	27,5[illegible]	11,38	14,10	9,39	[illegible]	11,45	15,05	19,63	15,68	8,50	2,79	9,63	20,16	19,30	11,60	[illegible]
[illegible]	1,66	1,50	1,63	1,34	1,48	1,60	1,64	1,55	1,90	1,64	1,77	1,86	[illegible]	2,41	2,44	[illegible]	1,74	1,94	[illegible]	1,[illegible]	1,87	1,62	1,54	1,98	1,[illegible]	1,44	1,[illegible]	1,81	1,89	1,56	1,43	1,29	1,44	1,85	[illegible]	1,68	1,28	[illegible]	1,19	1,77
[illegible]	2,23	3,[illegible]	3,00	2,40	2,56	3,61	3,05	2,72	3,02	[illegible]	[illegible]	3,64	1,92	[illegible]	3,42	3,14	1,45	[illegible]	[illegible]	[illegible]	2,56	[illegible]	[illegible]	[illegible]	1,78	[illegible]	[illegible]	3,16	3,98	3,21	2,81	2,69	2,84	3,65	3,85	3,40	2,39	2,65	2,81	4,02
[illegible]	0,08	0,11	0,13	0,14	0,12	0,14	0,13	0,12	0,13	0,10	0,14	0,18	0,09	0,12	0,10	0,11	0,07	0,0[illegible]	[illegible]	[illegible]	[illegible]	[illegible]	[illegible]	[illegible]	[illegible]	[illegible]	[illegible]	0,14	0,18	0,11	0,11	0,10	0,11	0,16	0,17	0,12	0,10	0,10	0,15	0,27
ppm																																								
[illegible]	29	33	39	39	24	35	36	37	44	29	28	30	151	37	34	62	17	16	10	22	24	33	17	19	31	34	18	758	342	181	158	178	105	145	124	114	64	90	124	86
	1 250	1 90[illegible]	530	932	413	190	93	71	290	936	675	65	122	63	36	48	73	766	64[illegible]	465	5[illegible]	869	529	354	98[illegible]	78	291	53	178	79	1 158	221	264	16	73	220	742	42	173	67

* The figure in brackets refers to the depth in metres.

CONFIDENTIAL

CONFIDENTIAL

TABLE 27: URANIUM, CARBONATE AND SULPHATE ANALYSES OF CALCRETE POWDERS FROM PERCUSSION BOREHOLES AT THE LANGER HEINRICH

Depth (m)	Borehole HJ1			Borehole HJ2			Borehole J1			Borehole C5			Borehole AD1		
	U(ppm)	$CaCO_3$(%)*	SO_4(%)	U(ppm)	$CaCO_3$(%)	SO_4(%)	U(ppm)	$CaCO_3$(%)	SO_4(%)	U(ppm)	$CaCO_3$(%)	SO_4(%)	U(ppm)	$CaCO_3$(%)	SO_4(%)
0,5 (1)+	122	21,8	12,2	2	1,2	0,01	13	12,4	0,01	-	-	-	120	6,8	2,6
1,0 (2)	63	25,5	1,76	-	-	-	34	11,6	0,01	335	30,9	0,14	-	-	-
1,5 (3)	36	20,5	0,74	16	9,4	0,01	49	11,7	0,01	-	-	-	-	-	-
2,0 (4)	40	20,2	0,38	30	17,8	0,01	93	10,6	0,01	-	-	-	37	1,4	0,02
2,5 (5)	19	43,8	0,14	21	28,8	0,01	74	11,3	0,01	73	40,2	0,04	-	-	-
3,0 (6)	-	-	-	1 250	40,7	0,03	74	13,1	0,01	-	-	-	-	-	-
3,5 (7)	-	-	-	-	-	-	163	13,5	0,34	-	-	-	-	-	-
4,0 (8)	13	48,2	0,19	1 890	24,1	0,01	244	10,4	0,23	-	-	-	53	19,8	0,02
4,5 (9)	-	-	-	-	-	-	105	6,5	0,48	-	-	-	-	-	-
5,0 (10)	-	-	-	530	22,6	0,01	230	15,6	0,02	366	31,9	0,03	-	-	-
5,5 (11)	-	-	-	52	12,9	0,24	944	17,9	0,01	434	36,5	0,02	-	-	-
6,0 (12)	15	46,1	1,26	-	-	-	675	26,4	0,01	641	27,2	0,02	178	2,9	0,02
6,5 (13)	-	-	-	935	12,9	0,02	260	11,4	0,02	405	25,6	0,02	-	-	-
7,0 (14)	-	-	-	757	12,9	0,01	65	9,1	0,01	587	18,6	0,01	-	-	-
7,5 (15)	-	-	-	419	41,6	0,02	25	2,1	0,02	870	19,8	0,03	47	16,1	0,01
8,0 (16)	8	45,3	0,04	-	-	-				460	25,3	0,03	80	24,0	0,01
8,5 (17)	-	-	-	-	-	-	SCHIST CONTACT			-	-	-	1 158	30,1	0,01
9,0 (18)	-	-	-	1 142	9,2	0,01				520	33,0	0,02	200	33,9	0,02
9,5 (19)	-	-	-	GRANITE CONTACT						-	-	-	220	36,2	0,01
10,0 (20)	2	39,4	0,01							-	-	-	264	29,9	0,02
10,5 (21)	-	-	-							-	-	-	114	26,7	0,02
11,0 (22)	-	-	-							-	-	-	70	22,5	0,03
11,5 (23)	-	-	-							-	-	-	-	-	-
12,0 (24)	46	38,0	0,02							354	23,8	0,01	-	-	-
12,5 (25)	-	-	-							-	-	-	10	14,1	0,02
13,0 (26)	-	-	-							382	20,2	0,01	-	-	-
13,5 (27)	-	-	-							-	-	-	-	-	-
14,0 (28)	142	37,6	0,01							70	18,5	0,01	73	3,1	0,01
14,5 (29)	-	-	-							-	-	-	220	15,5	0,02
15,0 (30)	-	-	-							-	-	-	740	35,2	0,03
15,5 (31)	-	-	-							-	-	-	62	34,1	0,24
16,0 (32)	30	26,1	0,01							442	17,0	0,01	123	21,2	0,02
16,5 (33)										-	-	-	-	-	-
17,0 (34)										-	-	-	-	-	-
17,5 (35)										-	-	-	-	-	-
18,0 (36)										290	25,3	0,03	18	15,6	0,01
18,5 (37)													-	-	-
19,0 (38)													-	-	-
19,5 (39)													-	-	-
20,0 (40)													42	14,5	0,02
20,5 (41)													-	-	-
21,0 (42)													-	-	-
21,5 (43)													-	-	-
22,0 (44)													20	19,8	0,02
22,5 (45)													-	-	-
23,0 (46)													-	-	-
23,5 (47)													-	-	-
24,0 (48)													67	2,3	0,02
24,5 (49)													-	-	-
25,0 (50)													-	-	-
25,5 (51)													-	-	-
26,0 (52)													48	15,6	0,02
26,5 (53)													-	-	-
27,0 (54)													-	-	-
27,5 (55)													-	-	-
28,0 (56)													40	10,9	0,02
28,5 (57)													-	-	-
29,0 (58)													-	-	-
29,5 (59)													42	8,9	0,02

* $CaCO_3$ content calculated from CO_2 values.

+ Number in brackets refers to the sample number, i.e. 0,5 (1) for borehole HJ1 means sample HJ1-1 from a depth of 0,5 m.

CONFIDENTIAL

TABLE 28: PARTIAL WHOLE-ROCK CHEMICAL ANALYSES OF THE HARDPAN CALCRETE OF THE LANGER HEINRICH CALCRETE FORMATION

%	LH 7	LH 24
SiO_2	32,9	32,6
TiO_2	0,15	0,16
Al_2O_3	4,74	5,27
Fe_2O_3	0,94	0,81
MnO	0,02	0,02
MgO	0,84	1,46
CaO	29,86	31,3
Na_2O	0,91	1,04
K_2O	2,18	1,84
P_2O_5	0,11	0,09
ppm		
Li	7	10
U	-	481

LH 7: Sample taken from the main body of hardpan overlying the Bloedkoppie Granite.

LH 24: Hardpan of the boulder calcrete type located on the Bloedkoppie Flats - contains carnotite.

TABLE 29: SEMI-QUANTITATIVE SPECTROGRAPHIC ANALYSES FOR TRACE ELEMENTS IN THE CALCRETE POWDERS FROM PERCUSSION BOREHOLES AT THE LANGER HEINRICH (COURTESY, ANGLO AMERICAN RESEARCH LABORATORIES)

SAMPLE NUMBER		PARTS PER MILLION													
		Bi	Pb	Zn	Sb	Sn	Y	Be	Mo	Nb	Cu	Ni	La	Ag	Co	V
C-5	5	<1,0	15	<10	<50	<5	<10	<0,1	<5	<100	60	15	<100	<0,1	<10	80
	10		40	10		5	15				15	15		0,2		200
	13		20	10		<5	100				10	20		<0,1	10	250
	14		15	<10			20				8	25			<10	300
	15		15				20				10	20				400
	16		10				<10				20	15				150
	18		25	10			10				15	10		0,1		200
	26		10	<10			30				30	40		<0,1	15	200
	28		10	<10			30				25	40		<0,1	10	200
	36		30	10			15				30	25		0,1	25	200
HJ-1	1		<10	<10			<10				15	<10		0,6	<10	150
	2		20								8			<0,1		80
	3		25								5					70
	4		20	10		5	25	0,1			30	30			15	100
	5		30	<10		5	15	<0,1			25	25			<10	300
HJ-2	6		20	15		<5	<10				20	30			15	300
	8		25								15	25			10	500
	10	5	20				50	0,1			25	25			10	300
	13	<1,0	30			5	10	<0,1			25	20			10	400
	15		20	10		<5	<10				10	<10		0,1	<10	100
	18		20				10				25	25				150
J-1	2		10			<5	10	<0,1			25	15				200
	4		15			<5	15	<0,1			25	20				80
	6		25	10		5	60	0,1			20	30			15	150
	8		10	<10		<5	15	0,8			15	15			<10	200
	10		25			8	20	<0,1	5		30	60			10	150
	12		15			<5	15		<5		25	40			15	200
	14		10				15				20	25			10	100
AD-1	8		20	10			<10				15	<10			<10	100
	12		15	<10			15				20	40				200
	16		15	15			20	1,5			15	10				100
	17		30	25			15	<0,1			25	40			20	600
	18		20	<10			<10				15	15			<10	100
	19		10	15			20				20	10				150
	20		25	<10			<10				10	<10				100
	25		15				15	<0,1			20	20				100
	28		25				<10				15	10				70
	29		25			5	10				20	15				200
	30		10	15		<5	20				20	10			10	250
	31		40	10		<5	10				20	20			<10	100
	32		30	10		5	25	0,1			25	60			30	200
	48	1	25	<10		5	30	<0,1	1		40	25			20	150

TABLE 30: PARTIAL CHEMICAL ANALYSES OF THE EPIGENETIC FRACTION OF CALCRETE POWDERS FROM PERCUSSION BOREHOLES AT THE LANGER HEINRICH.

%	1	2	3	4	5	6	7	8	9	10	11	12	13
	HJ2-3	HJ2-5	HJ2-10	HJ3-13	HJ2-15	AD1-8	AD1-17	AD1-25	AD1-30	J1-6	J1-11	C5-15	C5-24
SiO_2	4,3	2,9	2,8	1,9	1,1	1,8	1,3	0,5	0,8	1,4	1,1	1,3	0,8
Al_2O_3	5,8	1,3	2,6	4,0	1,5	2,6	1,8	5,4	1,6	4,0	2,6	4,6	2,8
Fe_2O_3	6,6	1,5	1,9	2,9	1,1	2,3	1,5	3,3	1,3	4,5	2,9	3,5	2,3
MgO	2,1	0,7	0,9	1,2	0,6	10,5	3,6	4,8	1,6	1,6	1,1	1,8	0,5
CaO	40,7	47,4	44,4	42,1	47,4	44,5	44,8	43,5	46,5	44,1	47,9	44,5	46,7
Na_2O	0,6	0,5	0,8	1,2	0,3	1,3	0,5	1,0	0,3	0,7	0,8	0,5	0,3
K_2O	2,2	0,7	1,4	1,9	0,6	1,2	0,9	2,4	0,8	1,1	1,1	2,0	1,2
Detritus	87,8	70,2	77,4	85,9	59,6	77,8	69,3	83,8	63,7	84,2	80,5	77,0	75,9
ppm													
Ba	249	47	116	217	51	117	47	902	82	311	511	113	51
Ce	72	18	20	37	17	21	9	47	13	34	37	34	16
Eu	21	9	8	13	3	9	5	25	3	19	23	8	5
Dy	3	1	2	4	1	1	1	1	1	1	3	2	1
Eu	1,2	0,4	0,6	1,0	0,3	0,5	0,2	0,9	0,3	0,5	0,6	0,8	0,3
La	51	12	15	30	18	13	9	32	7	21	25	23	8
Lu	0,3	0,1	0,2	0,3	0,05	0,1	0,03	0,2	0,2	0,1	0,2	0,2	0,1
Pb	8	7	15	22	4	8	3	22	6	6	9	9	6
Sc	6	3,3	2,8	4,6	1,4	2,3	2,0	3,3	0,8	1,5	1,6	1,7	1,2
Sm	12	3	4	7	3	2	2	8	2	5	6	8	3
Sr	180	9	111	208	166	164	25	110	194	419	281	418	177
Th	83	53	1 412	3 904	385	123	2 375	44	1 332	85	2 527	2 571	1 043
V	147	55	297	896	138	96	458	190	276	130	610	580	230
Yb	2,2	0,8	1,6	3,0	0,8	0,7	0,3	1,3	0,4	1,1	1,1	1,5	0,5
Ratio													
Th/V	0,56	0,96	4,75	4,36	2,97	1,28	5,19	0,23	4,83	0,65	4,14	4,43	4,53

Note:

(1) The results of the analyses are calculated on the basis of $CaCO_3$ only and not on the whole rock. (See text).

(2) The depth of the borehole in metres is obtained by dividing the last figure of the sample number by 3.

CONFIDENTIAL

CONFIDENTIAL

14.2 General Chemistry of the Calcretes

This section deals briefly with the general chemistry of the calcrete of the Langer Heinrich as represented by powders from the percussion boreholes (Tables 26 and 27) and the analysis of the hardpan (Table 28).

Perusal of the data of Table 26 reveals that the main constituents are silica, alumina and calcium oxide. The first two form part of the detrital fraction, and calcium oxide the cement. Of the minor constituents, the oxides of potassium, sodium, iron and magnesium form the next most abundant group of elements. Minor amounts of oxides of titanium, manganese and phosphorus were found. The only trace elements determined were lithium and uranium.

Comparing these results with the world average values (Table 31) as given by Goudie (1972) it is evident that the calcretes of the Langer Heinrich are dissimilar.

It would seem that Goudie's estimates, obtained from values in the literature, may be biased towards the calcrete types with higher $CaCO_3$ contents, i.e. hardpan and powder calcretes. All the analyses in Table 26 compare well with Netterberg's (1969(b), p. 111) calcified sands, which he regards as fairly immature calcrete.

The purpose of the analyses in Table 29 was to determine whether rapid trace element analyses on a whole-rock basis could be applied to regional exploration in calcretes to assist in the location of potential target areas of uranium mineralization. From the elements analyzed, vanadium has the highest variability and concentrations due

to the presence of carnotite. There is no other significant element that can be used as a tracer for uranium. Many elements have concentrations below their detection limits, but data of this type are nevertheless useful because they provide an upper limit to their concentration in calcrete.

TABLE 31: WORLD AVERAGE VALUES FOR CALCRETE
(Goudie, 1972, p. 450)

Element	%
CaO	42,6
SiO_2	12,3
Al_2O_3	2,1
Fe_2O_3	2,0
MgO	3,1
$CaCO_3$	79,3

14.3 Factor Analysis

Factor analysis was applied to the data in Table 30. Only chemical analyses were treated in this manner. Mineralogical proportions were ignored because the element distributions are primarily controlled by the absence or presence of minerals or discrete phases. Correct interpretation of the factors will therefore yield the precipitation history of the epigenetic minerals and the related processes.

TABLE 32: CORRELATION MATRICES OF THIRTEEN SAMPLES OF THE EPIGENETIC FRACTION OF THE CALCRETES FROM THE LANGER HEINRICH
(a) UNTRANSFORMED DATA
(b) LOG-TRANSFORMED DATA

(a) CORRELATION MATRIX OF 13 SAMPLES — NO TRANSFORMATION

	MEAN	STD DEV	SiO_2	Al	Fe	MgO	CaO	Na_2O	K_2O	Ba	Ce	Co	Dy	Eu	La	Lu	Pb	Sc	Sm	Sr	U	V	Yb
SiO_2	0.189E 01	0.107D 01	1.000	0.220	0.471	-0.071	-0.482	0.110	0.204	-0.250	0.456	0.152	0.407	0.472	0.484	0.407	-0.007	0.763	0.423	-0.190	-0.196	-0.165	0.582
Al	0.313D 01	0.151D 01	0.220	1.000	0.868	0.109	-0.796	0.368	0.935	0.582	0.860	0.697	0.436	0.877	0.812	0.653	0.520	0.582	0.908	0.286	-0.020	0.159	0.755
Fe	0.274D 01	0.152D 01	0.471	0.868	1.000	0.024	-0.716	0.211	0.687	0.384	0.915	0.789	0.448	0.776	0.866	0.620	0.153	0.592	0.875	0.445	-0.162	-0.014	0.702
MgO	0.238D 01	0.273D 01	-0.071	0.109	0.024	1.000	-0.252	0.619	0.159	0.172	0.010	0.097	-0.269	0.041	-0.004	-0.135	0.086	0.036	-0.115	-0.119	-0.272	-0.240	-0.172
CaO	0.450D 02	0.216D 01	-0.482	-0.796	-0.716	-0.252	1.000	-0.480	-0.779	-0.234	-0.685	-0.409	-0.459	-0.782	-0.529	-0.524	-0.500	-0.754	-0.696	-0.085	-0.052	-0.161	-0.728
Na_2O	0.677D 00	0.332D 00	0.110	0.368	0.211	0.619	-0.480	1.000	0.451	0.445	0.316	0.366	0.391	0.494	0.513	0.226	0.677	0.411	0.239	0.132	0.136	0.256	0.415
K_2O	0.135D 01	0.592D 00	0.204	0.935	0.687	0.159	-0.779	0.451	1.000	0.573	0.785	0.592	0.489	0.895	0.715	0.712	0.700	0.628	0.863	0.024	0.123	0.278	0.761
Ba	0.216D 03	0.246D 03	-0.250	0.582	0.384	0.172	-0.234	0.445	0.573	1.000	0.574	0.858	0.148	0.491	0.537	0.397	0.606	0.218	0.515	0.235	-0.122	0.058	0.311
Ce	0.288D 02	0.173D 02	0.456	0.880	0.915	0.010	-0.685	0.316	0.785	0.574	1.000	0.808	0.577	0.911	0.970	0.754	0.386	0.724	0.956	0.299	-0.113	0.071	0.811
Co	0.116D 02	0.779D 01	0.152	0.697	0.789	0.097	-0.409	0.486	0.592	0.858	0.808	1.000	0.399	0.671	0.755	0.525	0.462	0.469	0.721	0.401	-0.135	0.059	0.548
Dy	0.169D 01	0.103D 01	0.407	0.436	0.448	-0.259	-0.459	0.391	0.489	0.148	0.577	0.399	1.000	0.719	0.601	0.657	0.461	0.601	0.639	0.219	0.628	0.724	0.783
Eu	0.585D 00	0.308D 00	0.472	0.877	0.776	0.041	-0.782	0.494	0.895	0.491	0.911	0.671	0.719	1.000	0.848	0.817	0.642	0.803	0.935	0.144	0.122	0.295	0.932
La	0.195D 02	0.119D 02	0.484	0.812	0.866	-0.004	-0.629	0.213	0.715	0.537	0.970	0.755	0.601	0.848	1.000	0.684	0.266	0.701	0.917	00.210	-0.188	-0.017	0.770
Lu	0.152D 00	0.774D-01	0.407	0.658	0.620	-0.135	-0.524	0.226	0.712	0.397	0.754	0.525	0.657	0.817	0.684	1.000	0.481	0.561	0.798	0.169	0.150	0.262	0.758
Pb	0.977D 01	0.606D 01	-0.007	0.520	0.153	0.086	-0.500	0.677	0.700	0.606	0.386	0.462	0.481	0.642	0.286	0.481	1.000	0.501	0.449	-0.075	0.308	0.438	0.593
Sc	0.249D 01	0.149D 01	0.763	0.582	0.592	0.036	-0.754	0.411	0.628	0.218	0.724	0.469	0.601	0.803	0.701	0.561	0.501	1.000	0.704	-0.207	-0.025	0.088	0.777
Sm	0.492D 01	0.312D 01	0.423	0.908	0.875	-0.115	-0.696	0.239	0.863	0.515	0.956	0.721	0.639	0.935	0.917	0.798	0.449	0.704	1.000	0.196	0.079	0.244	0.856
Sr	0.1580 03	0.104D 03	-0.190	0.288	0.445	-0.119	-0.085	0.132	0.024	0.235	0.299	0.401	0.219	0.144	0.210	0.169	-0.075	-0.207	0.196	1.000	0.006	0.097	0.187
U	0.123D 04	0.127D 04	-0.196	-0.020	-0.162	-0.272	-0.052	0.136	0.123	-0.122	-0.113	-0.135	0.626	0.122	-0.188	0.150	0.308	-0.025	0.079	00.006	1.000	0.975	0.187
V	0.316D 03	0.250D 03	-0.185	0.153	-0.014	-0.240	-0.161	0.258	0.278	0.058	0.071	0.059	0.724	0.295	-0.017	0.262	0.438	0.088	0.244	0.097	0.975	1.000	0.330
Yb	0.1100 01	0.599D 00	0.582	0.755	0.702	-0.172	-0.728	0.415	0.761	0.311	0.811	0.548	0.783	0.932	0.770	0.758	0.593	0.777	0.856	0.187	0.187	0.330	1.000

(b) CORRELATION MATRIX OF 13 SAMPLES — LOG TRANSFORMATION

	MEAN	STD DEV	SiO_2	Al	Fe	MgO	CaO	Na_2O	K_2O	Ba	Ce	Co	Dy	Eu	La	Lu	Pb	Sc	Sm	Sr	U	V	Yb
SiO_2	0.157D 00	0.258D 00	1.000	0.030	0.234	-0.085	-0.897	0.235	0.067	-0.176	0.216	0.183	0.448	0.317	0.262	0.167	0.020	0.625	0.204	-0.251	-0.139	-0.228	0.437
Al	0.447D 00	0.217D 00	0.030	1.000	0.915	0.325	-0.775	0.497	0.936	0.724	0.839	0.714	0.483	0.823	0.738	0.596	0.582	0.472	0.864	0.510	-0.138	0.270	0.704
Fe	0.382D 00	0.225D 00	0.234	0.915	1.000	0.263	-0.700	0.459	0.791	0.696	0.874	0.814	0.501	0.782	0.763	0.580	0.382	0.478	.963	0.457	-0.257	0.105	0.679
MgO	0.203D 00	0.377D 00	-0.086	0.325	0.263	1.000	-0.444	0.571	0.365	0.351	0.149	0.292	-0.148	0.195	0.168	-0.001	0.212	0.202	0.033	0.028	-0.279	-0.063	-0.062
CaO	0.155D 01	0.211D-01	-0.397	-0.775	-0.700	-0.444	1.000	-0.517	-0.780	-0.426	-0.608	-0.491	-0.457	-0.694	-0.577	-0.407	-0.510	-0.711	-0.629	-0.219	0.172	-0.144	-0.594
Na_2O	-0.219D 00	0.220D 00	0.235	0.497	0.459	0.571	-0.517	1.000	0.555	0.645	0.506	0.715	0.409	0.627	0.451	0.328	0.728	0.601	0.410	0.141	-0.156	0.128	0.531
K_2O	0.900D-01	0.193D 00	0.067	0.936	0.791	0.365	-0.780	0.555	1.000	0.653	0.754	0.648	0.544	0.844	0.645	0.666	0.749	0.575	0.836	0.323	-0.030	0.358	0.689
Ba	0.213D 01	0.418D 00	-0.176	0.724	0.696	0.351	-0.426	0.645	0.653	1.000	0.804	0.867	0.410	0.727	0.731	0.605	0.639	0.338	0.726	0.499	-0.234	0.207	0.605
Ce	0.139D 01	0.251D 00	0.216	0.839	0.874	0.149	-0.608	0.506	0.754	0.804	1.000	0.840	0.609	0.932	0.927	0.722	0.543	0.504	0.921	0.447	-0.321	0.067	0.870
Co	0.965D 00	0.319D 00	0.183	0.714	0.814	0.292	-0.491	0.715	0.648	0.867	0.840	1.000	0.467	0.762	0.772	0.521	0.580	0.598	0.793	0.219	-0.372	0.031	0.673
Dy	0.165D 00	0.231D 00	0.448	0.483	0.501	-0.148	-0.457	0.409	0.544	0.410	0.609	0.467	1.000	0.707	0.562	0.623	0.521	0.523	0.691	0.315	0.431	0.609	0.727
Eu	-0.290D 00	0.236D 00	0.317	0.823	0.782	0.195	-0.694	0.627	0.844	0.727	0.932	0.762	0.707	1.000	0.838	0.807	0.743	0.692	0.900	0.347	-0.181	0.179	0.931
La	0.122D 01	0.247D 00	0.262	0.738	0.763	0.163	-0.577	0.451	0.645	0.731	0.927	0.772	0.562	0.838	1.000	0.515	0.422	0.623	0.852	0.324	-0.334	0.040	0.839
Lu	-0.888D 00	0.285D 00	0.167	0.596	0.580	-0.001	-0.407	0.328	0.666	0.605	0.722	0.521	0.623	0.807	0.515	1.000	0.636	0.331	0.723	0.414	-0.015	0.215	0.700
Pb	0.927D 00	0.231D 00	0.020	0.582	0.382	0.212	-0.510	0.728	0.749	0.639	0.543	0.580	0.521	0.743	0.422	0.636	1.000	0.591	0.606	0.116	0.041	0.364	0.651
Sc	0.331D 00	0.246D 00	0.625	0.472	0.478	0.202	-0.711	0.601	0.575	0.338	0.584	0.598	0.523	0.692	0.623	0.331	0.591	1.000	0.595	-0.261	-0.321	-0.070	0.672
Sm	0.613D 00	0.274D 00	0.204	0.864	0.863	0.033	-0.629	0.410	0.836	0.726	0.921	0.793	0.691	0.900	0.852	0.723	0.606	0.595	1.000	0.309	-0.100	0.295	0.846
Sr	0.209D 01	0.444D 00	-0.251	0.510	0.457	0.028	-0.219	0.141	0.323	0.499	0.447	0.219	0.315	0.347	0.324	0.414	0.116	-0.261	0.309	1.000	0.176	0.315	0.335
U	0.269D 01	0.730D 00	-0.139	-0.138	-0.257	-0.279	0.172	-0.156	-0.030	-0.234	-0.321	-0.372	0.431	-0.181	-0.334	-0.015	0.041	-0.321	-0.100	0.176	1.000	0.875	-0.140
V	0.237D 01	0.351D 00	-0.228	0.270	0.105	-0.063	-0.144	0.128	0.358	0.207	0.067	0.031	0.609	0.179	0.040	0.215	0.364	-0.070	0.295	0.315	0.875	1.000	0.142
Yb	-0.269D-01	0.267D 00	0.437	0.704	0.679	-0.062	-0.594	0.531	0.689	0.605	0.870	0.673	0.727	0.931	0.839	0.700	0.651	0.672	0.845	0.335	-0.140	0.142	1.000

CONFIDENTIAL
CONFIDENTIAL

Table 32 gives the correlation matrices for both normal and log-transformed data. Summaries of the two correlation matrices for the data below the diagonal are given in Table 33. For thirteen samples the 99 per cent and 95 per cent confidence limits are ± 0,7 and ± 0,56 respectively. Those elements with an asterisk denote the ones which are not correspondingly represented in either Table 32(a) or 32(b). For example, sodium in the normal untransformed data shows no significant correlation with the elements barium, europium, lanthanum and scandium as is found for the log-transformed data. In general though, most elements are correspondingly represented, but for those that are not, others act as synonyms, e.g. the rare-earth elements behave as a coherent group and therefore the correlation of one of the elements infers the presence of the others. As there is no significant deviation from normality the normal untransformed data were used in the factor analysis.

In the varimax factor matrix (Table 34) six coherent factors account for 94,1 per cent of the total variance of all the major and trace elements. The percentage contribution of each factor is calculated by dividing the sum of squares within each factor by the total sum of squares multiplied by the percentage variance, e.g. variance for factor 1 = (8,6/19,8) x 94,1 = 40,9 % (See Table 34 for the values above).

The loading of each element in all the factors gives the fraction of variance of every element that is explained by the factors. High loadings of a group of elements within a factor specify a covariant behaviour of those elements, e.g. alumina, iron oxide, potassium oxide, cerium, etc. in factor 1.

TABLE 33: SUMMARIES OF CORRELATION MATRICES IN TABLE 32
(a) UNTRANSFORMED DATA
(b) LOG-TRANSFORMED DATA

(a)

	99 %	95 %	99 %	95 %
	+	+	-	-
SiO_2	Sc	Yb*		
Al_2O_3	Fe_2O_3, K_2O, Ce, Eu, La, Sm, Yb		CaO	
Fe_2O_3	Ce, Co, Eu, La, Sm, Yb	K_2O, Lu, Sc*	CaO	
MgO		Na_2O		
CaO			K_2O, Eu, Sc, Yb*	Ce, La, Sm
Na_2O		Pb		
K_2O	Ce, Eu, La, Sm, Yb	Lu, Pb		
Ba	Co	Ce, La, Pb		
Ce	Fe, Eu, La, Co, Sc, Sm, Yb	Dy		
Eu	La, Sm	Ba		
Dy	Eu, Lu, Sc† Sm, V, Yb	U*		
Lu	La, Eu, Sc, Sm, Yb	Pb		
La	Eu, Sc, Sm, Yb			
Sm	Eu, Yb	Sc*		
Pb		Yb		
Sc	Sm, Yb			
Sm	Yb			
Sr				
U	V			

* Elements NOT correlated with the element in question for the log-transformed data

Confidence limits at n = 13

99 % = ± 0,7
95 % = ± 0,56

(b)

	99 %	95 %	99 %	95 %
	+	+	-	-
SiO_2		Sc		
Al_2O_3	Fe_2O_3, K_2O, Ba, Ce, Co, Eu, La, Sm, Yb	Lu, Pb*	CaO	
Fe_2O_3	K_2O, Ce, Co, Eu, La, Lu, Sm, Yb		CaO	
MgO		Na_2O		
CaO			K_2O, Sc	Ce, Eu, La, Sm
Na_2O	Co*, Pb	Ba†, Eu†, La†, Sc*		
K_2O	Ce, Eu, La, Pb, Sm	Ba†, Ce†, Lu, Yb		
Ba	Ce, Co, Eu†, La, Sm*	Lu, Pb, Yb*		
Ce	Co, Eu, La, Lu, Sm, Yb	Dy, Sc		
Co	Eu, La, Sm	Pb†, Sc†, Yb*		
Dy	Eu, Yb	La†, Lu, Sm, V		
Eu	La, Lu, Pb, Sm, Yb	Sc		
La	Sm, Yb	Lu, Sc		
Lu	Sm, Yb	Pb*		
Pb		Sc†, Sm†, Yb		
Sc		Sm, Yb		
Sm	Yb			
Sr				
U	V			

* Elements NOT correlated with the element in question for the untransformed data.

Confidence limits at n = 13

99 % = ± 0,7
95 % = ± 0,56

CONFIDENTIAL

TABLE 34: VARIMAX MATRIX OF THIRTEEN SAMPLES OF THE EPIGENETIC FRACTION OF THE CALCRETES FROM THE LANGER HEINRICH

VARIMAX MATRIX ACCOUNTING FOR 94,1 PER CENT OF TOTAL PROBLEM VARIANCE

NO TRANSFORMATION

	FACTOR	1	2	3	4	5	6
SUM OF SQUARES		8.606	3.116	1.928	2.368	1.472	2.268
0.975	SiO_2	0.359	0.151	0.014	0.226	-0.099	-0.873
0.983	Al	0.951	-0.053	-0.160	-0.197	0.088	0.071
0.973	Fe	0.881	0.122	-0.031	-0.030	0.380	-0.191
0.892	MgO	0.009	0.271	-0.895	-0.003	-0.049	0.120
0.895	CaO	-0.801	0.127	0.418	-0.113	0.068	0.212
0.989	Na_2O	0.151	-0.265	-0.816	-0.412	0.077	-0.232
0.982	K_2O	0.888	-0.203	-0.216	-0.253	-0.195	0.058
0.982	Ba	0.400	0.061	-0.129	-0.861	0.083	0.231
0.978	Ce	0.878	0.039	0.001	-0.302	0.201	-0.271
0.939	Co	0.553	0.071	-0.104	-0.697	0.336	-0.132
0.973	Dy	0.428	-0.710	0.048	-0.141	0.172	-0.483
0.978	Eu	0.855	-0.236	-0.137	-0.271	-0.014	-0.313
0.920	La	0.846	0.137	0.068	-0.274	0.147	-0.291
0.714	Lu	0.707	-0.241	0.139	-0.259	0.012	-0.264
0.899	Pb	0.356	-0.457	-0.317	-0.593	-0.330	-0.051
0.936	Sc	0.623	-0.062	-0.156	-0.133	-0.260	-0.659
0.982	Sm	0.927	-0.133	0.100	-0.233	0.068	-0.189
0.925	Sr	0.168	-0.081	0.006	-0.098	0.929	0.132
0.963	U	-0.040	-0.971	0.060	0.089	-0.021	0.079
0.965	V	0.099	-0.973	0.016	-0.051	0.036	0.068
0.916	Yb	0.750	-0.320	-0.013	-0.181	0.034	-0.466

CONFIDENTIAL

CONFIDENTIAL

Opposite signs indicate opposing covariances between the variables, e.g. alumine and calcium oxide.

Factor 1: Lithification

Factor 1 has the highest variability explained and therefore is statistically the most significant. Positive loadings are given for alumina, iron oxide, potassium oxide, cerium, europium, lanthanum, lutetium, samarium, ytterbium and scandium. On the negative side calcium oxide is found. Essentially this factor is one where the rare earths, alumina and iron oxide are leached and then co-precipitated, for they occur as a coherent group. Opposing this process was the epigenetic introduction of calcium which precipitated as calcite, thereby cementing the breccia. The overall abundance of calcite is so great that it acts as a diluting medium for the first-mentioned groups.

Owing to the limited solubility of the rare earths, scandium, aluminium and iron in weekly alkaline environments (Table 19), they are precipitated as hydroxides and are adsorbed onto clays (Roaldset, 1967). This last point is particularly important and will be dealt with further when the geochemistry of the individual and groups of elements is discussed.

Factor 2: Carnotite Precipitation

Both uranium and vanadium are rated with the highest negative loadings, followed by a slightly lower loading on dysprosium. Uranium and vanadium behave coherently with the

precipitation of carnotite from solution. Interpretation of the relation with dysprosium is more subtle. Factor loadings on dysprosium are distributed between factors 1, 2 and 6. Although in the first and last cases the loadings are fairly low, attention must nevertheless be focused on them. The effect produced is referred to here as the dysprosium anomaly.

Dysprosium would be expected to behave in a coherent manner with the other rare earths and be associated with factor 1. However, as it forms a coherent variable with uranium and vanadium, this implies that the precipitation of carnotite may be related to the presence of clays or hydrated oxides of iron or aluminium which formed the nucleating seed upon which the uranyl ion became attached.

Factor 3: Ion Exchange Properities and Formation of Clays

Clays associated with the calcrete are of the montmorillonite-smectite varieties. High factor loadings on both sodium and magnesium suggest an ion exchange mechanism: possibly two Na^+ ions are exchanged for each Mg^{2+} ion within the structural lattice of the authigenic clays.

Another important mechanism that can also account for this relationship is the formation of montmorillonite *in situ* by the reaction of magnesium ions on plagioclase feldspars.

Factor 4: Substitution in Calcite Lattice

Barium, cobalt and lead are capable of substituting in the calcite lattice. High factor loadings on these elements suggest that this has happened in this case.

Factor 5: Substitution in Calcite Lattice

This factor has the lowest variance, signifying its lack of importance. Strontium substitutes for calcium in the calcite lattice. It seems likely that strontium behaves differently from barium, cobalt and lead during substitution, and therefore has its own factor.

Factor 6: Silica

Silica and scandium have high factor loadings. Scandium also occurs in factor 1 and therefore factor 6 suggests that a certain amount of silica was released from biotite in the detrital material or from the clays during postdiagenetic leaching.

Factor analysis of the raw data provided pointers concerning the nature and mechanisms which were involved during the formation of the calcrete. The calcite and carnotite were precipitated as independent phases within the pore spaces of the detrital material from mineralized sub= surface waters. Simultaneously iron, aluminium and the rare earths were leached from the detrital material and co-precipi= tated as hydroxides on montmorillonite. The influence of clay on the precipitation of carnotite was noted.

Following the orthogonal varimax matrix, the vectors were rotated, from which the promax matrix was computed for up to five degrees of obliquity (KMIN = 5). This process simplifies the interpretation of the problem and allows correlations between the factors to be obtained, which was not possible from the varimax method.

TABLE 35: PROMAX MATRIX OF THIRTEEN SAMPLES OF THE EPIGENETIC FRACTION OF THE CALCRETES FROM THE LANGER HEINRICH

PROMAX OBLIQUE REFERENCE STRUCTURE MATRIX KMIN = 5

NO TRANSFORMATION

FACTOR	1	2	3	4	5	6
SiO_2	0.032	0.261	-0.008	0.300	0.113	-0.837
Al	0.728	-0.023	-0.064	-0.034	0.046	0.227
Fe	0.612	0.122	-0.029	0.112	0.319	-0.059
MgO	0.028	0.235	-0.870	0.055	0.047	0.061
CaO	-0.590	0.100	0.348	-0.293	0.033	0.098
Na_2O	-0.185	-0.136	-0.747	-0.246	0.153	-0.167
K_2O	0.663	-0.122	-0.067	-0.085	-0.215	0.217
Ba	0.113	0.200	0.001	-0.785	-0.003	0.339
Ce	0.492	0.137	0.064	-0.151	0.121	-0.113
Co	0.126	0.212	-0.037	-0.577	0.246	0.001
Dy	0.048	-0.575	0.078	0.033	0.184	-0.313
Eu	00.461	-0.103	-0.033	-0.084	-0.047	-0.139
La	0.482	0.233	0.128	-0.147	0.055	-0.149
Lu	0.375	-0.120	0.221	-0.124	-0.048	-0.104
Pb	0.047	-0.261	-0.142	-0.453	-0.318	0.079
Sc	0.204	0.117	-0.068	0.010	-0.276	-0.548
Sm	0.598	-0.042	0.187	-0.078	-0.005	-0.012
Sr	0.075	-0.177	-0.110	-0.034	0.901	0.196
U	-0.023	-0.957	0.088	0.179	0.060	0.176
V	0.031	-0.931	0.063	0.070	0.103	0.197
Yb	0.340	-0.181	0.058	-0.004	0.005	-0.296

TABLE 36: CORRELATION MATRIX OF FACTORS IN THE PROMAX MATRIX OF TABLE 35

CORRELATIONS BETWEEN PROMAX PRIMARY FACTORS KMIN = 5

NO TRANSFORMATION

FACTOR	1	2	3	4	5	6
1	1.000	-0.324	-0.205	-0.645	0.155	-0.661
2	-0.324	1.000	0.153	0.450	0.124	0.431
3	-0.205	0.153	1.000	0.276	0.250	0.099
4	-0.645	0.460	0.276	1.000	-0.114	0.530
5	0.155	0.124	0.250	-0.114	1.000	-0.101
6	-0.661	0.431	0.099	0.530	-0.101	1.000

Table 35 gives the promax matrix and Table 36 the correlation matrix between the promax factors. Essentially, the six factors remain as they were for the varimax but with successive rotations some of the weaker factor loadings are eliminated, thereby accentuating the stronger ones. However, with too many rotations the loadings on the variables become insignificant which results in much stronger correlations between the factors. This situation then becomes meaningless. An optimum number of rotations must be selected so that the interpretation remains relevant. At KMIN 5, loadings on all the rare earths with the exception of samarium are low. Here again is a case where interpretation must allow for synonyms, and samarium is regarded as being representative of the other rare earths.

Factors 1 and 4 are negatively correlated (Table 36) which suggests barium, cobalt and lead substitute in the calcite lattice. Factors 1 and 6 are positively correlated which indicates that silica, alumina, iron oxide, etc. have a common source.

14.4 Geochemistry of Individual Elements or Groups of Elements

Factor analysis has broadly established the nature of the mechanisms involved during the lithification of the breccia-conglomerate to produce a hard, indurated calcrete. Limited detail was provided concerning the actual mechanisms involved in the six factors and the geochemical parameters controlling the distribution of the elements. The geochemistry of individual and groups of elements is discussed with the

possible implications for the development of calcrete duricrust deposits.

14.4.1 Iron

Iron is distributed throughout the Gemsbok and Langer Heinrich calcrete formations. The colour of the pigmentation varies from yellowish-brown to red, implying that there are different degrees of oxidation of the iron.

The source of the iron lies in the alteration and decomposition of iron-bearing minerals such as biotite and hornblende from the Tinkas Formation and Bloedkoppie Granite. Haloes of red staining surrounding biotite crystals have been clearly observed in the Bloedkoppie Granite. Similar phenomena have been reported by Walker (1967) from the deserts of Colorado, where the halo is composed of minute euhedral grains of hematite. Complete alteration of these femic minerals results in the formation of authigenic montmorillonite, iron oxides and calcite. The release of iron is controlled by the Eh and pH of the water acting upon the mineral.

Depending on the oxidation potential, either soluble iron (II) is released to solution or *in situ* precipitation of iron (III) in the hydroxide form takes place. Those sediments with a greater proportion of iron (II) will be drab as opposed to the red colouration of the oxidized iron (III). There are three main forms of iron oxide pigment present in red beds (*ibid.*, p. 360):

(a) yellowish to reddish-yellow, amorphous ferric hydrate,

(b) amorphous red ferric hydrate,

(c) crystallized red hematite.

The conversion from the amorphous to the crystalline states is a time-dependent factor.

Iron is closely associated with the interstitial clays. Walker (ibid.) notes the existence of an iron-rich montmorillonite in red beds. Similarly Spencer et al (1969, p. 991) concluded that the ferric hydroxides occur in the finer fraction of some marine sediments.

Ferric hydroxide precipitates at a pH above 3,0 and acts as a good scavenger for the transition metals and the rare earths.

The iron contents of the acid-soluble fraction of the samples have a maximum value of 6,6 per cent and a low value of 1,1 per cent (Table 30). Sample HJ2-3 was taken at a depth of 1,5 m which indicates that very strong oxidizing conditions occur near the surface, thereby precipitating the iron in the red hydroxide form.

14.4.2 Alumina and silica

The main source of these species in the calcrete is the decomposition of hydrolysis of the feldspars, chiefly microcline and albite. Thermodynamics predicts (Helgeson et al, 1969, p. 463) that the following reaction will take place during the hydrolysis of coexisting albite and microcline.

$$KAlSi_3O_8 + NaAlSi_3O_8 + 16H_2O \rightarrow 2Al(OH)_4^- + K^+ + Na^+ + 6H_4SiO_4 \quad (14.1)$$

This equation therefore accounts for tetrahydroxo-aluminate (III) and silicic acid which can be precipitated from subsurface waters in moderately alkaline conditions. Sodium and potassium ions are likewise liberated in this reaction.

Amorphous silica in the form of silicic acid, formed in equation (14.1), has a solubility of 100 to 140 ppm at 25 °C in water (Morey et al, 1964, p. 1995). Due to this low solubility, the silica released is quickly precipitated and will establish the following equilibrium conditions, (ibid., p. 2001):

$$SiO_{2(\text{amorphous solid})} + nH_2O \rightleftharpoons SiO_{2(aq)} \qquad (14.2)$$

Mackenzie and Garrels (1965, p. 57) reported that some montmorillonites can release up to 21 ppm silica to seawater after six months, with the residue consisting of hydrated alumina. This indicates a preferential removal of silica with respect to alumina. Although the subsurface water at the Langer Heinrich is not as saline as seawater, a reaction would nevertheless occur at possibly a reduced rate. Fig. 57 is a plot of Al_2O_3 versus Fe_2O_3 and shows a good correlation (correlation coefficient = 0,87) between both oxides. It is suggested therefore that through the decomposition of minerals such as the feldspars and the iron-rich montmorillonite as described by Walker (1967), silicic acid is dissolved, leaving a residue of hydrated iron (III) ions and tetrahydroxo-aluminate (III). Ions of this type are capable of co-precipitating metals, viz. the rare earths in alkaline solutions.

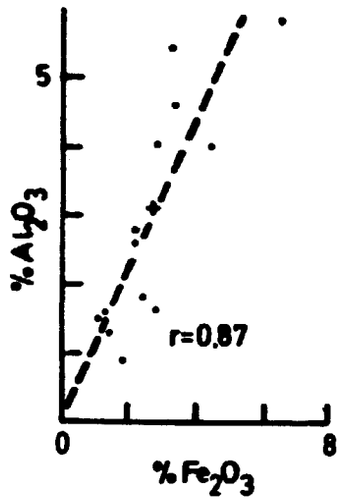


Fig. 57: Variation diagram of Al_2O_3 plotted against Fe_2O_3 (correlation coefficient r = 0,87) for the epigenetic fraction of the calcretes. (+ = mean).

14.4.3 Potassium, sodium and magnesium

These elements are generally involved in reactions and ion exchange processes in the clays of the calcrete. Factor analysis demonstrated this clearly and is corroborated by Graf (1960).

High correlation coefficients of potassium with the alumina, iron (III) oxide and rare earths are observed in Table 32(a). Potassium is probably involved largely with the ion exchange properties of the montmorillonite.

Consideration must now be given to the origin of montmorillonite clay. Montmorillonite is an authigenic mineral, having largely been formed *in situ* by the reaction of magnesium with albitic feldspar. The flow-rate of sub-surface water is an important factor (Berner, 1971, p. 173). Under almost stagnant conditions, which would be expected

in the subsurface water at the Langer Heinrich, a slow reaction between hydrated alumina, silica and certain cations takes place. The reaction can be considered in the following manner:

$$Mg^{2+} + 3NaAlSi_3O_8 + 4H_2O \rightarrow 2Na_{0,5}\,Al_{1,5}\,Mg_{0,5}\,Si_4O_{10}(OH)_2 + 2Na^+ + H_4SiO_4 \qquad (14.3)$$

The reactants, magnesium ions, albite and water combine to form the montmorillonite, releasing sodium ions and silicic acid to the aqueous phases.

The question why there is no kaolinite present at the Langer Heinrich may arise. According to Berner (ibid.) the formation of kaolinite is related to high flow-rates of sub= surface water in regions of greater rainfall. In humid, tropical climates the slow reaction given above cannot take place due to the removal of all reaction cations in solution, leaving a residue of hydrated alumina, eventually forming bauxites. Bicarbonate ions in solution are one of the chief agents in weathering and Garrels (in Berner, 1971, p. 175) has shown that montmorillonite can only form where the HCO_3^- content approaches 100 ppm.

Magnesium is freely interchangeable with calcium in calcite, and should the substitution proceed, the mineral dolomite will form. Table 30 shows that the magnesium oxide content is generally low, but one sample (AD1-8) has 10,8 per cent. Dolomite obviously has not formed, but in the latter case it might be referred to as a magnesian calcite. In

Table 32(a) MgO has an insignificant correlation coefficient with CaO. The ratio MgO/CaO versus percentage MgO gives a parabolic curve (Fig. 58).

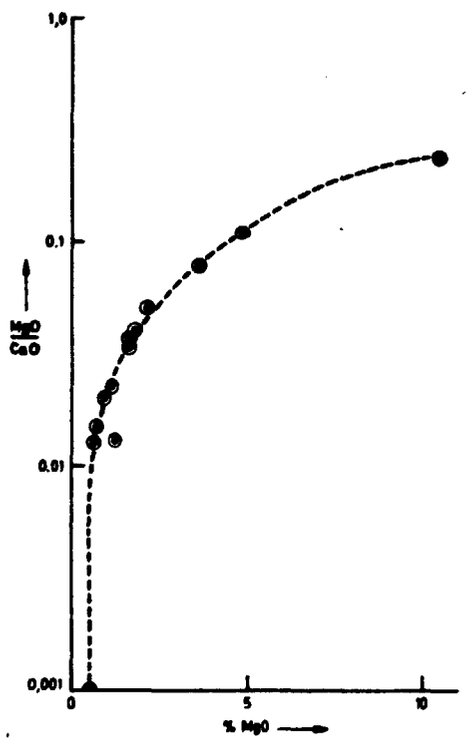


Fig. 58: The relationship between magnesium and calcium in epigenetic calcite as demonstrated by plotting the ratio MgO/CaO against MgO.

This indicates that there is a relationship of some sort between magnesium and calcium, but there has not been a systematic linear substitution of these elements with respect to each other. In other words magnesium in calcite also occurs in another form, e.g. clay. Wieder and Yaalon (1974, p. 118) found that an increase in calcium (i.e. calcite) was accompanied by a decrease in aluminium, magnesium and ion (i.e. clay). Electron probe studies by them revealed that these three elements were displaced to the fringes of crystallizing calcite. This situation would alter the

distribution of magnesium in the calcite, creating the relationship illustrated in Fig. 58.

14.4.4 The rare-earth elements

The distribution of the rare earths in the epigenetic calcite is governed by the scavenging of aluminium and iron (III) hydroxides which were adsorbed on montmorillonite, as demonstrated by the relationships in factor 1. Similar conclusions were reached by Roaldset (1973) who found that the rare earths were adsorbed under neutral and moderately alkaline conditions onto clay minerals, but at a lower pH desorption took place.

The relative abundances of the rare earths in calcretes of the Langer Heinrich, and sediments from other parts of the world, plotted as percentages of the total rare-earth concentrations, are shown in Fig. 59. Clearly the percentage abundances in both figures are very similar. The lighter rare earths, that is, lanthanum and cerium, are by far the most abundant elements and collectively comprise between 70 to 90 per cent of the total content. Cerium is the most abundant element whereas europium and lutetium are the least abundant.

Normalizing the rare-earth abundances to a composite of twenty chondritic meteorites, the relative distribution of the elements can be studied. Fig. 60 is a plot of some of the epigenetic calcite samples and limestones from the Russian Platform. The most striking feature is the uni= formity of distribution of the rare-earth patterns.

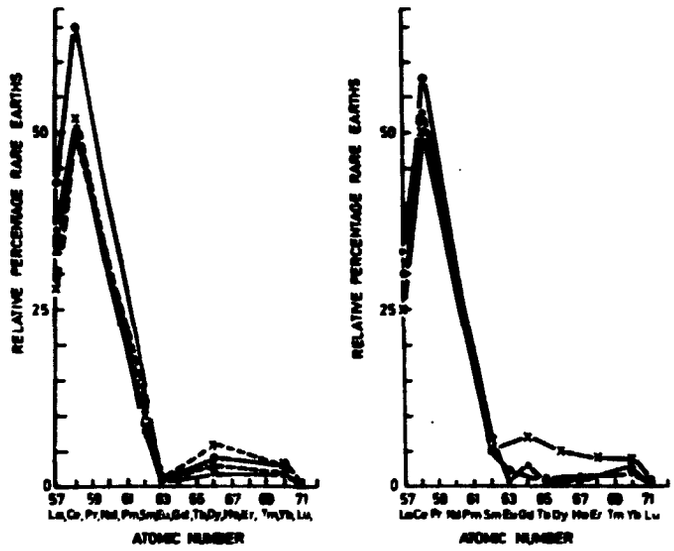


Fig. 59: Relative percentage rare-earth concentrations in
(a) Epigenetic calcite, Langer Heinrich.
(· = HJ2-3, o = HJ2-5, x = HJ2-13,
Δ = C5-15).
(b) Sediments from other parts of the world.
· = Belders Formation marble, USA;
x = average, 11 025 limestones from the Russian Platform;
o = composite 40 North American shales.
(Herrmann, 1970).

Fractionation between the lighter and heavier elements has taken place. The limestones from the Russian Platform have a rare-earth pattern very similar to those of the calcites from the Langer Heinrich. A more diagnostic approach in studying the fractionation patterns of the rare earths is to divide the concentrations of the light rare-earth by the heavy rare-earth concentrations. The function used here was (La + Ce)/(Yb + Lu) which was a modification of the function used by Balashow et al (1964, p. 951). The relationships between this ratio and total rare-earth content

and between this ratio and percentage Fe_2O_3 are shown in Fig. 61, where the overall trend appears to be positive and linear.

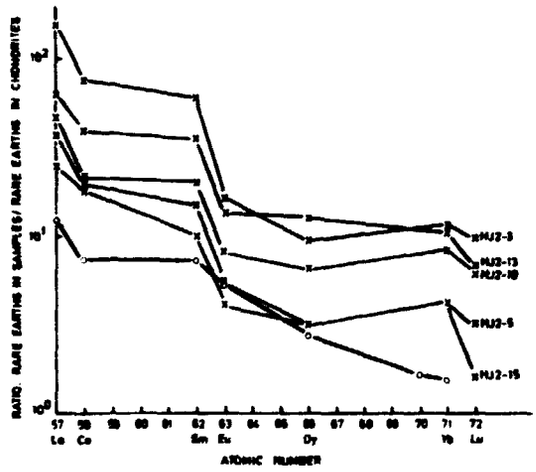
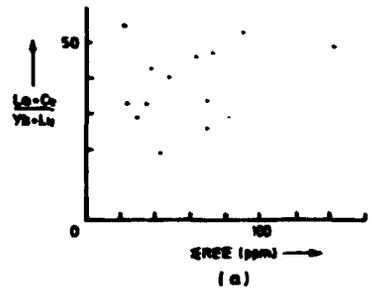


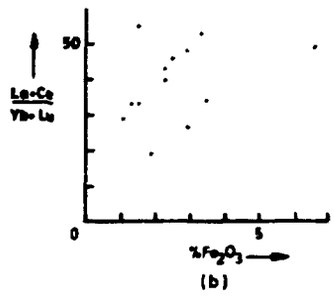
Fig. 60: Distribution patterns of rare earths, normalized to the abundances in 20 chondritic meteorites.
x = epigenetic calcite, Langer Heinrich area.
o = average, 11 025 limestones from the Russian Platform.
(Herrmann, 1970).

An increase in total rare-earth and iron contents is accompanied by an increase in the fractionation between the light and heavy rare earths. The implication was that the heavier rare earths were preferentially removed in solution to an amount of approximately 10 per cent.

Ronov et al (1967, p. 2) considered the possible mechanisms that cause the fractionation of the rare earths in nature. Basicity of the hydroxides decreases with increasing atomic number as would be expected because the ionic radii decreases due to the lanthanide contraction. This enables hydrolysis to take place at differing values of pH, thereby assisting the separation of the species.



61(a)



61(b)

Fig. 61: Plots of the fractionation function La + Ce/Yb + Lu against
(a) sum of the rare earths;
(b) percentage iron oxide.

A change in the oxidation state is a second causative factor. Normally rare earths are characteristically trivalent. Eu^{2+} and Ce^{4+} can occur under reducing and oxidizing conditions respectively. The desert environment of the Langer Heinrich is oxidizing, which will discount the occurrence of Eu^{2+}. Cerium (IV) behaves in a similar way to the heavier rare earths as its ionic radii decreases, thereby acquiring a stronger tendency to hydrolize and fractionate.

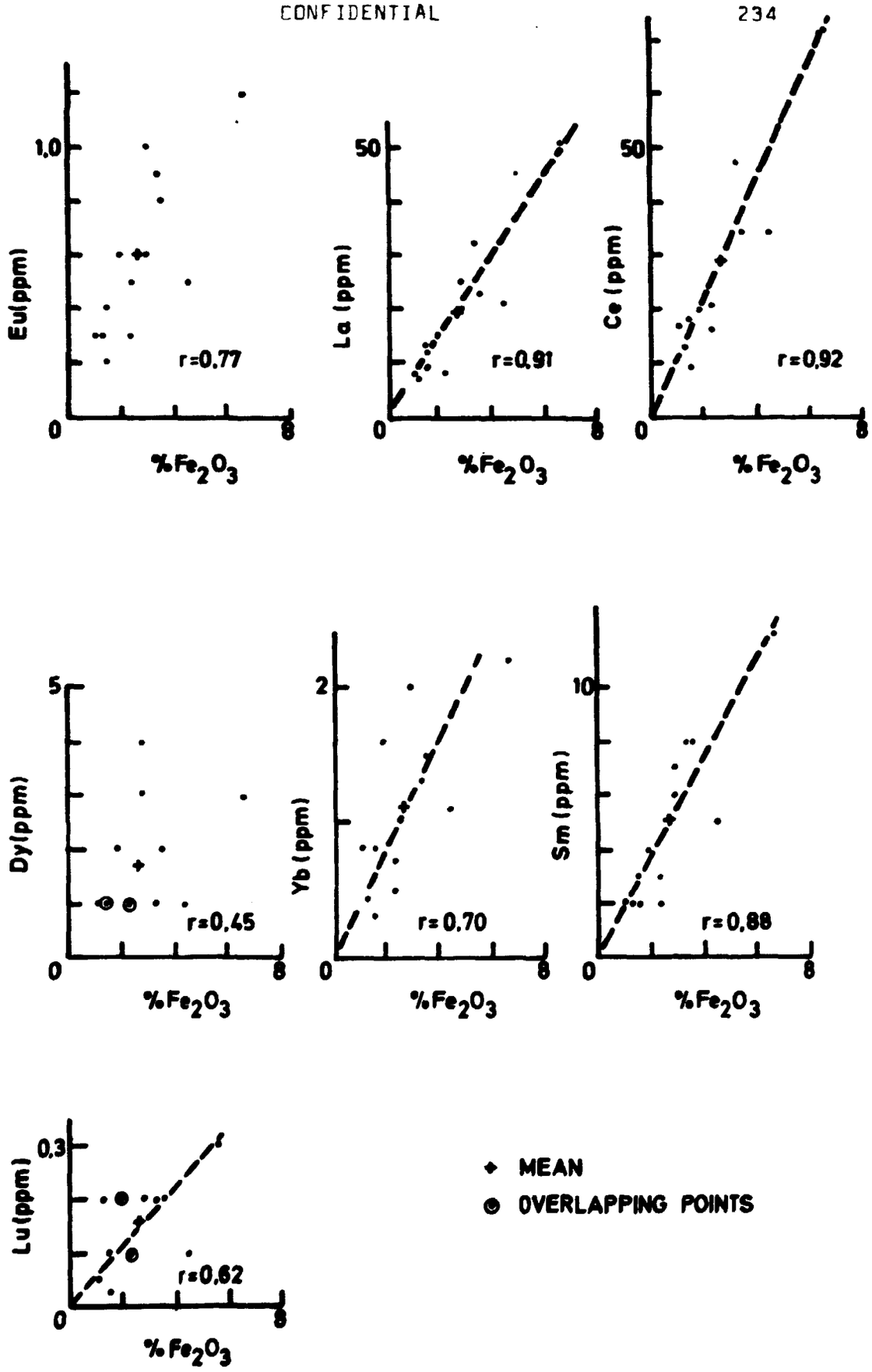


Fig. 62: Variation diagrams of rare-earth elements plotted against percentage iron oxide.

Correlation coefficients between the rare earths and Fe_2O_3 (Fig. 62) and between rare earths and Al_2O_3 (Table 32(a)) are high, except for dysprosium. It is very clear that co-precipitation with the hydrolyzate elements has taken place. The low correlation coefficient of dysprosium with respect to Fe_2O_3 and the other rare earths (Figs. 62 and 63, and Table 32(a)) and its significant loading in factor 2 (Table 34) indicates that it behaved in an anomalous manner.

A plot of the correlation coefficients (Table 32(a)) against the rare-earth atomic numbers in Fig. 63 shows a very distinct dysprosium anomaly. In all the diagrams dysprosium seems to have a closer coherence to the heavier rare earths. No explanation can be given to account for this feature and it has not been recorded in the literature. The close relationship between uranium and vanadium with dysprosium in factor 2 (Table 34) is significant, for it suggests that the uranium mineralization may be linked with the presence of montmorillonite and the precipitated hydroxides of iron and aluminium.

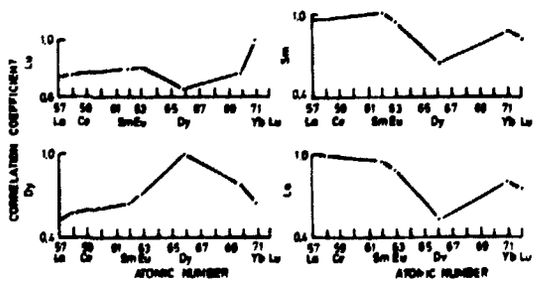


Fig. 63: Plots of the correlation coefficients of lutetium, dysprosium, samarium and lanthanum against the atomic number.

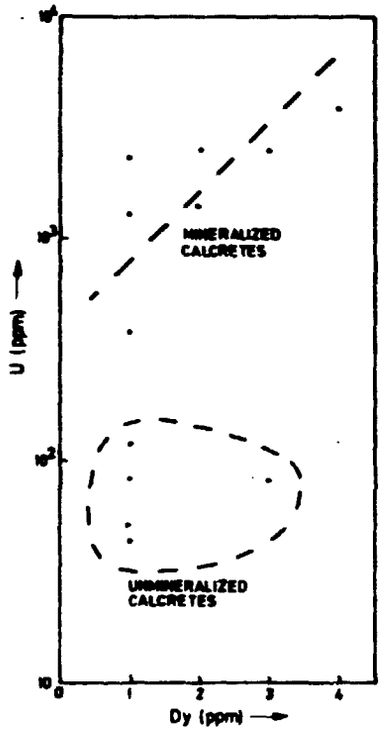
Figs. 64(a) and (b) are plots of uranium and vanadium respectively against dysprosium. Very distinct trends are observed. In both cases almost linear relationships were found in the carnotite-bearing calcretes as opposed to the unmineralized calcretes which plot much lower on the scale.

The distribution and fractionation patterns of the rare earths in the calcretes provide pointers to the chemical processes that resulted in their formation. Obviously the formation of calcrete was not purely the pre= cipitation of calcite from solution, but was accompanied by a host of syn- and post-lithification processes.

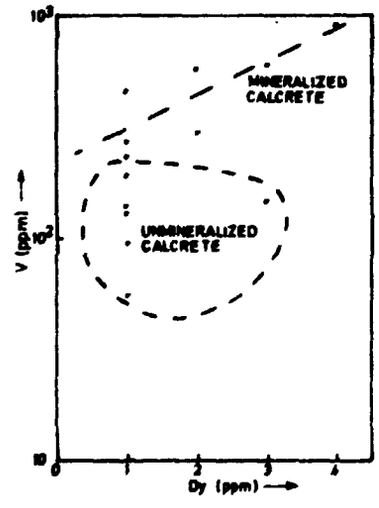
14.4.5 Vanadium and uranium

The ore deposit of the Langer Heinrich is typified by the presence of vanadium in the highest possible oxidation state, (+V). In igneous and metamorphic rocks, the latter of which includes the schists and granofelses of the Tinkas Formation, the (+III) oxidation state of vanadium is the most predominant. The source of the vandium is con= sidered to be the Tinkas Formation because it contains a high concentration of vanadium (Table 37). Vanadium concentrations in the Bloedkoppie Granite are below the 5 ppm detection limit of neutron activation analysis and therefore cannot be regarded as a significant source.

Carnotite, with the formula $K_2(UO_2)(VO_4)_2.2H_2O$, has a U/V ratio of 4,67. The U/V ratios (Table 30) have a fairly wide scatter but can be divided into two groups, the mineralized and unmineralized calcretes respectively.



64(a)



64(b)

Fig. 64: (a) Variation diagram of uranium plotted against dysprosium for both mineralized and unmineralized calcretes.
(b) Variation diagram of vanadium plotted against dysprosium for both mineralized and unmineralized calcretes.

TABLE 37: VANADIUM CONCENTRATION IN THE TINKAS FORMATION

Sample No.	V (ppm)
LH 21	128
LH 40	70
LH 41	44
LH 42	100
DJP 98	115
DJP 100	96

The former has values similar to the theoretical, whereas in the latter the ratio is much lower, indicating a relative enrichment of vanadium. A plot of uranium against vanadium is given in Fig. 65, where both groups are seen to define their own fields. The mineralized calcretes display a good correlation between uranium and vanadium, whereas unmineralized calcretes have variable ratios.

14.4.6 Geochemical mobility of the elements

Epigenetic deposits such as those found at the Langer Heinrich resulted from the supergene migration and precipitation of elements from the subsurface waters. Oxidizing conditions and a moderately alkaline environment are prerequisites which are typical of the climatic conditions in the Namib Desert. In order to gain a fuller understanding of the mechanisms involved it is necessary to devote some time to the geochemical mobility of elements during

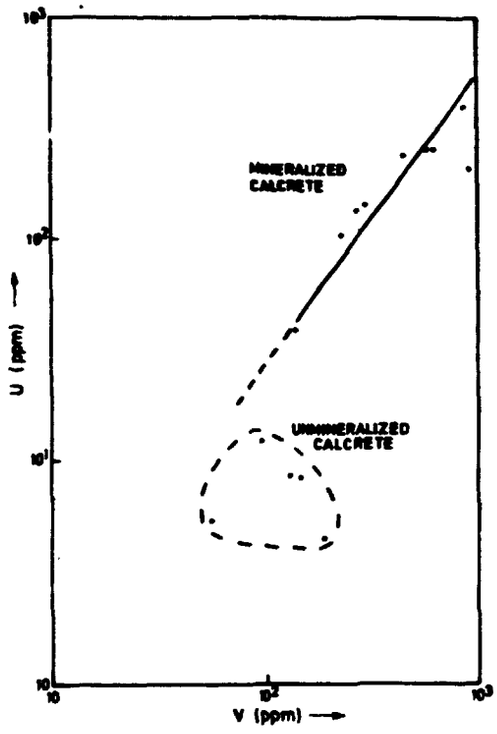


Fig. 65: Variation diagrams of uranium plotted against vanadium for both mineralized and unmineralized calcretes.

epigenetic processes in general. Dall'Aglio (1972) considered this subject in some detail and applied the fundamental concepts to studies of epigenetic uranium mineralization in Italy.

In relation to their chemical characteristics, elements will respond according to the prevailing conditions and therefore the geochemical balance in nature is governed by their geochemical behaviour. Broadly, the geochemical balance is a function of the distribution in igneous rocks, sediments and the hydrosphere. Accordingly the elements can be grouped into those which have low, medium and high

mobilities.

Fig. 66 is a measure of the geochemical mobility of the elements where the concentration within the rocks was normalized to the abundances in the hydrosphere. It was noted that when assessing the mobility of uranium and vanadium under desert conditions, they become highly mobile by oxidation and the formation of complexes, and therefore should be classed with group III. The reason for this is that the mobility of ionic complexes under supergene condi= tions is independent of the geochemistry of the element existing by itself.

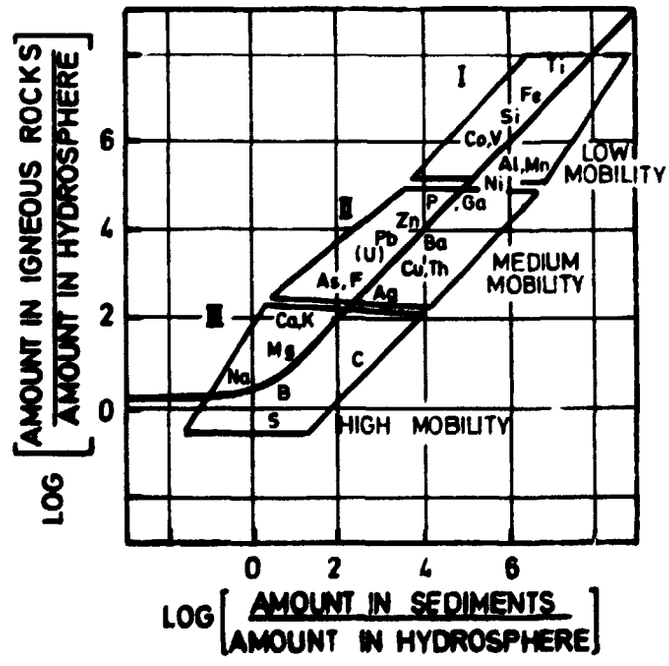


Fig. 66: Geochemical mobility of the elements in the supergene environment. (After Dall' Aglio, 1972, p. 123).

The mobility of uranium is restricted by two conditions:

(a) The manner in which it is present in the source rocks, e.g. if it is accommodated in a zircon crystal, which is resistant to weathering, there will be a minimal release of uranium. Alternatively if it is uraninite or molecules dispersed on crystal surfaces it will be more susceptible to solution.

(b) The epigenetic precipitation of insoluble minerals, in this case, carnotite.

Ronov et al (1967, p. 7) attempted to quantify these concepts in terms of the removal index, ρ.

$$\rho = \frac{Cp - Cs}{Cs}$$

Cp = concentration of an element in the parent rock, viz. Bloedkoppie Granite (Table 13). Although more than one rock type is represented at the Langer Heinrich, the Bloedkoppie Granite was selected for the parent rock because its major element composition lies between that of the rocks of the Etusis and Tinkas Formations (Table 14).

Cs = concentration of the same element in the sediment, viz. the epigenetic calcite (Table 30).

The sign of the removal index, ρ, may either be positive or negative. If it is positive the element is depleted in the calcrete, but when it is negative it is enriched in the calcrete. Graphically this is represented in Figs. 67 and 68. In both cases calcium, uranium, magnesium

and cobalt have accumulated in the calcrete and all the other elements are relatively depleted with respect to the Bloed= koppie Granite. Sample HJ2-5 (Fig. 67) has a close associa= tion between iron, scandium and the rare earths with the exception of cerium, which is depleted to a greater extent. This was not found for sample HJ2-15 (Fig. 68) as cerium occurs well within the rare-earth clustering. Similarly there is a discrepancy in the behaviour of lutetium, where the reverse is found in the respective samples.

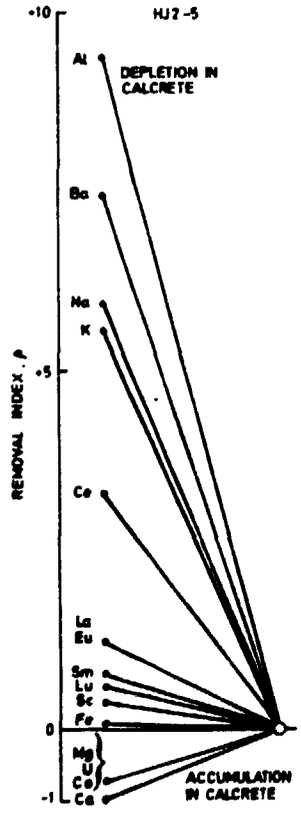


Fig. 67: The geochemical mobility of the elements in the epigenetic calcite of sample HJ2-5, with respect to the Bloedkoppie Granite. Represented in terms of the removal index.

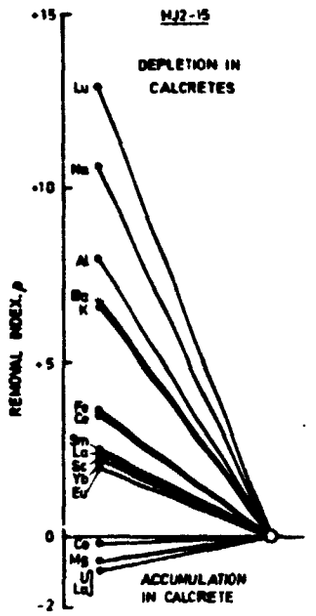


Fig. 68: The geochemical mobility of the elements in the epigenetic calcite of sample HJ2-15, with respect to the Bloedkoppie Granite. Represented in terms of the removal index.

The discrepant behaviour of cerium and lutetium in both samples can be accounted for by their depth of burial, for they were obtained from 2,5 and 7,5 m respectively (Table 27). Near the surface powerful oxidizing conditions prevailed which were sufficient to partially oxidize cerium from the (+III) to the (+IV) state. Lower down in the succession these conditions were not as severe. The stability of the lutetium inorganic complexes were greater lower down, enabling a greater fractionation to have taken place.

The elements sodium, barium and potassium were very mobile and would be expected to be relatively depleted in the calcretes.

14.5 Geochemistry and Origin of Calcrete

Uranium deposits and especially carnotite mineralization in desert, duricrust-type host rocks cannot really be regarded as unique for it was not the calcareous cement which was the main factor in their development, but the physico-chemical relationships that were common to the precipitation of both calcite and carnotite.

An assessment of the origin of the ore-body of the Langer Heinrich requires that all the components comprising the host rock be accounted for in the model. Sediments provided the passageways through which the subsurface waters migrated and also the precipitation sites for the calcite and carnotite. The mechanism for the precipitation of the calcite is by analogy extended to the formation of the carnotite.

Netterberg (1969, p. 237, 1971, p. 9) described the origin of calcrete as being due to the process of soil suction by which calcium carbonate is precipitated in a porous sediment above the water-table. Water in the pore spaces of a sediment exerts a force called the pore water pressure. Line A, Fig. 69, gives the distribution of this pressure above and below the water-table. Below the water-table the pores are saturated with water and the pore water pressure is greater than one atmosphere due to the hydrostatic head. Above the water-table the pore water pressure decreases to become less than one atmosphere and eventually zero due to capilliary action and surface tension forces, that is, the degree of pore saturation decreases upwards. The slope of line A is the suction gradient, pF, which Netterberg

defines as the negative log of the pore water pressure.

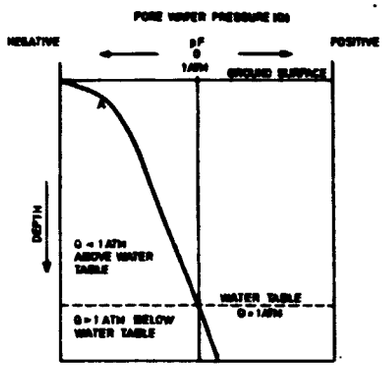


Fig. 69: Pore water pressure distribution in a sediment. (After Netterberg, 1971, p. 9).

At constant temperature, a decrease in the pore water pressure, that is, upward movement of water, will correspond to a decrease in the P_{CO_2} in equilibrium with the water, causing the precipitation of calcium carbonate. Therefore line A is a function of the solubility of calcium carbonate. Fig. 8 shows that the ore deposit has a layered structure. On a more localized scale the carnotite has precipitated in the form of concretions. Based on these facts the principles around which this discussion will centre is that the segrega= tion of carnotite resulted from a transport process, mainly upward diffusion caused by soil suction. Upward diffusion of elements in ground-water is brought about by the change in composition of the soluble components with depth. A restriction is placed on the volume of the sediment, that is, a small volume is initially required because large lateral variations in water composition are known to occur (Tables 15-18). Assume that the chemical composition of the water remains laterally constant, especially in uranium, vanadium and carbon dioxide at a specific depth. Based on this system

the vertical concentration gradients are dominant and a one-dimensional model may therefore apply. A mathematical treatment of such a system has been presented by Berner (1971, p. 25).

Vertical diffusion is a response to a chemical gradient which in this case is due to a change in the P_{CO_2}. During the formation of calcrete a decrease in P_{CO_2} will cause calcite to precipitate. When precipitation commences, concentration gradients develop and the cycle repeats itself. By analogy the precipitation of carnotite will follow the same pattern. If the detrital material is stable and upward diffusion is allowed to continue uninhibited over long periods, monomineralic layers and possibly concretions may develop. Diagramatically this process is represented in Fig. 70.

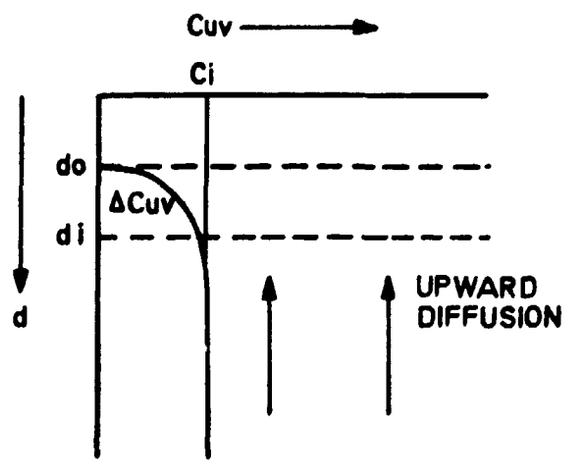


Fig. 70: Diffusion model for the formation of carnotite in layers and concretions at the Langer Heinrich. (After Berner, 1971, p. 103).

C_{uv} = concentration of UDC and vanadium in solution

d = depth of sediment

$d_1 - d_0$ = depth of sediment where the suction gradient is sufficiently high for dissociation of the UDC complex

d_1 = depth where carnotite first appears at the sediment/water interface

d_0 = depth where all uranium and vanadium have been precipitated

C_i = initial concentration of uranium and vanadium in solution

C_{uv} = a generalized curve showing the change in C_{uv} with depth.

The system will operate in the following way. Below a depth of d_1 the one-dimensional system has an initial concentration of uranium, vanadium and carbon dioxide in solution, C_i. Upward diffusion of the ions continues until the depth d_1 is reached where the process of soil suction becomes operative. The uranyl dicarbonate complex will disproportionate according to equation (13.8) and carnotite will precipitate by the reaction in equation (13.10). With an increasing suction gradient and decreasing depth, the concentration of the elements in solution will follow the idealized path C_{uv} until the depth d_0 is reached where all the uranium and vanadium will be consumed.

The system described is by no means so simple, as the mineralization is disjointed and occurs as possible concretionary-type accumulations (Fig. 9). Two mechanisms can be invoked to account for these phenomena.

The composition of the subsurface water is variable (Tables 15-18) over relatively short distances in which units of the one-dimensional system are closely stacked together to form a multidimensional model. Soil suction applied to such systems will lead to variations in the amount of carnotite precipitated because the composition of the water varies indiscriminately in a lateral direction. If the activities of the potassium, uranyl and vanadate ions do not reach that required for carnotite to precipitate, the ions will remain in solution. In adjacent portions of the host rocks the conditions could be favourable and carnotite will be precipitated, resulting in disjointing.

The presence of montmorillonite and its association with uranium mineralization was inferred from factors 2 and 3 in Table 30. Fig. 71 shows the variation of the factor scores of factor 3, with the carnotite concentration (plotted as U ppm). The mineralized calcrete has a scatter of points about the plotted line, whereas the unmineralized calcretes do not follow the same relationship. It is therefore postulated that crystallization of carnotite was related to the presence of montmorillonite, causing a concretionary-type of uranium accumulation.

The causative factor for the formation of concretions is the heterogeneous nucleation, after dissociation of UDC by soil suction, of uranyl and vanadate molecules by montmorillonite which act as pre-existing seed crystals.

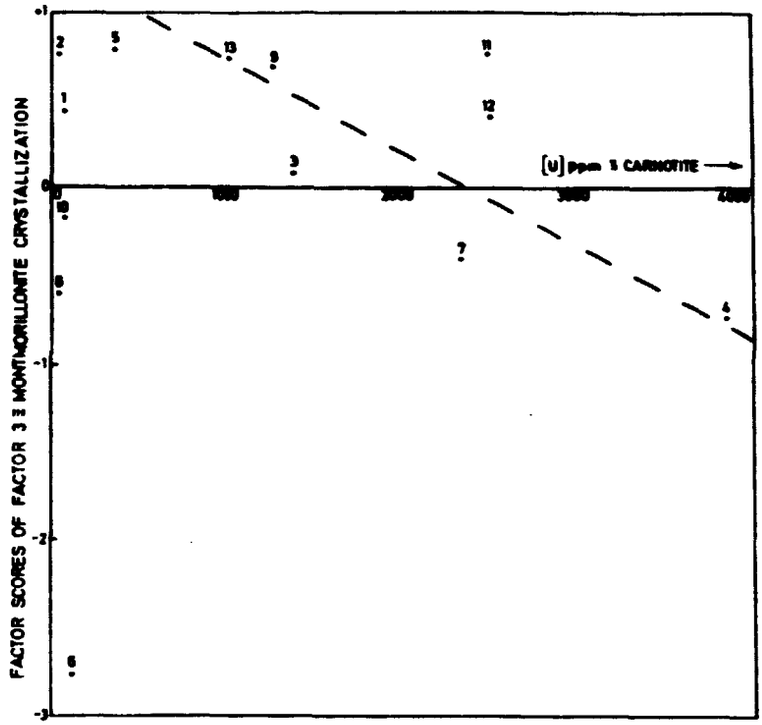


Fig. 71: A plot of the factor scores of factor 3 (Table 34) against carnotite mineralization in terms of the concentration of uranium. (Numbers as in Table 30).

Solids have a certain amount of excess free energy at the surface, which is the main thermodynamic feature of nucleation. Because of the abundance of grain surfaces available on the clay per unit volume of pore solution, heterogeneous nucleation is promoted, and supersaturation (necessary for precipitation) is low, i.e. precipitation from unsaturated solutions is possible (Berner, 1971, p. 95).

Finally there is the question of the differences in age relationship between the initial precipitation of calcite and that of carnotite, which is associated with the rims of the second generation calcite. From the geomorphological point of view the calcrete started to form in the mid-Tertiary.

Carnotite, on the other hand, formed much later.

The origin of the calcium in the calcrete is due to weathering of calcium-bearing minerals. Decomposition of feldspars is fairly rapid and widespread in desert environments. If this was the case for the Langer Heinrich at that period, why was uranium not mobilized and precipitated? The answer to this question must partly remain unsolved, but it can be stated that the activities of uranium, vanadium and potassium only reached their critical values at that time, thereby allowing carnotite to precipitate. Further it is noted that pluvials and interpluvials were characteristic of the Pleistocene (Netterberg, 1969(a)). With the onset of these climatic phases the subsurface water became sufficiently oxidizing and corrosive to leach and transport the uranium from the source rocks to finally precipitate it epigenetically in the calcrete.

14.6 Geochemistry and Origin of Gypcrete

The distribution of the gypcrete is schematically represented in Fig. 2. The main geochemical problem concerning the gypsum is that of its origin.

Martin (1963) proposed that the origin of gypsum was due to the reaction of sulphuric acid, formed from hydrogen sulphide by oxidation, on the calcite in calcrete. The hydrogen sulphide was derived from the gas emanations of the anaerobic basins on the continental shelf. He discounted the possibility of gypsum precipitation from ground-water on the basis that thereaction products would not be continued to

the surface.

It would appear that this interpretation concerning the origin of the gypsum is for the most part unlikely for it is very difficult to conceive that the anaerobic basins would be capable of having produced such large volumes of hydrogen sulphide. A new mechanism is therfore proposed based on sulphate precipitation by onshore fogs. Analyses of seawater and precipitated fog are given in Table 38.

Fog precipitation with the equivalent rainfall in 1958 and the actual mean rainfall at Swakopmund over 35 years is given in Table 39. The interpretation of the results, as calculated from values of both Tables, must be viewed with some caution because of the lapse of the time between the samples in Table 38 and the fog precipitation figures of Table 39. As these are the only figures available, no alternative solution could be found.

TABLE 38: ANALYSES OF SEAWATER AND FOGWATER (COURTESY CSIR)

	Sea= water	Fog 1	Fog 2	Fog 3	Fog 4
pH	7,6	7,3	7,6	7,6	8,1
*Conductivity	43000	13600	1 900	1 240	1 760
+TDS (ppm) (180 °C)	37562	9860	1 290	795	1 175
Na (ppm)	10900	2580	308	213	290
K (ppm)	71	100	11	6	26
SO_4 (ppm)	2683	1158	174	88	221
(NO_3) as N (ppm)	Trace				
(NO_2) as N (ppm)	ND	12,3	7,0	3,4	9,6
SiO_2 (ppm)	2	7,5	7,5	7,5	7,5
F (ppm)	0,9	8,8	1,9	0,4	1,7
Cl (ppm)	19690	4598	502	371	412
ΣCO_3 (ppm)	75	63	32	23	67
Ca (ppm)	118	292	49	36	40
Mg (ppm)	1281	217	35	19	46
NH_3 (ppm)	ND	Trace	Trace	Trace	Trace
PO_4 (ppm)	Trace	-	-	-	-
Sr (ppm)	5	-	-	-	-
B (ppm)	5	-	-	-	-

Seawater: Collected September, 1974, from beach between Walvis Bay and Swakopmund.
Fog 1 : Collected July 1966, Walvis Bay
Fog 2 : Collected 4 September, 1966, Rooibank
Fog 3 : Collected 13 August, 1966, Rooibank
Fog 4 : Collected from Gobabeb, analyzed 13 September 1966.

All analyses done by National Institute of Water Research, Windhoek.

Results of Fog 1 to 4 are by courtesy of the Transvaal Museum.

* Conductivity units, mho.

+ TDS = Total dissolved solids.

TABLE 39: FOG PRECIPITATION, EQUIVALENT RAINFALL IN 1958 AND ACTUAL MEAN RAINFALL AT SWAKOPMUND (NAGEL, 1962, p. 57)

MONTH	FOG PRECIPITATION IN 1958 (LITRES)	EQUIVALENT RAINFALL IN 1958 (mm)	ANNUAL MEAN RAINFALL OVER 35 YEARS (mm)
JANUARY	12,0	1,8	1,9
FEBRUARY	14,0	2,2	2,6
MARCH	29,1	4,5	5,3
APRIL	69,0	10,6	1,9
MAY	167,5	25,7	0,7
JUNE	112,0	17,2	0,2
JULY	156,3	24,1	0,3
AUGUST	143,3	22,0	0,7
SEPTEMBER	52,6	8,1	0,7
OCTOBER	27,0	4,2	0,9
NOVEMBER	32,3	5,0	1,0
DECEMBER	30,7	4,7	1,7
TOTAL/YEAR	845,8	130,1	17,9

Within the confines of the anaerobic basins on the continental shelf, the ocean water and the desert stretching to the Langer Heinrich, sulphur follows a definite cycle (Fig. 72). $(H_2S)_B$ is formed in the diatomaceous muds, which contain the sulphate-reducing desulfovibrio bacteria.

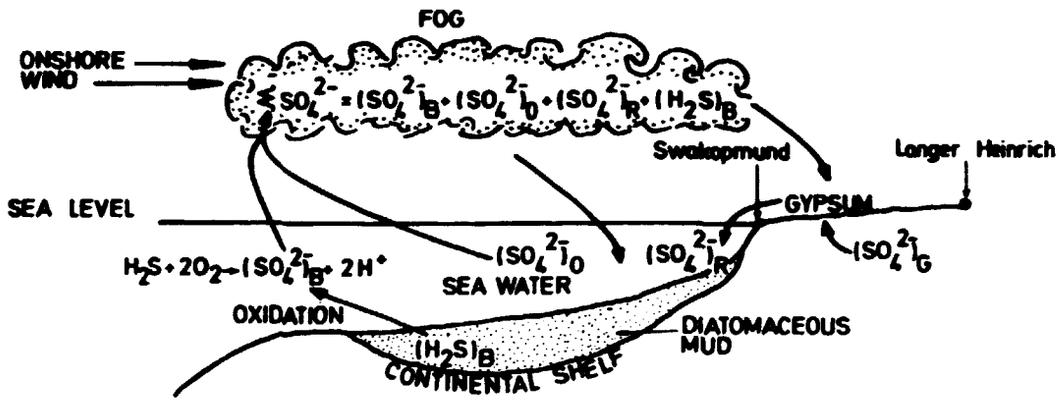


Fig. 72: The sulphur cycle in the diatomaceous sediments of the continental shelf, the Atlantic Ocean and the Namib Desert.

Upon being released to the seawater, having its own initial sulphate content, $(SO_4^{2-})_O$, part of it is oxidized to sulphate $(SO_4^{2-})_B$, thereby contributing in a small measure to the total sulphate content of the sea. The remainder is released to the atmosphere as $(H_2S)_B$. A very small amount of sulphate $(SO_4^{2-})_R$ is contributed by ephemeral drainage such as the Swakop River.

Onshore winds pick up water nuclei from the seawater (not just water from evaporation, as this will not contain significant dissolved solids) causing the formation of fogs which can be blown up to about 100 km inland. The sulphur balance in the fogwater will be made up of the following components:

$$\sum SO_4^{2-} = (SO_4^{2-})_B + (SO_4^{2-})_O + (SO_4^{2-})_R + (H_2S)_B \qquad (14.4)$$

The initial seawater sulphate will more than likely constitute the greater part of the total amount in equation (14.4). Condensation or precipitation of the fogwater in the desert takes place and the sulphate is precipitated as gypsum. A certain amount of sulphate $(SO_4^{2-})_G$ is contributed to this gypsum from the ground-water. A study of the sulphur isotopes within each unit of this system would be the only way in which to confirm or disprove this theory. As this is not currently possible, evaluation of the amount of the sulphate precipitated from the fogs can be calculated from the data in Tables 38 and 39. The months in which the fogs were collected is matched to the fog precipitation, as equivalent rainfall, for the corresponding month. Calcium sulphate precipitated per km^2 per month is tabulated below (Table 40). Assume that by averaging the sulphate contents of the fogs in Table 38, a mean value is obtained. The amount of gypsum (as $CaSO_4$) precipitated per year is calculated as 53 tons per km^2. However rough these estimates may be, they nevertheless serve to show that there is a considerable amount of gypsum that has been, and is being, precipitated anually in the Namib Desert.

A check should be made concerning the relationship of the composition of the fogwater to that of the seawater from which it was derived. For comparison, the composition of the seawater and fogwater are plotted on a Schoeller diagram (Fig. 73) using the technique described by Parker (1969, p. 120).

TABLE 40: PRECIPITATION OF GYPSUM EXPRESSED AS $CaSO_4$ IN TONS/km^2/MONTH

Month	Equivalent rainfall 1958 (mm)	$CaSO_4$ (tons/km^2/month)			
		Fog 1	Fog 2	Fog 3	Fog 4
July	23,1	39,6			
August	22,0			2,7	
September	8,1		2,0		2,6

The plot of the seawater follows the same trend and dimensions as the seawater in other parts of the world (ibid., p. 117). Trends for all the fogwaters follow very similar patterns with the exception of magnesium, which shows only a slight relative depletion with respect to the seawater. This confirms that the fogs were derived from seawater and were taken bodily as nuclei from the surface of the ocean and diluted to some extent by water vapour from evaporation.

14.7 Isotopic Disequilibrium of Uranium

This section deals with the state of equilibrium between the respective uranium isotopes and other daughter products.

Chemical separation procedures for thorium, protac= tinium and uranium are given in Chapter 7. Sources were counted until a maximum standard deviation of 3 per cent was obtained for each peak area.

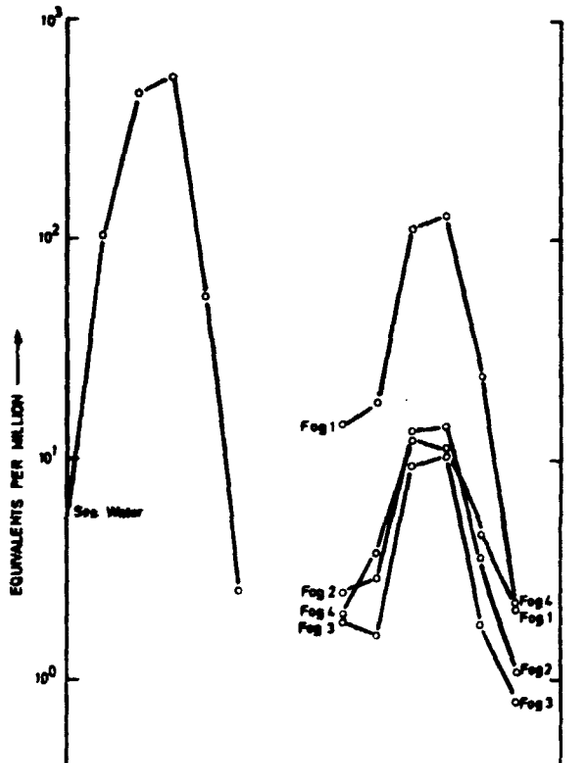


Fig. 73: Schoeller diagram, comparisons of the ionic distributions in sea- and fogwaters in terms of equivalents per million ionic species.

14.7.1 Isotopic equilibrium and disequilibrium

Equilibrium between the isotopes of a particular decay series is reached when all the daughter products decay at the same rate as they are being produced by their respective parents. This means that if equilibrium is to be reached, the activity ratio of the daughter product to that

of its parent must be constant. If this value deviates from the theoretical constant then a condition of disequilibrium has been created.

In the geological environment the equilibrium can be disturbed by some or other event during which uranium is removed from its place of origin and redeposited elsewhere.

Accompanying the decay of ^{238}U, a large amount of energy is released in the form of α-particles having an energy of about 4,2 MeV. From the conservation of momentum, the recoil energy imparted to the nucleus (now ^{234}Th) is simply

$$4{,}2 \left[\frac{\text{Mass of } \alpha\text{-particle}}{\text{Mass of } ^{234}\text{Th nucleus}}\right] \approx 0{,}07 \text{ MeV} \qquad (14.5)$$

The bond energy of most uranium compounds is less than 10 eV, therefore the transformed nucleus escapes from chemical bonding. Two mechanisms based on this concept have been suggested to account for the ^{234}U disequilibrium.

(a) ^{234}U is relocated, after recoil, into crystal defects and microcracks where it becomes more accessible to oxidation and subsequent removal in solution as the uranyl ion (Cherdyntsev et al, 1964).

(b) Rosholt et al (1965, 1966) suggested that as a result of recoil, breaking of chemical bonds takes place, accompanied by stripping of outer electrons by β-decay, thereby converting it in situ to the hexavalent form.

The difference between the two mechanisms is that in the first case the ^{234}U is subjected to selective exposure,

making it more susceptible to oxidation. In the second case the ^{234}U from its inception is in the hexavalent state and therefore does not require the need of external environmental oxidizing conditions.

Kolodny and Kaplan (1970) found in their study of phosphorites that case (a) was the most likely mechanism to account for the disequilibrium in the uranium isotopes.

In Table 41 the $^{234}U/^{238}U$ activity ratio is given for various duricrust samples from the Langer Heinrich and Von Stryk's pit. Equilibrium in most cases has not been completely established, but the deviations from unity are small. Only sample HJ2-13 falls below one. Generally, uranium is still migrating and being deposited with the exception of HJ2-13 where some in situ leaching has taken place.

TABLE 41: $^{234}U/^{238}U$ ACTIVITY RATIOS FOR THE DURICRUSTS OF THE LANGER HEINRICH AND VON STRYK'S PIT

Sample No.	$^{234}U/^{238}U$
HJ2-3	1,05
HJ2-5	1,00
HJ2-8	1,03
HJ2-10	1,03
HJ2-13	0,96
AD1-1	1,01
AD1-4	1,03
AD1-17	1,13
C5-15	1,02
Von Stryk's pit	1,01

The Bloedkoppie Granite has partially contributed to the supply of uranium to the duricrusts. From the $^{234}U/^{238}U$ activity ratio in the granites (Table 42), both precipitation

and leaching of uranium is indicated.

TABLE 42: $^{234}U/^{238}U$ ACTIVITY RATIO FOR THE BLOEDKOPPIE GRANITE

SAMPLE	$^{234}U/^{238}U$
LH16	1,09
HJ2-36	0,86

Sample HJ2-36 was a powder from a percussion borehole, taken from a depth of 27 m and equivalent to 18 m penetration into the granite. Even at this depth uranium is still being leached by subsurface waters. LH16 is an outcrop sample of granite and the high $^{234}U/^{238}U$ activity ratio is indicative of conditions where uranium is still circulating. Some of the uranium in this sample was precipitated after migration from elsewhere.

14.7.2 Geochronology

Disequilibrium has most widely been applied to the field of Pleistocene geochronology (Rosholt, 1970). Two models were developed that described and apply the principles of isotopic fractionation, which are the closed and open systems (Rosholt, 1967; Szabo and Rosholt, 1969).

Nomenclature

$^{230}Th/^{234}U$ = activity ratio of the isotopes ^{230}Th and ^{234}U, etc.

λ_{230} = decay constant for ^{230}Th ($9,2 \times 10^{-6}$)

λ_{231} = decay constant for ^{231}Pa ($2,1 \times 10^{-5}$)

λ_{234} = decay constant for ^{234}U ($2,8 \times 10^{-6}$)

t = time (age of sample, years)

The Closed System

In defining the closed system the assumption is made that all the ^{230}Th is produced by the decay of uranium isotopes that were taken up by the specimen when it was formed. No uranium and thorium were subsequently added or removed from the system. When disequilibrium of ^{234}U is taken into account the age of the samples, t, can be related to the ratio of ^{230}Th activity produced internally to the observed activity of ^{234}U as follows (Szabo and Rosholt, 1969, p. 3254).

$$\frac{^{230}Th}{^{234}U} = \frac{^{238}U}{^{234}U}\left[1-e^{-\lambda_{230}t}\right] + 1,435\left[1-\frac{^{238}U}{^{234}U}\right]\left[1-e^{-\lambda_{230}-\lambda_{234}\ t}\right] \qquad (14.6)$$

The Open System

Isotopic work on shells revealed that more uranium was available to the specimen than was actually assimilated (Rosholt, 1967, p. 299). The ^{231}Pa and ^{230}Th content was contributed by both the assimilated uranium and the mobile uranium which was not retained. An open-system model takes these problems into account and the concepts can be applied in general to the migration and occurrences of uranium in natural material. Fig. 74 represents the migration and decay

of uranium and the paths through which the ^{231}Pa and ^{230}Th accumulated.

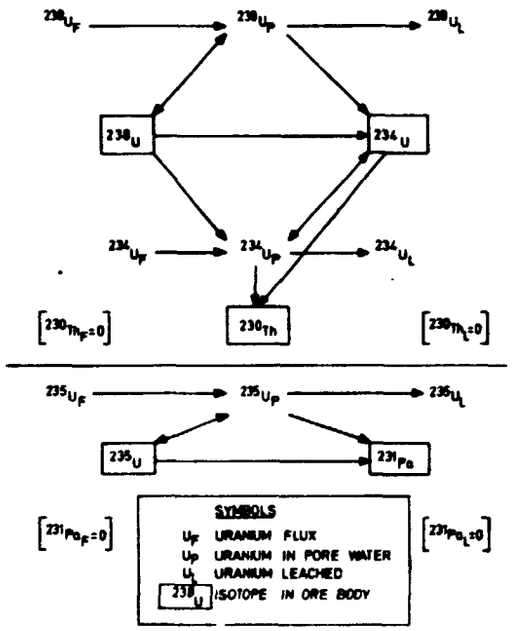


Fig. 74: A flow diagram of uranium and the accumulation of daughter isotopes in an open-system model.

Mathematically the system can be described by the following equations (Szabo and Rosholt, 1969, p. 3255):

$$A = B\left[\frac{k_3 - k_1 k_2}{k_4}\right] + C\left[\frac{k_5}{k_4} - B\frac{k_2 k_5}{(k_4)^2}\right] \qquad (14.7)$$

where $A = {}^{230}Th/{}^{234}U$

$B = {}^{231}Pa/{}^{234}U$

$C = {}^{231}Pa/{}^{238}U$

$k_1 = e^{-\lambda_{234}t}$

$k_2 = 1-e^{-\lambda_{234}t}$

$k_3 = 1-e^{-\lambda_{230}t}$

$$k_4 = 1-e^{-\lambda_{231}t}$$

$$k_5 = 1{,}435\ [1-e^{-\lambda_{230}-\lambda_{234}t}]$$

The open-system model is considered to be superior to the closed-system model as most samples from the natural environment are unlikely to yield to the rigid conditions required by the latter. Furthermore it tries to incorporate a material balance of incoming and outgoing uranium.

Table 43 gives the ages of the uranium mineralization in the calcretes of the Langer Heinrich. The discrepancy between the ages of the closed and open systems clearly indicates that the ore-body was subjected to an open system. Therefore the ore-body has a minimum age of 30 000 years.

TABLE 43: DISEQUILIBRIUM AGES OF URANIUM MINERALIZATION BY CLOSED AND OPEN-SYSTEM MODELS

Sample	$^{230}Th/^{234}U$	$^{231}Pa/^{234}U$	$^{231}Pa/^{238}U$	$^{238}U/^{234}U$	Age (years)	
					Closed	Open
HJ2-10	0,43	-	-	0,97	62000±2000	-
HJ2-13	0.45	0,93	0,96	-	65000±2000	30000±1000

14.7.3 Mass spectrographic analysis

The $^{235}U/^{238}U$ ratio was determined in certain calcrete samples from the Langer Heinrich and one sample of uranothorianite from Phalaborwa, the latter being used as the standard reference (Table 44).

TABLE 44: $^{235}U/^{238}U$ ATOM RATIOS IN CALCRETE FROM THE LANGER HEINRICH AND URANOTHORIANITE FROM PHALABORWA

Sample	$^{235}U/^{238}U$ (Atom %)
HJ2-8	0,007268
HJ2-13	0,007261
AD1-17	0,007247
C5-15	0,007257
Uranothorianite	0,007272

Relative to the uranothorianite, the calcretes are approximately 2 per cent depleted in ^{235}U.

14.8 Summary

Factor analysis of the raw data provided pointers concerning the nature and mechanisms which were involved during the formation of calcrete. Calcite and carnotite were precipitated as independent phases within the pore spaces of the detrital material from mineralized subsurface waters. Limited detail was provided concerning the actual mechanisms involved and therefore the geochemistry of individual and groups of elements was discussed with the possible implications for the development of calcrete duricrust deposits.

Calcite precipitated in the calcrete by the process of soil suction. By analogy, the segregation of carnotite resulted from a transport process, mainly upward diffusion caused by soil suction, and was precipitated by the nucleation of the uranyl ion on montmorillonite.

A new mechanism is proposed for the origin of gypcrete in the Namib Desert, which is based on the precipitation of calcium sulphate from onshore fogs.

The isotope ratio $^{234}U/^{238}U$ for the duricrusts and Bloedkoppie revealed that equilibrium had not been completely established and that the uranium is still migrating. Age determinations of the uranium mineralization using the prin= ciples of isotopic disequilibrium based on the closed-system and open-system models, were 63 000 years and 30 000 years respectively.

15. GEOCHEMISTRY OF THE DIATOMACEOUS MUDS

The diatomaceous muds in the anaerobic basins of the continental shelf are the final stage of the geochemical cycle of uranium. A discussion on the geochemistry of the muds would be incomplete without mention of the behaviour of trace elements in the ocean water, because it is from this source that the elements were and still are being derived.

The abundances of metal ions in seawater are determined by the solubilities of their respective compounds. Concentrations of certain elements in seawater, relevant to this discussion, are given in Table 45.

TABLE 45: THE CONCENTRATIONS OF SOME ELEMENTS IN SEAWATER. (KRAUSKOPF, 1956, p. 3, ALLEGRE AND MICHARD, 1974, p. 41)

Element	Concentration (ppm)
P	0,07
Mo	0,014
V	0,002
U	0,003

According to the calculated solubility products of elements in seawater, Krauskopf (1956, p. 9) reported that normal aerated seawater is undersaturated with respect to rare metals. In passing it is worthwhile to note that the oceans contain uranium resources equivalent to 4 000 times the total world reserves at 10 dollars per pound (Barnes and Ruzicka, 1972,

p. 162).

It is from the seawater that the diatomaceous muds derived their high concentrations of certain elements. The problem to be considered concerns the mechanisms involved that were responsible for concentrating elements from a source that is now known to be undersaturated. It is clear that a mechanism based purely upon a solubility function is entirely improbable.

The core samples analyzed in this investigation were taken from the Walvis Bay Basin (Fig. 15) and the results are given in Table 46.

15.1 Geochemistry of the Muds

The diatomaceous muds off South West Africa were the subject of four major trace element investigations (Calvert and Price, 1970; Baturin et al, 1971; Meyer, 1973; Veeh et al, 1974) and the three most recent studies were primarily concerned with the distribution of uranium.

Generally it has been shown that the distribution of the diatomaceous muds is governed by upwelling currents, creating a situation favourable for reducing conditions. The presence of hydrogen sulphide is a manifestation of such a system.

Using the mean concentrations of elements in Table 46 and comparing these with the concentrations of the elements in seawater (Table 45), a concentration factor for the elements in the muds was calculated (Table 47).

TABLE 46: ELEMENT CONCENTRATIONS IN TWO CORES OF DIATOMACEOUS MUDS

SWA 30

DEPTH (m)	0-0,05	0,05-0,08	0,08-0,12	0,12-0,18	0,18-0,23	0,23-0,28	0,28-0,33	0,33-0,38	0,38-0,43	0,43-0,48	MEAN
P_2O_5 (%)	0,66	0,33	1,51	0,27	0,24	0,22	0,25	0,23	0,81	3,66	0,80
Mo (ppm)	26	32	23	31	26	29	39	39	33	22	30
V (ppm)	70	54	50	43	48	31	38	40	48	22	44
U (ppm)	17	16	22	28	37	18	21	27	40	37	26
LOI (%)*	22,4	20,0	18,1	17,1	16,7	16,1	15,6	17,5	22,0	17,6	18,3

SWA 50

DEPTH (m)	0-0,1	0,1-0,2	0,2-0,3	0,3-0,4	0,4-0,5	0,5-0,6	0,6-0,66	0,66-0,72	MEAN
P_2O_5 (%)	0,34	0,3	0,3	0,27	0,58	0,25	0,3	0,42	0,35
Mo (ppm)	24	26	25	19	28	24	23	16	23
V (ppm)	30	59	56	74	43	71	65	20	52
U (ppm)	14	21	16	24	43	43	25	18	26
LOI (%)*	16,6	17,3	15,4	13,4	13,8	15,8	14,0	8,4	14,3

* LOI = Loss on ignition at 500 °C. This is regarded as being equivalent to the total organic matter concentration. Very Little $CaCO_3$ was present and was ignored.

CONFIDENTIAL
CONFIDENTIAL

It is clear that there is an enormous degree of concentration of the elements in the diatomaceous muds with respect to the seawater. Vanadium has the highest C_f value being more than a factor 10 greater than molybdenum and more than a factor 2 greater than uranium. Molybdenum has the lowest concentration factor.

TABLE 47: CONCENTRATION FACTORS, RELATIVE TO SEAWATER, FOR THE ELEMENTS IN THE DIATOMACEOUS MUDS

Sample	Element	Concentration Factor, C_f
SWA 30	Mo	$2,1 \times 10^3$
	V	$2,2 \times 10^4$
	U	$8,7 \times 10^3$
SWA 50	Mo	$1,6 \times 10^3$
	V	$2,6 \times 10^4$
	U	$8,7 \times 10^3$

Krauskopf (1956) studied the removal of certain elements from seawater and concluded that sulphide precipitation of vanadium and molybdenum was unlikely, but that chemical reaction with organic compounds appeared to be the most likely mechanism. Kaplan (1974), reviewing the precipitating mechanism for uranium, also pointed out that sulphide had little or no effect in removing it from seawater. Furthermore not all sediments rich in organic matter contain high uranium concentrations, and he suggested a selective uptake by certain

organic compounds only.

Figs. 75 and 76 show the depth profiles of phosphorus pentoxide, molybdenum, vanadium, uranium and loss on ignition at 500 °C. The latter function is a measure of the total organic matter content. Comparison of the profiles for sample SWA 30 (Fig. 75) shows that there is a partial measure of coherence between some of the variables. Both vanadium and LOI (loss on ignition) follow the same pattern, with the exception of the value of 0,2 m, where the vanadium increases slightly. A similar increase in uranium occurs at the same depth, but in this case the increase is gradual and therefore uranium and LOI do not correlate above 0,25 m. Correspondingly, no significant change in molybdenum or phosphorus pentoxide is noted. Below 0,25 m a good coherence is seen between LOI, uranium, vanadium, and to a lesser degree, molybdenum. All variables with the exception of phosphorus pentoxide decrease below 0,4 m. The log of the core revealed that below 0,38 m a shelly zone was found and the high phosphate content is mostly due to the presence of skeletons. Baturin et al (1971) report similar findings.

The patterns of core sample SWA 50 (Fig. 76) show that both uranium and the organic matter (LOI) are very similar, which again emphasizes the role that organic matter plays in the precipitation of uranium. For the upper 0,25 m, molybdenum and vanadium have similar tendencies, but below, their trends diverge from that of LOI until 0,55 m, where a reconvergence of trend patterns reappears. At about 0,63 m the amount of organic matter decreases in accordance with an increase in phosphorus pentoxide and detrital matter.

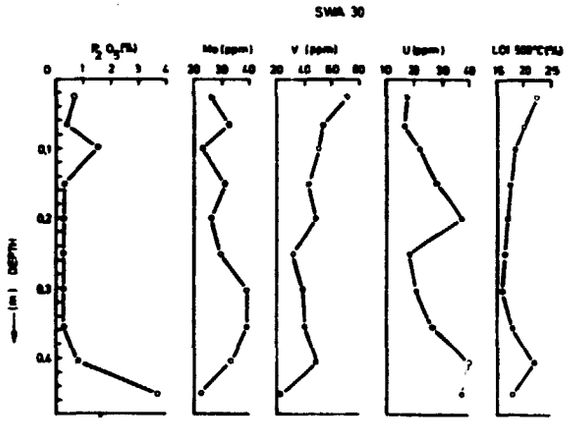


Fig. 75: Profiles through the diatomaceous mud for phosphorus pentoxide, molybdenum, vanadium, uranium and loss on ignition at 500 °C. (Borehole SWA 30)

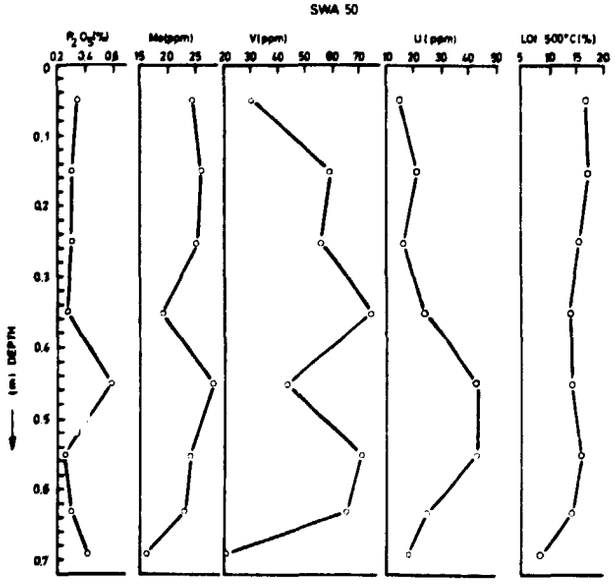


Fig. 76: Profiles through the diatomaceous mud for phosphorus pentoxide, molybdenum, vanadium, uranium and loss on ignition at 500 °C. (Borehole SWA 50).

It can be stated that it does appear that the organic material is the chief precipitatory medium for these metallic elements. Diverging patterns in places suggest that there are more than one possible mechanism controlling the precipi= tation of uranium, vanadium and molybdenum. Veeh et al (1974) report that phosphate in the form of apatite co-precipitated uranium.

A generalized equation for the decomposition of average marine organic matter by bacterial sulphate reduction is given in equation (15.1) (Ben-Yaakov, 1973, p. 88).

$$\frac{1}{53}(CH_2O)_{106}(NH_3)_{16}H_3PO_4 + SO_4^{2-} \rightarrow CO_2 + HCO_3^- + HS^- + H_2O +$$

$$\frac{16}{53}NH_3, + \frac{1}{53}H_3PO_4 \qquad (15.1)$$

Before organic complexing of the uranium can take place, it must first be reduced from the hexavalent to the quadravalent state. This is accomplished by the powerful reductant HS^-. The mechanism for uranium reduction is given in equation (15.2). It is likely that the UO_2 would be in an amorphous form absorbed onto or reacted with an organic molecule. Vanadium and molybdenum are not precipitated as sulphides due to their relatively high solubility. The only mechanism that remains is complex formation with an organic compound, and the close coherence of both elements with LOI in sample SWA 50 implies that an organic reaction took place.

$$2HS^- + [UO_2(CO_3)_3 \cdot 2H_2O]^{2-} \rightarrow H_2S + S^{2-} + UO_2 + 2CO_3^{2-} + 2H_2O \qquad (15.2)$$

Normalizing the concentrations of molybdenum, vanadium and uranium with LOI reveals that there is a closer relationship between uranium and vanadium than between uranium and molybdenum (Figs. 77 and 78). The nature of the controlling precipitating mechanism for molybdenum and vanadium does not appear to be the same. Kaplan's remark (1974) that the concentration of uranium may be controlled by certain classes of organic compounds, may also apply to vanadium and molybdenum. Vanadium, however, seems to be more closely associated with those compounds that precipitate uranium.

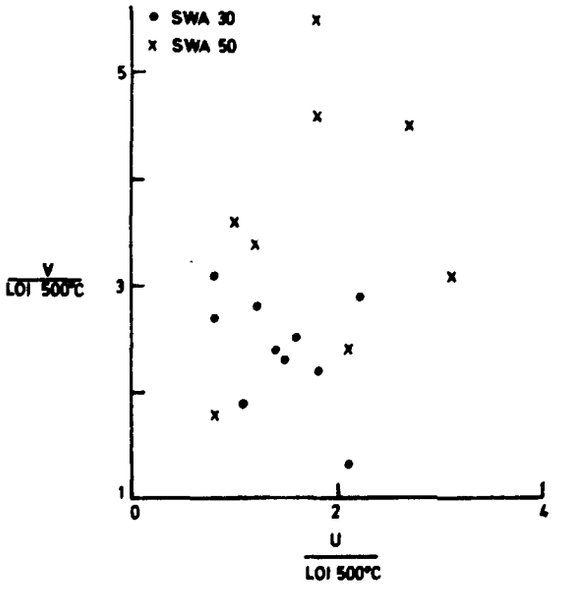


Fig. 77: Variation diagram of vanadium plotted against uranium for the diatomaceous muds. Normalized with loss on ignition at 500 °C.

Nissenbaum and Kaplan (1972, p. 570) suggested that marine organic matter is mostly the product of degraded plankton. The process of degradation takes place as a sequence of transformations in a sediment and is given as

follows, (1) Degraded cellular material → (2) water soluble complexes containing amino acids and carbohydrates → (3) fulvic acids → (4) humic acids → (5) kerogen.

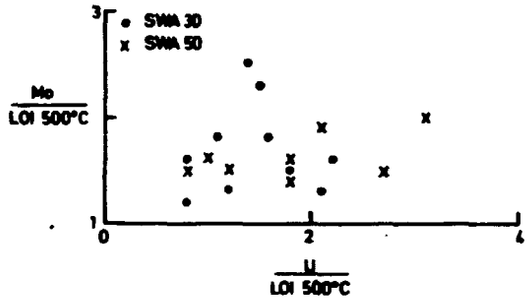


Fig. 78: Variation diagram of molybdenum plotted against uranium for the diatomaceous muds. Normalized with loss on ignition at 500 °C.

The adsorption of vanadium and molybdenum may occur at different stages within the degradation sequence. Throughout the basin the nature of the degradation need not necessarily follow exactly the same path due to some or other cause and this would give rise to heterogenetics in the trace element distribution patterns. Results (Rona, 1974) for similar anaerobic sediments of the Black Sea show a closer relationship between molybdenum and vanadium than do the sediments in this study. Again this may be a case where slight modifications in the organic degradation chain would co-precipitate both molybdenum and vanadium in the Black Sea in a sympathetic manner.

Meyer (1973) reports that there is a weak direct relationship between uranium and phosphate. Figs. 75 and 76 give no indication that this is the case for the two cores under study here.

The highest uranium concentrations in the submarine basins are situated opposite river mouths, past and present (Fig. 15). South of Walvis Bay the highest concentrations lie off old choked river mouths of the original Tsondab and Sossus Rivers respectively. It is certain that beneath the shifting sand dunes, water still flows, as the dunes are broken and disorientated in the region of ground-water flow (Fig. 1). These choked river valleys may be possible target areas for uranium exploration. From Walvis Bay northwards, the highest uranium concentrations lie opposite the Kuiseb, Swakop, Omaruru, Ugab, Unjab and Hoanib River mouths.

In the future, the diatomaceous muds may become an economic mining proposition, not only from the uranium aspect, but from the aspect of other metals as well (Table 48).

TABLE 48: MAXIMUM CONCENTRATIONS OF ELEMENTS IN DIATOMACEOUS MUDS (CALVERT AND PRICE, 1970, p. 594)

ELEMENT	CONCENTRATION (ppm)
Cu	129
Ni	455
Pb	32
Zn	337

Add to this list uranium, vanadium and molybdenum, and it certainly becomes more attractive, especially when considering the fact that all of these elements are directly associated

with the organic, and possibly the phosphate, fractions. The selective dissolution of the organic matter and separation of the metals from the inorganic fraction would provide a significant concentrating factor.

15.2 Summary

Seawater is undersaturated with respect to rare metals, whereas in the diatomaceous muds some elements are significantly concentrated. The mechanisms for enriching certain elements in the mud were considered. The distribution of uranium, vanadium and molybdenum in the muds is heterogeneous and it was suggested that the presence of organic matter was the main precipitating agent and that there was selective uptake of these metals by particular organic compounds.

Uranium is concentrated in the muds which are situated opposite river mouths, past and present, e.g. the Swakop River. The economic potential of the muds was discussed, as other metals such as copper, nickel, lead and zinc are also present in significant concentrations.

16. CLASSIFICATION AND AGE RELATIONSHIPS OF THE URANIUM DEPOSITS

The report released by the OECD (1973) concerning the resources, production by and demand for uranium by developed and underdeveloped countries, concluded that the rate of new discoveries must total $2,3 \times 10^5$ tons U_3O_8 per year until 1990. This means that the total potential reserves must increase by $2,5 \times 10^6$ tons U_3O_8 over this period. In basic terms, a further twenty-five deposits with the potential of the Langer Heinrich (10^5 tons U_3O_8) must be discovered over the next fifteen years. As a result greater orientation problems will be encountered during exploration for the hidden uranium ore deposits.

The establishment of a classification system of uraniferous ore bodies would group them in accordance with favourability criteria based on genetic sequences and mode of occurrence. Recognition of the parameters controlling the development of the uranium deposits in the Tumas River Valley has yielded a classification which would improve the efficiency of the location of prospective target areas. This type of regional evaluation is useful in quickly eliminating unlikely zones, and thereby saving time and expenditure.

Numerous types of classification of uranium deposits have been proposed. Ruzicka (1971) summarized the classifications of Russian, East European and Canadian deposits. A general classification embracing world deposits has been proposed by Barnes and Ruzicka (1972) and Ziegler (1974).

There appear to be four essential themes that run through the various classification systems:

(a) Morphological relationships to host rocks.

(b) Genetic associations.

(c) Metallotectonic controls.

(d) Element associations.

Barnes and Ruzicka (1972) developed a genetic classification in terms of the geochemical cycle and modes of transport and deposition. Although this may be suitable for a global approach, certain disadvantages arise when viewed from the more localized aspects, for they do not consider the morphological manifestation of the ore-bodies. Fig. 79 is an attempt to include these features. If treated in the broader aspects, both the Langer Heinrich and Tumas Types would be typical duricrust deposits. There are, however, some essential differences, such as the magnetic anomalies associated with the Tumas Type. The common features are the mode of introduction into geochemical cycle, the mode of deposition and, partially, the mode of transport.

Ziegler (1974) differentiates the world uranium ore-bodies in terms of metallotectonics and therefore classifies the Yeelerrie and Namib Desert epigenetic calcrete deposits into different types. The Yeelerrie deposit is related to a stable continental crust, whereas those in the Namib Desert are associated with an ancient mobile belt. In the opinion of the author this part of his classification falls down, for it is essentially a problem of the availability of uranium and the type of host rock in which it is deposited.

CONFIDENTIAL

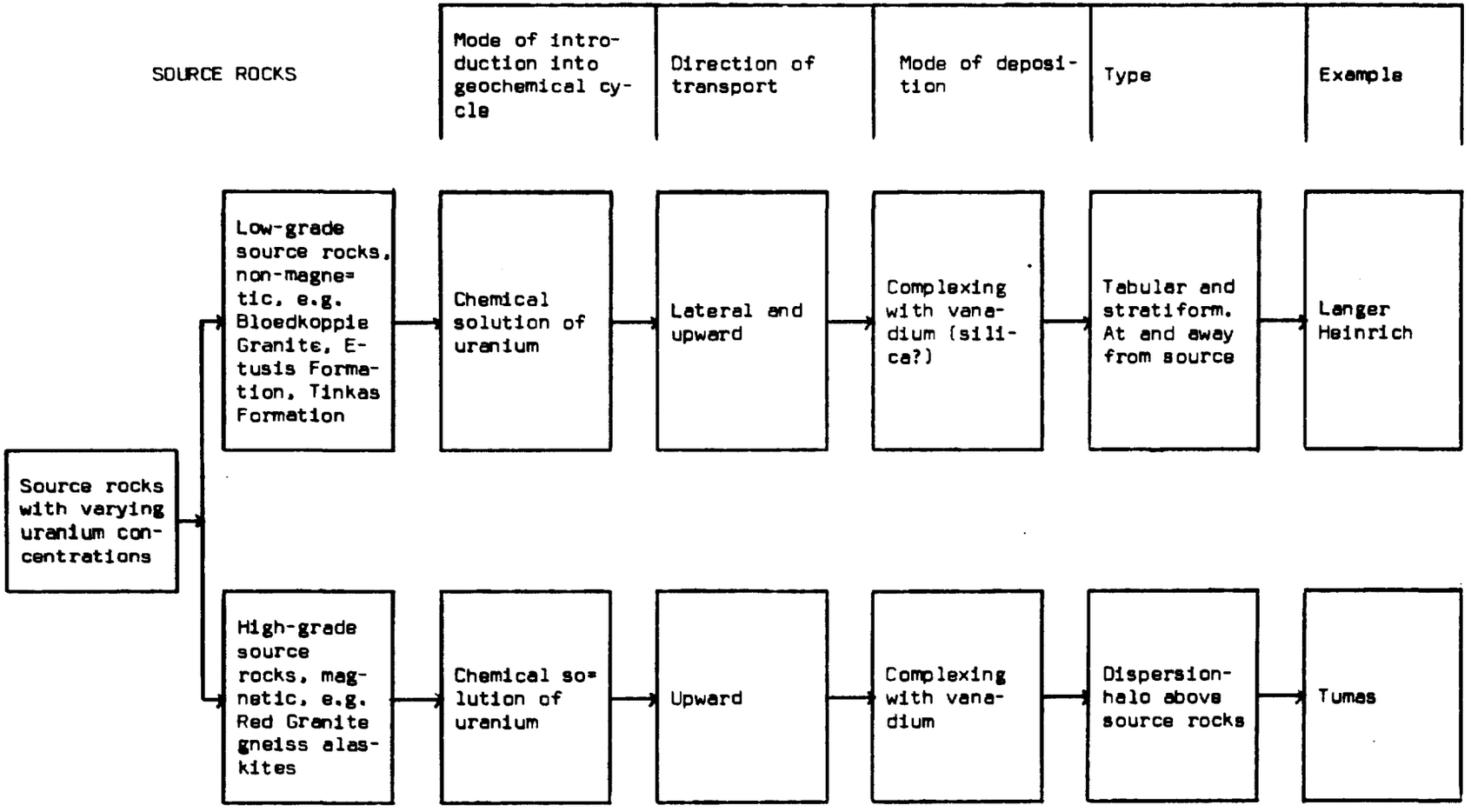


Fig 79 A genetic classification for the Langer Heinrich and Tumas Type uranium ore deposits in terms of the geochemical cycle and modes of transport and deposition.

CONFIDENTIAL

Firstly, the uranium for both the Langer Heinrich and Yeelerrie deposits was basically derived from a low-grade granitic source. Secondly, the host rock is very similar when the Langer Heinrich deposit itself is considered, but dissimilar for the Langer Heinrich Type deposits in the gypcretes of the Tumas River Valley.

This may be sufficient ground to further subdivide the deposits in terms of host rock and type, although possibly inadvisable with regard to (a) and (b) below:

(a) Stratiform deposits in calcrete.

(b) Stratiform deposits in gypcrete.

(c) Dispersion halo in gypcrete.

Generally a metallotectonic classification is important in the broader sense, but it does not find application when considering the duricrust deposits of the Yeelerrie, Langer Heinrich and Tumas Types on a local scale.

The affiliations of the duricrust deposits to other types of uranium deposits in Southern Africa are illustrated in Fig. 80, which has been adapted from the genetic classification proposed by Barnes and Ruzicka (1972). This system is in fact a behavioural account of the crustal characteristics of uranium through the mechanical, chemical (at both high and low temperatures and pressures) and magmatic processes resulting in its ubiquitous distribution throughout time and space.

The relationships between ages of host rock and the mineralization found in them for the Southern African uranium deposits are given in Fig. 81.

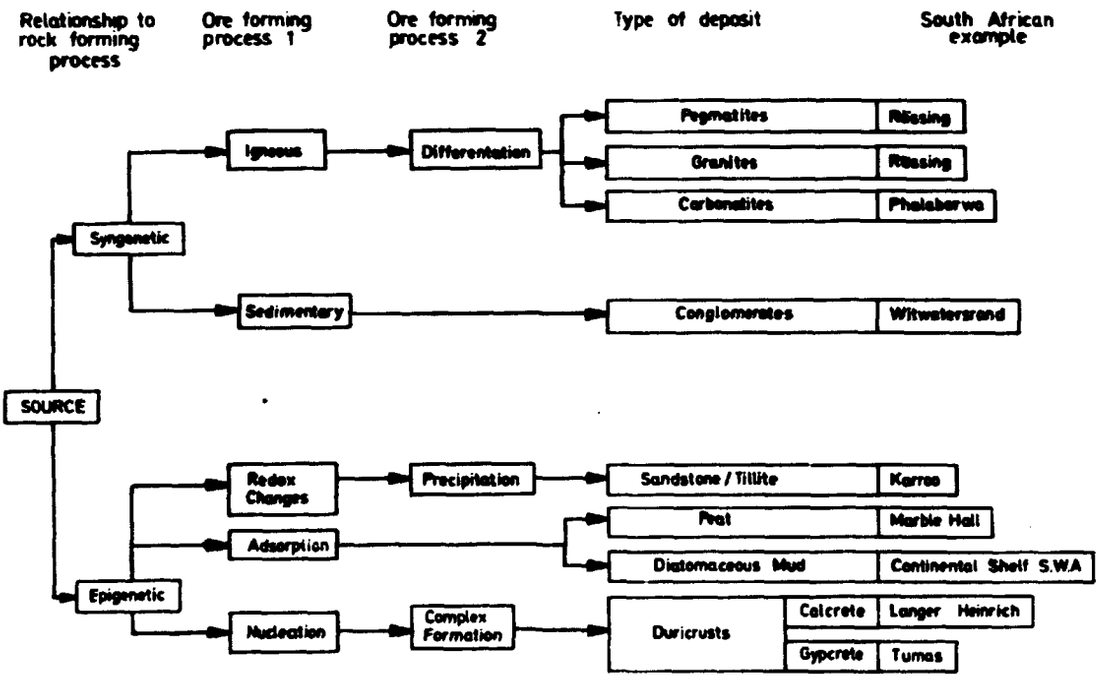


Fig. 80: The relationships of the duricrust deposits with respect to other types of uranium deposits in terms of ore-forming processes.

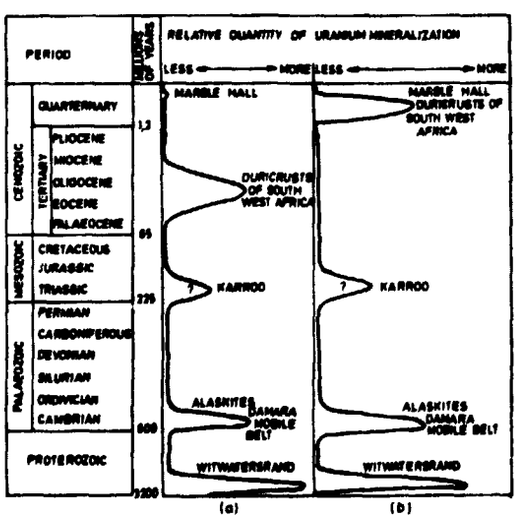


Fig 81: Relationships between ages of host rock and the associated uranium mineralization.
(a) Age of host rock enclosing the uranium mineralization
(b) Age of uranium mineralization.

A comparison between (a) and (b) of the Figure reveals that some uranium deposits are syngenetic, whereas the others are epigenetic. The age of the duricrust of the Namib Plain is mid-Tertiary, whereas the age of mineralization is Quarternary, which indicates their epigenetic character. The relative quantity of uranium in the Karoo is at this stage uncertain and therefore the peak height does not represent any magnitude of ore reserve.

A knowledge of the relationships given in Fig. 81 and the tectonic or petrogenetic processes that acted upon or formed the uranium deposits may yield fundamental information concerning classification and favourability criteria of the uranium mineralization and genetic history.

17. SUMMARY AND CONCLUSIONS

In the region near the Swakop River a geochemical cycle of uranium was established which comprises the distribution of uranium in three stages, the basement rocks, the subsurface waters and the sites of accumulation. Through all these stages the geological and geochemical aspects of uranium mineralization were investigated in order to determine the geochemical factors that controlled the formation of epigenetic deposits in the Namib Desert.

Paragenetic relationships between the basement rocks were established from rare-earth element distributions. The Bloedkoppie and Gawib Granites are late-syntectonic in age. The significance behind the origin of the Bloedkoppie Granite is that is was derived by partial melting from the Nosib Group rocks. Therefore the Nosib Groups was the initial source of the uranium in this later-forming granite which ultimately contributed to the supply of the epigenetic uranium in the Gawib River Valley.

Uranium was leached from the source rocks by the corrosive action of saline subsurface waters. The geochemistry of these waters provided an insight into the chemical processes involved during the epigenesis of the calcretes. From the data it was possible to infer which mineralogical phases were stable in the environment of the Namib Desert. The waters have a high degree of calcite saturation, indicating that the formation of calcrete is still in progress. Montmorillonite and not kaolinite is the stable clay mineral. It was predicted

that both soddyite and carnotite would coexist in calcrete and this was confirmed by X-ray diffraction analysis.

The distribution of uranium in the subsurface water is controlled by the pH and carbonate content, with uranium principally in the form of the soluble uranyl dicarbonate complex. Dissociation of the UDC by soil suction and nucleation of the uranyl ion on montmorillonite were the main controlling mechanisms involved in the precipitation of carnotite and soddyite.

Using the concentration of uranium in the subsurface water for prospecting purposes the following criteria were found to apply:

(a) U ≥ 30 ppb - potential uranium mineralization nearby but anomalous values do not necessarily imply a deposit.

(b) U<30 ppb - no uranium mineralization indicated but low background values do not necessarily mean the absence of a deposit.

Uranium is still circulating in the duricrusts and source rocks, as isotopic equilibrium between uranium and its daughter products has not been completely established. The isotopic ages were given for the uranium mineralization in the Gawib River Valley. For the closed-system and open-system models ages of 63 000 years and 30 000 years respectively were obtained. The discrepancy in ages is again indicative of migrating uranium which seems to obey the open-system model more closely.

The final stages of the geochemical cycle of uranium comprise the Atlantic Ocean and the diatomaceous muds on the continental shelf. The ocean water is undersaturated in

uranium (mean U = 0,003 ppm) and other elements, whereas the diatomaceous muds are enriched in those elements (mean U = 26 ppm). Organic matter was the main precipitating agent and the heterogenecus distribution of uranium, molybdenum and vanadium is due to the selective uptake of these elements by particular organic compounds.

A classification system was proposed that would provide guidelines concerning favourability criteria for uranium mineralization in this region.

REFERENCES

ADAMS, F., and DAMS, R., (1969) A compilation of precisely determined gamma-transition energies of radionuclides produced by reactor irradiation. Jour. Radioanalytical Letters, 3, 99-125

AHRLAND, S., LILJENZIN, J.O., and RYDBERG, J., (1973) Solution chemistry of the actinides. In Comprehensive Inorganic Chemistry, 5, 465-635. Ed. Bailar, J.C., Emeleus, H.J., et al. Pergamon Press, Oxford.

ALLèGRE, C-J., and MICHARD, G., (1974) Introduction to Geochemistry. D. Reidel Publ. Co., Dordrecht. 142 p.

ANNUAL PROSPECTING REPORTS (1972, 1973) Prospecting Grant M46/3/209. Over the Farms Dorstrivier 15, Nordenburg 76, Vlakteplaas 110 and a portion of Bloemhof 109, Registration "G" - South West Africa. Anglo American Prospecting Co. Ltd.

————————————, (1974) Prospecting Grant M46/3/430 over area known as ORYX Area, Registration Division "G" - South West Africa. Anglo American Prospecting Co. Ltd.

————————————, (1974) Prospecting Grant M46/3/433 over area known as TUBAS Area, Registration "G" - South West Africa. Anglo American Prospecting Co. Ltd.

————————————, (1974) Prospecting Grant M46/3/487 over area known as WELWITCHIA Area, Registration Division "G" - South West Area. Anglo American Prospecting Co. Ltd.

ARMSTRONG, F.C., (1974) Uranium resources of the future - "porphyry" uranium deposits. Proc. Symp. IAEA, Athens. Formation of Uranium Ore Deposits, 625-635.

BALASHOV, Yu. A., RONOV, A.B., MIGDISOV, A.A., and TURANSKAYA, N.V., (1964) The effect of climate and facies environment on the fractionation of the rare earths during sedimentation. Geokhimiya, 10, 995-1014.

BARNES, F.Q., and RUZICKA, V., (1972) A genetic classification of uranium deposits. Intern. Geol. Cong., Montreal, Section 4. Mineral Deposits, 159-166.

BATURIN, G.N., KOCHENOV, A.V., and SENIN, Yu. M., (1971) Uranium concentration in recent ocean sediments in zones of rising currents. Geokhimiya, 4, 456-462.

BENTOR, Y.K., (1969) On the evolution of subsurface brines in Israel. Chem. Geol., 4, 83-110.

BEN-YAAKOV, S., (1973) pH buffering of porewater of recent anoxic marine sediments. Limnol. and Oceanogra., 18, 86-94.

BERNER, R.A., (1971) Principles of Chemical Sedimentology McGraw-Hill, New York. 240 p.

BHOSE, H., ROSE-HANSEN, J., SØRENSEN, H., STEENFELT, A., LØVBORG, L., and KUNZENDORF, H., (1974) On the behaviour of uranium during crystallization of magmas with special emphasis on alkaline magmas. Proc. Symp. IAEA, Athens, Formation of Uranium Ore Deposits, 49-60.

BRITS, R.J.N., (1975) Rekenaarprogramme vir neutronaktiverings=

analise. PIN 265 (BR). 119 p.

BUCHANAN, R.F., and FARIS, J.P., (1960) Adsorption of the elements from nitric acid by anion exchange. Proc. Symp. IAEA, Copenhagen. The Use of Radioisotopes in the Physical Sciences and Industry, 2, 362-371.

BUTLER, A.P., (1969) Ground-water as related to the origin and search for uranium deposits in sandstone. Contrib. to Geology (Wyoming Uranium Issue), 8, 81-86.

CALVERT, S.E., and PRICE, N.B., (1970) Minor metal contents of Recent organic-rich sediments off South West Africa. Nature, 227, 593-595.

CAMERON, E.M., (1967) A computer program for factor analysis of geochemical and other data. Geol. Surv. Canada Paper, 67-34. 42 p.

CHERDYNTSEV, V.V., MALYSHEV, V.I., SOKOLOVA, Z.A., KAZACHEVSKY, I.V., and BIOSOV, I.V., (1964) Isotopic composition of uranium and thorium in the supergene zone. Geochem. Int., 1, 398-401.

COOKE, R.U., and WARREN, A., (1973) Geomorphology in Deserts. B.T. Bashford Ltd, London. 374 p.

CORNER, B., (1975) A preliminary report on the correlation between magnetic and radiometric data in the Damara Orogenic Belt-S.W.A. PIN-281(CV). 8 p.

DALL'AGLIO, M., (1972) Planning and interpretation criteria in hydrogeochemical prospecting for uranium, 121-134. In

Uranium Prospecting Handbook. Ed's Bowie, S.H.U., Davis, M., and Ostle, D. Inst. Min. and Met., London.

————————, GRAGNANI, R., and LOCARDI, E., (1974) Geo= chemical factors controlling the formation of the secondary minerals of uranium. Proc. Symp. IAEA, Athens. Formation of Uranium Ore Deposits, 33-48.

DIXEY, F., (1955) Some Aspects of the geomorphology of Central and Southern Africa. Geol. Soc. S. Afr. Alex. L. du Toit Memo= rial Lecture No. 4. 58 p.

DIXON, W.J., (1967) BMD Biomedical Computer Programs. Univ. of California Press, Berkeley and Los Angeles.

DOOLEY, J.R., GRANGER, H.C., and ROSHOLT, J.N., (1966) Uranium-234 fractionation in the sandstone-type uranium deposits of the Ambrosia Lake District, New Mexico. Econ. Geol., 61, 1362-1382.

FETH, J.H., ROBERSON, C.E., and POLZER, W.L., (1964) Mineral constituents in water from granitic rocks, Sierra Nevada, California and Nevada - Geochemistry of water. U.S. Geol. Surv. Water Supply Paper, 1535-I. 70 p.

GABLEMAN, J.W., (1970) Speculations on the uranium ore fluid. Proc. Symp. IAEA, Vienna. Uranium Exploration Geology, 315-330.

GARRELS, R.M., and THOMPSON, M.E., (1962) A chemical model for seawater at 25 °C and one atmosphere total pressure. Am. Jour. Sci., 260, 57-66.

GEVERS, T.W., (1942) The morphology of the Windhoek district, South West Africa. S. Afr. Geographical Jour., 24, 45-64.

GILE, L.H., PETERSON, F.F., and GROSSMAN, R.B., (1966) Morphological and genetic sequences of carbonate accumulations in desert soils. Soil Science, 101, 347-360.

GLENNIE, K.W., (1970) Desert Sedimentary Environments. In Developments in Sedimentology, 14. Elsevier Publ. Co., Amsterdam.

GLOSSARY OF GEOLOGY (1972) Ed. Gary, M., McAfee, R., and Wolf, C.L. American Geological Institute, Washington D.C. 805 p.

GOUDIE, A., (1970) Experimental investigation of rock weathering by salts. Area, 4, 42-48.

————, (1972) The chemistry of world calcrete deposits. Jour. Geol., 80, 449-463.

————, (1973) Duricrusts in Tropical and Subtropical Landscapes. Clarendon Press, Oxford. 174 p.

GRAF, D.L., (1960) Geochemistry of carbonate sediments and sedimentary carbonate rocks. Illinois State Geol. Surv. Circular 297. Parts I - IV.

GRIFFITH, W.P., and WICKINS, T.D., (1968) Cis-Dioxo- and Trioxo-complexes. Jour. Chem. Soc., (A), 400-404.

GRUTT, E.W., (1972) Prospecting criteria for sandstone-type uranium deposits, 47-78. In Uranium Prospecting Handbook.

Ed's Bowie, S.H.U., Davis, M., and Ostle D. Inst. Min. and Met., London.

HAMLIN, A.G., ROBERTS, B.J., and WALKER, S.G., (1961) Separation of uranium by reversed-phase partition chromatography on a Kel-F column. Anal. Chem., 33, 1547-1552.

HANSULD, J.A., (1966) Behaviour of molybdenum in secondary dispersion media - a new look at an old geochemical puzzle. Min. Engineering, 18, 73-77.

HART, T.J., and CURRIE, R.I., (1960) The Benguela Current. Discovery Reports, 31, 123-298.

HASKIN, L.A., FREY, F.A., SCHMITT, R.A., and SMITH, R.H., (1966) Meteoritic, solar, and terrestrial rare-earth distributions. Physics and Chemistry of the Earth, 7, 169-321.

HELGESON, H.C., GARRELS, R.M., and MACKENZIE, F.T., (1969) Evaluations of irreversible reactions in geochemical processes involving minerals and aqueous solutions - II. Applications. Geochimica et Cosmochimica Acta, 33, 455-481.

HELLWIG, D.H.R. (1969) Mineral composition and concentration of underground water in the Namib Desert. Symp. CSIR, Pretoria. Ground-water in Southern Africa. 12 p.

HERBOSCH, A., (1974) Facteurs controlant la distribution des elements dans les shales uraniferes du basin Permian de Lodeve (Herault, France). Proc. Symp. IAEA, Athens, Formation of Uranium Ore Deposits, 359-380.

HERRMANN, A.G., (1969) Yttrium and Lanthanides. In Handbook of Geochemistry, 2. Springer-Verlag, Berlin. Ed. Wedepohl, K.H.

HESS, P.C., (1966) Phase equilibria of some minerals in the K_2O-Na_2O-Al_2O_3-SiO_2-H_2O System at 25 °C and one atmosphere. Am. Jour. Sci., 264, 289-309.

HOSTETLER, P.B., and GARRELS R.M., (1962) Transportation and precipitation of uranium and vanadium at low temperatures, with special reference to sandstone-type uranium deposits. Econ. Geol., 57, 137-167.

HUGO, P.J., (1974) Damara nomenclature. Proc. Symp. Pelindaba. Uranium Exploration, 8 p.

JACOB, R.E., (1974) Geology and Metamorphic Petrology of Part of the Damara Orogen along the Lower Swakop River, South West Africa. Precambrian Res. Unit, Univ. Cape Town Bull. 17. 185 p.

KAPLAN, I.R., (1974) Biological cycling of elements and stable isotopes in marine environments. Prog. Report UCLA-34PA, 134-10. 16 p.

KASPAR, J., and HEJL, V., (1970) Thermodynamic conditions of the origin of uraninites. Proc. Symp. IAEA, Vienna, Uranium Exploration Geology, 301-314.

KING, L.C., (1963) South African Scenery, a Textbook of Geomorphology. Oliver and Boyd, Edinburgh. 308 p.

KOLJONEN, T., and ROSENBERG, R.J., (1974) Rare-earth elements in granitic rocks. Lithos, 7, 249-261.

KOLODNY, Y., and KAPLAN, I.R., (1970) Uranium isotopes in sea-floor phosphorites. Geochimica et Cosmochimica Acta, 34, 3-24.

KRAMER, J.R., (1969) Subsurface brines and mineral equilibria. Chem. Geol., 4, 37-50.

KRAUS, K.A., and NELSON, F., (1956) Anion exchange studies of the fission products. Proc. Intern. Conf., Geneva. Peaceful Uses of Atomic Energy, 7, 113-125.

————————, MOORE, G.E., and NELSON, F., (1956) Th (IV) and U (IV) in hydrochloric acid. Separation of thorium, protactinium and uranium. Jour. Am. Chem. Soc., 78, 2692-2694.

KRAUSKOPF, K.B., (1956) Factors controlling the concentrations of thirteen rare metals in seawater. Geochimica et Cosmochimica Acta, 9, 1-32.

LANGFORD, F.F., (1974) A supergene origin for vein-type uranium ores in the light of the Western Australian calcrete-carnotite deposits. Econ. Geol., 64, 516-526.

LEDERER, C.M., HOLLANDER, J.M., and PERLMAN, I., (1968) Table of Isotopes. John Wiley & Sons Inc., New York. 592 p.

MABBUTT, J.A., (1952) The evolution of the middle Ugab Valley, Damaraland, South West Africa. Roy. Soc. S. Afr. Trans., 33, 333-365.

MACKENZIE, F.T., and GARRELS, R.M., (1965) Silicate-reactivity with seawater. Science, 150, 57-58.

————————, and BRICKER, O.P., (1971) Cementation of sediments by carbonate minerals. Bermuda Biological Station for Research. Carbonate Cements Contrib., 493, 239-246.

MARTIN, H., (1963) A suggested theory for the origin and a brief description of some gypsum deposits of South West Africa. Trans. Geol. Soc. S. Afr., 66, 345-350.

MEYER, K., (1973) Uran-Prospektion vor Südwestafrika. Erzmetal, 26, 313-317.

MITCHELL, R.F., (1960) Electrodeposition of actinide elements at trace concentrations. Anal. Chem., 32, 326-328.

MOREY, G.W., FOURNIER, R.O., and ROWE, J.J., (1964) The solubility of amorphous silica at 25 °C. Jour. Geophys. Res., 69, 1995-2002.

MORRISON, G.H., GERARD, J.T., TRAVESI, A., CURRIE, R.L., PETERSON, S.F., and POTTER, N.M., (1969) Multi-element neutron activation analysis of rock using chemical group separations and high resolution gamma spectrometry. Anal. Chem., 41, 1633-1637.

NAGEL, J.F.,(1962) Fog precipitation measurements on Africa's southwest coast. Notos, 11, 51-60.

NELSON, F., RUSH, R.M., and KRAUS, K.A., (1960) Adsorbability of a number of elements in HCl-HF solutions. Jour. Am. Chem. Soc., 82, 339-348.

NETTERBERG, F., (1969a) Ages of calcretes in Southern Africa. S. Afr. Archaeological Bull., 24, 88-92.

————————, (1969b) The Geology and Engineering Properties of South African Calcretes. Ph.D. thesis, Unpubl., Univ. of Witwatersrand.

————————, (1971) Calcrete in road construction. CSIR Res. Rep. 286. NIRR Bull., 10. 73 p.

NISSENBAUM, A., and KAPLAN, I.R., (1972) Chemical and isotopic evidence for the in situ origin of marine humic substances. Limnol and Oceanogra., 17, 570-582.

OSTLE, D., and BALL, T.K. (1973) Some aspects of geochemical surveys for uranium. Proc. Symp. IAEA, Vienna. Uranium Exploration Methods, 171-187.

OECD NUCLEAR ENERGY AGENCY (1973) Uranium; Resources, Production and Demand. 140 p.

PARKER, J. Wm., (1969) Water history of Cretaceous aquifers, East Texas Basin. Chem. Geol., 4, 111-133.

PHILPOTTS, J.A., and SCHNETZLER, C.C., (1968) Europium anomalies and the genesis of basalt. Chem. Geol., 3, 5-13.

POTY, B.P., LEROY, J., and CUNEY, M., (1974) Les inclusions fluides dans les minerais des gisements d'uranium intergranitiques du Limousin et du Forz (Massif Central, France). Proc. Symp. IAEA, Athens. Formation of Uranium Ore Deposits, 569-582.

RACKLEY, R., (1972) Environment of Wyoming Tertiary uranium deposits. Am. Assoc. Petrol. Geol. Bull., 56, 755-774.

RASMUSSEN, S.E., (1973) Neutron activation analysis of samples from the Kimberley Reef conglomerate. NIM. Report, 1563. 241 p.

ROALDSET, E., (1973) Rare-earth elements in Quarternary clays of the Numedal area, Southern Norway. Lithos, 6, 349-372.

RONA, E., and JOENSU, O., (1974) Uranium geochemistry in the Black Sea. Am. Assoc. Petrol. Geol., 20, 570-572.

RONOV, A.B., BALASHOV, Yu. A., and MIGDISOV, A.A. (1967) Geochemistry of the rare earths in the sedimentary cycle. Geokhimiya, 1, 3-19.

ROSHOLT, J.N., BUTLER, A.P., GARNER, E.L., and SHIELDS, W.R., (1965) Isotopic fractiona ion of uranium in sandstone, Powder River Basin, Wyoming and Slick Rock District, Colorado. Econ. Geol., 60, 199-213.

————————, DOE, B.R., and TATSUMOTO, M., (1966) Evolution of the isotopic composition of uranium and thorium in soil profiles. Bull. Geol. Soc. Am., 77, 987-1004.

————————, (1967) Open System model for uranium-series dating of Pleistocene samples. Proc. Symp. IAEA, Vienna. Radioactive Dating and Methods of Low Level Counting, 299-311.

————————, (1970) Nuclear methods applied to uranium geochemistry. IEEE Trans. on Nuclear Science, NS-17, 173-176.

RUZICKA, V., (1972) Geological comparisons between East European and Canadian uranium deposits. Geol. Surv. Canada. Paper 70-48. 196 p.

SATO, M., (1960) Oxidation of sulphide ore-bodies, I. Geochemical environments in terms of Eh-pH. Econ. Geol., 55, 928-961.

SMITH, D.A.M., (1965) The Geology of the Area Around the Khan and Swakop Rivers in South West Africa. Geol. Surv. S. Afr., Mem. 3 (SWA Series) 113 p.

SOUTH AFRICAN COMMITTEE FOR STRATIGRAPHY (1971) South African code of stratigraphic terminology and nomenclature. Trans. Geol. Soc. S. Afr., 74, 111-129.

SPENCER, D.W., DEGENS, E.T., and KULBICKI, G., (1968) Factors affecting element distributions in sediments. In Origin and Distribution of Elements, 981-998. Ed. Ahrens, L.H., et al.

STRELOW, F.W.E., (1959) Separation of thorium from rare earths, zirconium, and other elements by cation exchange. Anal. Chem., 31, 1201-1203.

STRONSKI, I., (1969) Separation of some metal anion complexes by extraction chromatography in the system Aliquat-336-hydrochloric acid. Radiochem. Radioanal. Letters, 1, 191-197.

SZABO, B.J., and ROSHOLT, J.N., (1969) Uranium-series dating of Pleistocene molluscan shells from southern California - an open system model. Jour. Geophys. Res., 74, 3253-3260.

SZALAY, S., and SAMSONI, Z., (1969) Investigation of the leaching of uranium from crushed magmatic rock. Geochem. Intern., 6, 613-623.

TAYLOR, S.R., (1965) The application of trace element data to problems in petrology. Physics and Chemistry of the Earth, 6, 133-213.

TOENS, P.D., (1973) The mineral provinces of the Damara Orogenic Belt in South West Africa. Unpubl. Lecture. 9 p.

TRUESDELL, A.H., and JONES, B.F., (1969) Ion associations in natural brines. Chem. Geol., 4, 51-62

TRUSWELL, J., (1970) An Introduction to the Historical Geology of South Africa. Purnell, Cape Town. 167 p.

TURKSTRA, J., SMIT, H.J., and DE WET, W.J., (1971) Non-destructive neutron activation analysis of six South African standard samples utilizing high-resolution gamma spectrometry. Jour. S. Afr. Chem. Inst., 24, 113-125.

VEEH, H.H., CALVERT, S.E., and PRICE, N.B., (1974) Accumulation of uranium in sediments and phosphorites on the South West African Shelf. Mar. Chem., 2, 189-202.

VON BACKSTRÖM, J.W., (1974) Other uranium deposits. Proc. Symp. IAEA, Athens. Formation of Uranium Ore Deposits, 605-624.

WALKER, T.R., (1967) Formation of red beds in modern and ancient deserts. Geol. Soc. Am. Bull., 78, 353-368.

WIEDER, M., and YAALON, D.H., (1974) Effect of matrix composition on carbon te ncdule crystallization. Geoderma, 11, 95-121.

YULE, H.P. (1968) Computation of experimental results in activation analysis. In Modern Trends in Activation Analysis, 2, 1155-1204. NBS spec. publ. 312. Ed. De Voe, J.R., and La Fleur, P.D.

ZIEGLER, V., (1974) Essai de classification metallotectonique des gisements d'uranium. Proc. Symp. IAEA, Athens. Formation of Uranium Ore Deposits, 661-677.

APPENDIX 1

PREPARATION AND PURIFICATION OF THE SPIKES ^{229}Th, ^{233}Pa AND ^{232}U

^{229}Th ($7,3 \times 10^3$ y)

This is not a naturally occurring radioactive isotope and is therefore a very convenient one to use. All the other thorium isotopes are either found naturally or their half-lives are too short to be used. The ^{229}Th spike obtained from Harwell in the UK was not pure for it also contained ^{228}Th, which is naturally occurring. Fortunately this did not interfere with the determinations as ^{228}Th was not being sought. A correction nevertheless had to be applied to the total α-activity of the spike so as to eliminate it from the calculation.

Before ^{229}Th could be calibrated it was purified in the usual manner to remove any daughter products that had grown in. (For example ^{224}Ra and ^{220}Rn from ^{228}Th, and ^{225}Ac from ^{229}Th). Calibration was done on the same day as purification, otherwise the calibrated value would also include the α-activities of the daughters. Experimentation showed that ^{224}Ra could be detected after six hours.

^{233}Pa (27,4 d)

^{233}Pa was a synthetically prepared radioactive isotope and was produced by irradiating about 10 mg of purified reagent-grade thorium nitrate for 20 minutes in the

pneumatic facility (the method of purification was similar to that used in Table 9). Purification of the ^{233}Pa was necessary to remove all ^{232}Th remaining. The method used was exactly the same as for the general purification of protactinium. A milking procedure was used whenever ^{233}Pa was required. A new sample had to be prepared after two weeks because of the relatively short half-life of ^{233}Pa and the production of ^{233}U. About 70 µℓ of the ^{233}Pa solution was added to the sample and exactly the same volume evaporated to dryness on a separate disc. The γ-count of this disc was used as the initial ^{233}Pa activity, to which the yield correction was normalized.

^{232}U (71,7 y)

^{232}U does not occur naturally. It is, however, useful because it is mono-energetic and does not have other uranium isotope contaminants. The radiochemical centre, Amersham, UK, were the suppliers. Calibration was done after the ^{232}U had been purified using anion exchange in the chloride form (Table 9) from which ^{228}Th and ^{226}Ra daughters were removed.

APPENDIX 2

CALCULATIONS FOR THE DETERMINATION OF CHEMICAL YIELD FOR THORIUM, PROTACTINIUM AND URANIUM ISOTOPES

Nomenclature:

$(Ao)_{230}$ - actual activity of ^{230}Th

A^{m}_{234} - measured activity of ^{234}U

$(Ao)^{STD}_{231}$ - actual activity of ^{231}Pa in standard

A^{STD}_{231} - measured activity of ^{231}Pa in standard

A^{S}_{231} - measured activity of ^{231}Pa in sample

λ_{235} - decay constant of ^{235}U ($9{,}76 \times 10^{-10}$)

λ_{238} - decay constant of ^{238}U ($1{,}54 \times 10^{-10}$)

N_{235} - number of atoms of ^{235}U

N_{238} - number of atoms of ^{238}U

E_{α} - efficiency of α detector (i.e. geometry)

E_{γ} - efficiency of γ detector (i.e. geometry)

Y - chemical yield

Activity values are given per unit counting time, per unit weight. In this work the values were usually given as counts per hour per gram. The actual activity of the spike was corrected for weight, as the calibrated activity was quoted as counts per second per gram in the cases of ^{229}Th and ^{232}U only.

Uranium:

$$(Ao)_{234} = A^{m}_{234} . E_{\alpha} . Y \qquad (1)$$

$$(Ao)_{232} = A^{m}_{232} \cdot E_{\alpha} \cdot Y \qquad (2)$$

As uranium only was involved, the chemical yield (Y) and geometry (E_{α}) was constant for both ^{234}U and ^{238}U respectively. The same applies to ^{238}U.

$$\frac{(Ao)_{234}}{(Ao)_{234}} = \frac{A^{m}_{234}}{A^{m}_{232}} \qquad (3)$$

$$(Ao)_{234} = \frac{A^{m}_{234} \cdot (Ao)_{232}}{A^{m}_{232}} \qquad (4)$$

$$\text{Similarly } (Ao)_{238} = \frac{A^{m}_{238} \cdot (Ao)_{232}}{A^{m}_{232}} \qquad (5)$$

The $^{234}U/^{238}U$ ratio is derived from equations (4) and (5).

Thorium

The thorium spike was a mixture of ^{229}Th and ^{228}Th. A correction must be applied to remove the ^{228}Th activity contribution.

$$(Ao)_{TOTAL} = (Ao)_{229} + (Ao)_{228} \qquad (6)$$

$$(Ao)_{228} = A^{m}_{228} \cdot E_{\alpha} \cdot Y \qquad (7)$$

$$(Ao)_{229} = A^{m}_{229} \cdot E_{\alpha} \cdot Y \qquad (8)$$

$$\frac{(Ao)_{228}}{(Ao)_{229}} = \frac{A^{m}_{228}}{A^{m}_{229}} = R \qquad (9)$$

$$(Ao)_{228} = R(Ao)_{229} \qquad (10)$$

$$(Ao)_{TOTAL} = (Ao)_{229} + R(Ao)_{229} = (Ao)_{229}(1 + R) \qquad (11)$$

$$(Ao)_{229} = \frac{(Ao)_{TOTAL}}{(1 + R)}$$

$$= \frac{(Ao)_{TOTAL}}{1 + \frac{A^m_{228}}{A^m_{229}}} \qquad (12)$$

The value of (1 + R) should be constant for the spike solution. Using the samemethod of calculation, the activity of ^{230}Th is determined as follows:

$$(Ao)_{230} = \frac{A^m_{230} \cdot (Ao)_{229}}{A^m_{229}} \qquad (13)$$

The $^{230}Th/^{234}U$ ratio is derived from equations (4) and (13).

Protactinium

The calculation of the $^{231}Pa/^{234}U$ ratio is slightly more complicated because both isotopes come from different decay chains, the ^{235}U and ^{238}U chains respectively.

$$Pa: \quad (Ao)^{STD}_{231} = (Ao)^{STD}_{235} = \lambda_{235} \cdot N_{235} \qquad (14)$$

$$U: \quad (Ao)^{STD}_{234} = (Ao)^{STD}_{238} = \lambda_{238} \cdot N_{238} \qquad (15)$$

$$\left[\frac{(Ao)_{231}}{(Ao)_{234}}\right]^{STD} = \left[\frac{\lambda_{235}}{\lambda_{238}} \cdot \frac{N_{235}}{N_{238}}\right]^{STD} \qquad (16)$$

Relationships in equation (16) were determined from a standard uranothorianite sample from Phalaborwa which was in radioactive equilibrium. The atom ratio (N_{235}/N_{238}) is determined by mass spectrometer.

<u>Pa</u>:

$$\left.\begin{aligned}(Ao)^{STD}_{231} &= A^{STD}_{231}.Y^{1}.E_{\alpha}\\ (Ao)^{S}_{231} &= A^{S}_{231}.Y.E_{\alpha}\end{aligned}\right\} \quad (\alpha\text{-spectrometer}) \qquad (17)$$

$$\left.\begin{aligned}(Ao)^{STD}_{233} &= A^{STD}_{233}.Y^{1}.E_{\gamma}\\ (Ao)^{S}_{233} &= A^{S}_{233}.Y.E_{\gamma}\end{aligned}\right\} \quad (\gamma\text{-spectrometer}) \qquad (18)$$

$$\frac{A^{STD}_{231}}{A^{S}_{231}} = \frac{(Ao)^{STD}_{231}}{(Ao)^{S}_{231}}.\frac{Y}{Y^{1}} \qquad (19)$$

$$\frac{A^{STD}_{233}}{A^{S}_{233}} = \frac{(Ao)^{STD}_{233}}{(Ao)^{S}_{233}}.\frac{Y}{Y^{1}} \qquad (20)$$

Combine equations (19) and (20),

$$\frac{A^{STD}_{231}}{A^{S}_{231}}.\frac{A^{STD}_{233}}{A^{S}_{233}} = \frac{(Ao)^{STD}_{231}}{(Ao)^{S}_{231}}.\frac{(Ao)^{STD}_{233}}{(Ao)^{S}_{233}} \qquad (22)$$

<u>U</u>:

$$\left.\begin{aligned}(Ao)^{STD}_{234} &= A^{STD}_{234}.Y^{11}.E_{\alpha}\\ (Ao)^{S}_{234} &= A^{S}_{234}.Y^{11}.E_{\alpha}\end{aligned}\right\} \quad (\alpha\text{-spectrometer}) \qquad (23)$$

$$\frac{A^{STD}_{234}}{A^{S}_{234}} = \frac{(Ao)^{STD}_{234}}{(Ao)^{S}_{234}}.\frac{Y^{11}}{Y^{11}} \qquad (24)$$

$$\left.\begin{aligned}(Ao)^{STD}_{232} &= A^{STD}_{232}.Y^{11}.E_{\alpha}\\ (Ao)^{S}_{232} &= A^{S}_{232}.Y^{111}.E_{\alpha}\end{aligned}\right\} \quad (\alpha\text{-spectrometer}) \qquad (25)$$

$$\frac{A^{STD}_{232}}{A^{S}_{232}} = \frac{(Ao)^{STD}_{232}}{(Ao)^{S}_{232}} \cdot \frac{Y^{111}}{Y^{11}} \qquad (26)$$

Combine equations (24) and (26)

$$\frac{A^{STD}_{234}}{A^{S}_{234}} \cdot \frac{A^{STD}_{232}}{A^{S}_{232}} = \frac{(Ao)^{STD}_{234}}{(Ao)^{S}_{234}} \cdot \frac{(Ao)^{STD}_{232}}{(Ao)^{S}_{232}} \qquad (27)$$

Now

$$\frac{A^{S}_{231}}{A^{S}_{234}} = \frac{A^{S}_{231}}{A^{STD}_{231}} \cdot \frac{A^{STD}_{231}}{A^{STD}_{234}} \cdot \frac{A^{STD}_{234}}{A^{S}_{234}} \qquad (28)$$

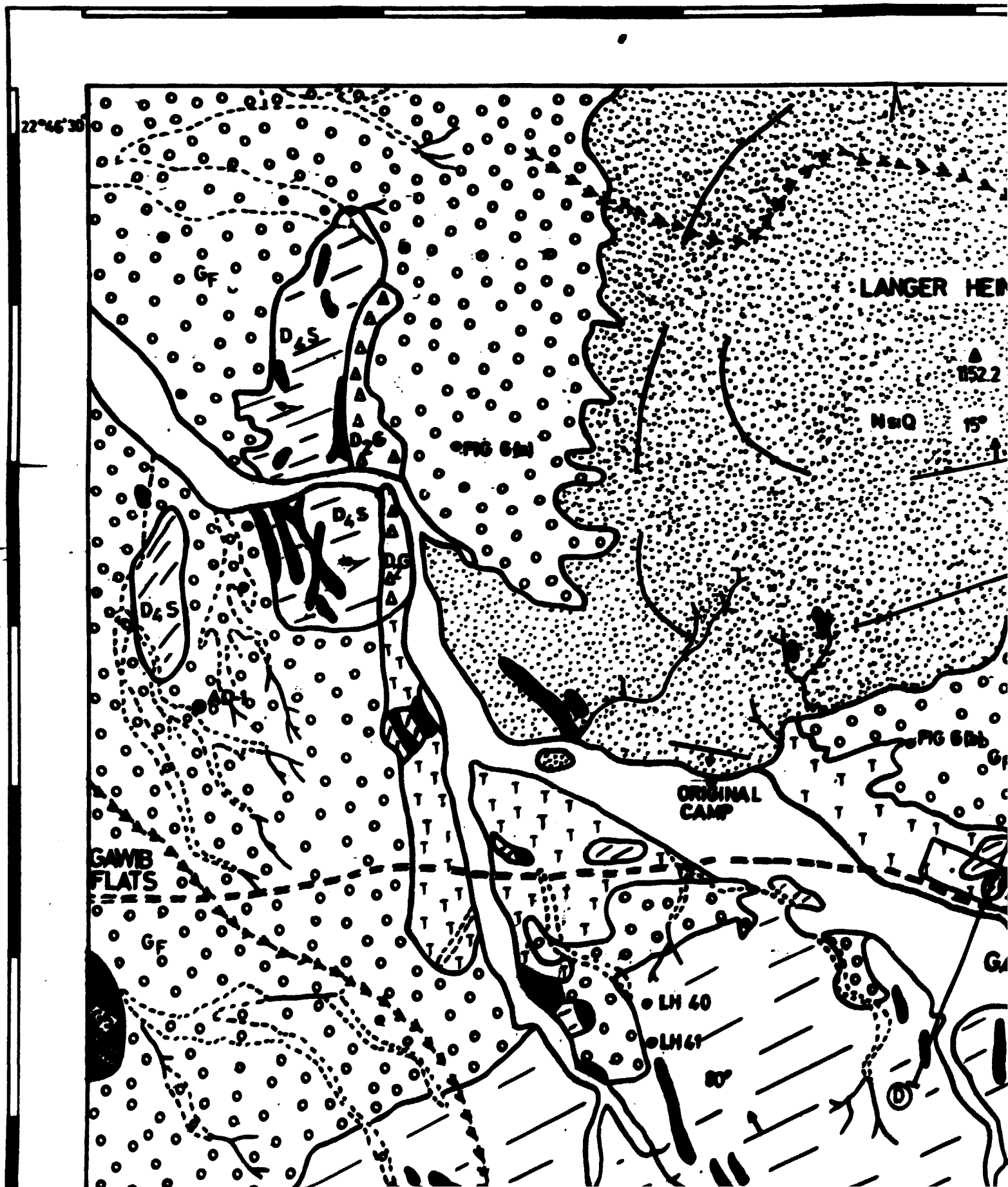
Substitute equations (16), (22) and (27) into (28)

$$\frac{A^{S}_{231}}{A^{S}_{234}} = \frac{\left[\frac{\lambda_{235}}{\lambda_{238}} \cdot \frac{N_{235}}{N_{238}}\right]^{STD} \cdot \frac{(Ao)^{STD}_{234}}{Ao)^{S}_{234}} \cdot \frac{A^{STD}_{232}}{A^{S}_{232}} \cdot \frac{(Ao)^{STD}_{233}}{(Ao)^{S}_{233}}}{\frac{(Ao)^{STD}_{232}}{(Ao)^{S}_{232}} \cdot \frac{A^{STD}_{233}}{A^{S}_{233}} \cdot \frac{(Ao)^{STD}_{231}}{(Ao)^{S}_{231}}} \qquad (29)$$

$$= \frac{^{231}Pa}{^{234}U} \quad \text{in sample} \qquad (30)$$

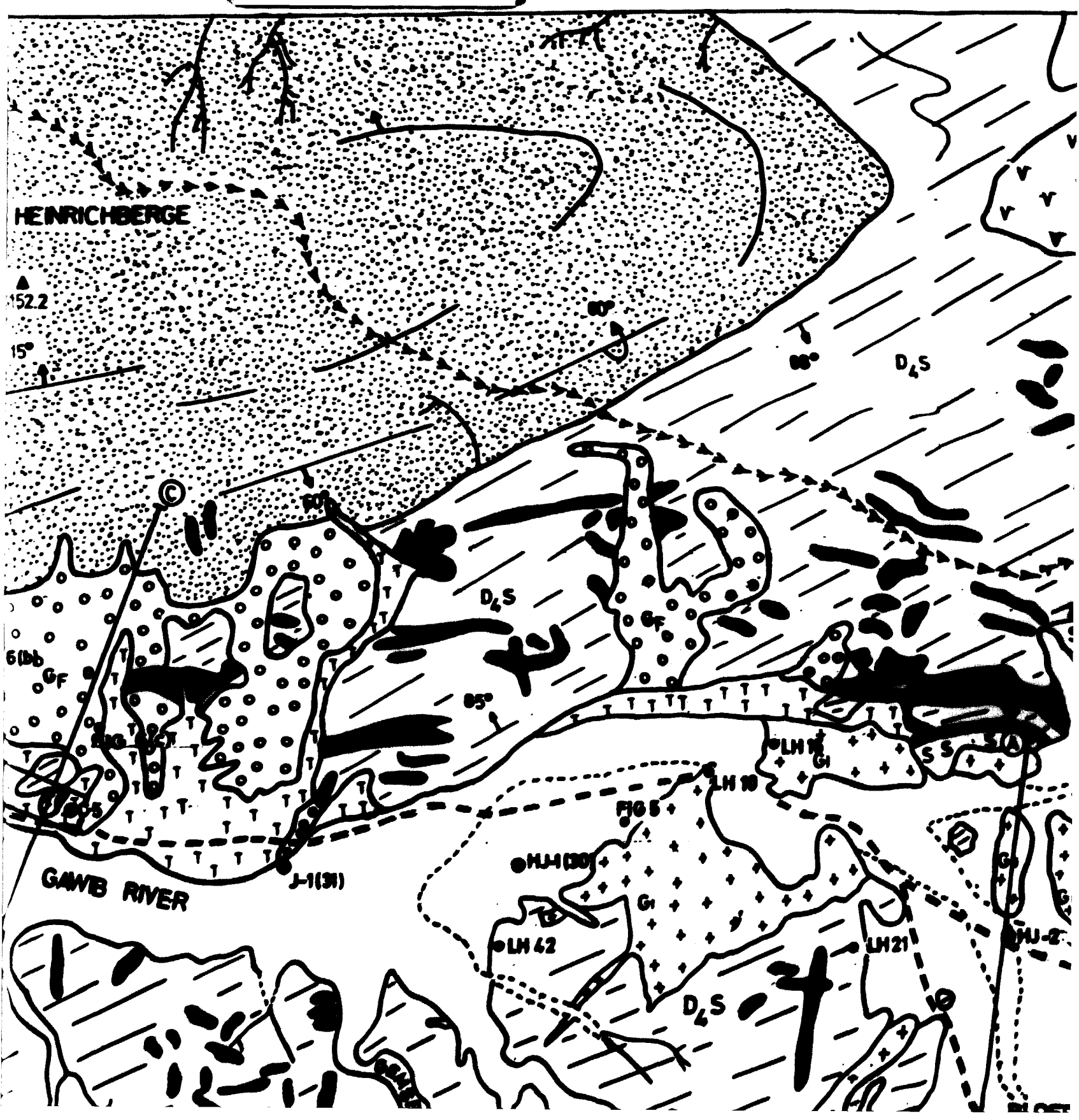
SECTION 1

GEOLOGICAL MAP O



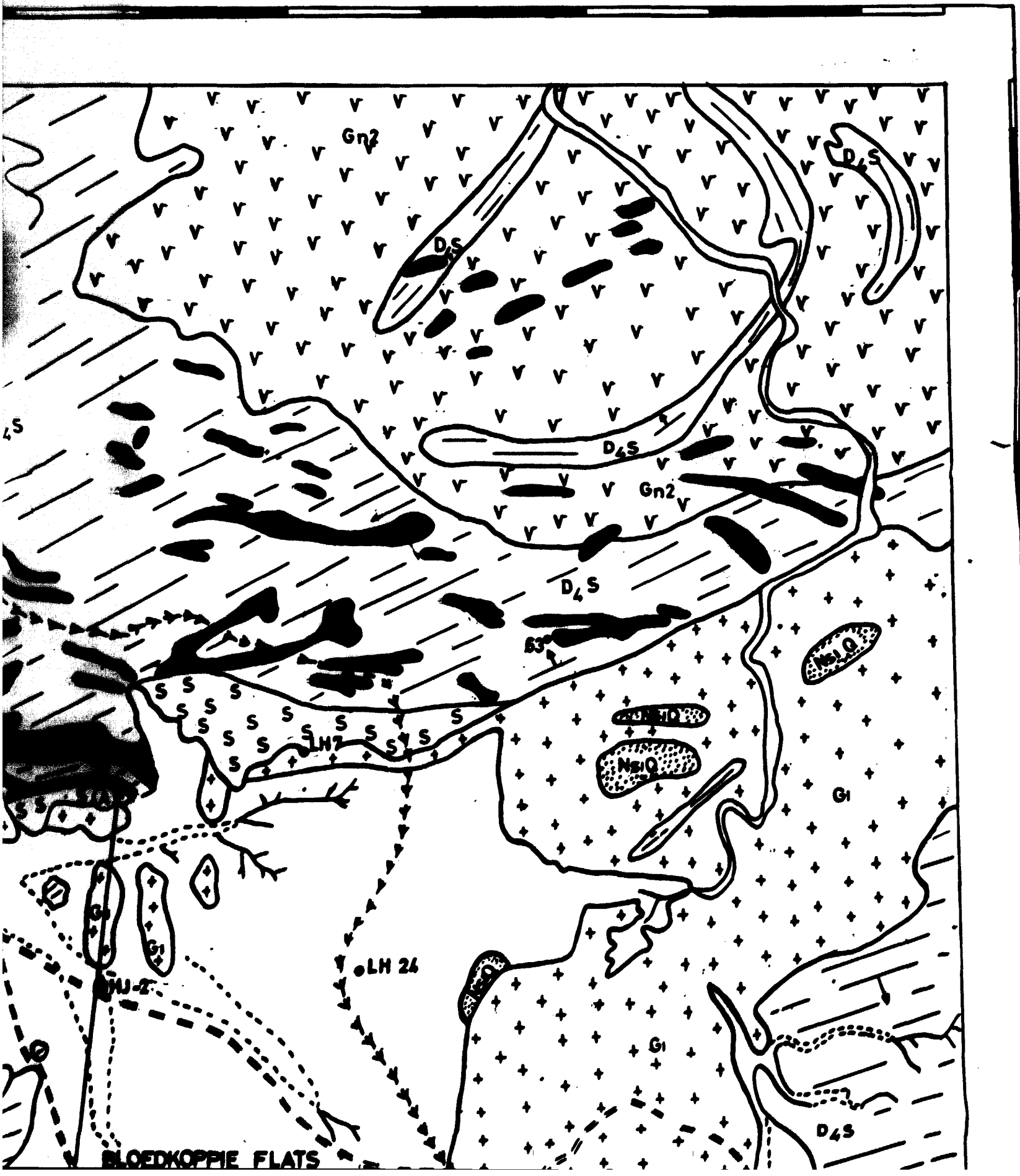
OF THE LANGER HEINRICH AND ENVI

SECTION 2



ENVIRONMENTS, SWA

SECTION 3



LEGEND

SECTION 4


SUPERFICAL GRAVELS


GEMSBOK CALCRETE FORMATION



HARD PAN] LANGER HEINRICH CALCRETE FORMATION


PEGMATITE; APLITE; QUARTZ VEIN



HOREBIS GRANITE] POST SWAKOP



GAWIB GRANITE



BLOEDKOPPIE GRANITE] SWAKOP



TINKAS FORMATION
CHUOS FORMATION] KHOMAS SUB GROUP] SWAKOP GROUP

METAMORPHIC EQUIVALENT



SALEM GRANITE



ETUSIS FORMATION] NOSIB GROUP


STREAMS AND DRAINAGE CHANNELS

ROAD

WATERSHED

TRACE OF GEOLOGICAL PROFILE



TRIGONOMETRICAL BEACON WITH HEIGHT IN METERES



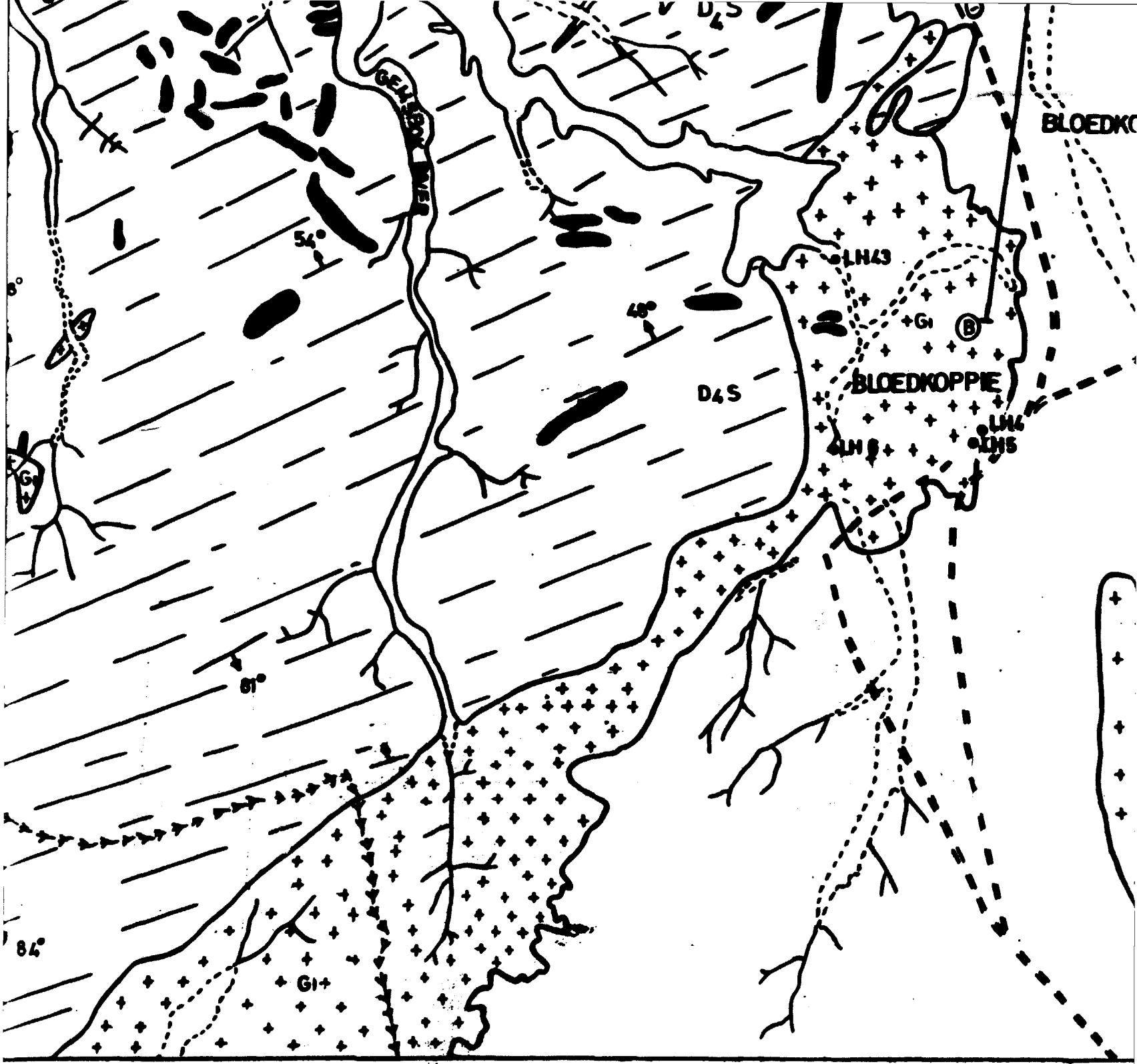
BEDDING INCLINED, VERTICAL, INVERTED



1: 25000

1000 500 0 1000 2000 3000 Met

MAP I SECTION E

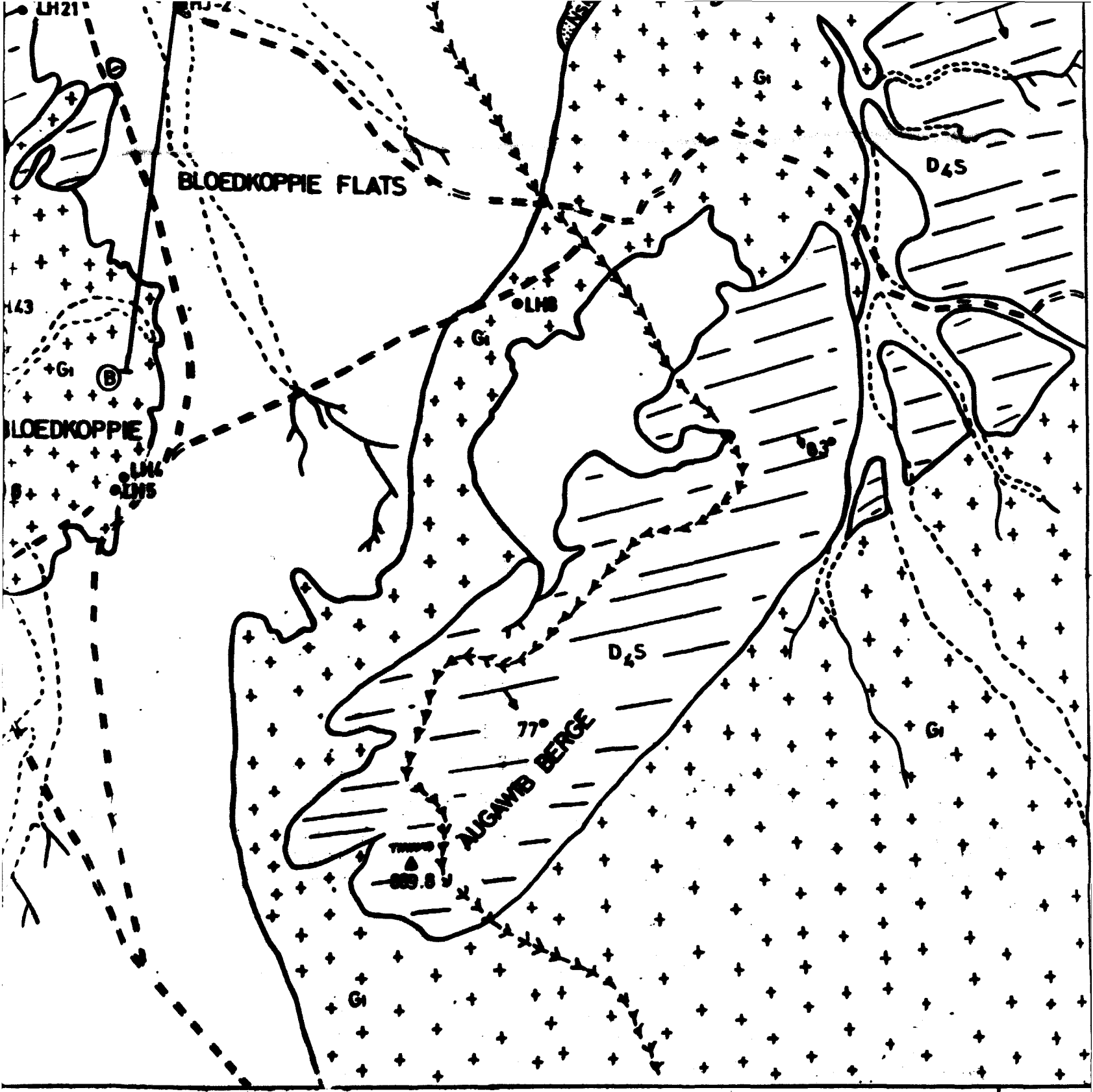


SECTION 6

3000 Meters

TRUE N

MAG. N


LH21
BLOEDKOPPIE FLATS
LH8
Gi
D4S
BLOEDKOPPIE
LH6
LH5
77°
AUGAWIB BERGE
15°26'00"

SECTION 7

STREAMS AND DRAINAGE CHANNELS

ROAD

WATERSHED

TRACE OF GEOLOGICAL PROFILE

869.8 TRIGONOMETRICAL BEACON WITH HEIGHT IN METERES

68° BEDDING INCLINED, VERTICAL, INVERTED

DIRECTION OF SCHISTOSITY

LITHOLOGICAL BOUNDARIES

LOCALITY OF FIGS 10 AND 11 (SEE TEXT)

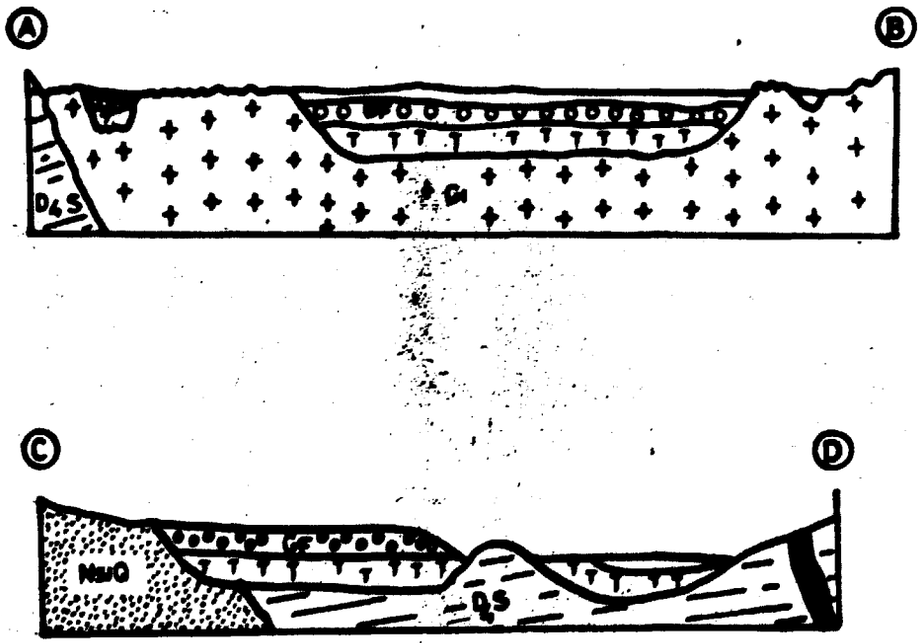
•FIG 6(a) LOCALITY OF PROFILE "IN FIG 6 (a) etc.

• LH4 SAMPLE LOCALITY

SECTIONS

SCALES

HORIZONTAL : 1:25 000
VERTICAL : NOT TO SCALE



SECTION 8